Aspects of Quantum Information and AdS/CFT Duality

by

Abdulrahim Al Balushi

A thesis
presented to the University of Waterloo
in fulfillment of the
thesis requirement for the degree of
Doctor of Philosophy
in
Physics

Waterloo, Ontario, Canada, 2021

Examining Committee Membership

The following served on the Examining Committee for this thesis. The decision of the Examining Committee is by majority vote.

External Examiner:	Alex Maloney Professor, McGill University
Supervisor:	Robert Mann Professor, University of Waterloo
Internal-External Member:	Achim Kempf Professor, University of Waterloo
Committee Member:	Niayesh Afshordi Associate Professor, University of Waterloo
Committee Member:	Jon Yard Associate Professor, University of Waterloo

Author's Declaration

This thesis consists of material all of which I authored or co-authored: see Statement of Contributions included in the thesis. This is a true copy of the thesis, including any required final revisions, as accepted by my examiners.

I understand that my thesis may be made electronically available to the public.

Statement of Contributions

This thesis is based on the following publications.

- Chapter 2 is based on:
  - A. Al Balushi, R. A. Hennigar, H. K. Kunduri and R. B. Mann, *Holographic complexity of rotating black holes*, 2010.11203
  - A. Al Balushi, R. A. Hennigar, H. K. Kunduri and R. B. Mann, *Holographic Complexity and Thermodynamic Volume*, *Phys. Rev. Lett.* **126** (2021) 101601, [2008.09138]
  - A. Al Balushi and R. B. Mann, *Null hypersurfaces in Kerr–(A)dS spacetimes*, *Class. Quant. Grav.* **36** (2019) 245017, [1909.06419]
  - M. T. N. Imseis, A. Al Balushi and R. B. Mann, *Null Hypersurfaces in Kerr-Newman-AdS Black Hole and Super-Entropic Black Hole Spacetimes*, *Class. Quant. Grav.* **38** (2021) 045018, [2007.04354]

  Most of the text of the chapter is based on the first paper, with extra modifications to clarify the presentation and correct some typos.

  A. Al Balushi did the calculations on the late-time rate of growth of complexity. R. A. Hennigar and A. Al Balushi did the calculations on the complexity of formation. R. A. Hennigar performed the numerical calculations. All authors contributed to the writing of the paper.

- Chapter 3 is based on:
  - A. Al Balushi, Z. Wang and D. Marolf, *Traversability of Multi-Boundary Wormholes*, *JHEP* **04** (2021) 083, [2012.04635]

  Most of the text of the chapter is based on the paper, with extra modifications to clarify the presentation and correct some typos.

  A. Al Balushi did the calculations on the properties of the hot limit. Z. Wang did the calculations on the total amount of time advance. All authors contributed to the writing of the paper.

- Chapter 4 is based on:
  - A. Al Balushi, W. Cong and R. B. Mann, *Optomechanical quantum Cavendish experiment*, *Phys. Rev. A* **98** (2018) 043811, [1806.06008]

  Most of the text of the chapter is based on the paper, with significant modifications to clarify and update the presentation as well as correct some typos.

  A. Al Balushi came up with the idea of the set-up. A. Al Balushi and W. Cong did the calculations and wrote the paper, with input from R. B. Mann.

- Chapter 5 is based on:
  - R. R. Ferguson, L. Dellantonio, A. Al Balushi, K. Jansen, W. Dür and C. A. Muschik, *A measurement-based variational quantum eigensolver*, 2010.13940 [To appear in Physical Review Letters]

  Most of the text of the chapter is based on the paper, with significant modifications and additions to clarify and update the presentation as well as correct some typos.

  A. Al Balushi did the simulations on the Schwinger model. R. R. Ferguson did the simulations on the perturbed toric code model. L. Dellantonio produced the figures. R. R. Ferguson wrote the first draft of the paper, with significant subsequent expansions and modifications by all the authors.

- Contributions not included in the thesis:
  - Z.-W. Wang, A. Al Balushi, R. Mann and H.-M. Jiang, *Safe Trinification*, *Phys. Rev. D* **99** (2019) 115017, [1812.11085]

Abstract

This thesis considers four different aspects of quantum information, AdS/CFT duality, and the interplay between them.

First, we study the holographic complexity conjectures in detail for rotating black holes. We focus on a particular class of odd-dimensional equal-spinning black holes for which considerable simplifications occur. We study the complexity of formation, uncovering a direct relation between the complexity of formation and thermodynamic volume for large black holes. We also consider the late-time growth of complexity, finding that at late times the growth approaches a constant, and that Lloyd's bound is generically violated.

Second, we generalize the Gao-Jafferis-Wall construction of traversable two-sided wormholes to multi-boundary wormholes in asymptotically AdS spacetimes in three dimensions. By focusing on a particular limit of the geometries where the horizons are exponentially close to each other, and with the three-boundary wormhole as our main example, we show that traversability between any two asymptotic regions in a multi-boundary wormhole can be achieved. We discuss how this construction differ from that of Gao-Jafferis-Wall and comment on its generalization to the case with non-trivial topologies.

Third, we propose an experimental set-up that uses well-tested techniques in cavity optomechanics to observe the effects of the gravitational interaction between two quantum micro-mechanical oscillators on the interference pattern of cavity photons through shifts in the visibility of interfering photons. We show that the gravitational coupling leads to a quantifiable shift in the period and magnitude of the visibility whose observability is within reach of current technology. We discuss the feasibility of the set-up as well as the gravity-induced entanglement between the two oscillators.

Finally, we propose a new approach to variational quantum eigensolver algorithms using the principles of measurement-based quantum computing. In contrast to the circuit-based model, our approach uses entangled resource states and local measurements to do the function evaluations. We illustrate this with two schemes. The first scheme shows how any circuit-based variational quantum eigensolver can be translated to a measurement-based one. The second scheme provides a new approach for constructing variational families that has no immediate analogue in circuit-based quantum computing. We discuss how both schemes offer problem-specific advantages in terms of the required resources and coherence times.

Acknowledgements

This thesis owes its existence to many people. Here, I would like to thank a number of them.

First, I thank my family for their unwavering support and encouragement, and for the value they placed on my education.

Second, I thank my supervisor Robert Mann for his guidance and support in both research and professional matters. I am deeply thankful for your patience and understanding.

Third, I have benefited greatly from discussions with many excellent researchers in quantum gravity and quantum information. I thank Ahmed Almheiri and Donald Marolf for many useful discussions in quantum gravity and for their patient explanations and answers to my questions. I also thank Luca Dellantonio, Ryan Ferguson and Christine Muschik for our work in quantum simulations.

Fourth, I thank all my collaborators for making research more fun. Special thanks to Robie Hennigar and Zhencheng Wang for their valuable input.

Last but not least, I thank all my committee members for taking the time from their schedules to be part of my thesis examination.

Table of contents

List of Tables

List of Figures

Chapter 1

Introduction

The motivation to find a theory of quantum gravity goes beyond the aesthetics of having a unified theory of the fundamental forces in physics. There are many phenomenon in the universe whose understanding seem to require precisely such a theory, such as the singularity at the beginning of the universe and the interior of black holes. Unlike other fundamental theories of physics, there is no experimental input to guide the development of any theory of quantum gravity. Ultimately, this is due to the fact that gravity is many orders of magnitude weaker than all other forces of nature at accessible energy scales. However, as Einstein taught us in formulating his theories of special and general relativity, one can still make progress in theoretical physics by relying only on thought experiments and theoretical considerations.

Black holes, besides being fascinating astrophysical objects in their own right, have become the standard theoretical tool by which quantum gravity is studied. This is because it stretches spacetime to an extent that allows Planck-scale dynamics to be relevant for low-energy experiments. This phenomenon was first famously illustrated by Hawking [9, 10], who showed, first, that it leads to black hole evaporation and, second, that this evaporation process is inconsistent with unitary evolution of quantum mechanics. This is the famous 'Black Hole Information Problem', which has become the central problem in quantum gravity research since Hawking first formulated it. Any theory of quantum gravity is expected to provide a clear answer to this problem.

Another clue for quantum gravity came from the study of black hole thermodynamics. The Bekenstein-Hawking entropy [11] indicates that the number of degrees of freedom in a black hole is proportional to its area. This is surprising since, in most thermal systems, the number of degrees of freedom is always proportional to the volume of the system. It

was proposed by 't Hooft [12] and Susskind [13] that this, in fact, is a feature of quantum gravity, which came to be known as the holographic principle. This is the idea that, in any quantum system that involves gravity, the degrees of freedom of the system are secretly encoded at the boundary of the volume it occupies [14].

The holographic principle is backed by evidence from one of the leading approaches to quantum gravity, namely string theory. Our best understood and defined aspect of quantum gravity within string theory is the AdS/CFT duality [15, 16, 17], which is a perfect realization of the holographic principle, as it shows that quantum gravity defined in anti de Sitter (AdS) spacetime is dual to a conformal field theory (CFT) living on the boundary of the spacetime. This provides a complete non-perturbative description of the gravitational theory in terms of a quantum field theory, and any question on one side should, in principle, have a well-defined and computable answer on the other one.

Ever since its discovery, the AdS/CFT duality has been at the centre of many recent advances in quantum gravity research. A large part of this work has gone to understanding the dictionary that encodes the geometry of spacetime as quantum information in the boundary CFT state; see [18, 19, 20, 21, 22] for reviews on these advances. These developments have culminated recently in a remarkable series of calculations of the quantum information content of evaporating black holes [23, 24, 25], which explicitly show that the entropy of radiation of evaporating black holes follows the Page curve [26]. It was then shown [27, 28] that these results can also be derived purely from the gravitational path integral, without assuming asymptotically AdS spacetimes or holography (see [29] for a review). This example best illustrates one of the reasons why studying quantum gravity in an imaginary universe with negative cosmological constant is not a waste of time: more often than not, the general lessons learned are applicable to other spacetimes, including our universe.

A large part of this thesis is concerned with understanding several aspects that lie at the interface between AdS/CFT duality and quantum information. Therefore, to provide context for this content, we begin with a high-level introduction and overview to AdS spacetime and the AdS/CFT duality, based on the discussions in [19, 20, 21, 22].

1.1 The anti de Sitter universe

AdS spacetime is the simplest maximally-symmetric solution of Einstein equations with a negative cosmological constant. Its geometry is best illustrated by considering a $(D+1)$-dimensional flat spacetime with two time directions, U and V. The metric for this

spacetime is then

$$ds^2 = -dU^2 - dV^2 + dX_1^2 + \cdots + dX_{D-1}^2. \tag{1.1}$$

The AdS spacetime is the D-dimensional hyperboloid embedded in this geometry with constraints

$$-U^2 - V^2 + X_1^2 + \cdots + X_{D-1}^2 = -\ell^2, \tag{1.2}$$

where ℓ is the AdS length, which is related to the cosmological constant Λ by

$$\Lambda = -\frac{(D-1)(D-2)}{2\ell^2}. \tag{1.3}$$

This hyperboloid can be conveniently covered by so-called global coordinates

$$U = \sqrt{\ell^2 + r^2}\cos(t/\ell), \quad V = \sqrt{\ell^2 + r^2}\sin(t/\ell), \quad X_i = r\hat{\mu}_i \tag{1.4}$$

where $\sum_i \hat{\mu}_i^2 = 1$ and $\hat{\mu}_i$ represent the angular coordinates on a sphere. The induced metric on the hyperboloid (1.2) in terms of these coordinates then becomes

$$ds^2 = -\left(1 + r^2/\ell^2\right)dt^2 + \left(1 + r^2/\ell^2\right)^{-1}dr^2 + r^2 d\Omega_{D-2}^2, \tag{1.5}$$

where $r \in [0, \infty)$, $t \in (-\infty, \infty)$, and $d\Omega_{D-2}^2$ is the standard line element on the $(D-2)$-dimensional unit sphere. Note that, for $r/\ell \ll 1$, the geometry manifestly resembles Minkowski spacetime. However, as $r/\ell \to \infty$, we start to see the interesting boundary structure that distinguishes AdS spacetime. The easiest way to describe this is with a Penrose diagram, which can be obtained by rewriting the metric after the coordinate transformation $r = \ell \tan\rho$

$$ds^2 = \frac{1}{\cos^2\rho}\left[-dt^2 + \ell^2 d\rho^2 + \ell^2 \sin^2\rho \, d\Omega_{D-2}^2\right], \tag{1.6}$$

where $\rho \in [0, \pi/2)$. By conformal compactification, we can ignore the divergent prefactor and draw the Penrose diagram shown in figure 1.1, including the boundary at $\rho = \pi/2$. We see that the main feature of AdS spacetime is that it has a timelike boundary of topology $\mathbb{R} \times S^{D-2}$, where $\mathbb{R}$ is the time direction. To illustrate, consider the radial geodesic equation in AdS spacetime

$$\left(\frac{dr(\tau)}{d\tau}\right)^2 - E^2 + 1 + \frac{r(\tau)^2}{\ell^2} = 0. \tag{1.7}$$

The constant E is the conserved energy associated with the Killing vector ∂_t. From this, it is easy to see that the equation of motion for timelike geodesics is a simple harmonic motion with period $2\pi\ell$

$$\frac{d^2 r(\tau)}{d\tau^2} + \frac{r}{\ell^2} = 0. \tag{1.8}$$

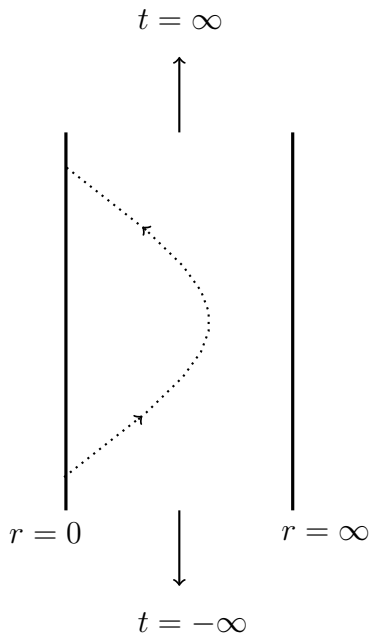

Figure 1.1: The Penrose diagram for AdS spacetime. The left boundary is the origin of polar coordinates at $r = 0$ and the right boundary is the timelike boundary of AdS spacetime at $r = \infty$. The proper time at $r = 0$ is equal to the time coordinate t. This means that a particle sent from the origin to the boundary will return in a finite proper time. Due to the gravitational potential, massive particles cannot reach the boundary of AdS and they follow a similar path to the one shown as the dotted line. The spacetime extends infinitely far in time in both directions.

This shows that AdS spacetime has a confining gravitational potential so that particles released from the origin experience a restoring force that returns them to the origin after $\pi\ell$ proper time, regardless of the initial energy E of the particle.

The AdS spacetime is maximally-symmetric with $D(D+1)/2$ Killing vectors that generate its isometry group $SO(D-1,2)$, which is large enough to send any point in the spacetime to any other point. Note also that, because of its timelike boundary, AdS spacetime is not globally hyperbolic.

A spacetime is said to be asymptotically AdS if it has a timelike boundary of topology $\mathbb{R} \times S^{D-2}$ and if its geometry approaches that of AdS near $r \to \infty$. Perhaps the strongest motivation to study such spacetimes is the AdS/CFT duality, to which we now turn.

1.2 An overview of AdS/CFT duality

The AdS/CFT duality was originally derived in the context of string theory, where it was shown that a type IIB string theory in $\text{AdS}_5 \times S^5$ is equivalent to $\mathcal{N} = 4$ super Yang-Mills theory on $\mathbb{R} \times S^3$ with an $SU(N)$ gauge group [15]. It is generally believed that this result is an example of a more universal statement: any CFT defined on $\mathbb{R} \times S^{D-2}$ (i.e. the boundary) is equivalent to a theory of quantum gravity in asymptotically $\text{AdS}_D \times M$ spacetime (i.e. the bulk), where M is some compact (possibly trivial) manifold. This is an example of a strong/weak duality, since in the limit when the field theory is strongly coupled and has a large number of degrees of freedom (i.e. taking the 't Hooft coupling $\lambda = g^2_{\text{YM}} N$ large while fixing g_{YM}), the gravitational theory becomes fully described by classical general relativity. So, the strongly-coupled regime of field theories that is hard to access perturbatively can now be studied with classical general relatively and its higher curvature extensions [30, 31, 32].

Observables in the boundary and the bulk are related to each other via the AdS/CFT dictionary. The first entry in this dictionary is that the Hilbert spaces of the bulk and boundary theories are isomorphic, $\mathcal{H}_{\text{bulk}} \cong \mathcal{H}_{\text{bdy}}$. This means that the spectrum of the Hamiltonian is the same on both sides, and the symmetry generators of $SO(D-1,2)$ in the CFT are equal to the bulk symmetry generators of asymptotically AdS spacetime. Furthermore, local bulk fields Φ can be related to boundary primary operators $\mathcal{O}$ with conformal dimension Δ by

$$\lim_{r\to\infty} r^{\Delta} \Phi(t, r, \vec{\Omega}) = \mathcal{O}(t, \vec{\Omega}). \tag{1.9}$$

The most interesting CFT theories are those with excitations. Boundary excitations induce field perturbations that propagate from the boundary to the bulk. This is clearly seen by writing the CFT partition function in terms of the quantum gravity partition function

$$Z_{\text{gravity}}[\Phi] = \left\langle \exp\left(\int dt d^{D-2}\vec{\Omega}\ \mathcal{O}\varphi_0 \right) \right\rangle_{\text{CFT}} \tag{1.10}$$

with the understanding that φ_0 is the boundary condition of the bulk field Φ. In the large N limit, the saddle point approximation can be used to evaluate the gravitational partition function, which is the essence of the power of AdS/CFT duality.

The most well-studied entry in the AdS/CFT dictionary in terms of connections with quantum information is the holographic entanglement entropy formula. Entanglement entropy is a field theory quantity used to understand important phenomenon such as quantum phase transitions [33, 34] and the dynamics of strongly correlated systems [35, 36].

For CFTs with well-defined gravitational duals, the entanglement entropy of a boundary spatial region R is given in the bulk simply by

$$S_R = \min_{\mathcal{E}_R} \frac{\mathcal{A}(\mathcal{E}_R)}{4G_N}, \tag{1.11}$$

where $\mathcal{E}_R$ is the bulk surface homologous to R in the boundary and $\mathcal{A}(\mathcal{E}_R)$ is its area. This is the celebrated Ryu-Takayanagi formula [37, 18], which was soon updated to include time-dependence and quantum corrections [38, 39, 40]. It currently reads

$$S_R = \frac{\mathcal{A}(\mathcal{E}_R)}{4G_N} + S_{\text{bulk}}(\mathcal{W}_R), \tag{1.12}$$

where $\mathcal{E}_R$ is now the bulk surface that extremize the entropy and is homologous to R, $\mathcal{W}_R$ is the entanglement wedge of R, and $S_{\text{bulk}}(\mathcal{W}_R)$ is the von Neumann entropy of bulk fields in $\mathcal{W}_R$. The entanglement wedge $\mathcal{W}_R$ is simply the bulk domain of dependence of a partial Cauchy slice Σ_R such that $\partial\Sigma_R = R \cup \mathcal{E}_R$. The quantum extremal surface formula (1.12) has led to many applications and results, and reviewing them all is outside the scope of this thesis. However, we mention here only two results. First, it implied that AdS/CFT dictionary satisfied the feature of subregion-subregion duality, which is the idea that the boundary subregion R encodes all information that is in the bulk subregion $\mathcal{W}_R$ [41, 42, 43]. This was both inspired and explained by the quantum error correction interpretation of AdS/CFT [44, 45], which gave rise to the use of tensor networks as toy models for AdS/CFT duality [46, 47]. Second, the quantum extremal surface formula (1.12) was the basis on which the quantum information content of evaporating black holes was calculated in AdS/CFT [23, 24]. The subsequent derivation of the Page curve from the gravitational path integral [27, 28] implied that the quantum extremal surface formula (1.12) is a general formula for the fine-grained entropy of quantum systems coupled to gravity, and is independent of AdS/CFT duality where it was first proposed [29].

The simplest realization of AdS/CFT duality is that between two copies of CFTs (labeled L and R) prepared in the thermofield double state

$$|\text{TFD}\rangle = \frac{1}{\sqrt{Z(\beta)}} \sum_n e^{-\beta E_n/2} |E_n\rangle_L \otimes |E_n\rangle_R \tag{1.13}$$

and the two-sided (eternal) black hole geometry [48]. There are at least two remarkable consequences of this proposal. First, if we interpret the individual terms in (1.13) in gravity as two disconnected asymptotically AdS geometries, then the proposal implies that the superposition of these disconnected geometries is a two-sided black hole with a

smooth (non-traversable) wormhole connecting the two sides, called the Einstein-Rosen (ER) bridge. This is a manifestation of the ER=EPR idea [49]. Second, if we consider the constant time slice that passes through the bifurcation point of the black hole geometry and calculate the entanglement entropy of either the left or right CFTs, we see that the quantum extremal surface formula (1.12) reduces to the Bekenstein-Hawking entropy formula

$$S_{L/R} = S_{\rm BH} = \frac{\mathcal{A}_{\rm BH}}{4G_N}. \tag{1.14}$$

This is consistent with the fact that, in the thermofield double state, the black hole entropy is equal to the entropy of a single CFT subsystem (i.e. the entanglement entropy measuring the entanglement of the two CFTs with each other).

Finally, it is worth pointing out that, though originally derived in the context of string theory, it has been suggested that AdS/CFT duality is logically independent from string theory. For example, [50] suggested that gauge/gravity dualities exist for any non-Abelian gauge theory. Furthermore, it was argued in [51] that diffeomorphism invariance makes quantum gravity in asymptotically AdS spacetimes holographic.

1.3 Plan of the thesis

The organization of the thesis is as follows:

First, we consider the complexity=volume [52] and complexity=action [53, 54] proposals, which were developed as new entries in the AdS/CFT dictionary that relate the quantum complexity of CFTs with the bulk geometry dual to it. Little success has been achieved in studying these proposals in the context of non-static solutions (e.g. rotating black holes) where, due to technical reasons, the computation of quantities of interest becomes convoluted. In chapter 2, we show how these difficulties can be overcome for a special class of odd-dimensional equally-rotating black holes. Based on this technical advance, we carry out a detailed study of holographic complexity in rotating spacetimes in light of the two proposals. We study the complexity of formation, uncovering a direct relationship between the complexity of formation and thermodynamic volume. We consider also the growth-rate of complexity, finding that at late-times the rate of growth approaches a constant, but that Lloyd's bound is generically violated. Our findings generalize the holographic complexity results found for static black holes to the case when there is no time symmetry.

In chapter 3, we generalize the Gao-Jafferis-Wall [55] construction of traversable two-sided wormholes in asymptotically AdS spacetimes to multi-boundary wormholes. In our

construction, we take the background spacetime to be multi-boundary black holes in AdS_3. To achieve this, we work in the hot limit where the dual CFT state in certain regions locally resembles the thermofield double state. Furthermore, we show that the hot limit makes the causal shadow exponentially small in these regions. Based on these two features of the hot limit, and with the three-boundary wormhole as our main example, we show that traversability between any two asymptotic regions in a multi-boundary wormhole can be triggered using a double-trace deformation. In particular, the two boundary regions need not have the same temperature and angular momentum. We comment on the generalization of this protocol to wormholes with more than three boundaries or with non-trivial topologies. We also discuss the non-trivial angular dependence of traversability in our construction, as well as the effect of the causal shadow region.

In chapter 4, we shift gears and turn away from AdS/CFT duality to consider the experimental study of gravitational effects in quantum regimes. In all experiments conducted so far on the effects of gravity in quantum systems, gravity can be described by classical theories only. It has been suggested that detecting the gravitational field of a mass in superposition state, or witnessing gravity-induced entanglement, would constitute the first experimental proof for the quantum nature of gravity. To this end, we propose an experimental set-up that uses well-tested techniques in cavity optomechanics to observe the effects of the gravitational interaction between two quantum micro-mechanical oscillators on the interference pattern of cavity photons through shifts in the visibility of interfering photons. We show that the gravitational coupling leads to a quantifiable shift in the period and magnitude of the visibility whose observability is within reach of current technology. We discuss the feasibility of the set-up as well as the gravity-induced entanglement between the two oscillators.

In chapter 5, we propose a new approach to variational quantum eigensolver (VQE) algorithms in quantum computation. VQEs are strong candidates to be the first practically useful application of near-term quantum devices, as they combine classical optimization techniques with efficient cost function evaluations on quantum computers. We propose a new approach to VQEs using the principles of measurement-based quantum computation, which is in contrast to the circuit-based approach that have been studied so far. This new strategy uses entangled resource states and local measurements to do the function evaluations. We present two measurement-based VQE schemes. The first one shows how any circuit-based VQE can be translated to measurement-based VQE. The second one provides a new approach for constructing variational families that has no immediate analogue in circuit-based quantum computing. We discuss how both schemes offer problem-specific advantages in terms of the required resources and coherence times.

Finally, we present some summarizing thoughts and future outlook in chapter 6.

Chapter 2

Holographic Complexity of Rotating Black Holes

2.1 Introduction

The AdS/CFT duality [15] continues to be the basis of many interesting connections between quantum information and gravity. Entanglement properties of the boundary CFT can be precisely related to geometric quantities in bulk AdS spacetime, most notably through the Ryu-Takayanagi construction [56, 57]. Studies of the growth of the ER bridge in AdS black holes have led to speculations of its duality to the growth of complexity of the dual boundary state [52]. This was refined to new conjectured entries in the AdS/CFT dictionary: the complexity=volume (CV) conjecture [58, 59] and the complexity=action (CA) conjecture [53, 54].

Complexity of quantum states is a measure of how hard it is to prepare a particular target state $|\psi_T\rangle$ from a given reference state $|\psi_R\rangle$ and an initial set of elementary gates $\mathcal{G}$

$$V_n \equiv g_n \dots g_1 g_0 \tag{2.1}$$

where $g_0, \dots g_n \in \mathcal{G}$. The complexity of a state $|\psi_T\rangle$ is then defined as the minimum number n of elementary gates that can approximate it according to some norm, starting from a fixed reference state $|\psi_R\rangle$

$$\mathcal{C}(|\psi_T\rangle) = \arg\min_n || \, |\psi_T\rangle - V_n \, |\psi_R\rangle \, ||^2 \tag{2.2}$$

In addition to discrete circuit models, complexity can also be defined for systems with continuous Hamiltonian evolution generated by

$$U(t) = \overleftarrow{\mathcal{T}} \exp\left[-i \int_0^t H(t')dt'\right], \qquad H(t) = \sum_k Y^k(t) M_k \tag{2.3}$$

with boundary conditions $U(0) = I$ and $U(1) = V_n$, where M_k are the basis Hermitian generators of the Hamiltonian, and $Y^k(t)$ are the time-dependent control functions specifying the tangent vector $\vec{Y}(t)$ of a trajectory in the space of unitaries [60]. The time-ordering operator $\overleftarrow{\mathcal{T}}$ ensures that earlier terms in the expansion of the evolution operator $U(t)$ act on the state before later terms — i.e. going from right to left. Thus, continuous Hamiltonian evolution defines a path in the space of unitaries of the circuit whose length is [61, 62]

$$\mathcal{D}(U) = \int_0^1 F(U(t), \dot{U}(t))dt' \tag{2.4}$$

where the cost function $F(U(t), \dot{U}(t))$ is a local functional of positions along $U(t)$ in the space of unitaries, with the overdot denoting a t derivative.[1] Thus,

$$\mathcal{C}(|\psi_T\rangle) = \min_{U(t)} \mathcal{D}(U) \tag{2.5}$$

An ongoing topic of active research is the extension of the concept of complexity to quantum field theories using the above geometric formulation of complexity (for example, see [63, 64, 65, 66, 67, 68]). The above definition of complexity clearly has many ambiguities [64, 69] associated with the choice of reference states, basis operators, and cost function, which is expected to be related to the ambiguities associated with calculating the action in CA proposal [70].

Complexity was originally discussed in the context of holography as the dual to the volume of the ER bridge in eternal black holes [52]. The eternal Schwarzschild-AdS black hole is dual to two copies of the CFT prepared in the thermofield double state [48]. The volume of the ER bridge continues to grow in time even after the system thermalizes, suggesting that any putative CFT dual to this quantity must be something that continues to evolve after equilibrium is reached [71, 72]. It was proposed that this growth captures some notion of complexity for the CFT state.

The idea that the growth of the black hole interior is connected to computational complexity has come to be refined into a number of concrete proposals, the most studied

[1] The properties of the cost function and its possible forms are discussed in [60].

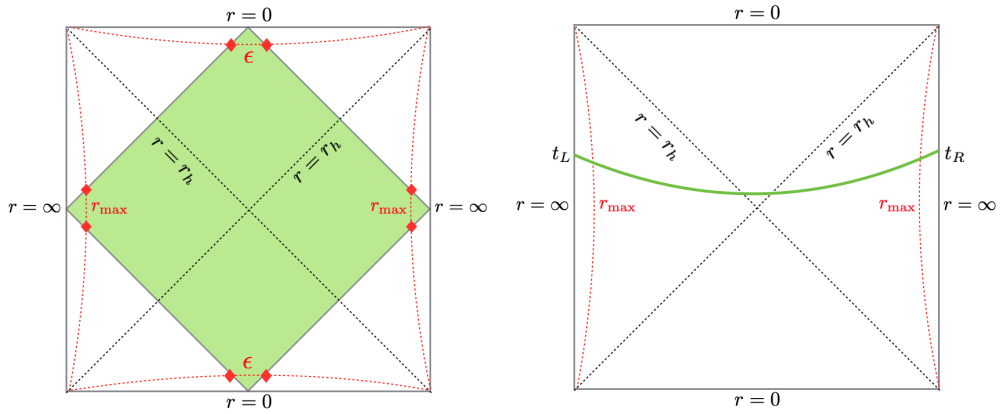

Figure 2.1: Penrose diagrams for the eternal two-sided black hole and the two holographic complexity conjectures. Left: CA conjecture states that the complexity is given by the gravitational action of the WDW patch (shown in green for the case $-t_L = t_R = 0$). Right: CV conjecture states that the complexity is given by the maximal volume slice connecting the two boundary slices (shown in green for a general t_L and t_R). Also shown are the regulator surfaces in red dotted lines.

of which are the CV and CA conjectures (see figure 2.1). The CV conjecture proposed that the complexity of the TFD state at boundary section Υ is equal to the volume of the extremal/maximal spacelike slice $\mathcal{B}$ anchored at t_L and t_R at the boundaries [59]

$$\mathcal{C}_{\mathcal{V}}(\Upsilon) = \max_{\Upsilon=\partial\mathcal{B}} \left[\frac{\mathcal{V}(\mathcal{B})}{G_N R}\right] \tag{2.6}$$

where R is a length scale associated with the bulk geometry (usually taken to be the AdS length ℓ) chosen to make the complexity dimensionless. This was generalized to the CA conjecture[2], where complexity depends on the whole domain of dependence of $\mathcal{B}$ — a region called the Wheeler-DeWitt (WDW) patch [53]. Explicitly, the CA conjecture asserts that the complexity of the CFT state is given by the numerical value of the gravitational action evaluated on the WDW patch:

$$\mathcal{C}_{\mathcal{A}}(\Upsilon) = \frac{I_{\text{WDW}}}{\pi\hbar}\,. \tag{2.7}$$

Both the CV and CA conjectures have received considerable attention and basic properties of each are now well-established. Initially, attention was given to the idea that, within

[2]For a discussion of the original motivation of the CA conjecture see [54]

the CA proposal, the late-time growth of complexity for the Schwarzschild-AdS black hole is $\pi\dot{\mathcal{C}}_{\mathcal{A}} = 2M$ [53, 54]. This was a suggestive connection with Lloyd's bound and was argued to support the idea that black holes are the fastest computers in nature [73]. However, subsequent careful analysis revealed that this late-time value is actually approached from above rather than from below, as Lloyd's bound would require [69]. It is now believed that the assumptions required for Lloyd's bound may be incompatible with holography [74, 75]. Nonetheless, there have been several rather interesting connections uncovered between complexity and black hole thermodynamics in both proposals, but the situation is especially clear in the CA proposal. For example, in the CA proposal the late-time growth rate of complexity for two-horizon geometries reduces to the difference in internal energies (or enthalpies) between the inner and outer horizons:

$$\pi\dot{\mathcal{C}}_{\mathcal{A}} = U_+ - U_- \equiv (F_+ + T_+S_+) - (F_- + T_-S_-)\,, \tag{2.8}$$

where F is the free energy, S the entropy, and T the Hawking temperature, while the $+/-$ corresponds to the outer/inner horizon, respectively. This relationship was first observed in Einstein gravity in [54], and then argued to hold for general theories of gravity in [76], and established rigorously for the full Lovelock family of gravitational theories in [77] (see also [78]). Many other properties have been explored, e.g., the effects of topology [79, 80, 65, 81]. If there are topological identifications in the spacetime then the complexity is rescaled by a factor dependent on the identifications [65].

In many instances, the properties of complexity are qualitatively similar in both the CV and CA proposals. For example, both proposals account for the expected linear time dependence at late times [59, 54] and both exhibit the switchback effect, which is the expected response of complexity to perturbations of the state at early times [59, 82, 83]. However, there are some situations in which the two proposals differ in their behaviour [84, 83, 85, 86, 81, 87, 88]. Understanding universal and divergent aspects of the two proposals is useful as there does not yet exist a first-principles derivation for complexity in the holographic dictionary.

Besides the time-dependent complexity rate of growth, another quantity of interest is the complexity of formation [64] of a black hole

$$\Delta\mathcal{C}_{\mathcal{A}}(\Upsilon) = \frac{1}{\pi\hbar}\left[I_{\text{WDW}}(\text{BH}) - 2I_{\text{WDW}}(\text{AdS})\right] \tag{2.9}$$

which measures the additional complexity present in preparing the thermofield double state in two copies of the CFT compared to two copies of the AdS vacuum alone. The complexity of formation was first defined and discussed in [64] for Schwarzschild-AdS black holes in

various dimensions, where it was found that it grows linearly with entropy in the high-temperature (equivalently, large black hole) limit — that is, $\Delta\mathcal{C}_{\mathcal{A}} \sim k_d S$, for a constant k_d that depends on the (boundary) dimension $d > 3$. These considerations were extended to charged black holes in [69] where it was found that the functional dependence of the complexity of formation is more complicated, but its dependence on the size of the black hole was still found to be controlled by the entropy in the limit of large black holes.

Our purpose in this chapter is to study various aspects of the holographic complexity conjectures for rotating black holes. The study of rotating black holes in the context of AdS/CFT was initiated in [89, 90, 91, 92, 93], where the thermodynamic properties of the black holes were compared with those of the boundary CFT. This holographic picture was further developed for astrophysical black holes with the "Kerr/CFT correspondence" [94], which conjectures that quantum gravity near the horizon of an extremal Kerr black hole is dual to a two-dimensional CFT (for reviews see [95, 96]). Rotating black holes are dual to thermofield double states with an additional chemical potential

$$|\text{rTFD}\rangle = \frac{1}{\sqrt{Z(\beta, \{\mu_i\})}} \sum_n e^{-\beta E_n/2} e^{-\beta \mu J_n/2} |E_n, J_n\rangle_L \otimes |E_n, J_n\rangle_R \tag{2.10}$$

associated with the rotation, where $\mu \equiv \mu_1 + \cdots + \mu_{(D-1)/2}$, and μ_i is the chemical potential associated with the angular momentum J_i along the ϕ_i circle, with $Z(\beta, \{\mu_i\})$ the grand canonical partition function. The time evolution of the state is modified by the chemical potentials

$$|\text{rTFD}(t_L, t_R)\rangle = e^{-i(H_L + \mu J_L)t_L - i(H_R + \mu J_R)t_R} |\text{rTFD}\rangle \tag{2.11}$$

where (H_L, J_L) and (H_R, J_R) are the Hamiltonians and angular momentum operators for the left and right boundaries, respectively.

To date, there have been only a few studies focussing on the effects of rotation in the context of complexity, and these studies are further limited to a derivation of the late-time rate of growth. The late-time complexity growth of Kerr-AdS black holes in CA conjecture was calculated in [97]. The effect of a probe string attached to a rotating black hole on its complexity was studied in [98]. One reason that a more detailed analysis is not straightforward is the more complicated causal structure of rotating black holes. In the case of rotating spacetimes, carrying out a computation of the action for a WDW patch (or of the volume of a spacelike slice) is a technically formidable task. The description of null hypersurfaces is somewhat complicated even for 4 spacetime dimensions [3], and no generalization to higher-dimensional cases presently exists. Fortunately there is a special case that renders the computations tractable: Myers-Perry-AdS spacetimes in odd dimensions with equal angular momenta in each orthogonal rotation plane. Compared to the

most general Myers-Perry-AdS black holes, these solutions enjoy enhanced symmetry that considerably simplifies the analysis of the causal structure. This particular configuration has some similarities with the charged case [68, 99], however, we shall see that there are interesting differences.

One of our main motivations for considering rotating black holes is to help develop an understanding of how the CV and CA proposals behave for less symmetric spacetimes. In the context of the AdS/CFT duality, understanding how a quantity responds to deformations of the state or the theory itself has been a fruitful approach in understanding which relationships may be universal and which may be specific to the state or theory. For example, this approach has been used with some success in the context of higher-curvature theories of gravity. Those theories introduce additional parameters into the action, which can then be used to discern between the various possible CFT charges. This method has also been used to understand the limitations of the Kovtun-Son-Starinets bound [100], argue for the existence of c-theorems in arbitrary dimensions [101, 102], and generate conjectures for the universal behaviour of terms in entanglement entropy or partition function [103, 104, 105]. Similarly, our hope here is that the more complicated metric structure of rotating black holes will help to discern both universal features of and particular distinctions between the CV and CA proposals.

Along these lines, one of the main results of this chapter concerns a connection between the thermodynamic volume of the black hole and the complexity of formation in both the CV and CA proposals. The thermodynamic volume is a quantity that arises naturally when one extends the definition of Komar mass from the asymptotically flat to asymptotically AdS setting [106, 107]. It also appears in the first law of black hole mechanics, governing the response of the mass to variations in the cosmological constant which, in this case, is interpreted as a pressure. In general, the thermodynamic volume is an independent thermodynamic potential. However in certain cases (such as those involving spherical symmetry) the thermodynamic volume and entropy are simply related via $S \propto V^{(D-2)/(D-1)}$. In some instances, the thermodynamic volume can be related to the spacetime volume inside the black hole [107, 108]. This fact has motivated some authors to consider its relevance in the context of holographic complexity. However, the results so obtained have either involved new proposals for complexity [109, 110], or have used thermodynamic identities to understand results in terms of the thermodynamic volume for interpretational reasons [76, 111, 112]. Our result is, to the best of our knowledge, the first to draw a clear connection between thermodynamic volume and the original CV and CA conjectures. Since the role of thermodynamic volume in holography has been little understood to date (though see [113, 114, 115, 116, 117, 118, 119, 120] for progress in this direction), this result may be viewed as an initial step toward that goal.

This chapter is organized as follows. In section 2.2, the geometry and causal structure of the Myers-Perry-AdS spacetimes is given. Section 2.3 describes the terms of the action calculations that needs to be evaluated to calculate the complexity according to the CA conjecture as well as the framework to calculate the extremal volume in CV conjecture. In section 2.4, we calculate the complexity of formation of the state (2.10) in reference to the vacuum AdS state, according to both the CA and CV conjectures. In section 2.5, we present the full time evolution of complexity rate of growth in both the CA and CV conjectures. We discuss the implications of our results and point toward possible future directions in section 2.6. A number of technical details and supporting calculations are left to appendix A.

2.2 Myers-Perry-AdS Spacetimes with Equal Angular Momenta

2.2.1 Solution and global properties

The Myers-Perry-AdS solution in odd dimension $D = 2N + 3$ is a cohomogeneity-$(N + 1)$ metric with isometry group $\mathbb{R} \times U(1)^{N+1}$, described by its mass M and $N + 1$ independent angular momenta J_i [121]. In the special case in which all angular momenta J_i, $i = 1 \dots N + 1$ are equal, there are considerable simplifications and the metric depends only on a single radial coordinate and on the parameters (m, a) [122]:

$$ds^2 = -f(r)^2 dt^2 + g(r)^2 dr^2 + h(r)^2 \left[d\psi + A - \Omega(r) dt\right]^2 + r^2 \hat{g}_{ab} dx^a dx^b \tag{2.12}$$

where

$$g(r)^2 = \left(1 + \frac{r^2}{\ell^2} - \frac{2m\Xi}{r^{2N}} + \frac{2ma^2}{r^{2N+2}}\right)^{-1}, \quad h(r)^2 = r^2 \left(1 + \frac{2ma^2}{r^{2N+2}}\right), \quad \Omega(r) = \frac{2ma}{r^{2N} h^2}, \tag{2.13}$$

and

$$f(r) = \frac{r}{g(r)h(r)}, \qquad \Xi = 1 - \frac{a^2}{\ell^2}. \tag{2.14}$$

We take $m > 0$ and by sending $t \to -t$, we can without loss of generality always choose $a \geq 0$. The metric $\hat{g}$ is the Fubini-Study metric on $\mathbb{CP}^N$ with curvature normalized so that $\mathrm{Ric}(\hat{g}) = 2(N + 1)\hat{g}$ and A is a 1-form on $\mathbb{CP}^N$ that satisfies $dA = 2J$ where J is the Kähler form on $\mathbb{CP}^N$. The isometry of the spacetime is enhanced to $\mathbb{R} \times U(1) \times SU(N+1)$.

The metric g satisfies the Einstein equations $G_{ab} + \Lambda g_{ab} = 0$ with a negative cosmological constant, normalized such that $\Lambda = -(D-1)(D-2)/2\ell^2$ where ℓ is the AdS length scale. The field equations can then be simply expressed as

$$R_{ab} = -\frac{(D-1)}{\ell^2} g_{ab}\,. \tag{2.15}$$

The solution above describes the exterior region of a stationary, multiply rotating asymptotically AdS black hole. The basic example is in $D = 5$, in which case $N = 1$ and we have $\mathbb{CP}^1 \cong S^2$ with the metric

$$\hat{g} = \frac{1}{4}\left(d\theta^2 + \sin^2\theta d\phi^2\right), \qquad A = \frac{1}{2}\cos\theta d\phi \Rightarrow J = -\frac{1}{4}\sin\theta d\theta \wedge d\phi. \tag{2.16}$$

The asymptotic region is obtained in the limit $r \to \infty$, where we recover the usual AdS_{2N+3} metric provided we periodically identify $\psi \sim \psi + 2\pi$. The line element above is valid in the exterior region of the spacetime; that is we also take $t \in \mathbb{R}$ and $r_+ < r < \infty$ where r_+ is the largest positive root of $g(r)^{-2}$. We will discuss below how the metric can be extended beyond r_+ to all $r > 0$. As we will review below, the hypersurface $r = r_+$ is in fact a smooth Killing horizon with null generator

$$\xi = \frac{\partial}{\partial t} + \Omega_H \frac{\partial}{\partial \psi}, \qquad \Omega_H = \frac{2ma}{r_+^{2N+2} + 2ma^2}\,. \tag{2.17}$$

Horizons are located at the positive roots of $g(r)^{-2}$. They can be more easily studied via the polynomial $P(r^2)$ where

$$P(x) = \frac{x^{N+2}}{\ell^2} + x^{N+1} - 2M\Xi x + 2ma^2. \tag{2.18}$$

Since there are only two sign changes between adjacent coefficients we can apply Descartes' rule of signs to argue there can be at most two real positive roots $x_+ > x_- > 0$ assuming $m > 0$. Thus we expect the causal structure to be qualitatively similar to that of a charged black hole, consisting of an outer (event) horizon and an inner Cauchy horizon. We will show this explicitly below. We can eliminate (m, a) in terms of (r_+, a)

$$m = \frac{r_+^{2N+2}(1 + r_+^2\ell^{-2})}{2(\Xi r_+^2 - a^2)}\,. \tag{2.19}$$

A similar formula holds for m with r_- replacing r_+. Note that regularity of the event horizon requires that

$$\Omega_H \leq \frac{1}{\ell}\sqrt{1 + \frac{N\ell^2}{(N+1)r_+^2}} \tag{2.20}$$

with the bound saturated when the black hole is extremal.

When $a = 0$ the solution is just Schwarzschild-AdS. Then there is one horizon and beyond this the function $g_{rr} < 0$ and $g_{tt} > 0$. The set $r = 0$, which is a spacelike hypersurface, is then a curvature singularity. We will focus on the case $a > 0$, for which the set $r = 0$ is still a curvature singularity but now is timelike (i.e. $|dr|^2 \to +\infty$). As $r \to 0$, the geometry of the base $\mathbb{CP}^N$ collapses. However, $h(r)^2 \sim r^{-2N}$ as $r \to 0$ so the S^1 grows to an infinite size. Meanwhile $g_{tt} \sim 2mr^{-2N}$ is also diverging (and ∂_t is spacelike). The metric still has to be Lorentzian however, since $\det g = -r^{4N+2} < 0$. Thus, instead of the singularity being a timelike worldline, it is a timelike cylinder (i.e. at constant t it has S^1 topology).

The conserved charges corresponding to mass and angular momentum are [121, 123]

$$M = \frac{\Omega_{2N+1} m}{4\pi G_N}\left(N + \frac{1}{2} + \frac{a^2}{2\ell^2}\right), \qquad J = \frac{\Omega_{2N+1}}{4\pi G_N}(N+1)ma\,, \tag{2.21}$$

where

$$\Omega_{2N+1} = \frac{2\pi^{N+1}}{\Gamma(N+1)} \tag{2.22}$$

is the area of a unit $2N+1$ sphere. Note that $M > 0$ imposes the constraint $\Xi r_+^2 - a^2 > 0$ from (2.19). We emphasize that the single angular momentum J corresponds to equal angular momenta $J_i = J/(N+1)$ in each of the $N+1$-orthogonal planes of rotation. Next, since the volume associated with $(\mathbb{CP}^N, \hat{g})$ is

$$\mathrm{Vol}(\hat{g}) = \frac{\pi^N}{\Gamma(N+1)} \tag{2.23}$$

we can read off the area of a spatial cross section of the event horizon at $r = r_+$

$$A_H = \frac{2h(r_+) r_+^{2N} \pi^{N+1}}{\Gamma(N+1)} = \Omega_{2N+1} h(r_+) r_+^{2N}\,. \tag{2.24}$$

It is easy to check that $h(r_+) = r_+^2/\sqrt{\Xi r_+^2 - a^2}$. Furthermore, the event horizon has surface gravity

$$\kappa_+ = \frac{h(r_+)}{2r_+}\partial_r f(r)^2\Big|_{r=r_+} = \frac{1}{h(r_+)}\left((N+1)\left(1 + \frac{r_+^2}{\ell^2}\right) - \frac{1}{1 - a^2(\frac{1}{r_+^2} + \frac{1}{\ell^2})}\right). \tag{2.25}$$

Finally, since

$$g_{tt} = \frac{1}{h^2}\left[\frac{4m^2a^2}{r^{4N}} - \left(r^2 + \frac{r^4}{\ell^2} - \frac{2m\Xi}{r^{2N-2}} + \frac{2ma^2}{r^{2N}}\right)\right] \tag{2.26}$$

one finds that there is an ergoregion since $g_{tt} > 0$ in a region exterior to the horizon, although for sufficiently large r, $g_{tt} < 0$. Note that the ergosurface is never tangent to the event horizon.

2.2.2 Extended thermodynamics

In addition to the mass M, angular momentum J, and angular velocity Ω_H given above, the black hole's entropy and temperature are given by

$$S = \frac{\Omega_{2N+1} h(r_+) r_+^{2N}}{4G_N}, \qquad T = \frac{1}{2\pi h(r_+)} \left((N+1)\left(1 + \frac{r_+^2}{\ell^2}\right) - \frac{1}{1 - a^2(\frac{1}{r_+^2} + \frac{1}{\ell^2})} \right) . \tag{2.27}$$

Within the framework of extended thermodynamics (see, e.g. the review [124]) one associates a thermodynamic pressure with the cosmological constant via

$$P = -\frac{\Lambda}{8\pi G_N} = \frac{(N+1)(2N+1)}{8\pi \ell^2 G_N} \tag{2.28}$$

along with

$$V = \frac{\sqrt{\Xi r_+^2 - a^2} A_H}{2(N+1)} + \frac{4\pi a J}{(2N+1)(N+1)} = \frac{r_+^{2(N+1)} \Omega_{2N+1}}{2(N+1)} + \frac{4\pi a J}{(2N+1)(N+1)} \tag{2.29}$$

which is its conjugate thermodynamic volume. One can then check that the following first law of extended thermodynamics holds for the Myers-Perry-AdS family [107]

$$dM = TdS + \Omega_H dJ + VdP \tag{2.30}$$

along with the Smarr relation

$$2NM = (2N+1)(TS + \Omega J) - 2VP \, . \tag{2.31}$$

In what follows, it will often be convenient to work in terms of the parameters (r_+, r_-) rather than (m, a). To make the connection between these quantities and the physical parameters of the black hole more explicit, in figure 2.2 we plot the mass and angular momentum as functions of r_+/ℓ for different values of the ratio r_-/r_+. The basic conclusion is that, for large black holes, both the mass and angular momentum grow with increasing r_+/ℓ. However, for black holes closer to extremality, the growth is stronger. Although we

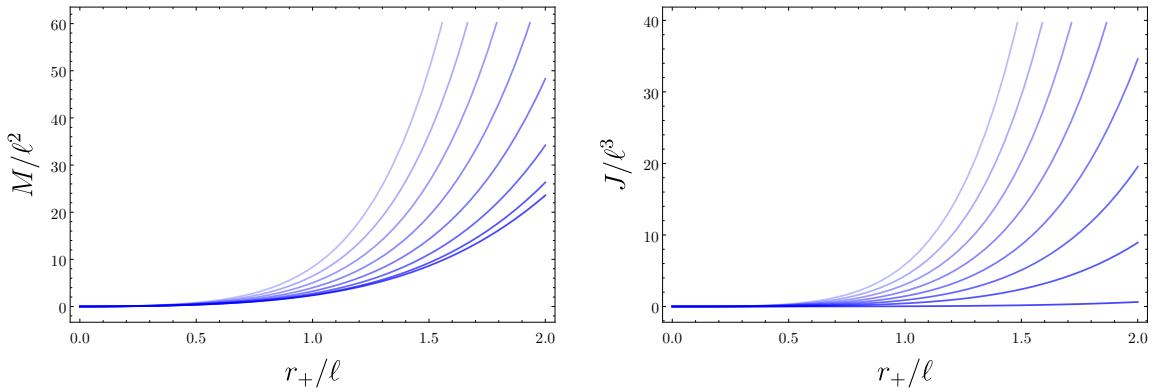

Figure 2.2: Left: A plot of the mass as a function of horizon radius for several values of r_-/r_+. Right: A plot of the angular momentum as a function of the horizon radius for several values of r_-/r_+. In each case, the lower dark blue curve corresponds to $r_-/r_+ = 1/100$, and this value increases in increments of $1/8$ as one moves vertically in the plot (lines of decreasing opacity). Both cases are for $D = 5$.

show this pictorially only for five dimensions, the plots are qualitatively similar in higher dimensions.

We show also in figure 2.3 the angular velocity of the horizon as a function of r_+/ℓ, again for different values of the ratio r_-/r_+. In the left plot, the dashed black line corresponds to the case where the black hole rotates at the speed of light with respect to an observer situated at infinity. For a ratio r_-/r_+ sufficiently below unity, the angular velocity exhibits a minimum for some intermediate value of r_+/ℓ and then increases. When this minimum coincides with the critical angular velocity $\Omega_H^c = 1/\ell$, the minimum disappears and the angular velocity is a monotonically decreasing function of the horizon radius, asymptoting to $\Omega_H^c = 1/\ell$ from above. The minimum of the angular velocity coincides with the critical value when

$$1 - 2\left(\frac{r_-}{r_+}\right)^2 + \left(\frac{r_-}{r_+}\right)^{2N+4} = 0\,. \tag{2.32}$$

Although it is not possible to obtain a simple-closed form, for five-dimensions it occurs when $r_-/r_+ = \sqrt{\sqrt{5}-1}/\sqrt{2}$ and decreases with increasing spacetime dimension, asymptoting to $r_-/r_+ = 1/\sqrt{2}$ in the limit $N \to \infty$. All black holes with r_-/r_+ above this threshold rotate faster than light. Provided that r_-/r_+ is less than the value corresponding to the

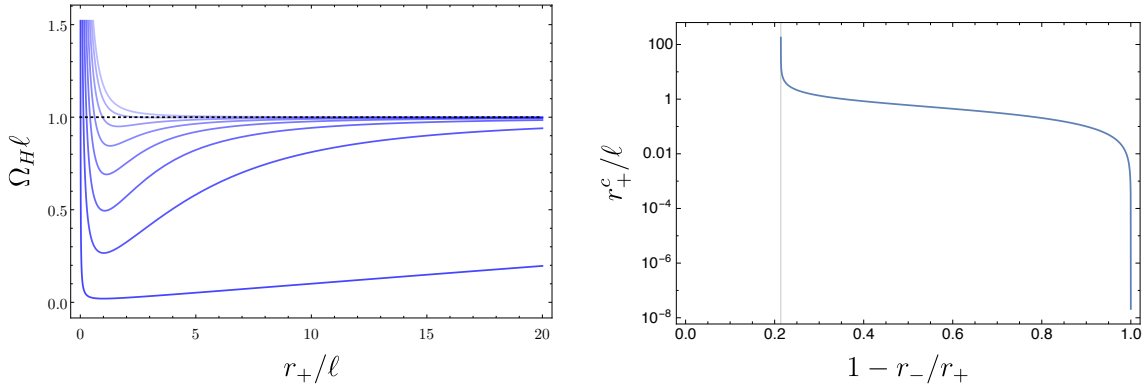

Figure 2.3: Left: Here we show the angular velocity of the horizon as a function of r_+/ℓ for several values of r_-/r_+. The curves correspond to $r_-/r_+ = 1/100$ (dark blue, bottom) and increase in increments of $1/8$ from bottom to top. The dashed black curve corresponds to the critical angular velocity $\Omega_H^c = 1/\ell$. Right: A plot of the value of r_+/ℓ at which the black hole rotates superluminally. The vertical line corresponds to $r_-/r_+ = \sqrt{\sqrt{5}-1}/\sqrt{2}$.

solution of (2.32), the location of the minimum of the angular velocity occurs at

$$\frac{r_+}{\ell} = \sqrt{\frac{y^2 - y^{2N+2} + (y^2-1)\sqrt{1-y^{2N}}}{1 - 2y^2 + y^{2N+4}}} \quad \text{where} \quad y \equiv \frac{r_-}{r_+}\,. \tag{2.33}$$

The equally-rotating Myers-Perry-AdS black holes considered here are unstable to linearized gravitational perturbations when they rotate faster than light [122]. The instability is 'superradiant' in the sense that certain perturbations are trapped by the AdS potential barrier and are reflected back to the black hole, creating an amplification process [91]. Note that extreme black holes in this class always rotate faster than the speed of light and are hence unstable. The endpoint of these instabilities are expected to be stationary, nonaxisymmetric black hole. Although it will not be particularly important for the considerations we are interested in here, it would be interesting to investigate the relation of our findings to known results on the dynamical stability of rotating, asymptotically AdS black holes.

2.2.3 Causal structure

Next, let us discuss the global structure of the spacetime. In general, the causal structure of spacetimes with nontrivial rotation is far more complicated than that of their static

counterparts. The reason for this, at least partly, is because in general rotating spacetimes the null hypersurfaces are no longer effectively two dimensional as they are in the static case. However, for the special case of odd-dimensional rotating black holes with equal angular momenta, some of these difficulties can be circumvented, as first emphasized in [81]. Let us illustrate this, following the methods of [125, 3, 4] (see also appendix A.6). For convenience we will focus on the non-extreme case $r_+ \neq r_-$.

Our task is to construct a suitable family of null hypersurfaces. We start with an ansatz

$$v = t + r^*(r, \psi_i) \tag{2.34}$$

where ψ_i stands for the various angular coordinates and r^* denotes a suitable 'tortoise' coordinate. We then demand that dv — the one-form normal to surfaces of constant v — is null, i.e. $g^{-1}(dv, dv) = 0$. A direct computation reveals that this condition admits an additively separable solution:

$$r^* = R(r) + \sum_i \Psi_i(\psi_i)\,. \tag{2.35}$$

Using an appropriate choice of integration constants the dependence on the angular coordinates can be eliminated, leaving

$$\frac{dr^*}{dr} = \frac{g(r)}{f(r)} = \frac{g(r)^2 h(r)}{r} \tag{2.36}$$

or in other words, r^* is a function only of the radial variable, somewhat akin to the static case. These rotating black holes possess the "simplest" causal structure, and are therefore natural candidates for a first foray into the properties of complexity in rotating backgrounds.

Unfortunately, the tortoise coordinate cannot be obtained in a useful closed form and numerical techniques are required for its evaluation. However, for later convenience, here we note both the asymptotic form of the tortoise coordinate, and that the integral can be massaged into a form much more amenable to numerical evaluation.

Working to the leading order at which differences between the tortoise coordinate for the black holes differ from that for global AdS we find

$$r^*(r) = \sum_{k=0}^{N+1} \frac{(-1)^{k+1}\ell^{2k+2}}{(2k+1)r^{2k+1}} + \frac{\ell^2(a^2 - 2\ell^2)m}{(2N+3)r^{2N+3}} + \mathcal{O}(r^{-2N-5})\,. \tag{2.37}$$

Of course, the tortoise coordinate will exhibit logarithmic singularities at the event and inner horizons. To better understand the behaviour of the tortoise coordinate it is useful to define

$$g(r)^2 = \frac{G(r)}{(r^2 - r_+^2)(r^2 - r_-^2)}\,, \tag{2.38}$$

where $G(r) > 0$ will be completely regular at both horizons. We can series expand the integrand in the vicinity of the horizon to obtain the behaviour near the poles. We find

$$\frac{dr^*}{dr} = \frac{G(r_+)h(r_+)}{2r_+^2(r_+^2 - r_-^2)(r - r_+)} + \mathcal{O}(1) \quad \text{as} \quad r \to r_+\,, \tag{2.39}$$

and

$$\frac{dr^*}{dr} = -\frac{G(r_-)h(r_-)}{2r_-^2(r_+^2 - r_-^2)(r - r_-)} + \mathcal{O}(1) \quad \text{as} \quad r \to r_-\,. \tag{2.40}$$

Noting this behaviour, we can then perform a splitting of the integral, subtracting the pole contributions from the integrand to leave a completely convergent integral, and then handle the poles separately. We choose

$$\begin{aligned}\frac{dr^*}{dr} =& \left(\frac{G(r)h(r)}{r(r^2 - r_+^2)(r^2 - r_-^2)} + \frac{G(r_-)h(r_-)}{r_-(r_+^2 - r_-^2)(r^2 - r_-^2)} - \frac{G(r_+)h(r_+)}{r_+(r_+^2 - r_-^2)(r^2 - r_+^2)}\right) \\ & - \frac{G(r_-)h(r_-)}{r_-(r_+^2 - r_-^2)(r^2 - r_-^2)} + \frac{G(r_+)h(r_+)}{r_+(r_+^2 - r_-^2)(r^2 - r_+^2)}\,.\end{aligned} \tag{2.41}$$

where we have kept $(r^2 - r_\pm^2)$ in the denominator to ensure that, when integrated, these terms converge also as $r \to \infty$. Note that the term in parentheses is now completely regular at $r = r_\pm$. The integrals involving the divergent parts can then be evaluated directly and we obtain

$$\begin{aligned}r^*(r) =& \frac{G(r_+)h(r_+)}{2r_+^2(r_+^2 - r_-^2)} \log\frac{|r - r_+|}{r + r_+} - \frac{G(r_-)h(r_-)}{2r_-^2(r_+^2 - r_-^2)} \log\frac{|r - r_-|}{r + r_-} \\ & + \int_r^\infty \frac{r_-r_+(r_-^2 - r_+^2)G(r)h(r) - rr_+G(r_-)h(r_-)(r^2 - r_+^2) + rr_-G(r_+)h(r_+)(r^2 - r_-^2)}{r(r^2 - r_-^2)(r^2 - r_+^2)(r_+^2 - r_-^2)r_-r_+} dr\,.\end{aligned} \tag{2.42}$$

Here we emphasize that the integrand in the last term is completely regular at both horizons. Furthermore, in so doing we have extended the integration at infinity, choosing $r^* \to 0$ as $r \to \infty$. This form of the tortoise coordinate is much more amenable to numerical evaluation.

By expressing the surface gravities at the inner and outer horizons in terms of $G(r)$ we find

$$\kappa_\pm = \pm \frac{r_\pm^2}{h(r_\pm)} \frac{(r_+^2 - r_-^2)}{G(r_\pm)} \tag{2.43}$$

which allows us to write the tortoise function in the simple form

$$r^*(r) = \mathcal{R}(r) + \frac{1}{2\kappa_+} \log\left(\frac{|r - r_+|}{r + r_+}\right) + \frac{1}{2\kappa_-} \log\left(\frac{|r - r_-|}{r + r_-}\right). \tag{2.44}$$

where $\mathcal{R}(r)$ is a smooth function defined by the integral term in (2.42).

So far we have shown that the null sheets v =constant in the equal-angular momenta Myers-Perry-AdS solution have a particularly simple form compared to the general situation. We next turn to investigating the causal structure of the solution. To begin, we will construct horizon-penetrating ingoing coordinates adapted to these light sheets. We first pass to corotating coordinates

$$T = t, \qquad \psi^+ = \psi - \Omega_H t\,, \tag{2.45}$$

so that the null generator of the event horizon $\xi = \partial_T$. Next, we introduce new coordinates (v, r, Ψ^+) by setting

$$v = T + r^*, \qquad \Psi^+ = \psi^+ - (\Omega_H - \Omega(r))r^*, \tag{2.46}$$

so that the metric becomes

$$ds^2 = -\frac{r^2 dv^2}{h(r)^2 g(r)^2} + \frac{2r}{h(r)} dv dr + h(r)^2 (d\Psi^+ + A + (\Omega_H - \Omega(r))dv)^2 + r^2 \bar{g}\,. \tag{2.47}$$

The metric is clearly smooth and non-degenerate at both horizons (i.e. at poles of $g(r)$). The coordinates cover one exterior region, and can be continued through the event horizon, beyond the inner horizon, and finally to the timelike singularity at $r = 0$. However, as in the well-known Reissner-Nordstrom case, to determine the maximal analytic extension, the ingoing coordinates are not sufficient. To construct the required Kruskal-like coordinates, we first define a new chart (v, u, Ψ^+) where $u = v - 2r^*$ to obtain the metric in 'double null coordinates'

$$ds^2 = -\frac{r^2}{h(r)^2 g(r)^2} du dv + h(r)^2 \left(d\Psi^+ + A + (\Omega_H - \Omega(r))dv)\right)^2 + r(u, v)^2 \hat{g}, \tag{2.48}$$

where $r^* = (v - u)/2$. The metric (2.48) is clearly degenerate at both the event and inner horizons. As $r \to r_+$ we see from (2.44) that $r^* \to -\infty$ whereas as $r \to r_-$, $r^* \to \infty$.

Therefore in a neighbourhood of the event horizon as $r \to r_+$, $v \to -\infty$ or $u \to \infty$ at the rate

$$v - u \to \frac{1}{\kappa_+} \log\left(\frac{|r - r_+|}{2r_+}\right) \tag{2.49}$$

which implies that $|r - r_+| \to 2r_+ e^{\kappa_+(v-u)}$ as $r \to r_+$. We next define coordinates

$$U^+ := -e^{-\kappa_+ u} < 0, \qquad V^+ := e^{\kappa_+ v} > 0. \tag{2.50}$$

Therefore as we approach the event horizon,

$$-\frac{r^2}{h(r)^2 g(r)^2} du dv \to -\frac{4r_+^4(r_+^2 - r_-^2)}{h(r_+)^2 G(r_+)} e^{\kappa_+(v-u)} du dv = -\frac{4r_+^2}{\kappa_+} dU^+ dV^+ , \tag{2.51}$$

Furthermore it is easily checked that $(\Omega_H - \Omega(r))dv$ is smooth as $r \to r_+$. This demonstrates that the metric

$$ds^2 = -\frac{r^2 e^{-2\kappa_+ r^*}}{h(r)^2 g(r)^2 \kappa_+^2} dU^+ dV^+ + h(r)^2 \left(d\Psi^+ + A + \frac{1}{\kappa_+ V^+}(\Omega_H - \Omega(r)) dV^+\right)^2 + r^2 \hat{g} \tag{2.52}$$

is smooth and non-degenerate at the event horizon in the (U^+, V^+, Ψ^+) chart and we can analytically continue the chart through the event horizon ($U^+ = 0$ or $V^+ = 0$) to a new region $U^+ > 0, V^+ < 0$ so that the metric (2.52) is regular for $r_- < r < \infty$. The chart covers four regions (quadrants in the $(U^+, V^+)-$plane) with a bifurcation S^3 at $(U^+, V^+) = (0, 0)$. The coordinate system breaks down near the inner horizon as $r \to r_-$ and there are radial null geodesics that reach this null hypersurface in finite affine parameter. We can extend beyond this coordinate singularity by reversing the above coordinate transformations to return to the ingoing coordinates (v, r, Ψ^+), which are regular at both horizons. Define

$$\Psi^- = \Psi^+ + (\Omega_H - \Omega(r_-))v \tag{2.53}$$

so that in the (v, r, Ψ^-) chart, the Killing field ∂_v is corotating with the inner horizon $r = r_-$. Introduce a second double null coordinate system $(\hat{v}, \hat{u})$ with

$$\hat{v} = v, \qquad \hat{u} = v - 2r^*, , \tag{2.54}$$

so that in particular $r^* = (\hat{v} - \hat{u})/2$. The metric in the $(\hat{v}, \hat{u}, \Psi^-)$ coordinate chart will resemble (2.48) with the obvious replacements and hence will be degenerate at $r = r_-$. We then introduce a second pair of Kruskal-like coordinates adapted to the inner horizon by setting

$$U^- = -e^{-\kappa_- \hat{u}} < 0, \qquad V^- = -e^{\kappa_- \hat{v}} < 0\,. \tag{2.55}$$

By repeating the above computations we find the metric in the (V^-, U^-, Ψ^-) chart is

$$ds^2 = \frac{r^2 e^{-2\kappa_- r^*}}{h(r)^2 g(r)^2 \kappa_-^2} dU^- dV^- + h(r)^2 \left(d\Psi^- + A + (\Omega(r_-) - \Omega(r)) \frac{dV^-}{\kappa_- V^-} \right)^2 + r^2 \hat{g}\,, \quad (2.56)$$

which is indeed smooth and non-degenerate at $r = r_-$ using the fact that $(r - r_-)e^{-2\kappa_- r^*} \to 2r_-$ as $r \to r_-$ and $(\Omega(r_-) - \Omega(r))/V^- = \mathcal{O}(1)$. In this coordinate system, the inner horizon corresponds to either $U^- = 0$ or $V^- = 0$ and we may analytically continue the metric in this chart to allow $U^- \geq 0$ and $V^- \geq 0$, corresponding to $0 < r < r_-$. This region contains a timelike coordinate singularity at $r = 0$, or $U^- V^- = e^{2\kappa_- \mathcal{R}(0)}$. Since this region is actually isometric to a region for which the event horizon lies to the future, we can introduce new coordinates $(\hat{U}^+, \hat{V}^+)$ and analytically continue the metric into new exterior regions $r > r_+$ that are isometric to the original asymptotically AdS regions described by the (U^+, V^+) coordinate chart. We can repeat this procedure indefinitely both to the future and past to produce a maximal analytic extension with infinitely many regions (see figure 2.4 below), qualitatively similar to the familiar maximal analytic extension of the non-extreme rotating BTZ black hole [126]. Note that in contrast to the Kerr black hole, and generic members of the Myers-Perry(-AdS) black holes, one cannot continue into a region of spacetime for which $r^2 < 0$.

2.3 Framework for Complexity Computations

2.3.1 Framework for Action calculations

Given a $D-$dimensional bulk region $\mathcal{M}$, the gravitational action, including all the various terms for boundary surfaces and joints [127], over this region is given by[3] [70]

$$\begin{aligned} I_{\text{grav}} = &\frac{1}{16\pi G_N} \int_{\mathcal{M}} \sqrt{-g} \left(R + \frac{(D-1)(D-2)}{\ell^2} \right) d^D x + \frac{1}{8\pi G_N} \int_{\mathcal{B}} \sqrt{|h|} K d^{D-1} x \\ &+ \frac{1}{8\pi G_N} \int_{\mathcal{B}'} \sqrt{\gamma} \kappa d\lambda d^{D-2}\theta + \frac{1}{8\pi G_N} \int_{\mathcal{J}} \sqrt{\sigma} \eta d^{D-2} x + \frac{1}{8\pi G_N} \int_{\mathcal{J}'} \sqrt{\sigma} \tilde{a} d^{D-2} x. \end{aligned} \quad (2.57)$$

The first term is the Einstein-Hilbert bulk action with cosmological constant Λ, which from (2.28) is

$$\Lambda \equiv -\frac{(D-1)(D-2)}{2\ell^2}, \quad (2.58)$$

[3] Note that we follow the conventions of [84] with the minor correction pointed out in [82].

integrated over $\mathcal{M}$. The second term is the Gibbons-Hawking-York boundary term [128, 129] that contributes at spacelike/timelike boundaries $\mathcal{B}$. The convention adopted here for the extrinsic curvature is that the normal *one-form* is directed outward from the region of interest. The third term is the contribution of the null boundary surface $\mathcal{B}'$ of $\mathcal{M}$. For a null boundary segment with normal k^α the parameter κ is defined in the usual way: $k^\beta \nabla_\beta k^\alpha = \kappa k^\alpha$, while γ is the determinant of the induced metric on the $(D-2)$-dimensional cross-sections of the null boundary and the parameter λ is defined according to $k^\alpha = \partial x^\alpha / \partial \lambda$. The fourth term is the Hayward term [130, 131] for joints $\mathcal{J}$ between non-null boundary surfaces — these terms will play no role in our construction. The last term is the contribution of joints $\mathcal{J}'$ from the intersection of at least one null boundary surface [127]. The parameter $\tilde{a}$ is defined according to

$$\text{timelike/null}: \quad \tilde{a} \equiv \epsilon \log |\mathbf{t}_1 \cdot \mathbf{k}_2| \qquad \text{with} \quad \epsilon = -\text{sign}(\mathbf{t}_1 \cdot \mathbf{k}_2)\text{sign}(\hat{\mathbf{n}}_1 \cdot \mathbf{k}_2)\,, \tag{2.59}$$

$$\text{null/spacelike}: \quad \tilde{a} \equiv \epsilon \log |\mathbf{k}_1 \cdot \mathbf{n}_2| \qquad \text{with} \quad \epsilon = -\text{sign}(\mathbf{k}_1 \cdot \mathbf{n}_2)\text{sign}(\mathbf{k}_1 \cdot \hat{\mathbf{t}}_2)\,, \tag{2.60}$$

$$\text{null/null}: \quad \tilde{a} \equiv \epsilon \log |(\mathbf{k}_1 \cdot \mathbf{k}_2)/2| \qquad \text{with} \quad \epsilon = -\text{sign}(\mathbf{k}_1 \cdot \mathbf{k}_2)\text{sign}(\hat{\mathbf{k}}_1 \cdot \mathbf{k}_2)\,, \tag{2.61}$$

where $\mathbf{k}_i$ is a null normal, $\mathbf{t}_i$ is a timelike unit normal, and $\mathbf{n}_i$ is a spacelike unit normal. Additionally, depending on the intersecting boundary segments, auxillary vectors — indicated with a hat — are required. These unit vectors are defined by the conditions of living in the tangent space of the appropriate boundary segment and pointing outward *as a vector* from the joint of interest.

The action as presented above is ambiguous when the spacetime region of interest contains null boundaries. Namely, the action is not invariant under reparameterizations of the normals to the null boundary segments. To ensure this invariance we add to the above the following counterterm [70]:

$$I_{\text{ct}} = \frac{1}{8\pi G_N} \int_{\mathcal{B}'} \Theta \log l_{\text{ct}} \Theta \sqrt{\gamma} d\lambda d^{D-2}\theta \tag{2.62}$$

where l_{ct} is an arbitrary length scale and

$$\Theta = \partial_\lambda \log \sqrt{\gamma} \tag{2.63}$$

is the expansion scalar of the null boundary generators, which depends only on the intrinsic geometry of the null boundary surfaces. While this term is not required to have a well-defined variational principle, it is known to have important implications for holographic complexity — for example, it is crucial for reproducing the switchback effect in the complexity equals action conjecture [132, 82, 83].

A further difficulty is that the gravitational action is divergent. To control these divergences (and allow for appropriate regularization in the complexity of formation calculations) we introduce a UV cut-off δ at the boundary CFT and integrate the radial dimension in the bulk up to $r = r_{\max}(\delta)$ [133, 134]. When calculating the complexity of formation, the choice of $r_{\max}(\delta)$ for the black hole spacetime should be consistent with that in vacuum AdS. This subtlety can be resolved [64] by expanding the metrics of both geometries in the Fefferman-Graham canonical form [135] and setting in both cases the radial cut-off surface at $z = \delta$. We discuss the Fefferman-Graham form of the rotating metrics in Appendix A.1.

To evaluate the complexity within the CA conjecture, we must evaluate the gravitational action and counterterm on the Wheeler-DeWitt patch of spacetime. Using the boost invariance of the spacetime, it is always possible to shift the WDW patch so that it intersects the left and right boundaries at the same times: $-t_L = t_R \equiv \tau/2$. We show the structure of the WDW patch in figure 2.4, which has the same structure for all the rotating black holes considered here. Of particular importance are the joints where the future/past boundaries of the WDW patch meet.

Let us determine the past meeting points of the boundaries of the WDW patch. We denote the future meeting point as r_{m_1} and the past meeting point as r_{m_2}. Consider first the past meeting point, and denote its coordinates inside the horizon as (t_{m_2}, r_{m_2}). From the right side of the Penrose diagram, this point lies along a $u = constant$ surface, while from the left it lies along a $v = constant$ surface. These facts translate into two equations:

$$t_{m_2} + r^*(r_{m_2}) = t_{\rm L} + r^*_\infty\,, \quad t_{m_2} - r^*(r_{m_2}) = t_{\rm R} - r^*_\infty\,, \tag{2.64}$$

where $t_{\rm L}$ and $t_{\rm R}$ denote the timeslices at which the lightsheets intersect the left and right boundaries, respectively. Note that t_{m_2} is the same in both equations as those points lie in a common patch of the diagram. Eliminating t_{m_2} from these equations we obtain

$$t_{\rm R} - t_{\rm L} + 2\,(r^*(r_{m_2}) - r^*_\infty) = 0\,. \tag{2.65}$$

Upon noting that $t_{\rm L} = -t_{\rm R}$ (which implies $t_{m_2} = 0$) and setting $t_{\rm R} = \tau/2$ we obtain

$$\frac{\tau}{2} + r^*(r_{m_2}) - r^*_\infty = 0\,. \tag{2.66}$$

An analogous derivation holds for r_{m_1}, the only difference being a sign in the last two terms:

$$\frac{\tau}{2} - r^*(r_{m_1}) + r^*_\infty = 0\,. \tag{2.67}$$

Note that here we have chosen to use the time τ instead of t to avoid possible confusion of this quantity with the t appearing in the metric (which, when considering the patches outside of the horizon, would be either t_L or t_R).

In general the values of $r_{m_{1,2}}$ must be obtained numerically. However, let us note that it is possible, starting from (2.42), to obtain an asymptotic form of this quantity valid for early times in the limit $r_-/r_+ \to 0$. This can be obtained by evaluating the integral appearing in (2.42) perturbatively in r_-/r_+. Here we note the result only in five dimensions:

$$r_m \approx r_- \left\{ 1 + \exp\left[-\frac{\pi(r_+^2+\ell^2)\ell + (r_+/\ell)\sqrt{\ell^2+r_+^2}(\ell^2+2r_+^2)\varepsilon\tau}{r_+(\ell^2+2r_+^2)} \frac{r_+^2}{r_-^2} + \cdots \right] + \cdots \right\}, \tag{2.68}$$

where the dots denote subleading terms and $\varepsilon = +1$ for r_{m_1} and -1 for r_{m_2}. This expression reveals that, as $r_-/r_+ \to 0$, the value of r_m tends exponentially towards the inner horizon — consistent with the discussion of charged black holes in [69], albeit with a slightly different rate of approach.

2.3.2 Evaluating the Action

Bulk Action

The bulk contributions to the action are very simple in this case since the black holes are vacuum solutions. In particular, we have

$$R = \frac{2D\Lambda}{(D-2)} \tag{2.69}$$

and thus

$$R - 2\Lambda = \frac{4\Lambda}{(D-2)}\,. \tag{2.70}$$

The bulk action is then simply the spacetime volume of the WDW patch weighted by this dimension-dependent prefactor:

$$I_{\text{bulk}} = \frac{\Lambda}{4(D-2)\pi G} \int_{\text{WDW}} \sqrt{-g} d^D x\,. \tag{2.71}$$

To evaluate the bulk contribution, we recall that the determinant of the metric is

$$\sqrt{-g} = r^{2N+1} d\Omega_{2N+1}\,. \tag{2.72}$$

We then split the integration domain into three regions where the (t, r) coordinates are valid, as shown in figure 2.4. In region I, the integration over t_{R} is between 0 (i.e. t_{m_1}) and

$$t_{\text{R}} = \frac{\tau}{2} + r_\infty^* - r^*(r)\,. \tag{2.73}$$

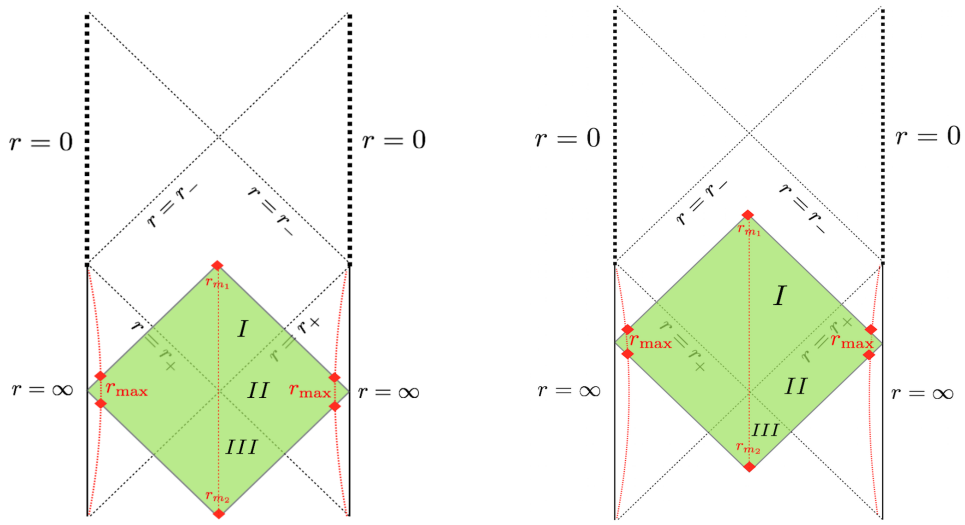

Figure 2.4: Penrose diagrams for the rotating black holes in (2.12) with the WDW patches corresponding to the TFD state at Left: $-t_L = t_R = 0$ and Right: $-t_L = t_R = \tau/2 > 0$ as the green shaded region. Joints contributing to the action terms are highlighted with red diamonds. Also shown are three regions I, II, and III defined for the bulk contribution to $I_{\rm WDW}$. The vertical dotted red line divides the WDW patch into two symmetric parts and define the regions I, II, and III. The curved dotted red line is the cut-off surface $r = r_{\rm max}(\delta)$.

In region II the integration over $t_{\rm R}$ is between

$$t_{\rm R} = \frac{\tau}{2} - r^*_\infty + r^*(r)\,, \quad \text{and} \quad t_{\rm R} = \frac{\tau}{2} + r^*_\infty - r^*(r)\,. \tag{2.74}$$

Finally, the integration in region III occurs between

$$t_{\rm R} = \frac{\tau}{2} + r^*(r) - r^*_\infty \tag{2.75}$$

and 0. We then have

$$I^I_{\rm bulk} = \frac{\Lambda\Omega_{2N+1}}{4(D-2)\pi G_N}\int_{r_{m_1}}^{r_+} r^{2N+1}\left(\frac{\tau}{2}+r^*_\infty - r^*(r)\right)\,dr\,, \tag{2.76}$$

$$I^{II}_{\rm bulk} = \frac{2\Lambda\Omega_{2N+1}}{4(D-2)\pi G_N}\int_{r_+}^{r_{\rm max}} r^{2N+1}\left(r^*_\infty - r^*(r)\right)\,dr\,, \tag{2.77}$$

$$I^{III}_{\rm bulk} = \frac{\Lambda\Omega_{2N+1}}{4(D-2)\pi G_N}\int_{r_{m_2}}^{r_+} r^{2N+1}\left(-\frac{\tau}{2}+r^*_\infty - r^*(r)\right)\,dr\,. \tag{2.78}$$

The total bulk action is then twice the sum of these three terms.

Surface contributions

There are two cut-off surfaces at $r = r_{\rm max}$, and each contribute a term

$$I_{\rm GHY} = \frac{1}{8\pi G_N}\int_{\mathcal{B}}\sqrt{|h|}K d^{D-1}x\,. \tag{2.79}$$

The normal to the timelike surface $r = r_{\rm max}$ is

$$n^\mu = \left(0,\sqrt{g^{rr}},0,0\right) \tag{2.80}$$

and the induced metric to the timelike surface of constant $r = r_{\rm max}$ has the determinant

$$\sqrt{|h|} = \frac{\sqrt{-g}}{\sqrt{g_{rr}}}\,. \tag{2.81}$$

The trace of the extrinsic curvature of the boundary surface is then

$$K = \nabla_\mu n^\mu = \frac{1}{\sqrt{-g}}\partial_\mu\left(\sqrt{-g}n^\mu\right) = \frac{1}{\sqrt{-g}}\partial_r\left(\sqrt{|h|}\right). \tag{2.82}$$

This gives a contribution for the two boundary surfaces at $r = r_{\rm max}$ of the form

$$I_{\rm GHY} = \frac{\Omega_{D-2}}{2\pi G_N}r^{D-2}\left[\frac{(D-2)}{rg(r)^2} - \frac{g'(r)}{g(r)^3}\right]\left(r^*_\infty - r_*(r)\right)\Big|_{r=r_{\rm max}}\,. \tag{2.83}$$

Note that this term is time-independent, so it does not contribute to the complexity rate of change $d\mathcal{C}_\mathcal{A}/d\tau$. Furthermore, it does not contribute to the complexity of formation $\Delta\mathcal{C}_\mathcal{A}$ because it is cancelled by the contribution made by the AdS_D vacuum — as shown explicitly in appendix A.2.

Joint contributions

There are two different types of joint contributions that arise here. First, there are the intersections of the null boundaries of the WDW patch with the regulator surface at $r = r_{\max}$. There are four of these joints in total. Second, there are the intersections of the null sheets of the WDW patch in the future and in the past. Let us begin with the first case.

Considering the future, right boundary of the WDW patch near the regulator surface $r = r_{\max}$, the relevant null normal is given by

$$k_R = \alpha \left[dt + dr^*\right] , \tag{2.84}$$

while the outward pointing normal to the surface $r = r_{\max}$ is

$$n = g(r)dr \, . \tag{2.85}$$

We need also a vector $\tilde{t}$ that is a future-pointing unit time-like vector directed outwards from the region. In this case the correct choice is

$$\hat{t} = -f(r)dt \tag{2.86}$$

where we have written it as a form, but the sign is chosen so that the corresponding vector is outward directed. The relevant dot products are easily computed

$$k_R \cdot n = \frac{\alpha}{f(r)} , \quad k_R \cdot \hat{t} = \frac{\alpha}{f(r)} , \tag{2.87}$$

and since $f(r) > 0$ near the boundary we obtain $\epsilon = -1$. We have then

$$\tilde{a} = -\log \frac{\alpha}{f(r)} \tag{2.88}$$

from (2.60), yielding

$$I_{\text{jnt}}^{r_{\max}} = \frac{\Omega_{2N+1} r^{2N} h(r)}{16\pi G_N} \log \frac{f(r)^2}{\alpha^2} , \tag{2.89}$$

where we have made use of the fact that

$$\sqrt{\gamma} = r^{2N} h(r) d\Omega_{2N+1} \tag{2.90}$$

on the joint. Note that by $d\Omega_{2N+1}$ we mean the volume form on the usual, round $2N+1$ sphere — when integrated over the angles this gives

$$\Omega_{2N+1} \equiv \int d\Omega_{2N+1} = \frac{2\pi^{N+1}}{\Gamma\left[N+1\right]} . \tag{2.91}$$

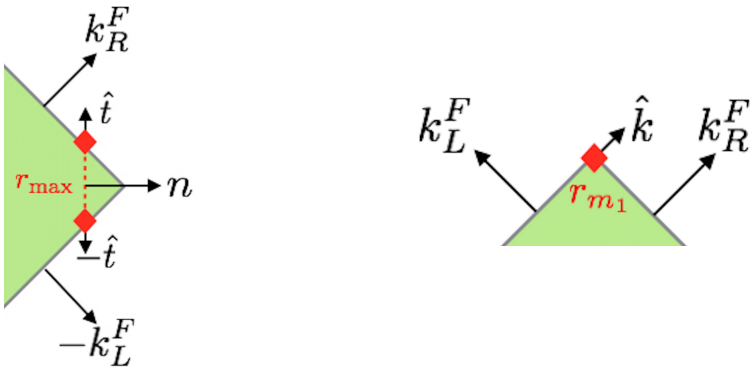

Figure 2.5: The joints in the WDW patch in figure 2.4 and the associated vectors needed to calculate their contribution to $I_{\rm WDW}$, according to (2.59)-(2.61).

An analogous computation for the remaining three joints can be shown to yield the same answer as that presented here.

Next let us consider the joints at the future and past meeting points of the WDW patch. The determinant of the induced metric at the intersection of the lightsheets is given by

$$\sqrt{\gamma} = h(r_m) r_m^{2N} d\Omega_{2N+1} \,, \tag{2.92}$$

where r_m is the value of r at the point of intersection. At the future meeting point the relevant null normals are

$$k_R^F = \alpha \left[dt + dr^*\right] \,, \quad k_L^F = \alpha \left[-dt + dr^*\right] \tag{2.93}$$

where, in determining the relevant signs, it is important to recognize that t increases from left to right inside the future horizon and dr^* points in the negative dr direction inside the horizon. Note also that the dt appearing in these normals is the t that appears in the metric, not the boundary time. We need also $\hat{k}$ — a null vector, living in the tangent space of the right sheet of of the WDW patch that is orthogonal to k_R^F and outward pointing as a vector. In this case, a one-form that points in the *negative* k_R^F direction yields a vector with the correct properties. We take

$$\hat{k} = -\left[dt + dr^*\right] \,. \tag{2.94}$$

We then find for the dot products

$$k_R^F \cdot k_L^F = \frac{2\alpha^2}{f(r)^2}\,, \quad \hat{k} \cdot k_L^F = -\frac{2\alpha}{f(r)^2}\,, \tag{2.95}$$

yielding $\epsilon = +1$ and from (2.61)

$$\tilde{a} = -\log\frac{|f(r_{m_1})^2|}{\alpha^2}\,. \tag{2.96}$$

Putting this all together we obtain for the joint contribution at the future meeting point

$$I^F_{\rm jnt} = -\frac{(r_{m_1})^{2N} h(r_{m_1})\Omega_{2N+1}}{8\pi G_N}\log\frac{|f(r_{m_1})^2|}{\alpha^2}\,. \tag{2.97}$$

A completely analogous calculation gives an identical form for the joint contribution at the past meeting point, with $r_{m_1} \to r_{m_2}$.

Null boundaries

Since the normals to the lightlike boundaries of the WDW patch are affinely parameterized, the boundary term on these surfaces makes no contribution. Nonetheless, we consider here the contribution from the counterterm for null boundaries that ensures the total action does not depend on the parameterization used for the null generators.

Considering the future segment on the right of the Penrose diagram, we have

$$\frac{\partial}{\partial\lambda} = \frac{\alpha}{g(r)f(r)}\frac{\partial}{\partial r}\,, \tag{2.98}$$

which yields

$$\Theta = \frac{1}{\sqrt{\gamma}}\frac{dr}{d\lambda}\frac{d\sqrt{\gamma}}{dr} = \frac{1}{h(r)r^{2N}}\frac{dr}{d\lambda}\frac{d\left(h(r)r^{2N}\right)}{dr} = \frac{\alpha}{f(r)g(r)}\left[\frac{2N}{r} + \frac{h'}{h}\right]\,. \tag{2.99}$$

We therefore have for the counterterm

$$I^{F,R}_{\rm ct} = \frac{\Omega_{2N+1}}{8\pi G_N}\int_{r_{m_1}}^{r_{\rm max}} \log\ell_{ct}\Theta\frac{d\left(h(r)r^{2N}\right)}{dr}\,dr\,. \tag{2.100}$$

We can use integration by parts to express this object in terms of two contributions at the joints and an integral independent of α and ℓ_{ct}:

$$I^{F,R}_{\rm ct} = \frac{\Omega_{2N+1}}{8\pi G_N}\left[r^{2N}h(r)\log\ell_{ct}\Theta\right]_{r_{m_1}}^{r_{\rm max}} - \frac{\Omega_{2N+1}}{8\pi G_N}\int_{r_{m_1}}^{r_{\rm max}} r^{2N}h(r)\frac{\Theta'}{\Theta}\,dr \tag{2.101}$$

where here we have used the shorthand $\Theta' = d\Theta/dr$. It can easily be confirmed that the counterterm evaluates to the same result for the future left segment. Additionally, the result for the past segments is equivalent with the substitution $r_{m_1} \to r_{m_2}$.

2.3.3 Framework for Complexity equals Volume calculations

We will compare our results obtained for the action with the results within the "Complexity equals Volume" framework [58, 59].[4] According to the CV proposal, the complexity of a holographic state at the boundary time slice Υ is related to the volume of an extremal codimension-one slice $\mathcal{B}$ by

$$\mathcal{C}_{\mathcal{V}}(\Upsilon) = \max_{\Upsilon=\partial\mathcal{B}} \left[\frac{\mathcal{V}(\mathcal{B})}{G_N R}\right]. \tag{2.102}$$

The fact that the CV conjecture requires an (arbitrary) length scale R was originally used as an argument in favour of CA over CV. However, there is as yet no universally accepted prescription for computing the bulk complexity, and useful information can be gleaned by comparing different proposals.[5]

To find the volume of the extremal codimension-one slice $\mathcal{B}$, write the metric (2.12) in ingoing coordinates $x^\mu = \left(v, r, \vec{\Omega}\right)$, and parameterize the surface with coordinates $y^a = \left(\lambda, \vec{\Omega}\right)$, where $\vec{\Omega}$ are the angular coordinates.[6] Below, we choose the symmetric case of boundary times $-t_L = t_R \equiv \tau/2$. The induced metric on the codimension-one slice is then

$$\sigma_{ab} = e^\mu_a e^\nu_b g_{\mu\nu}, \quad e^\mu_a \equiv \frac{\partial x^\mu}{\partial y^a} \tag{2.103}$$

where $g_{\mu\nu}$ is the MP-AdS metric (2.12). The volume functional of this slice can be shown to be

$$\mathcal{V} = \int \sqrt{|\sigma|} d^{D-1}x = \Omega_{D-2} \int h(r) r^{D-3} \sqrt{-f(r)^2 \dot{v}^2 + 2g(r) f(r) \dot{v}\dot{r}}\, d\lambda \tag{2.104}$$

where $v = v(\lambda)$ and $r = r(\lambda)$. We assume[7] a parametrization where

$$h(r) r^{D-3} \sqrt{-f(r)^2 \dot{v}^2 + 2g(r) f(r) \dot{v}\dot{r}} = 1. \tag{2.105}$$

[4] A related proposal, called the complexity=volume 2.0, was put forward in [109], which suggests that the complexity volume is the spacetime volume of the associated WDW patch.

[5] Moreover, it was subsequently realized that the CA proposal also possesses an ambiguous length scale, namely the one associated with the counter-term for null boundaries.

[6] This choice is possible due to the enhanced symmetry of the equal-spinning black holes studied here.

[7] This is possible because the volume functional (2.104) is reparametrization-invariant — that is, it is invariant under $\lambda \to \tilde{\lambda}(\lambda)$.

This Lagrangian is independent of v and hence there is a conserved quantity (analogous to energy) given by

$$E = -\frac{\partial \mathcal{L}}{\partial \dot{v}} = h(r)^2 r^{2(D-3)} \left(f(r)^2 \dot{v} - g(r) f(r) \dot{r} \right) . \tag{2.106}$$

Furthermore, we have from (2.105) and (2.106)

$$h(r)^{-2} r^{-2(D-3)} E^2 + f(r)^2 = h(r)^2 r^{2(D-3)} g(r)^2 f(r)^2 \dot{r}^2 . \tag{2.107}$$

The volume of this extremal surface is obtained by integrating (2.104) on-shell:

$$\mathcal{V} = 2\Omega_{D-2} \int_{r_{\min}}^{r_{\max}} \frac{dr}{\dot{r}} = 2\Omega_{D-2} \int_{r_{\min}}^{r_{\max}} \frac{h(r)^2 r^{2(D-3)} g(r) f(r)}{\sqrt{h(r)^2 r^{2(D-3)} f(r)^2 + E^2}} \, dr \tag{2.108}$$

where we included a factor of 2 to include the left half of the surface. Here we wish to take $r_{\max}$ to be infinity, but this will yield a divergent result in general. A finite result can be obtained by studying the time derivative of the volume (as relevant for the growth rate), or by performing a carefully matched subtraction of the AdS vacuum (as relevant for the complexity of formation). Here $r_{\min}$ is the turning point of the surface, determined by the condition $\dot{r} = 0$:

$$h(r_{\min})^{-2} r_{\min}^{-2(D-3)} E^2 + f(r_{\min})^2 = 0 . \tag{2.109}$$

A simple calculation shows that $r_{\min}$ will be on or inside the (outer) horizon, and so we have that, using (2.106), $f(r_{\min})^2 < 0, \dot{v}(\lambda_{\min}) > 0 \Rightarrow E < 0$ and we recall that $f(r)^2 < 0$ in the region between the inner and event horizon.

2.4 Complexity of Formation

In this section, we study the complexity of formation for rotating black holes in both the CA and CV conjectures. In both cases, we verify convergence to the static limit and study the dependence of the complexity of formation on thermodynamic parameters near the extremal limit and for large black holes.

2.4.1 Complexity Equals Action

Within the CA conjecture, the complexity of formation is given by the difference between the action of the WDW patch and the action of the global AdS vacuum both evaluated at the $\tau = 0$ timeslice.

Let us now put together the various pieces accumulated so far. First, consider the sum of the joint and counterterm contributions. As we know from the general arguments in [70], this result must be independent of the parameterization of the null generators, i.e. independent of α. We find that

$$I^{F}_{\rm jnt}+2I^{r_{\rm max}}_{\rm jnt}+I^{F,R}_{\rm ct}+I^{F,L}_{\rm ct}=\frac{\Omega_{2N+1}}{8\pi G_N}\left[r^{2N}_{\rm max}h(r_{\rm max})\log\frac{\ell^2_{ct}\Theta(r_{\rm max})^2|f(r_{\rm max})^2|}{\alpha^2}\right.$$
$$\left.-(r_{m_1})^{2N}h(r_{m_1})\log\frac{\ell^2_{ct}\Theta(r_{m_1})^2|f(r_{m_1})^2|}{\alpha^2}\right]-\frac{\Omega_{2N+1}}{4\pi G_N}\int_{r_{m_1}}^{r_{\rm max}}r^{2N}h(r)\frac{\Theta'}{\Theta}\,dr\,. \tag{2.110}$$

Note that this expression is completely independent of α — Θ is proportional to α and thus all α dependence precisely cancels out. This is, of course, necessary, but it nonetheless provides a consistency check of our computations. It can further be shown — assuming the scale ℓ_{ct} is the same for both the AdS vacuum and the black hole solutions — that the first term evaluated at $r_{\rm max}$ cancels precisely with the corresponding ones occurring in the global AdS vacuum. A completely analogous computation holds for the past sheets of the WDW patch yielding the same result as above with the substitution $r_{m_1}\to r_{m_2}$. However, in this case we can further simplify matters by noting that, since $\tau=0$ for the complexity of formation, $r_{m_1}=r_{m_2}\equiv r_{m_0}$. Noting that for the AdS vacuum we have

$$\Theta_{\rm AdS}=\frac{(2N+1)\alpha}{r}\,, \tag{2.111}$$

and combining the above with the relevant background subtraction we obtain for the joint and counterterms:[8]

$$\Delta\left(I_{\rm jnt}+I_{\rm ct}\right)=-\frac{\Omega_{2N+1}(r_{m_0})^{2N+1}}{2\pi G_N(2N+1)}-\frac{\Omega_{2N+1}}{4\pi G_N}(r_{m_0})^{2N}h(r_{m_0})\log\frac{\ell^2_{ct}\Theta(r_{m_0})^2|f(r_{m_0})^2|}{\alpha^2}$$
$$-\frac{\Omega_{2N+1}}{2\pi G}\int_{r_{m_0}}^{\infty}r^{2N}\left[h(r)\frac{\Theta'}{\Theta}+1\right]\,dr\,. \tag{2.112}$$

where we have extended the range of integration to infinity in the last term since the subtraction has made the integral convergent. Note also that r_{m_0} is obtained by solving the equation

$$r^*(r_{m_0})-r^*_\infty=0\,. \tag{2.113}$$

[8] In obtaining this we have made use of the fact that the caustics at the future meeting point of the WDW patch do not contribute for global AdS.

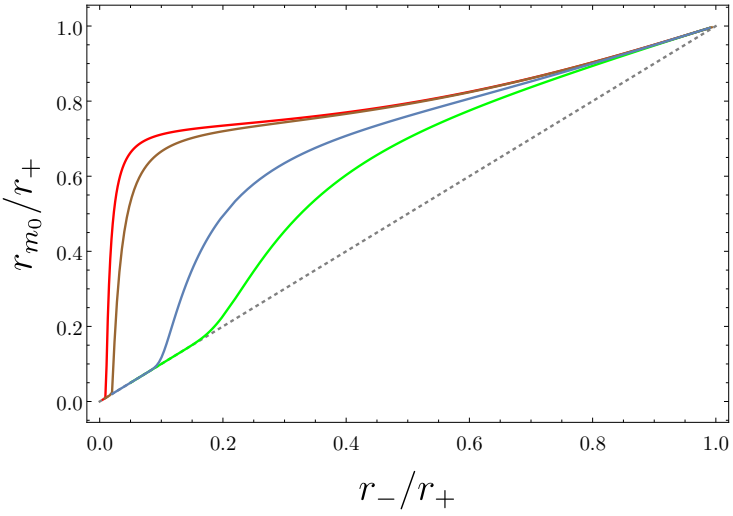

Figure 2.6: A plot showing the value of r_{m_0} vs. r_-/r_+ for several different values of r_+/ℓ. The curves correspond to $r_+/\ell = 5, 10, 50, 100$ in order from bottom to top.

For the case of the complexity of formation, additional simplifications occur for the bulk integral. It becomes (including the necessary factor of two)

$$I_{\text{bulk}} = \frac{\Lambda\Omega_{2N+1}}{(2N+1)\pi G_N}\int_{r_{m_0}}^{r_{\max}} r^{2N+1}\left[r_\infty^* - r^*(r)\right]dr\,. \tag{2.114}$$

Since r^* must be computed numerically, followed by a numerical evaluation of this integral, it is actually more convenient to use integration by parts to eliminate the appearance of $r^*(r)$ inside this expression, leaving only a single integral to evaluate numerically. Doing so, we find that

$$I_{\text{bulk}} = \frac{\Lambda\Omega_{2N+1}}{2(N+1)(2N+1)\pi G_N}\left(r^{2(N+1)}\left[r_\infty^* - r^*(r)\right]\Big|_{r_{m_0}}^{r_{\max}} + \int_{r_{m_0}}^{r_{\max}} r^{2N+1}g(r)^2h(r)dr\right)\,. \tag{2.115}$$

Note that the evaluation of the first term at r_{m_0} vanishes by virtue of the equation defining r_{m_0}. It can further be shown, using the asymptotic form of the tortoise coordinate, that the evaluation at $r_{\max}$ cancels with the analogous one coming from the global AdS vacuum.

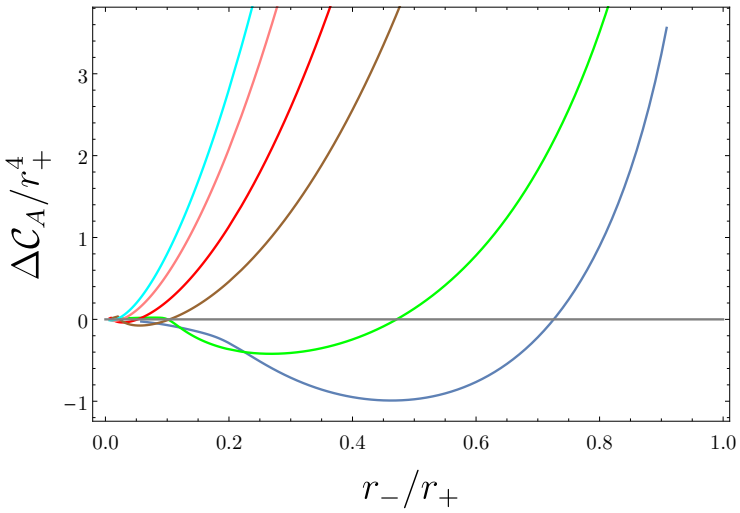

Figure 2.7: A plot showing the complexity of formation in the action formalism for different values of r_+/ℓ and for $D = 5$. The curves correspond to $r_+/\ell = 5, 10, 50, 100, 200, 300$ in order from bottom to top in a vertical slice on the right side of the plot. Here we have set $\ell_{\rm ct} = \ell$.

Taking this into account and performing the background subtraction we obtain the result

$$\Delta I_{\rm bulk} = \frac{\Lambda\Omega_{2N+1}}{2(N+1)(2N+1)\pi G_N}\left[\int_{r_{m_0}}^{\infty} r^{2N+1}\left(g(r)^2h(r) - \frac{r}{1+r^2/\ell^2}\right)dr - \int_0^{r_{m_0}} \frac{r^{2(N+1)}}{1+r^2/\ell^2}dr\right], \tag{2.116}$$

where we have extended the range of the first integral to $r = \infty$ since the subtraction has made it convergent.

The most complicated aspect of determining the complexity of formation within the action framework is computing the value of r_{m_0} numerically. We show in figure 2.6 the resulting curves for several values of r_+/ℓ. The difficulty arises in determining accurate results in the limit where r_-/r_+ becomes small. As discussed previously, in this limit the value of r_{m_0} can be worked out perturbatively and, for five dimensions, reads

$$r_{m_0} = r_-\left[1 + \exp\left(-\frac{\pi\ell(r_+^2+\ell^2)}{r_+(\ell^2+2r_+^2)}\frac{r_+^2}{r_-^2} + \cdots\right) + \cdots\right]. \tag{2.117}$$

Thus, as $r_-/r_+ \to 0$, the difference between r_{m_0} and r_- tends to zero like $\exp(-1/r_-^2)$, and so increasing numerical precision is required in this limit. For sufficiently small r_-/r_+

the problem effectively becomes numerically intractable and we are forced to resort to perturbative techniques.

In figure 2.7, we show the complexity of formation $\Delta\mathcal{C}_{\mathcal{A}}$ for five-dimensional rotating black holes with different values of r_+/ℓ. There are a few noteworthy things here. The basic structure of the curves is qualitatively similar for different values of r_+/ℓ. A somewhat strange feature is that there is a range of parameter values over which the complexity of formation actually becomes negative. While strange, it must be kept in mind that complexity of formation is a relative quantity: it is computed by subtracting one (infinite) result from another. Moreover, in some cases, namely involving gravitational solitons, a negative complexity of formation has been previously observed [79, 81], and so this result in and of itself is not new. While there is an intermediate regime in which the complexity of formation is negative, it is always positive at the two extremes of the plot: in the extremal and nonrotating limits. That the former is true is obvious from the plot, but the static limit is subtle and requires additional scrutiny.

The static limit is examined in detail in appendix A.3. Here, for conciseness, we will present a discussion relevant to the five-dimensional case. In the static limit $r_-/r_+ \to 0$ all contributions to the corner/joint term vanish except for the term involving the logarithm,

$$-\frac{\Omega_{2N+1}}{4\pi G_N}(r_{m_0})^{2N}h(r_{m_0})\log\frac{\ell_{ct}^2\Theta(r_{m_0})^2|f(r_{m_0})^2|}{\alpha^2}\,. \tag{2.118}$$

Using the perturbative expansion for r_{m_0} shown above, we can work out that this term yields a finite limit

$$-\frac{\Omega_{2N+1}}{4\pi G_N}(r_{m_0})^{2N}h(r_{m_0})\log\frac{\ell_{ct}^2\Theta(r_{m_0})^2|f(r_{m_0})^2|}{\alpha^2} \to \frac{\pi^2 r_+^2(r_+^2+\ell^2)^{3/2}}{2G_N(\ell^2+2r_+^2)} \tag{2.119}$$

and we reiterate that here we are considering the case of five dimensions ($N = 1$). This result is *exactly half* the contribution arising from the GHY terms on the future/past singularity in the Schwarzschild-AdS geometry. A similar analysis can be carried out for the bulk term, which in the static limit (see appendix A.3 for details) yields

$$\lim_{r_-/r_+\to 0}\Delta I_{\text{bulk}} = \Delta I_{\text{bulk}}^{\text{Schw}}\,. \tag{2.120}$$

That is, the bulk contribution of the rotating black hole limits to exactly the bulk contribution for the non-rotating black hole. As a result, there is an order of limits problem for the action computation: taking the static limit of the action result gives an answer that does not agree with the direct computation done for the Schwarzschild-AdS black hole.

It is insightful here to consider how this limit compares with the analogous neutral limit for charged black holes. Again, we consider this in full detail and in all dimensions in appendix A.3. For the charged black hole, the joint term reduces to a fraction of the Schwarzschild-AdS GHY term in the neutral limit, while the bulk action for charged black holes reproduces the full Schwarzschild-AdS bulk action *along with the remaining fraction of the GHY term*. Thus, for charged black holes, there is not an order of limits problem. However, the manner in which the various terms conspire to give the neutral limit is rather nontrivial. The main difference here in the rotating case is that the limit of bulk term does not include an additional fraction of the GHY term. This can be traced, mathematically, to the behaviour of the metric function $h(r)$ in this limit.

It should be noted that while when $a = 0$ the metric is simply the usual static AdS black hole, the limit considered here is different and this is the mathematical reason behind the order of limits issue. Effectively, here we are simultaneously zooming in on the inner horizon while taking the limit $r_- \to 0$. In this limit the metric function h is not simply r (as it would be for the static black hole), but instead it limits to a constant value. As discussed in appendix A.3, this behaviour is the source of the order of limits issue, which in general dimensions becomes:

$$\lim_{r_-/r_+\to 0} \pi\Delta\mathcal{C}_{\mathcal{A}} = \frac{I^{\text{Schw}}_{\text{GHY}}}{N+1} + \Delta I^{\text{Schw}}_{\text{Bulk}} \neq \pi\Delta\mathcal{C}^{\text{Schw}}_{\text{form}} \tag{2.121}$$

where the complexity of formation of the static black hole $\Delta\mathcal{C}^{\text{Schw}}_{\text{form}}$ is the sum of the bulk $\Delta I^{\text{Schw}}_{\text{Bulk}}$ and surface $I^{\text{Schw}}_{\text{GHY}}$ contributions.

There are (at least) two perspectives one could have on this issue. First, it could be viewed as simply a genuine feature of the CA proposal. The CA proposal is highly sensitive to the detailed causal structure of spacetime, and the order of limits issue found here is not the first of its kind. For example the rate of growth of complexity for dilaton black holes was found to be highly sensitive to the details of the causal structure [136]. Moreover in the usual framework the complexity growth rate for magnetic black holes is precisely zero [136, 137], leading to an obvious order of limits problem (though it is possible to remedy this case through the addition of an electromagnetic counterterm). Furthermore, the growth rate of complexity for charged black holes in higher-curvature theories exhibits an order of limits problem in the neutral limit [97, 77, 138]. Thus there is precedent for subtle behaviour of the CA conjecture, and it would be interesting to better understand whether this is consistent with CFT expectations.

An alternate perspective is that this order of limits issue is a problem that must be resolved. One means to do so is to consider an alternative regularization scheme for the

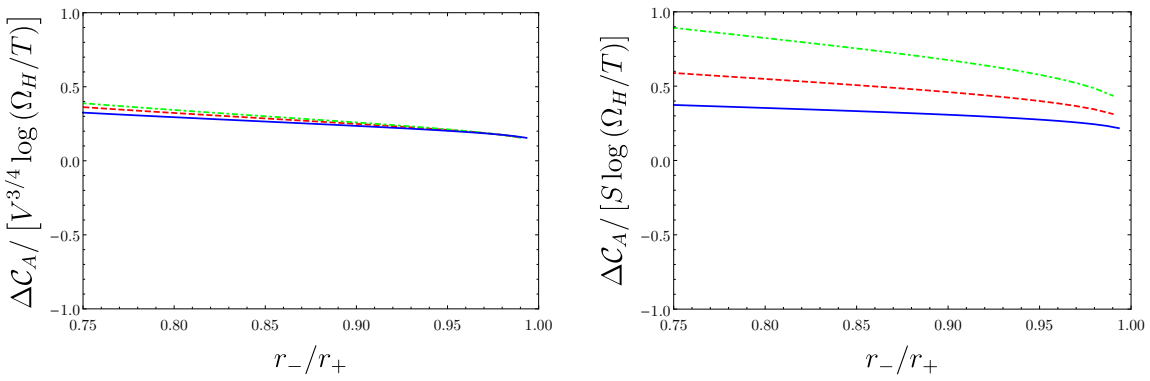

Figure 2.8: Comparing the complexity of formation near extremality normalized by the thermodynamic volume (left) vs. the entropy (right) for $D = 5$ black holes. The curves correspond to $r_+/\ell = 50, 100, 200$ corresponding to the blue, red dashed, and green dot-dashed curves respectively. Here we have set $\ell_{\rm ct} = \ell$.

WDW patch — which we explain in detail in appendix A.4. The basic idea is to introduce space-like regulator surfaces cutting off the future and past tips of the WDW patch at $r = r_{m_0} + \Delta r$. This could be motivated from the perspective that the inner Cauchy horizon is expected to be unstable to generic perturbations [139, 140, 141], and therefore this cutoff would encode some level of agnosticism of what happens precisely at the inner horizon. This leads to a well-defined static limit to the complexity

$$\lim_{\Delta r\to 0}\lim_{r_-/r_+\to 0}\pi\Delta\mathcal{C}_{\mathcal{A}} = I^{\rm Schw}_{\rm GHY} + \Delta I^{\rm Schw}_{\rm Bulk} = \pi\Delta\mathcal{C}^{\rm Schw}_{\rm form} \tag{2.122}$$

but it must be noted that the limits do not commute. Moreover, for sufficiently small Δr there is no appreciable effect of this term on the results when both r_- and r_+ are sufficiently large, but it becomes important in the limit $r_-/r_+ \to 0$.[9]

Let us now leave aside this issue of limits and consider in more detail some further interesting properties of the complexity of formation. Our focus here is primarily on the scaling behaviour of complexity in the limit of large ($r_+/\ell \gg 1$) black holes. For neutral and charged static black holes this behaviour is governed by the entropy [64, 69], leading to the idea that the complexity of formation is effectively controlled by the number of

[9]It is also worth noting that there appears to be no simple modification of the action proposal itself that would account for the order of limits problem. For example, if one considers only the bulk action as the relevant term then there would be no order of limits issue for rotating black holes, but it would introduce one for charged black holes — see appendix A.3.

degrees of freedom possessed by the system. We can schematically write this relationship for charged black holes as:

$$\Delta\mathcal{C}_{\mathcal{A}}^{\text{charged}} \underset{\frac{r_+}{\ell}\gg 1}{\sim} S\log\frac{\mu}{T} + f(\epsilon_i)S \tag{2.123}$$

where μ is the chemical potential and ϵ_i represent various parameters that characterize the state, such as μ or T. The function $f(\epsilon_i)$ has a smooth, non-vanishing limit as $\mu \to 0$. The relationship above is schematic and so neglects possible constant terms in the coefficients and so on. However it conveys the important features: the complexity of formation exhibits a logarthmic singularity near extremality and the general form is controlled by the entropy.

We consider the analogous problem in detail for rotating black holes in appendix A.5. Again, there is a logarthmic singularity in the extremal limit that is controlled by the entropy. However, the general behaviour is markedly different. The schematic form for the complexity of formation for large rotating black holes takes the form

$$\Delta\mathcal{C}_{\mathcal{A}} \underset{\frac{r_+}{\ell}\gg 1}{\sim} S\log\frac{\Omega_H}{T} + f(\epsilon_i)V^{\frac{D-2}{D-1}}\,, \tag{2.124}$$

where Ω_H is the angular velocity of the horizon, V is the thermodynamic volume and again $f(\epsilon_i)$ is some function of the ratio r_-/r_+ (which could, of course, be reexpressed as a function of Ω_H and T). The implication of the above relationship is that, for sufficiently large black holes, the complexity of formation is always controlled by the thermodynamic volume rather than the entropy. The validity of this conclusion can be seen clearly in the plots shown in figure 2.8 for five dimensions — see also figure A.7 in appendix A.5. We emphasize that this observation is possible due to the independence of the thermodynamic volume and the entropy for rotating black holes. In the case of static (charged or neutral) black holes, these quantities are not independent and one is free to write the final result in terms of either S or V as the two quantities are related by

$$S \underset{\text{static limit}}{\sim} V^{(D-2)/(D-1)}\,. \tag{2.125}$$

We will return to discuss the implications of this result in the discussion.

2.4.2 Comparison with Complexity=Volume Conjecture

The complexity of formation in the CV proposal is straightforward to calculate. The volume of the maximal slice in vacuum AdS_D is

$$\mathcal{V}_0 = \Omega_{D-2}\int_0^{r_{\text{max}}^{\text{AdS}}} \frac{r^{D-2}}{\sqrt{f_0(r)}}\,dr, \quad f_0(r) = 1 + \frac{r^2}{\ell^2}\,. \tag{2.126}$$

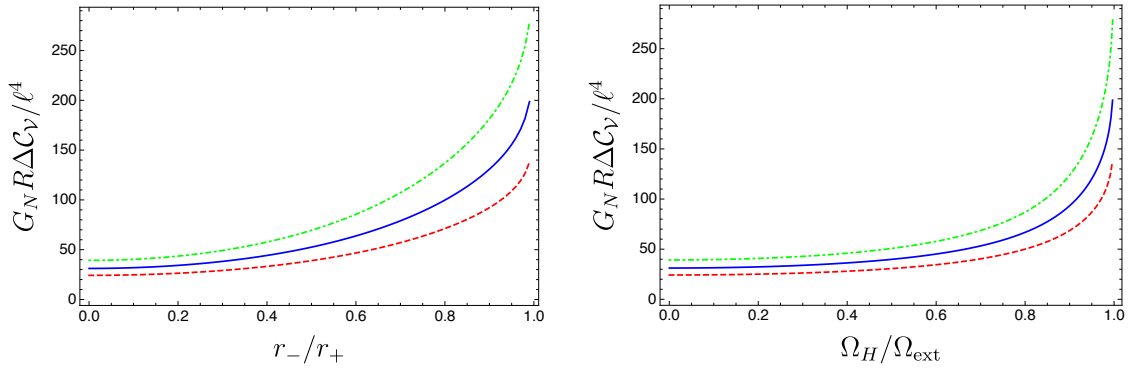

Figure 2.9: Here we show the complexity of formation within the CV proposal. *Left*: The curves correspond to $r_+/\ell = 9/10, 1, 11/10$ from bottom to top for $D = 5$. The complexity of formation diverges in the extremal limit and tends to a constant (r_+/ℓ-dependent) value as $r_-/r_+ \to 0$. *Right*: The same curves now plotted against the rotation of the boundary CFT in the form of the ratio $\Omega_H/\Omega_{\text{ext}}$ where Ω_H is the angular velocity of the boundary CFT and Ω_{ext} is the zero temperature limit of this angular velocity.

In the black hole geometry, we are interested in the maximal slice at $\tau = 0$. In this case we have $r_{\text{min}} = r_+$ which gives $E = 0$ from (2.106). The complexity of formation is then

$$\Delta\mathcal{C}_\mathcal{V} = \frac{\mathcal{V} - 2\mathcal{V}_0}{G_N R} = \frac{2\Omega_{D-2}}{G_N R}\left[\int_{r_+}^{r_{\text{max}}} h(r) r^{D-3} g(r)\, dr - \int_0^{r_{\text{max}}^{\text{AdS}}} \frac{r^{D-2}}{\sqrt{f_0(r)}}\, dr\right]. \tag{2.127}$$

The integral can be evaluated numerically in a straightforward manner, and we show some representative examples in figure 2.9. The qualitative structure of the curves is independent of the value of r_+/ℓ. Though, since $\Delta\mathcal{C}_\mathcal{V}$ is not a homogeneous function of r_+/ℓ, there is no simple factor that collapses the different curves to a single line for all values of r_+/ℓ. When $r_-/r_+ \to 0$, the complexity of formation tends to a constant value, whereas it diverges in the extremal limit. This divergence is consistent with results obtained previously for charged black holes [69].

In the CA framework we encountered an order of limits issue when taking $r_-/r_+ \to 0$. Here there is no such issue, which is due to the fact that the CV proposal is less sensitive to the detailed properties of the causual structure than the CA proposal. In the static limit, the complexity of formation (2.127) reduces directly to that of the static black hole $\Delta\mathcal{C}_\mathcal{V}^{\text{Schw}}$ [64] since

$$\lim_{a\to 0} h(r)g(r) = \frac{r}{\sqrt{f^{\text{Schw}}(r)}} \tag{2.128}$$

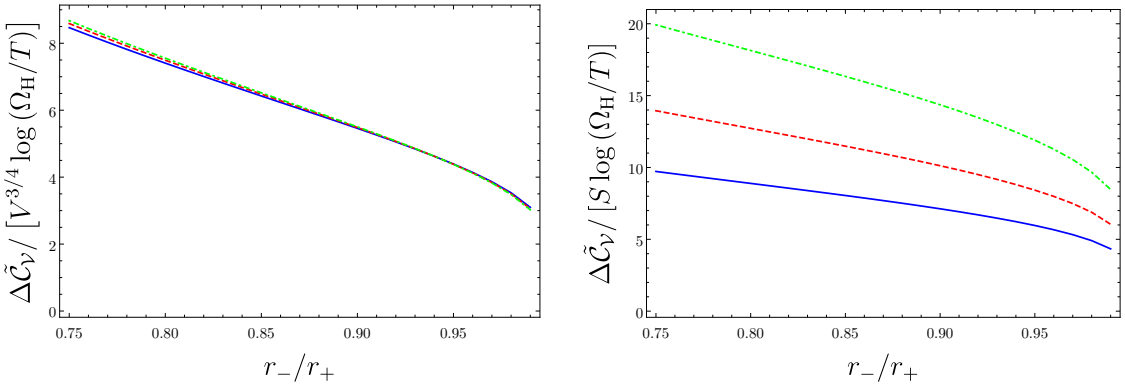

Figure 2.10: Here we show the complexity of formation within the CV proposal near extremality. Near extremality, the complexity of formation diverges logarithmically. In the left plot, we compare with the thermodynamic volume, while in the right plot we compare with the entropy. In each case we have defined $\Delta\tilde{\mathcal{C}}_{\mathcal{V}} = G_N R\Delta\mathcal{C}_{\mathcal{V}}/\ell$ to simplify the plot labels. In each case the curves correspond to $r_+/\ell = 50, 100, 200$ (solid blue, dashed red, and dot-dashed green, respectively) for $D = 5$.

where $f^{\rm Schw}(r)$ is the metric function of the Schwarzschild-AdS spacetime.

It is interesting to further compare the general behaviour of the complexity of formation of large black holes within the CV proposal to the CA proposal. The details of this analysis are presented in appendix A.5, but the conclusion is the same. The complexity of formation exhibits a logarithmic singularity near extremality that is controlled by the entropy, while the non-logarthmic terms are controlled by the thermodynamic volume. Thus we once again arrive at the result that for sufficiently large black holes the complexity of formation is controlled by the thermodynamic volume:

$$\Delta\mathcal{C}_{\mathcal{V}} \underset{\frac{r_+}{\ell}\gg 1}{\sim} S\log\frac{\Omega_H}{T} + \tilde{f}(\epsilon_i)V^{\frac{D-2}{D-1}}\,. \tag{2.129}$$

The validity of this can be seen directly in figure 2.10 — see also figure A.6 in appendix A.5.

2.5 Growth Rate of Holographic Complexity

In this section, we use the CA and CV proposals to study the full time evolution of holographic complexity of the boundary state (2.11) dual to the MP-AdS black hole geometry.

Our interest here will be in understanding the growth rate of complexity, and how this quantity evolves in time.

2.5.1 Complexity Equals Action

As before, we begin our considerations with the action conjecture. The various terms appearing in the computation were assembled in section 2.3, and here we proceed and use these directly. Taking the time derivative of all action terms, we see that only the bulk and joint terms contribute, giving

$$\begin{aligned}\frac{dI_{\text{WDW}}}{d\tau} &= -\frac{(D-1)\times\Omega_{D-2}}{8\pi G_N \ell^2}\int_{r_{m_1}}^{r_{m_2}} r^{2N+1}\,dr \\ &+ \frac{\Omega_{D-2}}{8\pi G_N}\left[\partial_r\left(r^{2N}h(r)\right)\log\left|\frac{\alpha^2}{\ell_{ct}^2\Theta^2 f^2}\right| - 2r^{2N}h(r)\frac{(f^2)'}{f^2}\right]_{r=r_{m_2}}\frac{dr_{m_2}}{dt} \\ &+ \frac{\Omega_{D-2}}{8\pi G_N}\left[\partial_r\left(r^{2N}h(r)\right)\log\left|\frac{\alpha^2}{\ell_{ct}^2\Theta^2 f^2}\right| - 2r^{2N}h(r)\frac{(f^2)'}{f^2}\right]_{r=r_{m_1}}\frac{dr_{m_1}}{dt}. \end{aligned} \tag{2.130}$$

The first line in the above is the time derivative of the bulk action, while the second and third lines correspond to the time derivatives of the combined joint and counterterm contributions at the future and past tips of the WDW patch. We recall that since $\Theta \propto \alpha$, this result is actually independent of the parameterization of the null vectors normal to the WDW patch, as it must be. From (2.66) and (2.67),

$$\frac{dr_{m_2}}{d\tau} = -\frac{1}{2}\frac{f(r_{m_2})}{g(r_{m_2})}, \quad \frac{dr_{m_1}}{d\tau} = \frac{1}{2}\frac{f(r_{m_1})}{g(r_{m_1})}, \tag{2.131}$$

and so once the values of r_{m_1} and r_{m_2} are known, it is possible to evaluate directly the growth rate of complexity.

Just as in the case of the complexity of formation, the difficulty here arises in determining the values of r_{m_i}, which is a numerically subtle problem. We show some representative results in figure 2.11. While we show the results here for a particular value of r_+/ℓ, this is unimportant for understanding the general behaviour which depends much more strongly on the value of r_-/r_+. We see from the top-left figure that, when r_-/r_+ is a small value, r_{m_1} and r_{m_2} present a phase where they are effectively constant. The implication of this is a period in the growth rate where the complexity effectively stalls and does not exhibit significant dependence on time. As r_-/r_+ increases, r_{m_i} exhibit stronger time dependence,

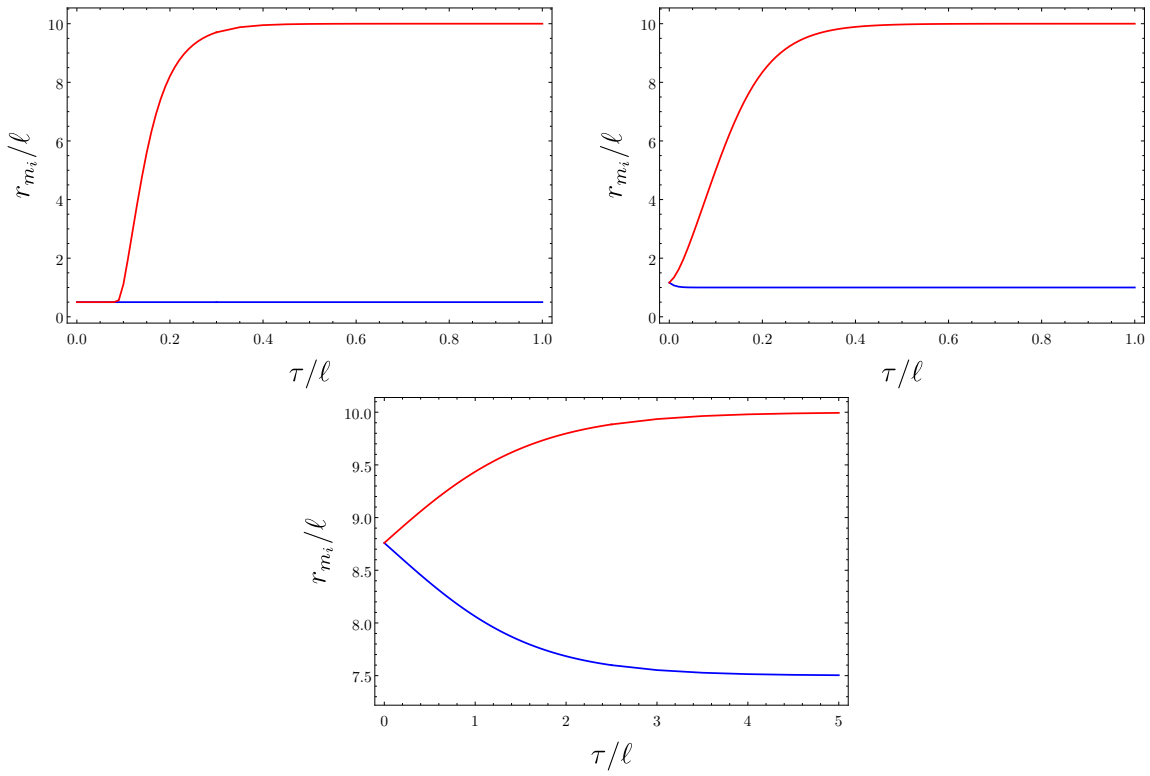

Figure 2.11: Here we show plots of r_{m_1} (blue) and r_{m_2} (red) as a function of time. In each plot we have set $r_+/\ell = 10$, while the different plots correspond to $r_-/r_+ = 1/20, 1/10, 3/4$ (left to right).

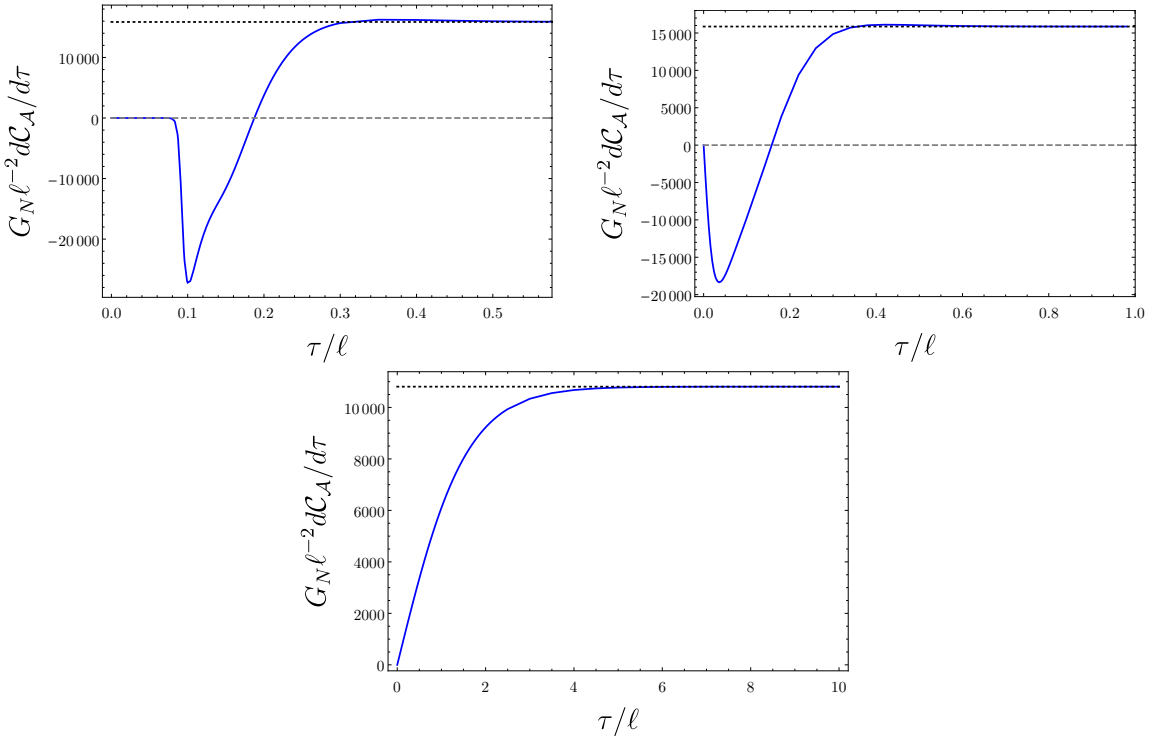

Figure 2.12: Here we show plots of the growth rate of complexity as a function of time. In each plot we have set $r_+/\ell = 10$, while the different plots correspond to $r_-/r_+ = 1/20, 1/10, 3/4$ (left to right). We have set $\ell_{\rm ct} = 1$. The dotted black line shows the growth rate of complexity in the limit $\tau \to \infty$.

but generally become "squished" in a smaller interval (since they must lie between r_- and r_+). In all cases, r_{m_1} and r_{m_2} asymptote to the inner and outer horizons, respectively.

Once the values of r_{m_i} have been determined, it is straightforward to determine the growth rate as a function of time. We show representative results in figure 2.12 for the same cases for which we displayed r_{m_i} in figure 2.11. The results are qualitatively similar to what has been previously observed for charged black holes (c.f. figure 10 of [69]). There are some general features that can be remarked on. First, we note that in the limit of small rotation (equivalently, small r_-/r_+) the growth rate develops a minimum. As the rotation is decreased, the minimum becomes sharper and deeper. Moreover, in the same case, the growth rate exhibits a phase where it is close to zero before this oscillatory behaviour manifests. These observations are consistent with the growth rate limiting to that of the static black holes [69]. As the rotation is increased, both the late-time limit of the growth

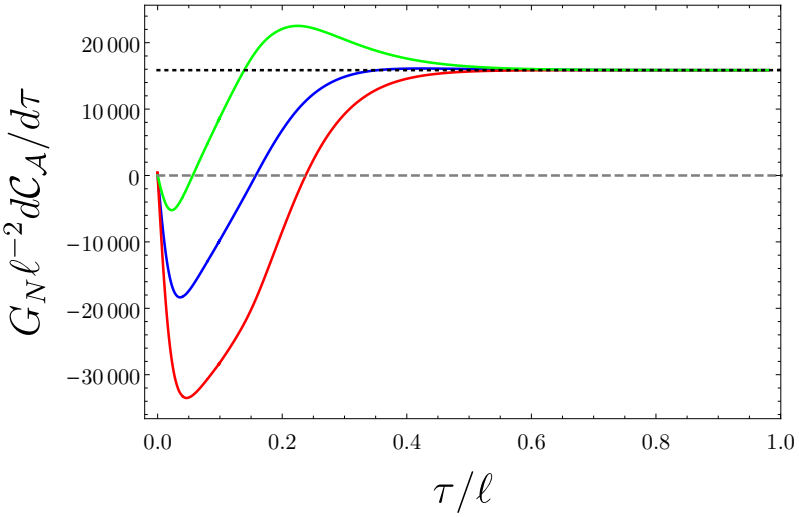

Figure 2.13: Here we show a plot of the growth rate of complexity for the parameter choices $r_+/\ell = 10$, $r_-/r_+ = 1/10$ for the choices $\ell_{\rm ct} = 10, 1, 1/10$ corresponding to red, blue, green curves, respectively — or bottom to top. The dotted black line shows the growth rate of complexity in the limit $\tau \to \infty$.

rate decreases and the transient oscillations become less significant. The ultimate limiting case is the extremal limit, where the late-time growth actually goes identically to zero (this will be justified below). While we have shown the growth rate for the particular choice of $\ell_{\rm ct} = 1$, the precise value of this parameter affects significantly only the early-time behaviour — we show an example of this in figure 2.13.

Perturbative expansion at late times

Having presented numerical computations for the full time-dependent growth rate of complexity, let us now turn to discuss some general features at late times. At large τ, using (2.42), we can solve (2.66) and (2.67) perturbatively to find that

$$\begin{aligned} r_{m_1}(\tau) &= r_- \left(1 + c_1 \exp\left[-\frac{r_-^2(r_+^2 - r_-^2)\tau}{G(r_-)h(r_-)}\right]\right) + \dots, \\ r_{m_2}(\tau) &= r_+ \left(1 - c_2 \exp\left[-\frac{r_+^2(r_+^2 - r_-^2)\tau}{G(r_+)h(r_+)}\right]\right) + \dots \end{aligned} \tag{2.132}$$

where the dots indicate subleading terms in the large τ expansion and

$$c_1 = 2\left(\frac{r_+ - r_-}{r_+ + r_-}\right)^{\frac{r_-^2 G(r_+)h(r_+)}{r_+^2 G(r_-)h(r_-)}} \exp\left[\frac{2r_-^2(r_+^2 - r_-^2)}{G(r_-)h(r_-)}\int_{r_-}^{\infty} H(r')\,dr'\right],$$
$$c_2 = 2\left(\frac{r_+ - r_-}{r_+ + r_-}\right)^{\frac{r_+^2 G(r_-)h(r_-)}{r_-^2 G(r_+)h(r_+)}} \exp\left[-\frac{2r_+^2(r_+^2 - r_-^2)}{G(r_+)h(r_+)}\int_{r_+}^{\infty} H(r')\,dr'\right] \tag{2.133}$$

where $H(r)$ is the integrand of $\mathcal{R}(r)$ defined in (2.44). In the limit $\tau \to \infty$, it can be shown that

$$\frac{g^{tt}_{,r}(r)}{g^{tt}(r)}\frac{f(r)}{g(r)}\bigg|_{r\to r_\pm} = -\frac{r_\pm \mathcal{G}'(r_\pm)}{2h(r_\pm)} = -2\pi T_\pm \tag{2.134}$$

where we have introduced the notation $\mathcal{G}(r) \equiv g(r)^{-2}$, $T_\pm$ is the temperature of the black hole at the horizon $r_\pm$ given in (2.27), and

$$\lim_{r_{m_1}\to r_-} \frac{f(r_{m_1})}{g(r_{m_1})}\log\left|\frac{\alpha^2 g^{tt}(r_{m_1})}{\ell_{ct}^2\Theta(r_{m_1})^2}\right| = \lim_{r_{m_2}\to r_+} \frac{f(r_{m_2})}{g(r_{m_2})}\log\left|\frac{\alpha^2 g^{tt}(r_{m_2})}{\ell_{ct}^2\Theta(r_{m_2})^2}\right| = 0. \tag{2.135}$$

Expanding (2.130) in this limit using (2.132) gives

$$\begin{aligned}\frac{dI_{\rm WDW}}{d\tau} &= \frac{dI_{\rm WDW}}{d\tau}\bigg|_{\tau\to\infty} + \frac{\Omega_{D-2}}{8\pi G_N}\left(r_+^2 - r_-^2\right)^2\tau \\ &\times\left(\frac{r_+^{D+1}\left((D-3)h(r_+) + r_+h'(r_+)\right)}{G(r_+)^2h(r_+)^2}c_2\exp\left[-\frac{r_+^2(r_+^2-r_-^2)\tau}{G(r_+)h(r_+)}\right]\right. \\ &\left. - \frac{r_-^{D+1}\left((D-3)h(r_-) + r_+h'(r_-)\right)}{G(r_-)^2h(r_-)^2}c_1\exp\left[-\frac{r_-^2(r_+^2-r_-^2)\tau}{G(r_-)h(r_-)}\right]\right) + \dots\end{aligned} \tag{2.136}$$

where the dots indicate subleading terms in the large τ expansion, and

$$\begin{aligned}\frac{dI_{\rm WDW}}{d\tau}\bigg|_{\tau\to\infty} &= \frac{\Omega_{D-2}}{8\pi G_N}\left[-\frac{r_+^{2N+2} - r_-^{2N+2}}{\ell^2} + \frac{r_+^{2N+1}\mathcal{G}'(r_+) - r_-^{2N+1}\mathcal{G}'(r_-)}{2}\right] \\ &= \frac{\Omega_{D-2}}{8\pi G_N}\,2ma^2\left[\frac{1}{r_-^2} - \frac{1}{r_+^2}\right](N+1) \\ &= \frac{\Omega_{D-2}}{8\pi G_N}2ma^2\left[\frac{2m}{r_-^{2N+2} + 2ma^2} - \frac{2m}{r_+^{2N+2} + 2ma^2}\right](N+1) \\ &= (\Omega_- - \Omega_+)J\,.\end{aligned} \tag{2.137}$$

It is easiest to see the equality of the second and third lines by writing the parameters (m, a) in the bracket in the third term in terms of (r_+, r_-), which yields the second term. Furthermore, this agrees with

$$\left.\frac{dI_{\rm bulk}}{d\tau}\right|_{\tau\to\infty} = M - TS - \Omega J\Big|_{r_-}^{r_+} \tag{2.138}$$

which is the difference in thermodynamic free energy between the outer and inner horizons, and

$$\left.\frac{dI_{\rm jnt}}{d\tau}\right|_{\tau\to\infty} = TS\Big|_{r_-}^{r_+} \tag{2.139}$$

where we note that $S_\pm$ is given by (2.27). Therefore, the late-time complexity rate of growth is simply the difference in internal energy between the outer and inner horizons[10]

$$\pi\left.\frac{d\mathcal{C}_\mathcal{A}}{d\tau}\right|_{\tau\to\infty} = (F_+ + T_+S_+) - (F_- + T_-S_-) = U_+ - U_- \tag{2.140}$$

where $F_\pm$ and $U_\pm$ are the free and internal energies, respectively, of the outer and inner horizons. The second term in (2.136) was checked for various dimensions and found that it is always positive and less than 1. This strongly suggests that the late-time limit of action rate of growth (2.137) is always approached from above.

Using the fact that the Smarr relation (2.31) holds for both outer and inner horizons, we can rewrite (2.140) as

$$\pi\left.\frac{d\mathcal{C}_\mathcal{A}}{d\tau}\right|_{\tau\to\infty} = T_+S_+ - T_-S_- - \frac{2}{2N+1}P\Delta V \tag{2.141}$$

where $\Delta V = V_+ - V_-$ is the difference between the thermodynamic volumes of the outer and inner horizons. Interestingly, in the limit of large black holes, the TS factors and $P\Delta V$ term become proportional to each other and one can show that

$$\lim_{r_+/\ell\to\infty} \pi\left.\frac{d\mathcal{C}_\mathcal{A}}{d\tau}\right|_{\tau\to\infty} = \frac{2N+2}{2N+1}P\Delta V. \tag{2.142}$$

As will be shown below, a similar result also holds for the complexity rate of growth in CV conjecture.

[10]This thermodynamic interpretation of complexity rate of growth was first noted in [76]. In [77] it was shown to hold for charged black holes in Lovelock gravity. Thus, we expect that (2.138) and (2.139) exhibit a universal feature of complexity growth in black holes with two horizons.

2.5.2 Comparison with Complexity=Volume Conjecture

We will compare the complexity rate of growth according to the CV conjecture $d\mathcal{C}_\mathcal{V}/d\tau$ with the results found according to the CA conjecture. The volume of the extremal codimension-one slice was found in (2.104). To relate to boundary time, note first that

$$v_{max} = t_R + r_*(\infty), \quad v_{min} = t_{min} + r_*(r_{min}) \tag{2.143}$$

where $t_{min} = 0$ by left-right symmetry (we have left-right symmetry because the functional $\mathcal{V}$ is invariant under $t \to -t$ and $a \to -a$), and r_{min} is defined by (2.109). Therefore,

$$t_R + r_*(\infty) - r_*(r_{min}) = \int_{v_{min}}^{v_{max}} dv = \int_{r_{min}}^{r_{max}} \frac{g(r)}{f(r)} \left[\frac{E}{\sqrt{h(r)^2 r^{2(D-3)} f(r)^2 + E^2}} + 1 \right] dr \tag{2.144}$$

where we used (2.106). Note that the integrand here is convergent at $r = r_\pm$. Finally, it is easy to see that

$$\frac{\mathcal{V}}{2\Omega_{D-2}} = \int_{r_{min}}^{r_{max}} \frac{g(r)}{f(r)} \left[\sqrt{h(r)^2 r^{2(D-3)} f(r)^2 + E^2} + E \right] dr - E\left(t_R + r_*(\infty) - r_*(r_{min})\right). \tag{2.145}$$

Choosing the symmetric case $-t_L = t_R \equiv \tau/2$, it is straightforward to show using (2.109) that

$$\frac{1}{\Omega_{D-2}} \frac{d\mathcal{V}}{d\tau} = -E = r^{D-2}\sqrt{-\mathcal{G}(r_{min})} \equiv W(r_{min}) \tag{2.146}$$

where $\mathcal{G}(r) \equiv g(r)^{-2}$. The complexity rate of change is then

$$\frac{d\mathcal{C}_\mathcal{V}}{d\tau} = \frac{\Omega_{D-2}}{G_N R} W(r_{min}). \tag{2.147}$$

To find its total dependence on time, one first notes that equation (2.144) can be written as

$$\frac{\tau}{2} + r_*(\infty) - r_*(r_{min}) = \int_{r_{min}}^{r_{max}} \frac{g(r)}{f(r)} \left[\frac{W(r_{min})}{\sqrt{-W(r)^2 + W(r_{min})^2}} + 1 \right] dr \tag{2.148}$$

from which one can solve for $r_{min}(\tau)$. However, if we focus on the late-time limit $\lim_{\tau\to\infty} r_{min}(\tau) = \tilde{r}_{min}$, it can be shown that

$$0 = W'(\tilde{r}_{min}) = (D-2)\tilde{r}_{min}^{D-3}\sqrt{-\mathcal{G}(\tilde{r}_{min})} - \frac{\tilde{r}_{min}^{D-2}\mathcal{G}'(\tilde{r}_{min})}{2\sqrt{-\mathcal{G}(\tilde{r}_{min})}}. \tag{2.149}$$

This is because, from (2.109), r_{min} is also the largest root of

$$-W(r_{min})^2 + E^2 = 0 \tag{2.150}$$

and as $\tau \to \infty$, $|E|$ increases until the two roots meet at the extremum of $W(r_{min})$. Therefore,

$$\left.\frac{d\mathcal{C}_{\mathcal{V}}}{d\tau}\right|_{\tau\to\infty} = \frac{\Omega_{D-2}}{G_N R} W(\tilde{r}_{min})\,. \tag{2.151}$$

Numerical studies have shown that

$$\lim_{r_+/\ell\to\infty} \left.\frac{d\mathcal{C}_{\mathcal{V}}}{d\tau}\right|_{\tau\to\infty} = \frac{8\pi}{D-1}\left[(M-\Omega_+ J)-(M-\Omega_- J)\right]\,. \tag{2.152}$$

This reduces to the result [69] found for Schwarzschild-AdS black holes, which was $8\pi M_{sch}/(D-2)$[11], since it is straightforward to show that

$$\lim_{r_-\to 0}\left(\Omega_- - \Omega_+\right) J = \frac{D-1}{D-2} M_{sch}. \tag{2.153}$$

For illustration, we will prove (2.152) in spacetime dimensions $D = 3$ and $D = 5$ below, where generalization to other spacetime dimensions follows the same methods.

Late-time complexity growth in $D = 3$

In this case, we can explicitly solve (2.149) and find that

$$\tilde{r}_{min} = \frac{\sqrt{2m\ell^2 - 2ma^2 - \ell^2}}{\sqrt{2}} \tag{2.154}$$

and

$$r_+ = \sqrt{\tilde{r}_{min}^2 + \sqrt{\tilde{r}_{min}^4 - 2ma^2\ell^2}}, \quad r_- = \sqrt{\tilde{r}_{min}^2 - \sqrt{\tilde{r}_{min}^4 - 2ma^2\ell^2}}. \tag{2.155}$$

[11] M_{sch} is the thermodynamic mass of Schwarzschild-AdS black hole, given by taking the $a \to 0$ limit of M in (2.21). Note that for the BTZ black hole with $D = 3$, we have $M_{sch} = \frac{r_+^2}{8G_N\ell^2}$ which is different from the one naively obtained from the $D \to 3$ limit of the blackening factor of Schwarzschild-AdS black hole, giving $M_{sch} = \frac{r_+^2+\ell^2}{8G_N\ell^2}$. This is because for Schwarzschild-AdS black holes with $D > 3$ we implicitly assume that the $r_+ \to 0$ limit corresponds to the Neveu-Schwarz vacuum of AdS_D with blackening factor $f(r) = 1 + \frac{r^2}{\ell^2}$ of the metric in Schwarzschild coordinates, whereas the $r_+ \to 0$ limit of the BTZ black hole corresponds to the Ramond vacuum of AdS_3 with blackening factor $f(r) = \frac{r^2}{\ell^2}$ of the metric in Schwarzschild coordinates. For more details on this, see [142].

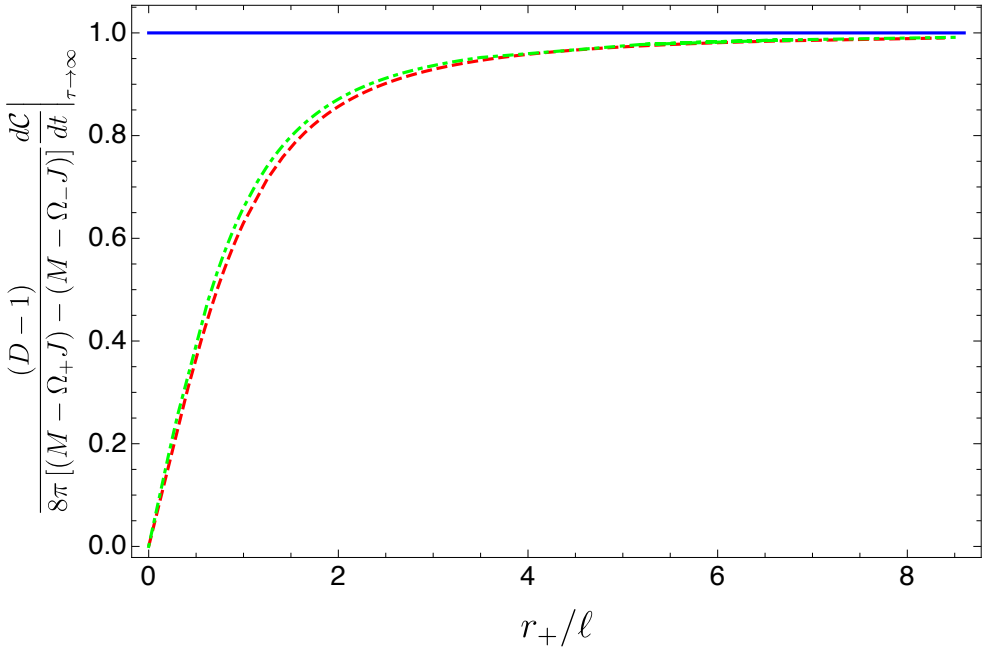

Figure 2.14: The late-time rate of complexity growth $d\mathcal{C}_{\mathcal{V}}/d\tau$ is shown as a function of r_+/ℓ for spacetime dimensions $D = 3, 5, 7$ (solid blue, dashed red, and dot-dashed green, respectively). It is shown that the limit (2.152) is always approached from below. The fact that the late-time $d\mathcal{C}_{\mathcal{V}}/d\tau$ can be expressed in this way in terms of the thermodynamic quantities of the black hole only in the large r_+/ℓ limit shows one of its shortcomings compared to $d\mathcal{C}_A/d\tau$, which can expressed at late-times in terms of thermodynamic quantities of the black hole for all r_+/ℓ.

Using this, it is straightforward to show that

$$W(\tilde{r}_{min}) = \frac{\sqrt{\tilde{r}_{min}^4 - 2ma^2\ell^2}}{\ell}, \quad (\Omega_- - \Omega_+)\, J = \frac{W(\tilde{r}_{min})}{2G_N\ell} \tag{2.156}$$

from which we get (2.152) by setting $R = \ell$. In fact, as shown in figure 2.14, the late-time rate of complexity growth $d\mathcal{C}_{\mathcal{V}}/d\tau$ is independent of r_+/ℓ.

Late-time complexity growth in $D = 5$

In this case, the expression for $\tilde{r}_{min}$ is considerably more complicated. However, we can use it to expand the two sides of (2.152) as a series in large r_+, from which we get

$$\begin{aligned}(\Omega_- - \Omega_+)\, J &= \frac{\pi}{2G_N\ell^2} r_+^4 + \frac{\pi}{2G_N} r_+^2 - \frac{\pi r_-^2 (r_-^2 + \ell^2)}{2G_N\ell^2} + \mathcal{O}\left(\frac{1}{r_+^2}\right), \\ \frac{\Omega_3}{G_N\ell} W(\tilde{r}_{min}) &= \frac{\pi^2}{G_N\ell^2} r_+^4 + \frac{\pi^2\left[(\sqrt{2}-1)\ell^2 - (2-\sqrt{2})r_-^2\right]}{\sqrt{2}G_N\ell^2} r_+^2 \\ &\quad + \frac{\pi^2\left(\ell^2 + 2r_-^2\right)\left((4\sqrt{2}-5)\ell^2 + 2(2\sqrt{2}-1)r_-^2\right)}{16G_N\ell^2} + \mathcal{O}\left(\frac{1}{r_+^2}\right). \end{aligned} \tag{2.157}$$

Expanding the ratio of these two expressions in the large r_+ limit gives

$$\frac{1}{(\Omega_- - \Omega_+)\, J} \times \frac{\Omega_3}{G_N\ell} W(\tilde{r}_{min}) = 2\pi - \left[\pi\sqrt{2}\ell^2 + (2-\sqrt{2})r_-^2\right] \frac{1}{r_+^2} + \mathcal{O}\left(\frac{1}{r_+^4}\right) \tag{2.158}$$

which yields (2.152) as $r_+/\ell \to \infty$. Interestingly, it also shows that the limit is always approached from below, which agrees with the behaviour of $d\mathcal{C}_\mathcal{V}/d\tau$ found for Schwarzschild-AdS black holes [69].

2.6 Discussion

We have considered several aspects of the CA and CV proposals for holographic complexity in the context of rotating black holes. While the behaviour of these proposals for numerous static and/or spherically symmetric spacetimes has been thoroughly studied, their extension to rotating black holes is a somewhat nontrivial task. In large part, the difficultly arises due to the comparative lack of symmetry in rotating solutions and therefore more complicated causal structure. Here we have partly side-stepped this issue by considering equal-spinning odd-dimensional rotating black holes, which enjoy enough additional symmetry to make the computations tractable, while still revealing a number of non-trivial features. Here our focus has been devoted to understanding the complexity of formation and also the time-dependent growth rate of complexity.

First, we introduced the Myers-Perry-AdS spacetimes with equal angular momenta in odd dimensions and discussed the enhancement of symmetry and the associated causal structure and thermodynamic properties. In studying holographic complexity, especially

within the action proposal, it is necessary to have a thorough understanding of the causal structure of the spacetime of interest. We have done this here by analysing the structure of light cones in this geometry. The enhanced symmetry of the equal-spinning case allows for us to choose $SU(N+1) \times U(1)$ invariant hypersurfaces, effectively making the causal structure two-dimensional as is the case for static, spherically symmetric black holes. This represents a significant technical simplification over the most general case.[12] Despite this simplification, the solutions maintain the classical features associated with rotating black holes (such as ergoregions, for example), which allow us to rigorously study holographic complexity for rotating black holes for the first time.

Second, we studied the complexity of formation for rotating black holes in both the CA and CV conjectures. As shown in detail in appendix A.3, there is an order of limits problem when taking the static limit of $\Delta\mathcal{C}_{\mathcal{A}}$. We note that there have been previous investigations where such order of limits problems have been observed for the growth rate in the CA conjecture [136, 137, 97, 77, 138], however we believe this is the first observation of this for the complexity of formation. This issue can be resolved by an alternative regularization scheme where the future and past tips of the WDW patch are ignored near the singularity and at the static limit (see appendix A.4). It would be interesting to explore more deeply the implications of this alternative regularization, in particular the mechanism and/or interpretation of the regulator itself.

Our most intriguing result concerns the role that the thermodynamic volume plays in both the CA and CV conjectures. We have shown for the first time that the complexity of formation of large black holes does not scale with thermodynamic entropy but rather obeys the same scaling as the thermodynamic volume to leading order in ℓ/r_+

$$\Delta\mathcal{C} = \Sigma_{\rm g} C_T \left(\frac{V}{V_{\rm AdS}}\right)^{\frac{D-2}{D-1}} + \dots \tag{2.159}$$

where $V_{\rm AdS} = \ell^{D-1}$, $\Sigma_{\rm g}$ is a factor that depends on the specific metric, dimension, etc. (but not on the size of the black hole), and C_T is the central charge of the CFT as computed from Newton's constant G_N. The thermodynamic volume has been conjectured [107] to obey a 'reverse' isoperimetric inequality:

$$\mathcal{R} \equiv \left(\frac{(D-1)V}{\Omega_{D-2}}\right)^{1/(D-1)} \left(\frac{\Omega_{D-2}}{4G_N S}\right)^{1/(D-2)} \geq 1\,. \tag{2.160}$$

[12] For the most general rotating black holes the light cones can be defined using PDEs as discussed in [125, 3, 4] (see also appendix A.6), though they must be solved numerically.

The inequality is saturated by (charged) Schwarzschild-AdS spacetimes. Assuming the relationship (2.159) is general, the reverse isoperimetric inequality becomes the statement

$$\Delta\mathcal{C} \geq \beta_D S \tag{2.161}$$

where β_D is a positive constant that can be easily worked out from the above. This means that the complexity of formation for large black holes is *bounded from below* by the entropy (equivalently, the number of degrees of freedom).

Finally, we examined the time-dependent rate of complexity growth using both the CA and CV conjectures. Previous studies have shown that the late time limit of complexity growth in black holes with two horizons is bounded by the difference in internal energy between the outer and inner horizons[13]

$$\pi \frac{d\mathcal{C}}{d\tau}\bigg|_{\tau\to\infty} \leq (F_+ + T_+S_+) - (F_- + T_-S_-) = U_+ - U_-. \tag{2.162}$$

This surprising result seems to be of near universal scope and it suggests a deep connection between complexity and black hole thermodynamics [144, 87, 88]. In the CV conjecture, we have shown that the complexity is a positive function of time whose late time rate of growth saturates the bound (2.162) in the $r_+/\ell \to \infty$ limit, up to a constant that depends on the spacetime dimension. We have also explicitly shown that the bound is always approached from below as r_+/ℓ is varied. In the CA conjecture, the bound (2.162) is always saturated, and we have shown that it is always approached from above as time is varied. Both of these results agree with the behaviour found for the charged black hole [69]. Furthermore, we found that the arbitrary length scale ℓ_{ct} does not affect the late-time rate of complexity growth but does affect its early behaviour, as shown in figure 2.13.

Going forward, there are a number of directions worth exploring. Perhaps the most interesting one concerns the result (2.159). While we have not offered a definitive proof of this relationship, it reduces to known results for static black holes, holds also for large gravitational solitons [81], and we have provided robust evidence that it is obeyed in general for large rotating black holes. It would be interesting to test the full range of validity of this relationship, which could be done most effectively by studying other black hole solutions for which the entropy and thermodynamic volume are independent and scale differently. Such explorations could provide useful insight from which a general proof of the relationship could be deduced, or a counter-example from which its limitations could be assessed. It would also be interesting to explore this feature in light of the recently proposed first law of complexity [87]. While the CFT interpretation of thermodynamic volume is yet

[13] Though see [143] for a recent example where the situation is more subtle.

to be fully understood (though see [113, 114, 115, 116, 117, 118, 119, 120] for progress in this direction), our results provide impetus to investigate in greater detail the holographic interpretation of thermodynamic volume and its relationship to complexity.

It would be worthwhile to extend the analysis here to the most general class of rotating black holes, though this may be a formidable task. Exploring the implications of the known instabilities (e.g. superradiance) of rotating black holes for complexity would also be of interest. Although our complexity calculations were done in the case of odd-dimensional equal angular momenta in each independent plane of rotation, we expect that the general family of Myers-Perry-AdS black holes should possess similar qualitative behaviour.

Chapter 3

Traversability of Multi-Boundary Wormholes

3.1 Introduction

Wormholes have long been of interest since the time of Einstein and Rosen [145]. Although Einstein-Rosen bridges connect different asymptotic regions of spacetime, topological censorship [146, 147] forbids their traversability when only classical matter fields are present. The same is of course true of their multi-boundary wormhole generalizations. However in some cases, quantum matter fields can cause violations of the averaged null energy condition (ANEC). In such cases the arguments of [146, 147] cannot be applied, so that such ANEC violations might make the wormholes traversable. Recall that the ANEC is satisfied when the integral of stress tensor along any complete null geodesic is non-negative,

$$\int_\gamma T_{ab} k^a k^b \geq 0. \tag{3.1}$$

In recent years, there have been many approaches to constructing traversable wormholes from ANEC violations, see [55, 148, 149, 150, 151, 152, 153, 154]. In particular, in the seminal paper by Gao, Jafferis and Wall [55], the authors construct a traversable wormhole using a two-sided BTZ black hole as the background, where the dual CFT state is the thermofield double (TFD) state. With an appropriate sign of coupling, a double-trace deformation that directly couples the two boundary CFTs can cause the violation of the ANEC. Adding the coupling shifts the horizons so as to allow certain causal geodesics

to travel from one asymptotic boundary to the other. In [148], this construction was generalized to rotating BTZ black holes. It is also interesting to recall that the transmission of such signals was interpreted in [152] from the dual field theory perspective as being due to enacting a quantum teleportation protocol between entangled quantum systems. This connection with quantum information has been of great interest (see e.g. [155, 156, 157, 158, 159, 160]) as a concrete realization of the ER=EPR idea [49].

In this chapter, we generalize this construction to any pair of asymptotic regions in certain (non-rotating or rotating) multi-boundary black holes[14] in AdS_3. For a general multi-boundary black hole, a finite-sized causal shadow separates the horizons of different asymptotic regions, making the wormhole hard to traverse. In our construction, we focus on the hot limit considered in [161], where the temperatures related to all horizons are large. In that limit, for any two horizons, there exists a region where the causal shadow between them is exponentially small. A double-trace deformation can then easily render the wormhole traversable. As we will see, the hot limit will also give us convenience in doing the calculations, which otherwise would be difficult to perform.

Our construction has several interesting features that differ from those of [55] and [148]. The first is that the pair of boundaries in our traversable wormhole construction is quite general, and the associated horizons can have different temperatures and angular momenta. Furthermore, our spacetimes have non-trivial angular dependence, and this can be seen in features related to traversability. In particular, signals from a given asymptotic region will be able to reach a second asymptotic region only when fired from appropriate regions of the first boundary. Signals launched from other parts of the first boundary may instead traverse to a third asymptotic region, or they may become stuck behind an event horizon. It is a general feature of our construction that some such event horizon will remain even though our wormholes are traversable. Again, this is associated with the lack of rotational symmetry in our spacetimes.

The chapter is organized as follows: In section 3.2, we review the construction of multi-boundary wormholes in AdS_3 and their important properties that will be useful in later sections. The geometry of these wormholes in the hot limit is also discussed, as well as the entanglement structure of the dual CFT state. A general review of the Gao-Jafferis-Wall construction is then given in section 3.3, where we emphasize a rather general form of the coupling between boundaries that can induce traversability. Using these two ingredients, we proceed to construct the multi-boundary traversable wormhole in section 3.4. We

[14] Note that, while there is some freedom in the use of such terms, our choice is to use "multi-boundary black holes" when the context refers to the background spacetime, and use "multi-boundary wormholes" when the context refers to traversable wormholes in particular.

summarize our findings and discuss their implications and connections with recent work in the literature in section 3.5. A number of technical details and supporting calculations are left to appendix B.

Throughout this chapter, we use the AdS length as our unit of distance.

3.2 Multi-boundary black holes in AdS_3

In this section, we will first review how to construct multi-boundary black holes by quotienting empty AdS_3 with isometries, following an algebraic approach [162, 163, 164, 165, 166, 167][15]. Then we discuss fixed points of those isometries, (renormalized) geodesic distances in different conformal frames, and how they behave in the hot limit. Those results will be useful in our construction of multi-boundary traversable wormholes. Finally, we briefly describe the CFT states that are dual to these geometries.

3.2.1 Quotients of AdS_3 space

In three-dimensional Einstein gravity, the Ricci tensor completely specifies the Riemann tensor. The consequence of this is that all solutions of Einstein equations are locally isometric to AdS_3, which is the Lorentzian, maximally-symmetric spacetime with constant negative curvature and isometry group $SO(2,2) \simeq SL(2,\mathbb{R}) \times SL(2,\mathbb{R})$. Besides pure AdS_3, other solutions to the equations of motion are locally AdS_3 but differ globally from it and can be obtained by quotienting AdS_3 by a discrete subgroup Γ of $SO(2,2)$. The spacetime AdS_3 can be defined as the submanifold of

$$\mathbb{R}^{2,2} = \left\{ p = \begin{pmatrix} U+X & -V+Y \\ V+Y & U-X \end{pmatrix} \right\}, \quad ds^2 = -\det(dp) \equiv \bar{\eta}_{ab} d\bar{x}^a d\bar{x}^b, \tag{3.2}$$

given by the hyperboloid $\det(p) = 1$[16], where we defined the 4-vector $\bar{x}^a = (U, V, X, Y)$ and metric $\bar{\eta}_{ab} = \mathrm{diag}\,(-1,-1,1,1)$. In global coordinates, this hyperboloid is parametrized by the intrinsic coordinates (t, r, ϕ) defined by

$$X = r\cos\phi, \quad Y = r\sin\phi, \quad U = \sqrt{1+r^2}\cos t, \quad V = \sqrt{1+r^2}\sin t \tag{3.3}$$

[15] For construction of these geometries using explicit forms of the Killing vectors, see [168].

[16] dp is the matrix defined by taking the differential of every element of the matrix p.

which gives the induced metric

$$ds^2 = -(1+r^2)dt^2 + \frac{dr^2}{1+r^2} + r^2 d\phi^2 \tag{3.4}$$

where $t \sim t + 2\pi$[17] and $\phi \sim \phi + 2\pi$. The connected part of the group $SO_c(2,2)$ is $SL(2,\mathbb{R}) \otimes SL(2,\mathbb{R})/\mathbb{Z}_2$. The group elements $(g_L, g_R) \in SO_c(2,2)$ act on a point p according to

$$p \to g_L p g_R^t. \tag{3.5}$$

From this, we see that the $\mathbb{Z}_2$ symmetry correspond to the equivalence relation $(g_L, g_R) \sim (-g_L, -g_R)$. A convenient basis of generators $\{J_1, J_2, J_3\} \times \{\tilde{J}_1, \tilde{J}_2, \tilde{J}_3\}$ of the isometry group $SL(2,\mathbb{R}) \times SL(2,\mathbb{R})$ is

$$\begin{aligned}
J_1 &\equiv -\frac{1}{2}(J_{XU} - J_{YV}), \quad & \tilde{J}_1 &\equiv -\frac{1}{2}(J_{XU} + J_{YV}) \\
J_2 &\equiv -\frac{1}{2}(J_{YU} + J_{XV}), \quad & \tilde{J}_2 &\equiv -\frac{1}{2}(J_{YU} - J_{XV}) \\
J_3 &\equiv -\frac{1}{2}(J_{UV} - J_{XY}), \quad & \tilde{J}_3 &\equiv \frac{1}{2}(J_{UV} + J_{XY})
\end{aligned} \tag{3.6}$$

where the Killing vectors $J_{ab} = \bar{x}_a \bar{\partial}_b - \bar{x}_b \bar{\partial}_a$ obey the $SO(2,2)$ algebra

$$[J_{ab}, J_{cd}] = \bar{\eta}_{ac} J_{bd} - \bar{\eta}_{ad} J_{bc} - \bar{\eta}_{bc} J_{ad} + \bar{\eta}_{bd} J_{ac} \tag{3.7}$$

In matrix representation, the generators are expressed as

$$J_1 = -\frac{1}{2}\gamma_1, \quad J_2 = -\frac{1}{2}\gamma_2, \quad J_3 = -\frac{1}{2}\gamma_3 \tag{3.8}$$

where[18]

$$\gamma_1 = \begin{pmatrix} 1 & 0 \\ 0 & -1 \end{pmatrix}, \quad \gamma_2 = \begin{pmatrix} 0 & 1 \\ 1 & 0 \end{pmatrix}, \quad \gamma_3 = \begin{pmatrix} 0 & 1 \\ -1 & 0 \end{pmatrix} \tag{3.9}$$

and similarly for $\tilde{J}_i$[19].

[17] Usually the universal cover of t is taken by unwrapping it, but as we will see, it is not necessary here since the wormhole constructions will automatically remove closed timelike curves.

[18] Our matrix representation of p is different from that defined in [166, 167], which causes the generators to be slightly different.

[19] In matrix representation, $\tilde{J}_i$ takes the same matrix form as $J_i = -\frac{1}{2}\gamma_i$ but the infinitesimal transformations on p are different from those of J_i's, since $J_i : p \to -\frac{1}{2}\gamma_i p$ while $\tilde{J}_i : p \to -\frac{1}{2} p \gamma_i^t$.

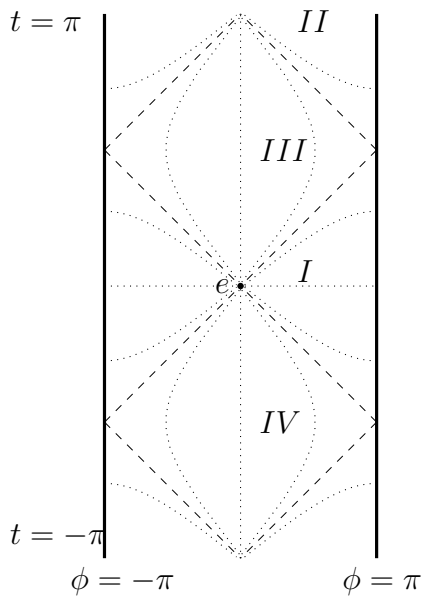

Figure 3.1: The group manifold of $SL(2,\mathbb{R})$, which is also the Penrose diagram of AdS_3. The dotted lines represent the action of the group elements of $SL(2,\mathbb{R})$ on the identity element e placed at the origin of AdS_3 in global coordinates. The isometries of $SL(2,\mathbb{R})$ are classified depending on which region the element e is mapped to. Dashed lines represent null rays.

To understand the action of the group elements (g_L, g_R), we will describe AdS_3 as the group manifold of $SL(2,\mathbb{R})$, with the Penrose diagram shown in figure 3.1. The action of group elements $g \in SL(2,\mathbb{R})$ on the identity element e is shown there, according to which they are classified into conjugacy classes depending on where the point $e \to geg^t = gg^t$ lies,

Hyperbolic	$\mathrm{Tr}\, g > 2$	$gg^t \in I$
Hyperbolic	$\mathrm{Tr}\, g < -2$	$gg^t \in II$
Elliptic	$\lvert \mathrm{Tr}\, g \rvert < 2$	$gg^t \in III, IV$
Parabolic	$\lvert \mathrm{Tr}\, g \rvert = 2$	$gg^t \in$ light cones

We will focus on the action of subgroups $\Gamma \subseteq SO_c(2,2)$ with $\mathrm{Tr}\, g > 2$ hyperbolic elements, whose fixed points are on the boundary of AdS_3. This is because it ensures that AdS_3/Γ is free of conical singularities and closed timelike curves [162, 164]. Removing from the spacetime the past and future of those fixed points yields the restricted spacetime $\widehat{AdS_3}$ where the action of the quotient on the spacetime is free of pathologies and leads to a spacetime $\widehat{AdS_3}/\Gamma$. We will illustrate this process by reviewing the construction of $\widehat{AdS_3}/\Gamma$ in the case of BTZ black holes [169, 126] and three-boundary black holes [163, 162, 164]. We also discuss generalizations to n-boundary black holes with and without non-trivial topologies [162, 164, 166]. A Cauchy slice of these geometries is a Riemannian manifold of genus g and boundary number n. So, we can classify the black hole geometries by a 2-tuple (n, g). In the non-rotating case, the number of parameters (or in other words, dimension of the moduli space) needed to specify the (n, g) geometry is equal to 1 for $(2, 0)$ and is $6g - 6 + 3n$ otherwise. In the rotating case, this number is doubled.

Before reviewing the construction of these geometries, we will give general formulas for calculating the geodesic distance. The group manifold representation allow us to easily calculate the geodesic distances $d(p, q)$ between two arbitrary points, p and q [165]. In particular, if p and q are connected by a spacelike geodesic, then

$$d(p,q) = \cosh^{-1}\left(\frac{\mathrm{Tr}\,(p^{-1}q)}{2}\right). \tag{3.10}$$

With a timelike geodesic connecting p and q, the geodesic distance is

$$d(p,q) = \cos^{-1}\left(\frac{\mathrm{Tr}\,(p^{-1}q)}{2}\right). \tag{3.11}$$

When $\mathrm{Tr}\,(p^{-1}q) < -2$, there is no geodesic connecting p and q.

We now discuss various cases of (n, g) geometries in detail.

BTZ black hole

In this case, the subgroup Γ is generated by a single element

$$\gamma_{BTZ} = (g_{L,BTZ}, g_{R,BTZ}) = \left(e^{\ell \xi_{L,BTZ}}, e^{\tilde{\ell} \xi_{R,BTZ}}\right) \tag{3.12}$$

and a convenient choice for $\xi_{L,BTZ}$ and $\xi_{R,BTZ}$ is

$$\xi_{L,BTZ} = -J_2, \quad \xi_{R,BTZ} = -\tilde{J}_2 \tag{3.13}$$

with $\ell = 2\pi(r_+ + r_-)$ and $\tilde{\ell} = 2\pi(r_+ - r_-)$ being two positive real parameters. In matrix representation, this gives

$$g_{L,BTZ} = \begin{pmatrix} \cosh\left(\frac{\ell}{2}\right) & \sinh\left(\frac{\ell}{2}\right) \\ \sinh\left(\frac{\ell}{2}\right) & \cosh\left(\frac{\ell}{2}\right) \end{pmatrix}, \quad g_{R,BTZ} = \begin{pmatrix} \cosh\left(\frac{\tilde{\ell}}{2}\right) & \sinh\left(\frac{\tilde{\ell}}{2}\right) \\ \sinh\left(\frac{\tilde{\ell}}{2}\right) & \cosh\left(\frac{\tilde{\ell}}{2}\right) \end{pmatrix}. \tag{3.14}$$

The isometry γ has two fixed points at the boundary given by $t = 0, \phi = \pi/2$ and $t = 0, \phi = 3\pi/2$. Removing the past and future regions of these fixed points gives the restricted space $\widehat{\mathrm{AdS}_3}$. Any two geodesics that are related by the isometry γ_{BTZ} are identified, and we can choose a region that is bounded by such a pair of geodesics as the fundamental domain of $\widehat{\mathrm{AdS}_3}/\Gamma$, see figure 3.2. The minimal length between these two geodesics is uniquely determined by r_+ and r_-, and is the intersection of the geodesic connecting the fixed points with the fundamental domain. This defines the two-sided BTZ black hole, where each side is covered by the usual BTZ coordinates

$$ds^2 = -\frac{\left(r_B^2 - r_+^2\right)\left(r_B^2 - r_-^2\right)}{r_B^2} dt_B^2 + \frac{r_B^2}{\left(r_B^2 - r_+^2\right)\left(r_B^2 - r_-^2\right)} dr_B^2 + r_B^2 \left(d\phi_B - \frac{r_+ r_-}{r_B^2} dt_B\right)^2 \tag{3.15}$$

where the subscript B means that we are using BTZ coordinates. The thermodynamic quantities related to the black hole are [169]

$$\begin{aligned} M &= \frac{r_+^2 + r_-^2}{8G_N} = \frac{\ell^2 + \tilde{\ell}^2}{64\pi^2 G_N}, \quad J = \frac{r_+ r_-}{4G_N} = \frac{\ell^2 - \tilde{\ell}^2}{64\pi^2 G_N} \\ T_H &= \frac{1}{\beta} = \frac{r_+^2 - r_-^2}{2\pi r_+} = \frac{\ell\tilde{\ell}}{2\pi^2(\ell + \tilde{\ell})}, \quad \Omega_H = \frac{r_-}{r_+} = \frac{\ell - \tilde{\ell}}{\ell + \tilde{\ell}}. \end{aligned} \tag{3.16}$$

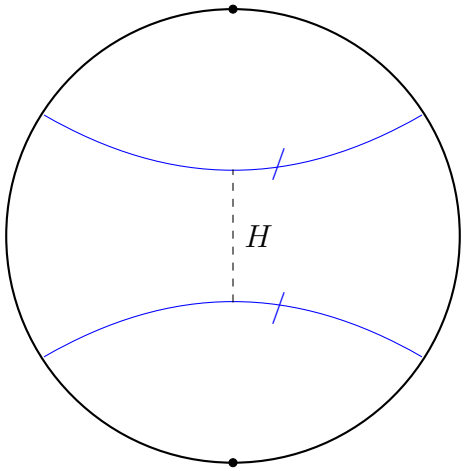

Figure 3.2: A Cauchy slice of a BTZ black hole shown as a quotient of AdS_3. The action of γ identifies the two blue geodesics, and the region between them is the fundamental domain of the quotient. The minimal geodesic H separating the two coincides with the event horizon of the black hole. In the non-rotating case, this slice is at $t = 0$. But in the case of rotation, there is a relative boost between the two identified geodesics.

By writing the point p in (3.2) in terms of the BTZ coordinates using the transformation

$$\begin{aligned} U &= \sqrt{\frac{r_B^2 - r_-^2}{r_+^2 - r_-^2}} \cosh\left(r_+\phi_B + r_- t_B\right), \quad X = \sqrt{\frac{r_B^2 - r_+^2}{r_+^2 - r_-^2}} \cosh\left(r_+ t_B + r_-\phi_B\right), \\ V &= \sqrt{\frac{r_B^2 - r_+^2}{r_+^2 - r_-^2}} \sinh\left(r_+ t_B + r_-\phi_B\right), \quad Y = \sqrt{\frac{r_B^2 - r_-^2}{r_+^2 - r_-^2}} \sinh\left(r_+\phi_B + r_- t_B\right) \end{aligned} \tag{3.17}$$

one can show that the action of γ_{BTZ} on p is simply to map $\phi_B \to \phi_B + 2\pi$. The length of the bifurcation surface (horizon length) generated by γ can be found from (3.10) to be [165]

$$h = \cosh^{-1}\left(\frac{\mathrm{Tr}\, g_{L,BTZ}}{2}\right) + \cosh^{-1}\left(\frac{\mathrm{Tr}\, g_{R,BTZ}}{2}\right) \tag{3.18}$$

From (3.12), we see that this gives the expected horizon length of $\frac{\ell+\tilde{\ell}}{2} = 2\pi r_+$.

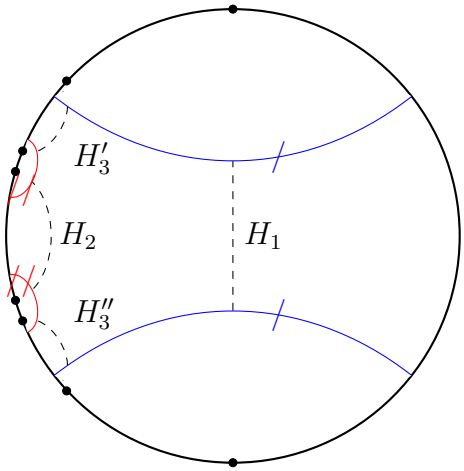

Figure 3.3: A Cauchy slice of the three-boundary black hole shown as a quotient of AdS_3. The action of γ_1 identifies the two blue geodesics while γ_2 identifies the two red geodesics. The event horizons of the three boundaries H_1, H_2, and $H_3 = H_3' \cup H_3''$ are also shown, where each of them coincide with the geodesic connecting the fixed points of the isometries γ_1, γ_2, and γ_3, respectively. Note that γ_3 has four fixed points instead of two, because it defines the third asymptotic region as the union of two separate regions in the Cauchy slice. In the case of no rotation, this slice is that of $t = 0$.

Three-boundary black hole

The subgroup Γ in this case is generated by two elements $\gamma_i = (g_{iL}, g_{iR}), i = 1, 2$. We choose the first one to be the same as the isometry used to construct the BTZ black hole[20]

$$\gamma_1 = (g_{1L}, g_{1R}) = (e^{\ell_1 \xi_{1L}}, e^{\tilde{\ell}_1 \xi_{1R}}) \tag{3.19}$$

where $\xi_{1L} = -J_2$ and $\xi_{1R} = -\tilde{J}_2$. The second element is given by

$$\gamma_2 = (g_{2L}, g_{2R}) = (e^{\ell_2 \xi_{2L}}, e^{\tilde{\ell}_2 \xi_{2R}}) \tag{3.20}$$

[20]Note that, here, the choice of generators γ_i is not unique. Other choices could be used, as long as they fall in certain conjugacy classes. Our choice here is convenient for calculation, but as we will see, it defines a conformal frame in which the third boundary region becomes vanishingly small in the hot limit. In appendix B.1, we give an example of another construction of the same geometry and discuss how it differs from the one used here.

where $\xi_{2L} = -(J_2 \cosh\alpha + J_3 \sinh\alpha)$ and $\xi_{2R} = -(\tilde{J}_2 \cosh\tilde{\alpha} + \tilde{J}_3 \sinh\tilde{\alpha})$. In matrix representation, this is

$$g_{2L} = \begin{pmatrix} \cosh\left(\frac{\ell_2}{2}\right) & e^{\alpha}\sinh\left(\frac{\ell_2}{2}\right) \\ e^{-\alpha}\sinh\left(\frac{\ell_2}{2}\right) & \cosh\left(\frac{\ell_2}{2}\right) \end{pmatrix}, \quad g_{2R} = \begin{pmatrix} \cosh\left(\frac{\tilde{\ell}_2}{2}\right) & e^{\tilde{\alpha}}\sinh\left(\frac{\tilde{\ell}_2}{2}\right) \\ e^{-\tilde{\alpha}}\sinh\left(\frac{\tilde{\ell}_2}{2}\right) & \cosh\left(\frac{\tilde{\ell}_2}{2}\right) \end{pmatrix}. \tag{3.21}$$

These two isometries define the first and second asymptotic regions, with the event horizons of these regions lying along the geodesics connecting the fixed points of γ_1 and γ_2, respectively.

The isometries that define the third asymptotic region are not independent of the above two. They are $\gamma_3' = -\gamma_1\gamma_2^{-1} \Rightarrow (g_{3L}', g_{3R}') = (-g_{1L}g_{2L}^{-1}, -g_{1R}g_{2R}^{-1})$ and $\gamma_3'' = -\gamma_1^{-1}\gamma_2 \Rightarrow (g_{3L}'', g_{3R}'') = (-g_{1L}^{-1}g_{2L}, -g_{1R}^{-1}g_{2R})$[21], corresponding to the two parts of the third boundary region as seen from the covering space. The resulting spacetime is a black hole with three asymptotic boundaries, as shown in figure 3.3. The spacetime in each asymptotic region is isometric to the exterior region of a BTZ black hole. Hence, each asymptotic region can be covered by the same metric (3.15) for $r_B > r_+$. The lengths of the horizons generated by these isometries can be found from (3.18) to be

$$h_1 = \frac{\ell_1 + \tilde{\ell}_1}{2}, \quad h_2 = \frac{\ell_2 + \tilde{\ell}_2}{2}, \quad \text{and} \quad h_3 = \frac{\ell_3 + \tilde{\ell}_3}{2}, \tag{3.22}$$

where we have defined

$$\ell_3 \equiv 2\cosh^{-1}\left(\frac{\mathrm{Tr}\, g_{3L}}{2}\right), \quad \text{and} \quad \tilde{\ell}_3 \equiv 2\cosh^{-1}\left(\frac{\mathrm{Tr}\, g_{3R}}{2}\right). \tag{3.23}$$

The parameter α can in turn be expressed using $\ell_i, i = 1, 2, 3$:

$$\cosh\alpha = \frac{\cosh\frac{\ell_3}{2} + \cosh\frac{\ell_1}{2}\cosh\frac{\ell_2}{2}}{\sinh\frac{\ell_1}{2}\sinh\frac{\ell_2}{2}}, \tag{3.24}$$

and similarly for $\tilde{\alpha}$. Each asymptotic region can be associated with independent thermodynamic parameters (3.16). The angular velocity associated to a horizon generated by an isometry γ_i can be given in terms of the isometry elements as [167]

$$\Omega_i = \frac{\cosh^{-1}\left(\frac{\mathrm{Tr}\, g_{iL}}{2}\right) - \cosh^{-1}\left(\frac{\mathrm{Tr}\, g_{iR}}{2}\right)}{\cosh^{-1}\left(\frac{\mathrm{Tr}\, g_{iL}}{2}\right) + \cosh^{-1}\left(\frac{\mathrm{Tr}\, g_{iR}}{2}\right)}, \tag{3.25}$$

[21] Although γ_3' and γ_3'' are both isometries defining the third region, for simplicity of notation, later we will refer to them collectively as γ_3.

which gives

$$\Omega_1 = \frac{\ell_1 - \tilde{\ell}_1}{\ell_1 + \tilde{\ell}_1}, \quad \Omega_2 = \frac{\ell_2 - \tilde{\ell}_2}{\ell_2 + \tilde{\ell}_2}, \quad \text{and} \quad \Omega_3 = \frac{\ell_3 - \tilde{\ell}_3}{\ell_3 + \tilde{\ell}_3} \tag{3.26}$$

for the three boundaries. From this and the fact that the horizon lengths h_i are given by $2\pi r_{+,i}$, we can relate the geometric parameters ℓ_i and $\tilde{\ell}_i$ for each boundary to the inner and outer horizon lengths of the corresponding black hole. The resulting relation is

$$r_{\pm,i} = \frac{\ell_i \pm \tilde{\ell}_i}{4\pi} \tag{3.27}$$

for $i = 1, 2, 3$. We see that setting $\tilde{\ell}_i = 0$ corresponds to the extremal case[22], while setting $\ell_i = \tilde{\ell}_i$ corresponds to the non-rotating case. The unique feature of $(3, 0)$ geometry (and any geometry (n, g) other than BTZ) is the existence of a region between the horizons H_1, H_2, and H_3 that does not intersect the causal past and future of the boundary of any asymptotic region. This region is called the causal shadow of the spacetime [170], and it will be important in our discussion of traversability below. The causal shadow region is bounded by closed geodesics, which allow us to calculate its area using the Gauss-Bonnet theorem, giving $A_{\text{CS}} = 2(n - 2 + 2g)\pi$ for general (n, g) spacetimes [161]. This shows that the causal shadow region exists for all geometries except $(2, 0)$.

General (n, g) black holes

More general black hole geometries can be constructed following the same method as discussed above. For the case without rotations, general (n, g) geometries could be constructed using a cut-and-paste procedure [162, 164], and this could be easily generalized to cases with rotations, as we review below.

The simplest way to see this is to note that any (n, g) black hole can be constructed from $2g + n - 2$ copies of the $(3, 0)$ geometry (so-called "pair-of-pants" geometry) through a process of cutting, twisting, and gluing. Since the $(3, 0)$ geometry is everywhere locally AdS_3, the geometry that results from a process of cutting, twisting, and gluing different copies of it is also locally AdS_3 and, therefore, is a solution of Einstein gravity. We will illustrate this process in the case of n asymptotic regions and in case of genus g.

For instance, to construct the rotating $(4, 0)$ geometry, we need two pairs of pants, each having 6 parameters (i.e. the mass and angular momentum of each asymptotic region). We

[22]Here we have implicitly chosen a direction of spinning. For the other choice, $\ell_i = 0$ would correspond to an extremal black hole.

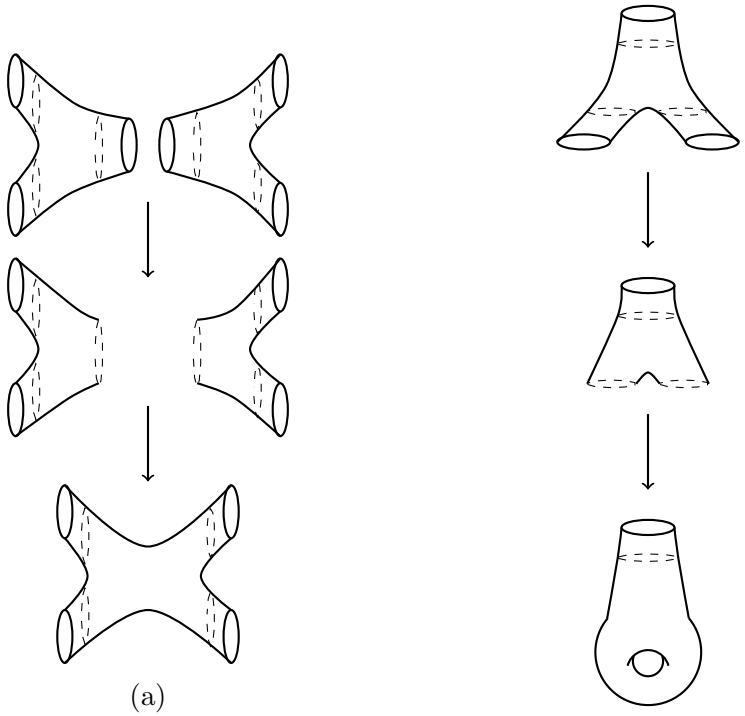

(a) (b)

Figure 3.4: Construction of the $(4,0)$ and $(1,1)$ geometries using two and one pairs of pants, respectively. The dashed lines represent horizons of asymptotic regions. Note that each pair of pants is constructed from the process shown in figure 3.3, but here the shape of the Riemann surface is shown explicitly.

consider the Cauchy slices where both pairs are of the form shown in figure 3.3. As shown in figure 3.4a, if we cut only one asymptotic region in each of the pair of pants and glue the horizons together, this forces the lengths and orientations of the glued horizons to be equal (the ℓ's and $\tilde{\ell}$'s of the two glued regions) and introduces two new twist parameters. So, the total number of parameters is 12, which is the correct dimension of the moduli space of the rotating $(4,0)$ geometry. From the resulting Cauchy slice, we can time evolve and obtain the whole required geometry. Similarly, to construct general rotating $(n,0)$ geometries, we need $n-2$ pairs of pants. By cutting $2n-6$ asymptotic regions and gluing them together, we can construct a Cauchy slice of the rotating $(n,0)$ spacetime from which the whole geometry can be obtained by time evolution. One can easily check that the number of parameters in the resulting geometry is the correct dimension of the moduli space, which is $2\,(3n-6)$.

In the case of non-zero genus, we consider the simple case of rotating $(1,1)$ spacetime, which was first constructed in [166]. Using a Cauchy slice of a single rotating $(3,0)$ geometry, we can cut two asymptotic regions and then glue their horizons together. The remaining asymptotic region is now the exterior of a rotating BTZ black hole with the topology of a torus behind the horizon, as shown in figure 3.4b. One can easily check that this process gives the correct number of dimensions of the moduli space, which is 6 in the case of rotating $(1,1)$ spacetime.

3.2.2 Fixed points and the conformal boundary

We now discuss the action of isometries $\gamma \in \Gamma$ on the conformal boundary of AdS_3, following the method discussed in [166]. Here we will be using the conformal frame

$$ds^2_{\text{global}} = -dt^2 + d\phi^2 \tag{3.28}$$

which is naturally related to the global coordinates.

Taking $r \to \infty$ for a bulk point p (3.2) gives a boundary point p_∂. Up to a diverging factor, it is

$$p_\partial \propto \begin{pmatrix} \cos\phi + \cos t & \sin\phi - \sin t \\ \sin\phi + \sin t & -\cos\phi + \cos t \end{pmatrix} = 2 \begin{pmatrix} \cos\frac{v}{2}\cos\frac{u}{2} & -\cos\frac{v}{2}\sin\frac{u}{2} \\ \sin\frac{v}{2}\cos\frac{u}{2} & -\sin\frac{v}{2}\sin\frac{u}{2} \end{pmatrix} = 2\vec{v}\vec{u}^t \tag{3.29}$$

where $\vec{v}\vec{u}^t = \vec{v} \otimes \vec{u}$ is the outer product,

$$\vec{v} = \begin{pmatrix} \cos\frac{v}{2} \\ \sin\frac{v}{2} \end{pmatrix}, \quad \vec{u} = \begin{pmatrix} \cos\frac{u}{2} \\ -\sin\frac{u}{2} \end{pmatrix} \tag{3.30}$$

and $v = t + \phi$ and $u = t - \phi$ are the null coordinates at the boundary. The isometries of interest $\gamma = (g_L, g_R) \in \Gamma$ are hyperbolic elements with their fixed points at the boundary of AdS_3. Being a fixed point amounts to

$$p_\partial = g_L p_\partial g_R^t \Rightarrow \vec{v}\vec{u}^t = g_L \vec{v}(g_R\vec{u})^t, \tag{3.31}$$

where the equality holds up to an overall factor, since we are on the conformal boundary.

This means that we could find fixed points by finding eigenvectors of g_L and g_R. In general, g_L and g_R each have two eigenvectors, and combinations of them give "corners" of the "boundary diamond" of γ where the action of γ takes place. Next, we will illustrate these notions for the BTZ black hole and the three-boundary black hole. Analysis of fixed points for general (n,g) geometries could be performed in a similar manner.

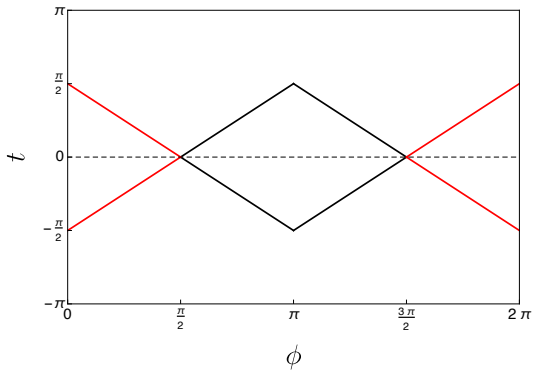

Figure 3.5: Boundary diamonds for the BTZ black hole, where $\phi \sim \phi + 2\pi$. As we can see, there are two diamonds, each containing one asymptotic boundary of the fundamental domain.

For the BTZ black hole, all elements of Γ are integer powers of γ_{BTZ}. Both $g_{L,BTZ}$ and $g_{R,BTZ}$ have two eigenvectors

$$g_{L,BTZ}\vec{v}_\pm = e^{\pm\ell/2}\vec{v}_\pm, \quad g_{R,BTZ}\vec{u}_\pm = e^{\pm\tilde{\ell}/2}\vec{u}_\pm \tag{3.32}$$

where

$$\vec{v}_\pm = \frac{1}{\sqrt{2}}\begin{pmatrix}\pm 1\\ 1\end{pmatrix}, \quad \vec{u}_\pm = \frac{1}{\sqrt{2}}\begin{pmatrix}\pm 1\\ 1\end{pmatrix}. \tag{3.33}$$

As shown in figure 3.5, there are only two boundary diamonds for the BTZ black hole, with their left and right corners at $(t = 0, \phi = \pi/2)$ and $(t = 0, \phi = 3\pi/2)$. Inside each diamond, there are infinitely many copies of the fundamental domain, or in other words, the fundamental domain and its images.

For the three-boundary black hole, we could find the fixed points and boundary diamonds in a similar manner. But in this case, we have infinitely many fixed points (and diamonds) since the group Γ not only contains elements like $\gamma_i^m, i = 1, 2$ but also more general "words" like $\gamma_1^m\gamma_2^n\gamma_1^k$... etc. For $\gamma_i, i = 1, 2$ we have

$$g_{iL}.\vec{v}_{\pm,i} = e^{\pm\ell_i/2}\vec{v}_{\pm,i}, \quad g_{iR}.\vec{u}_{\pm,i} = e^{\pm\tilde{\ell}_i/2}\vec{u}_{\pm,i} \tag{3.34}$$

with $\vec{v}_{\pm,1}$ and $\vec{u}_{\pm,1}$ the same as those of the BTZ black hole, and

$$\vec{v}_{\pm,2} = \frac{1}{\sqrt{1+e^{2\alpha}}}\begin{pmatrix}\pm e^{\alpha}\\ 1\end{pmatrix}, \quad \vec{u}_{\pm,2} = \frac{1}{\sqrt{1+e^{2\tilde{\alpha}}}}\begin{pmatrix}\pm e^{\tilde{\alpha}}\\ 1\end{pmatrix}. \tag{3.35}$$

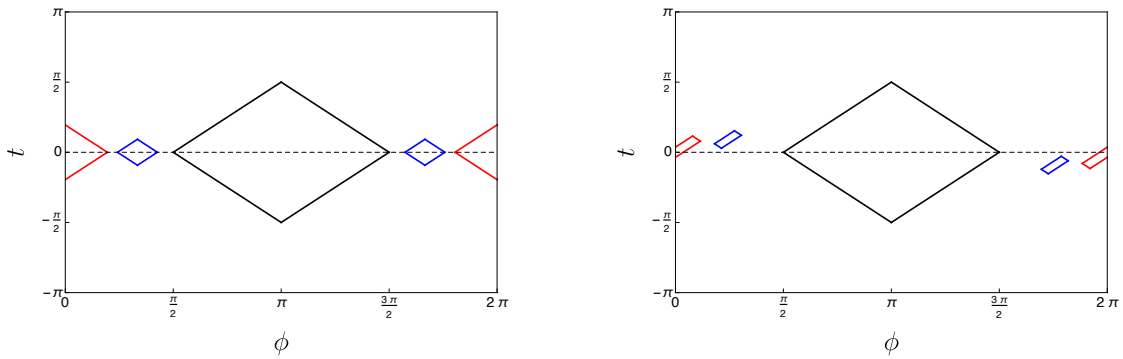

Figure 3.6: The fundamental diamonds of $(3,0)$ geometry at the boundary of AdS_3 in global coordinates. The fixed points $p_{++,i}$, $p_{--,i}$, $p_{-+,i}$, and $p_{+-,i}$ correspond to the corners of the diamonds. The diamonds of regions 1, 2, and 3 are bounded by black, red, and blue lines respectively. In (a), the parameters are $\ell_i = \tilde{\ell}_i = 3$ for the non-rotating case, and in (b) the parameters are $\ell_i = 3\tilde{\ell}_i = 3$ for the rotating case.

For the three-boundary black hole, the three asymptotic boundaries of the fundamental domain are contained in the diamonds which we call "fundamental diamonds" generated by $\gamma_i, i = 1,2,3$. Other diamonds will be dubbed "image diamonds". In figure 3.6, we show the fundamental diamonds of the three-boundary black hole. The corners of the fundamental diamonds can be found from

$$p_{++,i} = \vec{v}_{+,i}\vec{u}^t_{+,i} \quad , \quad p_{+-,i} = \vec{v}_{+,i}\vec{u}^t_{-,i} \quad , \quad p_{-+,i} = \vec{v}_{-,i}\vec{u}^t_{+,i} \quad , \quad p_{--,i} = \vec{v}_{-,i}\vec{u}^t_{-,i}. \tag{3.36}$$

where again $i = 1,2,3$.

For any point p_∂ on the i^{th} asymptotic region of the fundamental domain, there are two types of image points under the group action:

1. Points that are in the same fundamental diamond as p_∂: these points are generated by acting on p_∂ with isometries that only involve integer powers of γ_i;

2. Points that are in the image diamonds: these points are generated by acting with other kinds of isometries on p_∂.

Although it is hard to find the explicit locations of all of the image diamonds, they must all lie between diamonds 1 and 2, and topological censorship guarantees that any

pair of diamonds must be spacelike separated. The boundary distance from the left corner of diamond 1 ($p_{++,1}$) to the right corner of diamond 2 ($p_{++,2}$) is

$$\begin{aligned} d_{\text{bdy}}(p_{++,1}, p_{++,2}) &= \sqrt{|(u_{++,1} - u_{++,2})(v_{++,1} - v_{++,2})|} \\ &= \sqrt{\left(\frac{\pi}{2} - 2\tan^{-1} e^{-\alpha}\right)\left(\frac{\pi}{2} - 2\tan^{-1} e^{-\tilde{\alpha}}\right)}. \end{aligned} \tag{3.37}$$

When α and $\tilde{\alpha}$ are small (i.e. ℓ_i and $\tilde{\ell}_i$ are large), to leading order, the distance is

$$d_{\text{bdy}}(p_{++,1}, p_{++,2}) = (\alpha\tilde{\alpha})^{\frac{1}{2}} + \mathcal{O}((\alpha\tilde{\alpha})^{\frac{3}{2}}). \tag{3.38}$$

Given a choice of the boundary conformal frame, we can also define the regularized geodesic distance through the bulk between boundary points. First, note that for any 2×2 matrix p with $\det p = 1$ we have

$$p^{-1} = R_\perp p^t R_\perp^t, \quad \text{where} \quad R_\perp = \begin{pmatrix} 0 & -1 \\ 1 & 0 \end{pmatrix} \tag{3.39}$$

Also, the elements of a matrix p of any bulk point scales linearly with r. So, in the limit $r \to \infty$ we find

$$\begin{aligned} d_{\text{bulk}}(p_1, p_2) &= \cosh^{-1}\left(\frac{\text{Tr}\left(p_1^{-1} p_2\right)}{2}\right) \\ &= \cosh^{-1}\left(\frac{\text{Tr}\left(R_\perp p_1^t R_\perp^t p_2\right)}{2}\right) \\ &= \log\left(r^2\right) + \log\left(\text{Tr}\left(R_\perp p_{\partial 1}^t R_\perp^t p_{\partial 2}\right)\right) + \mathcal{O}\left(r^{-2}\right) \\ &= \log\left(r^2\right) + \log\left(4\,\text{Tr}\left(R_\perp \left(\vec{v}_1 \vec{u}_1^t\right)^t R_\perp^t \left(\vec{v}_2 \vec{u}_2^t\right)\right)\right) + \mathcal{O}\left(r^{-2}\right) \end{aligned} \tag{3.40}$$

To find the renormalized boundary geodesic distance, we subtract $\log(r^2)$ then take the $r \to \infty$ limit, giving

$$d_{\text{ren}}^{\text{global}}(p_{1\partial}, p_{2\partial}) = \log\left(4\left(\vec{u_1}^{\perp}.\vec{u_2}\right)\left(\vec{v_1}^{\perp}.\vec{v_2}\right)\right), \tag{3.41}$$

where

$$\vec{u}^{\perp} = R_\perp \vec{u} \quad \text{and} \quad \vec{v}^{\perp} = R_\perp \vec{v}. \tag{3.42}$$

Similarly, the renormalized geodesic distance between a bulk point p and a boundary point $q_\partial = 2\,\vec{v}\vec{u}^t$ is given by

$$d_{\text{ren}}^{\text{global}}(p, q_\partial) = \log\left(\text{Tr}\left(p^{-1} q_\partial\right)\right) = \log\left(2\,\text{Tr}\left(p^{-1}\vec{v}\vec{u}^t\right)\right). \tag{3.43}$$

An important question is finding the corresponding expressions to the renormalized geodesic distances (3.41)-(3.43) for the boundary of an asymptotic region that is in the BTZ conformal frame $ds^2_{BTZ} = -dt_B^2 + d\phi_B^2$. This question is resolved in subsection 3.2.3.

3.2.3 Geodesic distances in the BTZ conformal frame

In this subsection, we calculate the renormalized geodesic distance from a bulk point p to a boundary point q_∂ that is in the BTZ conformal frame. We assume that q_∂ is on the boundary of the fundamental domain, so it is in one of those fundamental diamonds defined in section 3.2.2. In that diamond, we choose the BTZ conformal frame, and the renormalized distance we calculate here is compatible with that frame. We also assume that p and q_∂ are spacelike separated so that we use (3.10) rather than (3.11) to calculate the distance.

First let us work out the conformal transformation between the AdS global conformal frame and the BTZ frame. For simplicity, we first study a boundary diamond of the BTZ black hole, as shown in figure 3.5. Then we convert our results to smaller diamonds using isometries.

Recall that global AdS_3 and the BTZ coordinates are related to the embedding coordinates via (3.3) and (3.17). On the boundary where both radial coordinates go to infinity one finds

$$Y/X = \tan\phi = \frac{\sinh\frac{-\tilde{\ell}u_B+\ell v_B}{4\pi}}{\cosh\frac{\tilde{\ell}u_B+\ell v_B}{4\pi}}, \quad V/U = \tan t = \frac{\sinh\frac{\tilde{\ell}u_B+\ell v_B}{4\pi}}{\cosh\frac{-\tilde{\ell}u_B+\ell v_B}{4\pi}}, \tag{3.44}$$

where $u_B = t_B - \phi_B$, $v_B = t_B + \phi_B$. Then, using null coordinates $u = t - \phi$ and $v = t + \phi$ on the global AdS_3 boundary, the above equations simplify to

$$u = \tan^{-1}\sinh\frac{\tilde{\ell}u_B}{2\pi}, \quad v = \tan^{-1}\sinh\frac{\ell v_B}{2\pi}. \tag{3.45}$$

These observations allow us to compute the conformal transformation between the two conformal frames,

$$ds^2_{\text{global}} = -dudv = \Omega^2(-du_B dv_B) = \Omega_u^2\Omega_v^2(-du_B dv_B) = \Omega_u^2\Omega_v^2 ds^2_{\text{BTZ}} \tag{3.46}$$

where the conformal factor Ω^2 factorizes into the "left-moving" and "right-moving" conformal factors

$$\Omega_u^2 = \frac{\tilde{\ell}}{2\pi\cosh\frac{\tilde{\ell}u_B}{2\pi}} = \frac{\tilde{\ell}}{2\pi}\cos u, \quad \Omega_v^2 = \frac{\ell}{2\pi\cosh\frac{\ell v_B}{2\pi}} = \frac{\ell}{2\pi}\cos v. \tag{3.47}$$

As we can see, when $u = \pm\frac{\pi}{2}$ or $v = \pm\frac{\pi}{2}$ either u_B or v_B will diverge and the conformal factors vanish. This marks the boundary of the "boundary diamond" being considered. Note also that the conformal factors reach their maximal value at the "center"of the diamond where $u = 0$ and $v = 0$.

For any wormhole, each asymptotic region is isometric to the exterior of some BTZ solution. So up to conformal transformations each boundary of any wormhole is identical to the boundary diamonds just described. While this always yields another diamond, the ranges Δu and Δv for general boundary diamonds can differ from π. But we can use the appropriate conformal transformations to generalize the analysis above.

Indeed, for the construction described in section 3.2, the relevant conformal transformations are those induced by isometries of AdS_3. Recall that the generators of AdS_3 isometries act on the boundary as

$$2J_1 = -\left(J_{XU} - J_{YV}\right) = \sin v \partial_v \equiv \partial_x, \quad 2\tilde{J}_1 = -\left(J_{XU} + J_{YV}\right) = \sin u \partial_u \equiv \partial_y, \tag{3.48}$$

where we have defined

$$x = \log\tan\frac{v}{2}, \quad y = \log\tan\frac{u}{2}. \tag{3.49}$$

These actions, written here as translations in x and y, change the size of the boundary diamond. We analyze this in detail for v direction below, from which corresponding expressions for the u direction follow from the symmetry $u \leftrightarrow v$.

We first note that translating x by $x_0 = \log\tan\frac{v_0}{2}$ changes the diamond boundaries from $v = \pm\frac{\pi}{2}$ to $v = \pm v_0$. Denoting the left-moving coordinate in the new diamond by v' we have

$$\tan\frac{v'}{2} = \tan\frac{v}{2}\tan\frac{v_0}{2}. \tag{3.50}$$

Here we assume $v_0 < \frac{\pi}{2}$ and $v' = \pm v_0 = \pm\frac{\Delta v}{2}$ are the boundaries of the new diamond given by the images of $v = \pm\frac{\pi}{2}$. This relation implies

$$dv' = \frac{1 - \cos v' \cos v_0}{\sin v_0} dv. \tag{3.51}$$

The left-moving conformal factor then becomes

$$\Omega_v^2 = \left(\frac{\ell}{2\pi}\cos v\right)\left(\frac{1 - \cos v' \cos v_0}{\sin v_0}\right) = \frac{\ell}{2\pi}\frac{\cos v' - \cos v_0}{\sin v_0} \tag{3.52}$$

Inside a diamond, it is bounded by

$$\Omega_v^2 \leq \frac{\ell}{2\pi}\tan\frac{v_0}{2} = \frac{\ell}{2\pi}\tan\frac{\Delta v}{4}, \tag{3.53}$$

where the equality holds at $v' = 0$. When a diamond has a small size, this bound is approximately

$$\Omega_v^2 \lesssim \frac{\ell v_0}{4\pi} = \frac{\ell \Delta v}{8\pi}. \tag{3.54}$$

Also inside a diamond, when the point is close to one edge of the diamond (i.e. when v' is close to $v_{\text{bdy}} = v_0$ or $-v_0$), Ω_v^2 has the expansion

$$\Omega_v^2 = \frac{\ell}{2\pi}(|v' - v_{\text{bdy}}|) + \mathcal{O}((v' - v_{\text{bdy}})^2). \tag{3.55}$$

Similar relations hold for the u direction. Diamonds that are not centred at $v = 0, u = 0$ can of course be translated to this standard position using the boundary isometries ∂_v and ∂_u so that corresponding bounds and expressions apply.

As discussed in section 3.2.2, if we regulate a boundary point q_∂ by moving it to a finite global AdS_3 radial coordinate r, the geodesic distance between a bulk point p and a boundary point q_∂ is

$$\begin{aligned} d_{\text{bulk}}(p, q) &= \cosh^{-1}\left(\frac{\text{Tr}\left(p^{-1}q\right)}{2}\right) \\ &= \log(r) + \log\left(\text{Tr}\left(p^{-1}q_\partial\right)\right) + \mathcal{O}\left(r^{-2}\right). \end{aligned} \tag{3.56}$$

To renormalize the distance in the BTZ conformal frame associated with a given asymptotic region of our wormhole, we should take the limit $r \to \infty$ after subtracting $\log r_B$ from the above expression for a properly chosen radial coordinate r_B associated to the boundary diamond containing q_∂.

In Fefferman-Graham coordinates, when we transform between the global and BTZ conformal frames, to leading order in z, we have $z_B = z/|\Omega|$. Also, to leading order, $z \sim 1/r$ and $z_B \sim 1/r_B$, so we have $r_B \sim r|\Omega| = r|\Omega_u\Omega_v|$. A properly defined renormalized geodesic distance is thus given by

$$d_{\text{ren}}^{\text{BTZ}}(p, q_\partial) = \log\left(\text{Tr}\left(p^{-1}q_\partial\right)\right) - \log|\Omega_u\Omega_v| = d_{\text{ren}}^{\text{global}}(p, q_\partial) - \log|\Omega_u\Omega_v|. \tag{3.57}$$

3.2.4 The hot limit of multi-boundary wormholes

In order to construct multi-boundary traversable wormholes in section 3.4, we will need to take a limit that produces the following features: 1) two horizons are separated only by an exponentially thin causal shadow over a sufficiently large region of those horizons,

and 2) we can find a point q_∂ on the boundary of the fundamental domain such that the conformal factors $\Omega^2 = \Omega_u^2\Omega_v^2$ associated with its non-trivial images under the group Γ are exponentially small. For reasons that will be clear below, we use the term "hot limit" to describe this limit for any (n, g).

For multi-boundary wormholes with trivial topologies, we choose to take a limit where all ℓ_i and $\tilde{\ell}_i$ are large, with $\ell_i/\tilde{\ell}_i$ fixed (i.e. M_i/J_i fixed)[23]. In the case without rotation, this is exactly the "hot limit" considered in [161]. In the case with rotation, this is also a limit where the temperatures in all asymptotic regions are large. It also implies that all horizon lengths are large compared to the AdS scale (although the converse is not necessarily true). We explain the two advertised features below, using the three-boundary wormhole as our main example.

First, we study the minimal distance between two neighbouring horizons. For non-rotating $(3, 0)$ geometries, this has been computed in [161] by focusing on the half-plane of the $t = 0$ slice. The minimal distance d_{ij} between horizons H_i and H_j depends on the horizon lengths, and is given by

$$\cosh d_{ij} = \frac{\cosh(h_i/2)\cosh(h_j/2) + \cosh(h_k/2)}{\sinh(h_i/2)\sinh(h_j/2)}. \tag{3.58}$$

Applying (3.58) to horizons H_1 and H_2 in our construction, we have from (3.24) that

$$d_{12} = \alpha = \tilde{\alpha}. \tag{3.59}$$

In appendix B.2, we generalize (3.58) to the case with rotations, where the minimal distance between horizons H_1 and H_2 was shown to be given simply by

$$d_{12} = \frac{\alpha + \tilde{\alpha}}{2}. \tag{3.60}$$

Other minimal horizon distances can be found from this expression by simple permutations. It can be easily shown that α and $\tilde{\alpha}$ are exponentially small in the hot limit, and that d_{ij} is as well. As a special case, when all $\ell_i = \ell$ and $\tilde{\ell}_i = \tilde{\ell}$ are large, we have $\alpha \sim 2e^{-\ell/4}, \tilde{\alpha} \sim 2e^{-\tilde{\ell}/4}$ and $d_{ij} \sim e^{-\ell/4} + e^{-\tilde{\ell}/4}$. Furthermore, in this limit, it was found [161] that the distance between the horizons is exponentially small over a large subset D_ϕ of the angular domain, for which the lateral extent along each horizon is large compared with the AdS scale. In appendix B.2, we show that this feature also applies in the rotating case. In addition, we

[23]For wormholes with internal parameters (i.e. non-trivial topologies or with $n > 3$), the proper limit will also involve taking certain internal parameters to be large, in addition to having ℓ_i and $\tilde{\ell}_i$ large, with $\ell_i/\tilde{\ell}_i$ fixed. We will discuss this briefly in section 3.5.

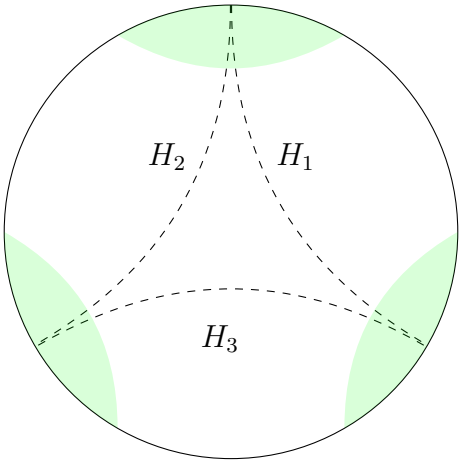

Figure 3.7: A schematic diagram of the $t = 0$ slice of a three-boundary black hole in the hot limit. For any pair of horizons (dashed lines), there is a large region which we call D_ϕ (highlighted in green) where the horizons are exponentially close to each other. The causal shadow is the region bounded by the three horizons.

show there that this is no longer the case when only one of ℓ_i or $\tilde{\ell}_i$ are taken to be large. The latter limit makes the horizons large but the horizon temperatures remain bounded[24].

Similar results also hold in the case of a general n-boundary black hole. As discussed in section 3.2.1, a general $(n, 0)$ spacetime with $n \geq 3$ can be constructed from $n-2$ copies of $(3, 0)$ geometry. Here we compute the minimal distance d_{ij} between any two horizons H_i and H_j that live in a single copy of $(3, 0)$ geometry, though we comment on the more general case below. For $n > 3$ the third horizon H_k in this copy will become part of the causal shadow of the new $(n, 0)$ geometry and its length h_k will be one of the parameters of the moduli space associated with the casual shadow region. Therefore, the same minimal distance d_{ij} between horizons H_i and H_j as in the $(3, 0)$ geometry will hold. Choosing $h_k \ll h_i + h_j$ as in the hot limit above, d_{ij} will again be exponentially small. In the more general case[25] $g \neq 0$, or for two horizons in the $(n, 0)$ geometry which are separated by an intervening extremal surface[26] and thus which lie in distinct copies of the $(3, 0)$ geometry, taking the hot limit for each copy of the $(3, 0)$ geometry allows us to write the separation

[24] This has some interesting consequences for the extremal limit that we briefly discuss in section 3.5.

[25] We have not yet discussed the case $g > 0$ in detail, but see section 3.5 for comments.

[26] In the case without time-symmetry, this means that the intervening extremal surface lies in the domain of dependence of any partial (connected) Cauchy slice Σ for which $\partial\Sigma = H_i \cup H_j$.

between H_i and H_j as the union of a fixed finite number of exponentially small separations. Thus we find the separation between H_i and H_j to be exponentially small in the hot limit for all n, g.

The other important feature of the geometry in the hot limit is that we can find points q_∂ on the boundary for which the non-trivial image points $q_\partial^{\text{image}}$ all have conformal factors that are exponentially small. This property will be established below, but its important consequence follows from equation (3.57) governing the renormalized distance between p and $q_\partial^{\text{image}}$ in BTZ frame. From this it follows that

$$d_{\text{ren}}^{\text{BTZ}}(p, q_\partial^{\text{image}}) = \log\left(\text{Tr}\left(p^{-1} q_\partial^{\text{image}}\right)\right) - \log|\Omega_u \Omega_v| = d_{\text{ren}}^{\text{global}}(p, q_\partial^{\text{image}}) - \log|\Omega_u \Omega_v|. \quad (3.61)$$

Here Ω_u and Ω_v are the conformal factors associated with $q_\partial^{\text{image}}$. So when we have a bulk point p that is in the same asymptotic region as q_∂, in the BTZ frame, the exponentially small conformal factors associated with the images require $d_{\text{ren}}^{\text{BTZ}}(p, q_\partial^{\text{image}}) > d_{\text{ren}}^{\text{BTZ}}(p, q_\partial)$ with their difference being linear in ℓ_i and $\tilde{\ell}_i$.

To show for appropriate q_∂ that the conformal factor associated with non-trivial images is exponentially small in the hot limit, recall from section 3.2.2 that the image points are classified into two types. We will take q_∂ to lie in the fundamental domain (for which the boundary diamond is not small). We first treat image points that lie in other boundary diamonds (i.e. image diamonds). Recall from section 3.2.3 that the associated conformal factors satisfy

$$\Omega_u^2 \leq \frac{\tilde{\ell} \Delta u^{\text{image}}}{8\pi} \quad \text{and} \quad \Omega_v^2 \leq \frac{\ell \Delta v^{\text{image}}}{8\pi} \quad (3.62)$$

where Δu^{image} and Δv^{image} determine the size of the diamond to which $q_\partial^{(m)}$ belongs. Note that since $d_{\text{bdy}}(p_{++}^{\text{image}}, p_{--}^{\text{image}}) = \sqrt{\Delta u^{\text{image}} \Delta v^{\text{image}}}$, equation (3.62) implies that $\Omega_u \Omega_v \leq \frac{\sqrt{\tilde{\ell}\ell}}{8\pi} d_{\text{bdy}}(p_{++}^{\text{image}}, p_{--}^{\text{image}})$.

Let us take the $(3, 0)$ geometry as our example. There all the image diamonds lie between diamonds 1 and 2 and are spacelike separated from them. Then, using (3.38), we have in the hot limit

$$d_{\text{bdy}}(p_{++}^{\text{image}}, p_{--}^{\text{image}}) < d_{\text{bdy}}(p_{++,1}, p_{++,2}) \sim \sqrt{\alpha \tilde{\alpha}}. \quad (3.63)$$

Therefore

$$\Omega^2 = \Omega_u^2 \Omega_v^2 \lesssim \frac{\tilde{\ell}\ell}{64\pi^2} \alpha \tilde{\alpha}. \quad (3.64)$$

In the hot limit, Ω^2 is exponentially small. As a special case, when $\ell_i = \ell$ and $\tilde{\ell}_i = \tilde{\ell}$ we have $\Omega^2 \lesssim e^{-(\ell+\tilde{\ell})/4}$, and since $d_{\text{ren}}^{\text{global}} = \mathcal{O}(1)$ we also have $d_{\text{ren}}^{\text{BTZ}} \gtrsim \ell + \tilde{\ell}$.

The remaining case to consider occurs when $q_\partial^{\text{image}}$ belongs to the same boundary diamond as q_∂. Let us take q_∂ to lie at some fixed boundary location independent of $\ell_i, \tilde{\ell}_i$. Then in the hot limit the analysis of section 3.2.3 requires $q_\partial^{\text{image}}$ to be exponentially close to one of the fixed points associated with the corners of the fundamental diamond. Recall from (3.55) that when this is the case the conformal factors can be approximated as

$$\Omega_u^2 \simeq \frac{\tilde{\ell}}{2\pi}\left(|u - u_{\text{bdy}}|\right) \quad \text{and/or} \quad \Omega_v^2 \simeq \frac{\ell}{2\pi}\left(|v - v_{\text{bdy}}|\right), \tag{3.65}$$

where $u_{\text{bdy}}, v_{\text{bdy}}$ are the coordinates of the relevant corner.

We will show that these conformal factors will be exponentially small and that the renormalized distance to $q_\partial^{\text{image}}$ will be large. In the $(3,0)$ geometry we may derive an explicit expression by recalling the action of the quotient construction on boundary diamonds. In particular, the quotient of any such diamond is a cylinder. We may thus discuss a 'fundamental domain' within the boundary diamond which we take to be an open set that covers the cylinder precisely once (or, at least, up to a set of measure zero associated with the boundary of the fundamental domain). We will also choose this domain to be centered at the origin $u, v = 0$ and to have a simple form.

The details of such a fundamental domain were computed in [171] for the case where the bulk is a non-rotating BTZ black hole. On the $t = 0$ slice, a corresponding fundamental domain in the bulk may be taken to lie between the codimension-1 surfaces

$$\phi = \pi \pm \sin^{-1}\left(\tanh\left(\pi r_+\right)\right). \tag{3.66}$$

As a result, the maximal boundary distance d_∂ between the boundary limit of (3.66) and the left/right corner of the diamond is

$$d_\partial = \cos^{-1}\left(\tanh\left(\pi r_+\right)\right). \tag{3.67}$$

In the case of rotation, one can show that this expression generalizes to[27]

$$d_\partial = \sqrt{\left(\cos^{-1}\tanh\frac{\ell}{2}\right)\left(\cos^{-1}\tanh\frac{\tilde{\ell}}{2}\right)} \tag{3.68}$$

[27] The idea is to realize that, since γ_{BTZ} defined in (3.12) maps the two boundaries of the fundamental domain to each other, then $\gamma_{BTZ}^{1/2}$ will map the boundary centre of the fundamental domain to one of the boundary corners of the fundamental domain. This centre point, in global coordinates, is $(t = 0, \phi = \pi)$. Acting on this point with $\gamma_{BTZ}^{1/2}$ gives the coordinates of the corner of the fundamental domain at the boundary, from which we calculate d_∂.

Note that this equation reduces to (3.67) when $\ell = \tilde{\ell}$, using (3.18). In the hot limit we find $d_\partial \sim 2e^{-(\ell+\tilde{\ell})/4}$. Since every domain of outer communication (i.e., every region outside the black hole) is isometric to the domain of outer communication for some BTZ black hole, the corresponding expressions will also hold for our multi-boundary wormholes.

Without loss of generality, we assume that $\ell_1 \leq \ell_2, \ell_3$ and $\tilde{\ell}_1 \leq \tilde{\ell}_2, \tilde{\ell}_3$. So, from (3.68), the largest d_∂ will occur for diamond 1, where it is given by (3.68) with ℓ and $\tilde{\ell}$ replaced by ℓ_1 and $\tilde{\ell}_1$, respectively. In particular, if ϵ is the distance between $q_\partial^{(m)}$ and the fixed point of the fundamental diamond, then $\epsilon < d_\partial$. Furthermore, from (3.65), we have $\Omega^2 \sim \epsilon^2$. This provides a lower bound on $d_{\text{ren}}^{\text{BTZ}}(p, q_\partial^{\text{image}})$ that in the hot limit yields

$$d_{\text{ren}}^{\text{BTZ}}(p, q_\partial^{\text{image}}) \geq -\log \Omega^2 \sim -\log \epsilon^2 \geq -\log d_\partial^2 \gtrsim \ell_1 + \tilde{\ell}_1 \tag{3.69}$$

This verifies explicitly that the conformal factors associated with $q_\partial^{\text{image}}$ are exponentially small in the hot limit, whether $q_\partial^{\text{image}}$ is in an image diamond or in the fundamental diamond. As a consequence, $d_{\text{ren}}^{\text{BTZ}}(p, q_\partial^{\text{image}}) \gtrsim \ell + \tilde{\ell}$.

3.2.5 The CFT dual of (n, g) geometries

The bulk (n, g) spacetime is dual to a CFT state $|\Sigma_{n,g}\rangle \in \mathcal{H}_1 \otimes \cdots \otimes \mathcal{H}_n$, where $\mathcal{H}_i$ is the Hilbert space of a CFT state on a circle. In the energy eigenbasis, this state can be expressed as[28]

$$|\Sigma_{n,g}\rangle = \sum_{i_1,\ldots,i_n} A_{i_1,\ldots,i_n} |i_1\rangle_1 \ldots |i_n\rangle_n \tag{3.70}$$

where the coefficient $A_{i_1,\ldots,i_n}$ is a function of the $2(6g - 6 + 3n)$ moduli of rotating (n, g) geometry. A Cauchy slice of (n, g) spacetime is a Riemann surface $\Sigma_{n,g}$ with n boundaries and genus g. Suppose that the state of the CFTs at the n boundaries is $|\phi_1 \ldots \phi_n\rangle \in \mathcal{H}_1 \otimes \cdots \otimes \mathcal{H}_n$. In the large temperature limit, the gravitational path integral over the Euclidean Riemann surface with boundary conditions fixed by $|\phi_1 \ldots \phi_n\rangle$ is dominated by the fully-connected bulk geometry, which by Wick rotation gives a Cauchy slice $\Sigma_{n,g}$ that can give the full (n, g) spacetime by Lorentzian time-evolution - see [171, 161, 172] for details. Varying the moduli changes the dominant bulk geometry in the gravitational path integral, which induces first-order phase transitions that generalize the Hawking-Page transition [173] in the $(2, 0)$ spacetime. For example, for sufficiently large temperatures,

[28] Note that, for simplicity of notation, we are ignoring rotation for a moment. However, these equations can easily be generalized to the case of rotation.

the CFT state dual to the BTZ black hole is a thermofield double state and (3.70) becomes [174]

$$|\Sigma_{2,0}\rangle = \sum_i e^{-\beta E_i/2} |i\rangle_1 |i\rangle_2 . \tag{3.71}$$

In general, determining the coefficients $A_{i_1,\ldots,i_n}$ from the path integral over an arbitrary $\Sigma_{n,g}$ is difficult. However, the CFT dual of $\Sigma_{n,0}$ in the puncture limit where $h_i \ll 1$ was investigated in [171]. It was found that in this case (3.70) becomes [171]

$$|\Sigma_{n,0}\rangle = \sum_{i_1,\ldots,i_n} C_{i_1\ldots i_n} e^{-\tilde{\beta}_1 E_{i_1}/2} \ldots e^{-\tilde{\beta}_n E_{i_n}/2} |i_1\rangle_1 \ldots |i_n\rangle_n , \tag{3.72}$$

where $C_{i_1\cdots_n}$ depend on the n-point function of the CFTs and the moduli parameters,

$$\tilde{\beta}_i = \beta_i - \log r_d - 2\log 3, \tag{3.73}$$

β_i is the inverse temperature of the BTZ geometry in the exterior of the i^{th} asymptotic region, and r_d is an undetermined constant that is independent from the moduli parameters for $(3,0)$ geometry but in general depends on the internal moduli for $n > 3$ (see [171]).

In the hot limit, the entanglement structure of $|\Sigma_{n,0}\rangle$ was investigated in [161]. In particular, it was found that the bipartite entanglement between any two CFTs at different boundaries, up to exponentially small corrections, is that of the thermofield double state over a large region of AdS scale size[29]. Thus, the CFT state dual to the local geometry in this particular region (extending between the i^{th} and j^{th} asymptotic regions through the causal shadow) is well approximated by $|\Sigma_{2,0}\rangle_{ij} = |\text{TFD}\rangle_{ij}$. This result will be important below in making hot multi-boundary wormholes traversable.

3.3 Traversability in BTZ black holes

In this section, we give a general review of the construction of traversable wormholes in BTZ black holes via double-trace deformations [55], including the case with rotation [148] and nontrivial dependence on the transverse coordinate (following [149]).

In general, the perturbative construction of traversable wormholes is associated with violations of the ANEC along generators of Killing horizon in some classical background spacetime. We review the relation between such a violation and its perturbative backreaction on the BTZ metric below. We will then review how a double-trace deformation can cause such a violation.

[29] This is the same region denoted by D_ϕ in section 3.2.4 where the distance d_{ij} between the two horizons H_i and H_j is exponentially small.

3.3.1 Metric perturbation

The metric of a rotating BTZ black hole in the co-rotating coordinates is obtained by substituting for the co-rotating transverse coordinate $x = \phi - \frac{r_-}{r_+}t$ into (3.15) to find[30]

$$ds^2 = -\frac{\left(r^2 - r_+^2\right)\left(r^2 - r_-^2\right)}{r^2}dt^2 + \frac{r^2}{\left(r^2 - r_+^2\right)\left(r^2 - r_-^2\right)}dr^2 + r^2(\mathcal{N}(r)dt + dx)^2 \tag{3.74}$$

where

$$\mathcal{N}(r) = \frac{r_-}{r_+}\frac{r^2 - r_+^2}{r^2}. \tag{3.75}$$

We can pass to Kruskal coordinates by defining the right- and left-moving null coordinates. In the right exterior region, they are defined as

$$U = e^{\kappa u}, \quad V = -e^{-\kappa v}, \tag{3.76}$$

where $\kappa = (r_+^2 - r_-^2)/r_+$ is the surface gravity, $u, v = t \pm r_*$ are the outgoing/ingoing coordinates, and the tortoise coordinate r_* is

$$r_* = \frac{1}{2\kappa}\log\frac{\sqrt{r^2 - r_-^2} - \sqrt{r_+^2 - r_-^2}}{\sqrt{r^2 - r_-^2} + \sqrt{r_+^2 - r_-^2}}. \tag{3.77}$$

This gives the metric

$$\mathrm{d}s^2 = \frac{1}{(1+UV)^2}\left\{-4\mathrm{d}U\mathrm{d}V + 4r_-(U\mathrm{d}V - V\mathrm{d}U)\mathrm{d}x + \left[r_+^2(1-UV)^2 + 4UVr_-^2\right]\mathrm{d}x^2\right\}. \tag{3.78}$$

Note that the asymptotic boundary in Kruskal coordinates is located at $UV = -1$.

To linear order, the geodesic equation implies that a null ray starting from the left boundary in the far past (where $V = 0$ and $U = -\infty$) satisfies

$$V(U) = -\left(2g_{UV}(V=0)\right)^{-1}\int_{-\infty}^{U}\mathrm{d}U h_{kk} = \frac{1}{4}\int_{-\infty}^{U}\mathrm{d}U h_{kk}, \tag{3.79}$$

where h_{kk} is the norm of $k^a = (\partial/\partial U)^a$ after first-order backreaction from the quantum stress tensor. To get h_{kk} from the stress tensor, we use the linearized Einstein equations:

$$\begin{aligned} 8\pi G_N\langle T_{kk}\rangle = -\frac{1}{2r_+^2}\Big[&\left(r_-^2 - r_+^2\right)h_{kk} + 2r_-\partial_x h_{kk} + \partial_x^2 h_{kk} \\ &+ \left(r_-^2 - r_+^2\right)\partial_U\left(U h_{kk}\right) - 2\partial_U\partial_x h_{kx} + \partial_U^2 h_{xx}\Big], \end{aligned} \tag{3.80}$$

[30] In sections 3.3 and 3.4, for simplicity of notation we use coordinates without subscripts for the BTZ coordinates. Such coordinates should not be confused with the global AdS_3 coordinates of section 3.2.

where $T_{kk} = T_{ab}k^a k^b$. To find the shift ΔV at $U = +\infty$, one merely needs to integrate this equation over all U. This yields

$$8\pi G_N \int_{-\infty}^{+\infty} \langle T_{kk} \rangle \, \mathrm{d}U = -\frac{1}{2r_+^2} \left[\left(r_-^2 - r_+^2 \right) + 2r_- \partial_x + \partial_x^2 \right] \int_{-\infty}^{+\infty} h_{kk} \mathrm{d}U, \tag{3.81}$$

where asymptotic AdS boundary conditions have been used.

In [55, 148], the authors consider boundary couplings that are independent of the transverse coordinate for simplicity. In that case, h_{kk} is independent of x, and equation (3.81) can be simplified to take the form

$$8\pi G_N \int \langle T_{kk} \rangle \, \mathrm{d}U = \frac{r_+^2 - r_-^2}{2r_+^2} \int h_{kk} \mathrm{d}U, \tag{3.82}$$

and the shift of V coordinate at $U = +\infty$ is

$$\Delta V(+\infty) = \frac{1}{4} \int_{-\infty}^{+\infty} \mathrm{d}U h_{kk} = \frac{4\pi G_N r_+^2}{r_+^2 - r_-^2} \int \langle T_{kk} \rangle \, \mathrm{d}U. \tag{3.83}$$

More generally, we could consider a boundary coupling that has nontrivial dependence on the transverse coordinate. Then we could solve (3.81) using a Green's function H [149]

$$\left(\int \mathrm{d}U h_{kk} \right)(x) = 8\pi G_N \int \mathrm{d}x' H(x - x') \int \mathrm{d}U \, \langle T_{kk} \rangle (x') \tag{3.84}$$

with

$$H(x - x') = \begin{cases} \frac{r_+ e^{-(r_+ - r_-)(x' - x)}}{1 - e^{-2\pi(r_+ - r_-)}} + \frac{r_+ e^{(r_- + r_+)(x' - x)}}{e^{2\pi(r_- + r_+)} - 1} & x' \geq x \\ \frac{r_+ e^{(r_- + r_+)(2\pi - x + x')}}{e^{2\pi(r_- + r_+)} - 1} + \frac{r_+ e^{-(r_+ - r_-)(2\pi - x + x')}}{1 - e^{-2\pi(r_+ - r_-)}} & x' \leq x \end{cases} \tag{3.85}$$

in position space where $x, x' \in [0, 2\pi)$. In Fourier space, H takes the form

$$H(x - x') = \sum_q e^{iq(x - x')} H_q, \quad H_q = \frac{1}{2\pi} \frac{2r_+^2}{r_+^2 - r_-^2 - 2iqr_- + q^2}. \tag{3.86}$$

If we are working with planar BTZ black holes, H takes the following form,

$$H(x - x') = \begin{cases} r_+ e^{-(r_- + r_+)(x' - x)} & x' \geq x \\ r_+ e^{-(r_+ - r_-)(x - x')} & x' \leq x, \end{cases} \tag{3.87}$$

where x and x' can take value on the whole real axis, and in Fourier space one should just adapt the sum in the compact case to an integral.

Note that, in particular, the zero-mode Green's function diverges in the extremal limit. This means that our perturbation theory breaks down in that limit, although this still suggests that the wormhole will be open for quite a long time, as will be shown below.

In contrast, the non-zero modes of H_q remain finite at extremality. So in the extremal limit, it suffices to study only the zero mode. Recalling that the BTZ temperature is given by $T_H = \frac{r_+^2 - r_-^2}{2\pi r_+}$, we have

$$\frac{\pi T_H}{r_+} \int h_{kk} \mathrm{d}U \mathrm{d}x = 8\pi G_N \int \langle T_{kk} \rangle \, \mathrm{d}U \mathrm{d}x, \tag{3.88}$$

so that (3.79) gives the average shift $\Delta V(U) \equiv V(U) - V(-\infty)$ as

$$T_H \Delta V_{\text{average}}\,(U) = 2G_N r_+ \int_{-\infty}^{U} \int_0^{2\pi} \langle T_{kk} \rangle \, \mathrm{d}U \mathrm{d}x. \tag{3.89}$$

But in any case, we could use (3.79) and (3.84) to calculate the shift $\Delta V(U)$. In particular, the shift at $U = +\infty$ is given by

$$\Delta V(+\infty) = \frac{1}{4} \int_{-\infty}^{\infty} \mathrm{d}U h_{kk} = 2\pi G_N \int \mathrm{d}x' H\,(x - x') \int_{-\infty}^{\infty} \mathrm{d}U \, \langle T_{kk} \rangle \,(x')\,. \tag{3.90}$$

By choosing the boundary conformal frame to be $ds^2_{\partial BTZ} = -dt^2 + d\phi^2 = -dt^2 + \left(dx + \frac{r_-}{r_+} dt\right)^2$, we can relate the boundary time with the V coordinate via

$$t = -\frac{r_+}{r_+^2 - r_-^2} \log\left(\pm V\right). \tag{3.91}$$

Here the sign is $+$ for the left boundary and is $-$ for the right boundary. The shortest transit time t_* from left to right boundary is realized by the geodesic that leaves the left boundary at $V = -|\Delta V|/2$ and arrives at the right boundary at $|\Delta V|/2$ so that

$$t_* = -\frac{2r_+}{r_+^2 - r_-^2} \log\left(\frac{|\Delta V|}{2}\right). \tag{3.92}$$

We can also calculate the shift of the boundary angular coordinate between one end of the null geodesic and the other. Since on the horizon of the unperturbed geometry we simply follow a particular generator where x is constant, on the boundary the change in ϕ is

$$\phi_* = -\frac{2r_-}{r_+^2 - r_-^2} \log\left(\frac{|\Delta V|}{2}\right). \tag{3.93}$$

3.3.2 Violation of ANEC from a double-trace deformation

In AdS/CFT, the eternal BTZ black hole is dual to the thermofield double state

$$|\Psi\rangle = \frac{1}{\sqrt{Z(\beta, \Omega_H)}} \sum_n e^{-\beta(E_n - \Omega_H J_n)/2} |E_n, J_n\rangle_L |E_n, J_n\rangle_R . \tag{3.94}$$

Traversability is achieved by coupling the two boundaries using a double-trace deformation

$$\delta S = \int dt dx \; h(t,x) \mathcal{O}_R(t,x) \mathcal{O}_L(-t,x) = -\int dt \; \delta H, \tag{3.95}$$

where $\mathcal{O}_{L/R}$ is a scalar operator living in the left/right CFT, and we choose its scaling dimension to be $\Delta = \frac{d}{2} - \sqrt{\left(\frac{d}{2}\right)^2 + m^2}$ in order to have a relevant deformation [55]. The boundary operator $\mathcal{O}_{L/R}$ is dual to a bulk scalar field $\Phi_{L/R}$ with mass m[31]. To make the wormhole traversable, $h(t,x)$ needs to be of some definite sign for a period of time, which we denote as $[t_0, t_f]$.

We now show how such a boundary coupling leads to a violation of the ANEC. The starting point is to evaluate the bulk two-point function along the horizon $V = 0$:

$$G(U, U') \equiv \langle \Phi_R(U, x) \Phi_R(U', x) \rangle . \tag{3.96}$$

In a perturbative expansion in powers of the boundary coupling, the one-loop contribution to the two-point function is [55]

$$G_h = 2\sin(\pi\Delta) \int_{t_0}^{t} dt_1 dx_1 \; h(t_1, x_1) \mathcal{K}(r', t', x'; -t_1 + i\beta/2, x_1) \mathcal{K}_{\text{ret}}(r, t, x; t_1, x_1) + (t \leftrightarrow t') \tag{3.97}$$

where $\mathcal{K}$ is the bulk-to-boundary propagator, and $\mathcal{K}_{\text{ret}}$ is the retarded bulk-to-boundary propagator. Since the BTZ black hole is just quotiented AdS_3, the propagators take the same form as those in AdS_3 but with a sum over images. The bulk-to-boundary propagator in the right exterior region in rotating BTZ metric is [55, 148]

$$\mathcal{K}(z, t, x; t_1, x_1) = \frac{\left(r_+^2 - r_-^2\right)^{\frac{\Delta}{2}}}{2^{\Delta+1}\pi} \sum_{n=-\infty}^{\infty} \left[-\sqrt{z-1}\cosh(\kappa\delta t - r_-\delta x_n) + \sqrt{z}\cosh(r_+\delta x_n)\right]^{-\Delta} \tag{3.98}$$

[31] It was shown in [175] that sufficiently small masses of the bulk field in general (n, g) geometries leads to instabilities.

where

$$z=\frac{r^2-r_-^2}{r_+^2-r_-^2},\quad \delta t=t-t_1,\quad \delta x_n=x-x_1+2\pi n. \tag{3.99}$$

We may convert this to Kruskal coordinates in the right exterior region using the relations

$$t=\frac{1}{2\kappa}\log\left(-\frac{U}{V}\right),\quad z=\left(\frac{1-UV}{1+UV}\right)^2. \tag{3.100}$$

Evaluated along $V=0$, $\mathcal{K}$ becomes

$$\mathcal{K}(U,0,x;U_1,x_1)=\frac{\left(r_+^2-r_-^2\right)^{\frac{\Delta}{2}}}{2^{\Delta+1}\pi}\sum_{n=-\infty}^{\infty}\left[-\frac{U}{U_1}e^{-r_-\delta x_n}+\cosh\left(r_+\delta x_n\right)\right]^{-\Delta}. \tag{3.101}$$

The other ingredient in G_h is the retarded bulk-to-boundary propagator

$$\mathcal{K}_{\text{ret}}\left(z,t,x;t_1,x_1\right)=\left|\mathcal{K}\left(z,t,x;t_1,x_1\right)\right|\theta(\delta t)\theta\left(\sqrt{z-1}\cosh\left(\kappa\delta t-r_-\delta x\right)-\sqrt{z}\cosh\left(r_+\delta x\right)\right). \tag{3.102}$$

Now we are ready to write down $G_h(U,U')$:

$$\begin{aligned}G_h(U,U')=&C_0\sum_{n=-\infty}^{\infty}\int_0^{2\pi}dx_n\int_{U_0}^{U}\frac{dU_1}{\kappa U_1}h\left(\frac{\log(U_1)}{\kappa},x_n\right)\\&\left[\left(e^{-r_-\delta x_n}U_1U'+\cosh\left(r_+\delta x_n\right)\right)\left(e^{-r_-\delta x_n}\frac{U}{U_1}-\cosh\left(r_+\delta x_n\right)\right)\right]^{-\Delta}\tilde{\theta}+(U\leftrightarrow U')\end{aligned} \tag{3.103}$$

where $C_0=\frac{r_+^{\Delta}\kappa^{\Delta}\sin(\pi\Delta)}{2(2^{\Delta}\pi)^2}$, $\tilde{\theta}=\theta\left(e^{-r_-\delta x}U-U_1\cosh\left(r_+\delta x\right)\right)$, and we have used the fact that on the right boundary $t=\frac{\log(U)}{\kappa}$.

For planar BTZ black holes we would discard the image sum and extend the range of the x_1 integral to the whole real axis [55]. But one should not forget the constraint imposed by the θ-function in the retarded propagator, which requires

$$e^{-r_-\delta x}U-U_1\cosh\left(r_+\delta x\right)\geq 0. \tag{3.104}$$

With the Green's function at hand, the bulk stress tensor associated with the scalar field is

$$\langle T_{\mu\nu}\rangle=\lim_{\mathbf{x}\to\mathbf{x}'}\left(\partial_\mu\partial_\nu G\left(\mathbf{x},\mathbf{x}'\right)-\frac{1}{2}g_{\mu\nu}g^{\rho\sigma}\partial_\rho\partial_\sigma G\left(\mathbf{x},\mathbf{x}'\right)-\frac{1}{2}g_{\mu\nu}m^2G\left(\mathbf{x},\mathbf{x}'\right)\right). \tag{3.105}$$

When evaluated along the horizon at $V = 0$, the g_{UU} component of the unperturbed metric vanishes, so to leading order we have

$$\langle T_{kk} \rangle = \lim_{U' \to U} \partial_U \partial_{U'} G_h \left(U, U' \right) . \tag{3.106}$$

Finally one can compute the opening of the traversable wormhole by inserting (3.103) and (3.106) into (3.90). As shown in [55], the result is generally non-zero. So for the right sign of the coupling function h it will give a time-advance that makes the wormhole traversable.

3.4 Traversability of multi-boundary wormholes in AdS_3

As shown in [161], for non-rotating multi-boundary wormholes in the hot limit, the boundary state locally resembles the thermofield double state in region D_ϕ discussed in section 3.2.4. This could be easily generalized to rotating wormholes by adding an angular potential. In regions that we call D_x (since x is a more well-defined coordinate on the horizon in the rotating case), the horizons are exponentially close to each other, and the corresponding local state is exponentially close to a piece of the TFD

$$|\Psi\rangle = \frac{1}{\sqrt{Z\left(\beta_{TFD}, \Omega_{TFD}\right)}} \sum_n e^{-\beta_{TFD}(E_n - \Omega_{TFD} J_n)/2} \left| E_n, J_n \right\rangle_L \left| E_n, J_n \right\rangle_R . \tag{3.107}$$

Since our state is only locally TFD, the parameters β_{TFD} and Ω_{TFD} can take any value depending on the conformal frame. They thus should not be confused with the actual black hole inverse temperature and angular velocity. In the hot limit, one expects that such wormholes can be made traversable by the approach described in section 3.3. We will show this below focussing on the three-boundary wormhole, and in particular on the process of traversing from boundary 1 to boundary 2.

We will first set the stage by describing and justifying the planar BTZ coordinates to be used below. In these coordinates, our calculations will be very similar to those of [55]. We will then show that, in the hot limit, the image sum in the Green's function is well approximated by the leading term. This greatly simplifies our calculation. Finally, we calculate the wormhole opening with a double-trace deformation, which we require to be larger than the local thickness of the causal shadow.

3.4.1 Planar BTZ coordinates and the boundary coupling

Any BTZ black hole is locally isometric to AdS_3, and thus also to planar BTZ. As a result, in any contractible region D_x, we may use planar BTZ coordinates to describe the spacetime. Here, we use the following planar coordinates to describe both sides of the wormhole:

$$ds^2 = -(\tilde{r}^2 - \tilde{r}_+^2)d\tilde{t}^2 + \frac{d\tilde{r}^2}{\tilde{r}^2 - \tilde{r}_+^2} + \tilde{r}^2 d\tilde{x}^2. \tag{3.108}$$

We think of $\tilde{x}$ as ranging over the entire real axis, though we are most interest in some domain that corresponds to D_x. The choice of $\tilde{r}_+$ is arbitrary. The corresponding Kruskal metric is

$$\mathrm{d}s^2 = \frac{1}{(1+\tilde{U}\tilde{V})^2}\left(-4\mathrm{d}\tilde{U}\mathrm{d}\tilde{V} + \tilde{r}_+^2(1-\tilde{U}\tilde{V})^2\mathrm{d}\tilde{x}^2\right). \tag{3.109}$$

Although there is a causal shadow between the two horizons in the hot limit, it is exponentially small in ℓ and $\tilde{\ell}$ over large stretches of the horizons. So if we put the origin of the Kruskal coordinates at the bifurcation surface of horizon 1 or 2 (or any place between them) in the region where this separation is small, we make only an exponentially small error if we then identify the above coordinates with natural BTZ coordinates in either exterior. This justifies using the metric (3.109) for D_x. We will come back to this in section 3.4.3.

Note that, in the planar BTZ metric, the horizon size parameters can be scaled arbitrarily as long as we change the definition of coordinates accordingly. To be more concrete, there are two kinds of coordinate transformations that we can make (they are expressed in the ordinary angular coordinate ϕ for now and we will come back to the co-rotating x later):

1. "Adjusting the temperature" (rescaling r_+ and r_- by the same amount):

$$\tilde{r} = \lambda r, \quad \tilde{t} = \frac{t}{\lambda}, \quad \tilde{\phi} = \frac{\phi}{\lambda}. \tag{3.110}$$

   with the new horizon parameters $\tilde{r}_\pm = \lambda r_\pm$;

2. "Changing the angular velocity" (changing the relative size of r_+ and r_-):

$$\begin{aligned}(\tilde{t}, \tilde{\phi}) &= (t\cosh\gamma + \phi\sinh\gamma, t\sinh\gamma + \phi\cosh\gamma)\\ \tilde{r}^2 &= r^2 + \tilde{r}_-^2 - r_-^2.\end{aligned} \tag{3.111}$$

with the new horizon parameters $\tilde{r}_+ = r_+ \cosh\gamma + r_- \sinh\gamma$ and $\tilde{r}_- = r_+ \sinh\gamma + r_- \cosh\gamma$. As a special case, we could set $\tilde{r}_- = 0$ by choosing $\gamma = -\tanh^{-1}\frac{r_-}{r_+}$. In this case we have

$$\begin{aligned}(\tilde{t},\tilde{\phi}) &= (r_+ t - r_-\phi, r_+\phi - r_- t)\,/\sqrt{r_+^2 - r_-^2} \\ \tilde{r}^2 &= r^2 - r_-^2.\end{aligned} \tag{3.112}$$

with $\tilde{r}_+^2 = r_+^2 - r_-^2$.

Note that we are not changing the actual temperature and angular momentum associated with any particular global BTZ horizon (which are uniquely determined by the bulk geometry). The point is that the above description is valid only in a contractible domain where the full global structure is not apparent. In that domain we have described the system to good approximation as a planar BTZ black hole, for which the temperature and angular velocity depend on the choice of the boundary conformal frame and are not fixed by the bulk metric.

For simplicity, we would like to choose $\tilde{r}_- = 0$ and $\tilde{r}_+$ be some fixed $\mathcal{O}(1)$ number when the $r_{+,i}$'s become large. To clarify our notation, from here on, we use tildes to mark quantities associated with the bulk planar BTZ coordinates (for which $\tilde{r}_- = 0$), and we use symbols without tildes to refer to quantities associated with the BTZ conformal frame in some asymptotic region – perhaps with additional labels to denote the asymptotic region of interest.

Combining (3.110) and (3.112), the coordinate transformations we will use on boundaries 1 and 2 are

$$\begin{aligned}(\tilde{t},\tilde{\phi}) &= (r_{+,i}t_i - r_{-,i}\phi_i, r_{+,i}\phi_i - r_{-,i}t_i)\,/\tilde{r}_+ \\ \frac{\tilde{r}^2}{\tilde{r}_{+,i}^2} &= \frac{r_i^2 - r_{-,i}^2}{r_{+,i}^2 - r_{-,i}^2},\end{aligned} \tag{3.113}$$

where $i = 1, 2$ indicate different asymptotic regions. The above should be understood as two different coordinate transformations, one for each value of i. As a result, the two boundaries will naturally define distinct notions of 'time advance' $\Delta V_1 \neq \Delta V_2$ (and also for similar quantities).

It will sometimes also be useful to consider the inverse transformation:

$$(t_i, \phi_i) = \frac{\tilde{r}_+}{r_{+,i}^2 - r_{-,i}^2}(r_{+,i}\tilde{t} + r_{-,i}\tilde{\phi}, r_{-,i}\tilde{t} + r_{+,i}\tilde{\phi}). \tag{3.114}$$

In terms of the co-rotating coordinates, the transformations and inverse transformations for (t, x) and $(\tilde{t}, \tilde{x})$ are

$$\tilde{t} = \frac{\kappa_i t_i - r_- x_i}{\tilde{r}_+}, \quad \tilde{x} = \frac{r_{+,i}}{\tilde{r}_+} x_i = \tilde{\phi} \tag{3.115}$$

$$t_i = \frac{\tilde{r}_+}{\kappa_i} \left(\tilde{t} + \frac{r_-}{r_+} \tilde{x} \right), \quad x_i = \frac{\tilde{r}_+}{r_{+_i}} \tilde{x}. \tag{3.116}$$

In particular, it will be convenient to take points on the horizons with $x = 0, x_i = 0$ to lie deep inside the domain D_x where the separation between horizons is exponentially small. The associated Kruskal null coordinates are related by

$$\tilde{U} = e^{-r_{-,i} x_i} U_i, \quad \tilde{V} = e^{r_{-,i} x_i} V_i, \tag{3.117}$$

so that at $\tilde{x} = 0$ (where $x_i = 0$) we have $\tilde{U} = U_i, \tilde{V} = V_i$. One may interpret this as saying that we have chosen all three sets of coordinates to be associated with the same reference frame at $\tilde{x} = 0$.

From the planar coordinates we use, it is tempting to conclude that our setup can be directly reduced to that of [55], reviewed in section 3.3. But, here, the subtlety is that the boundary coupling is not naturally defined in the conformal frame related to our bulk metric. To perform calculations, we need to first look at the conformal transformations and how they act on boundary operators. To this end, we recall that the boundary metric in the i^{th} asymptotic region is

$$ds_i^2 = -dt_i^2 + d\phi_i^2 = \frac{\tilde{r}_+^2}{r_{+,i}^2 - r_{-,i}^2} \left(-d\tilde{t}^2 + d\tilde{\phi}^2 \right). \tag{3.118}$$

A general bi-local double-trace deformation coupling boundaries 1 and 2 will take the form[32]

$$\delta S = \int dt_1 dt_2 dx_1 dx_2 \; f(t_1, t_2, x_1, x_2) \mathcal{O}_1(t_1, x_1) \mathcal{O}_2(t_2, x_2). \tag{3.119}$$

Local couplings, analogous to those used in [55] are obtained by taking f proportional to a delta-function. But as opposed to the TFD case studied in [55], there is no preferred natural way to identify points on boundary 1 with points on boundary 2. We must therefore choose some diffeomorphism η from boundary 1 to boundary 2 and write

$$f(t_1, t_2, x_1, x_2) = h(t_1, x_1) \; \delta^{(2)}(\mathbf{x_2} - \eta(\mathbf{x_1})), \tag{3.120}$$

[32] In contrast with section 3.3 (e.g. in (3.95)) we will take the boundary times to increase toward the future on all boundaries.

where $\mathbf{x_i} = (t_i, x_i)$, $i = 1, 2$. Integrating out the delta function then expresses the coupling in terms of a single set of boundary coordinates. For computational convenience, we will choose the the functions h and η such that the double-trace deformation takes a simple form when expressed in the conformal frame associated with the tilded bulk coordinates. In particular, we take

$$\delta S = \int d\tilde{t} d\tilde{x}\ \tilde{h}(\tilde{t}, \tilde{x}) \left(\frac{r_{+,1}^2 - r_{-,1}^2}{\tilde{r}_+^2} \right)^{\frac{\Delta-1}{2}} \left(\frac{r_{+,2}^2 - r_{-,2}^2}{\tilde{r}_+^2} \right)^{\frac{\Delta-1}{2}} \tilde{\mathcal{O}}_1(\tilde{t}, \tilde{x}) \tilde{\mathcal{O}}_2(\tilde{t}, \tilde{x}) \tag{3.121}$$

where $\tilde{\mathcal{O}}_{1/2}$ is the quantity $\mathcal{O}_{1/2}$ conformally transformed to the above frame. Note that the expression (3.121) includes conformal factors from (3.118) to account for the transformations of boundary operators with conformal dimension Δ as well as for the Jacobian associated with the change of integration variables.

We can also choose a simple explicit form of $\tilde{h}(\tilde{t}, \tilde{x})$ that turns on at some time $\tilde{t}_0$ and turns off at some later time $\tilde{t}_f$. For example, for every $\tilde{t}$ in between we could either choose a constant (and in particular $\tilde{x}$-independent) coupling,

$$\tilde{h}(\tilde{t}, \tilde{x}) = h\lambda^{2-2\Delta} \tag{3.122}$$

or a Gaussian in $\tilde{x}$ to make it localize near some angular position $\tilde{x}_0$; i.e., for $\tilde{t}_i < \tilde{t} < \tilde{t}_f$, we may take

$$\tilde{h}(\tilde{t}, \tilde{x}) = h\lambda^{2-2\Delta} \exp\left(-\frac{\tilde{r}_+^2 (\tilde{x}_1 - \tilde{x}_0)^2}{\sigma^2} \right), \tag{3.123}$$

where λ is some fixed quantity with dimension of temperature and h is a small and dimensionless parameter. Note that [55, 148] both set λ equal to the temperature of their BTZ background. But there is no unique temperature associated with a general multi-boundary black hole, as the temperatures of the three horizons can differ. This is not a problem. We are free to choose λ in any way we like, including to choose it independent of the background, as long as it has the correct dimensions.

3.4.2 Image sum in the hot limit

We now show that the image sum in G_h can be well approximated by keeping only the leading term. Since G_h is built from two bulk-to-boundary propagators, it will be useful to study them first.

The extrapolate dictionary [176, 177] tells us that the bulk-to-boundary propagator in the global AdS_3 conformal frame can be obtained from the bulk two-point function via

$$\mathcal{K}(p, q_\partial) = \lim_{r' \to \infty} r'^{\Delta} G(p, q) = \lim_{r' \to \infty} r'^{\Delta} G(r, t, x; r', t', x'). \tag{3.124}$$

Here p and q are two points in the AdS_3 bulk. The coordinates of q are those marked with primes, and the unprimed coordinates are those of p.

In AdS_3, the two-point function for a free scalar field is given by

$$G(p, q) = G_{\mathrm{AdS}_3}(Z) = \frac{1}{4\pi} \left(Z^2 - 1\right)^{-1/2} \left(Z + \left(Z^2 - 1\right)^{1/2}\right)^{1-\Delta}, \tag{3.125}$$

where $Z = 1 + \frac{\sigma(p,q)}{2}$ and $\sigma(p, q)$ is the (squared) distance between p and q in the four dimensional embedding space (sometimes called "chordal distance" [178]), and with all fractional powers of positive real numbers defined by using the positive real branch. The chordal distance is related to the geodesic distance $d(p, q)$ in AdS space by

$$\sigma(p, q) = 4 \sinh^2 \left(\frac{d(p, q)}{2}\right). \tag{3.126}$$

When Z is large, the two-point function has the expansion

$$G_{AdS_3}(p, q) = \frac{Z^{-\Delta}}{4\pi} \left(2^{1-\Delta} + \frac{1 + \Delta}{2^{1+\Delta}} Z^{-2} + \mathcal{O}\left(Z^{-3}\right)\right). \tag{3.127}$$

In AdS_3, the (unrenormalized) distance between a bulk point p and a boundary point q_∂ has the divergent part $\log r'$, so $G_{AdS_3}(x, x')$ decays as $(r')^{-\Delta}$. But this decay is precisely cancelled by the $(r')^{\Delta}$ in the extrapolate dictionary (3.124). As a result, the bulk-to-boundary propagator can also be obtained from the bulk-to-bulk propagator by inserting into (3.125) an appropriately-renormalized (and thus finite) distance between p and q_∂. According to the analysis of section 3.2.2, in the conformal frame associated with the global coordinates, this renormalized distance is defined by subtracting $\log r'$ from the unrenormalized distance.

In a general conformal frame the extrapolate dictionary becomes

$$\mathcal{K} = \lim_{\bar{r}' \to \infty} \bar{r}'^{\Delta} G(r, t, x; r', t', x') \tag{3.128}$$

where $\bar{r}' = r'|\Omega|$ and Ω^2 is the conformal factor such that the boundary metric ds^2_Ω satisfies $ds^2 = -dt^2 + d\phi^2 = \Omega^2 ds^2_\Omega$. Equivalently, we could obtain the correct bulk-to-boundary

propagator by inserting into (3.125) an appropriately renormalized bulk-to-boundary distance associated with our conformal frame.

Since the three-boundary wormholes of section 3.2 are quotients of AdS_3, their bulk-to-boundary propagators are given by sums of AdS_3 propagators over image points. In particular, for points p and q_∂, we need to include AdS_3 propagators for the point pairs $(p, g_L q_\partial g_R^t)$, where g_L and g_R are any "words" formed from the left and right generators of the quotient group Γ used to construct the wormhole.

We would like to locate the image points $g_L q_\partial g_R^t$ and find how they contribute to the bulk-to-boundary propagator in the hot limit. Recall from section 3.2.2 that there are two types of image points: 1) points inside the same boundary diamond as q_∂ and 2) points in other diamonds (i.e. outside the boundary diamond that q_∂ is in). As shown in section 3.2.4, when q_∂ is taken to lie at a fixed location in the largest diamond non-trivial image points in the same diamond must be exponentially close to one of the fixed points at the left or right corners of the diamond. For those in other diamonds it suffices to note that such non-trivial image diamonds are exponentially small in the hot limit.

Since all (AdS-)Cauchy slices of the wormhole spacetime lift to surfaces that run through the left and right corners of each boundary diamond, and since any bulk point p can be taken to lie on a spacelike (AdS-)Cauchy surface, p will have spacelike separation from points close enough to these corners. This will in particular be true of the non-trivial images of q_∂ in the hot limit. This means that we use (3.10) rather than (3.11) to calculate the geodesic length between p and those image points.

In section 3.2.3, we calculated the geodesic distance between spacelike separated bulk and boundary points in the BTZ frame. Applying that result to our image points, we found in section 3.2.4 that the geodesic distance is at least linearly large in $(\ell_i + \tilde{\ell}_i)$ in the hot limit. From (3.125) and (3.126) we then see that the contributions to the bulk-to-boundary propagator from the image points are exponentially suppressed, and thus that they can be ignored in the hot limit.

3.4.3 Traversing the causal shadow

We now show in the hot limit that the $|\Delta V|$ induced by a fixed boundary coupling becomes larger than the gap $|\Delta V_{CS}|$ between horizons associated with the existence of the causal shadow region (see figure 3.8). Thus $\Delta V_{total} \equiv |\Delta V| - |\Delta V_{CS}|$ becomes positive and therefore the wormhole is traversable.

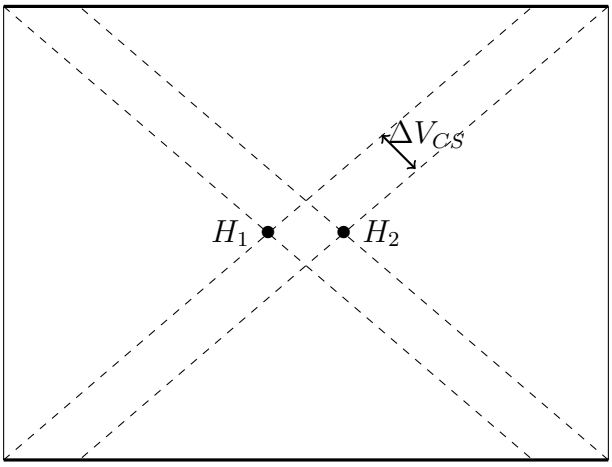

Figure 3.8: The Penrose diagram of a black hole spacetime with causal shadow. In particular, this could represent the causal structure of a section that contains two asymptotic regions in the three-boundary wormhole geometry. In the figure, we mark the two bifurcation surfaces H_1 and H_2, and ΔV_{CS} caused by the causal shadow. In the hot limit that we consider in the text, ΔV_{CS} is exponentially small in ℓ and $\tilde{\ell}$ in region D_x.

From the above two subsections, the one-loop contribution to the Green's function is

$$\tilde{G}_h(\tilde{U},\tilde{U}') = \tilde{C}_0 \int d\tilde{x}_1 \int_{\tilde{U}_0}^{\tilde{U}} \frac{d\tilde{U}_1}{\tilde{r}_+ \tilde{U}_1} \tilde{h}\left(\frac{\log \tilde{U}_1}{\tilde{r}_+}, \tilde{x}_1\right) \left[\left(\tilde{U}_1\tilde{U}' + \cosh\left(\tilde{r}_+\delta\tilde{x}\right)\right)\left(\frac{\tilde{U}}{\tilde{U}_1} - \cosh\left(\tilde{r}_+\delta\tilde{x}\right)\right)\right]^{-\Delta} + (\tilde{U} \leftrightarrow \tilde{U}'), \tag{3.129}$$

where $\tilde{U}_0 = e^{\tilde{r}_+\tilde{t}_0}$, $\delta\tilde{x} = \tilde{x} - \tilde{x}_1$ and

$$\tilde{C}_0 = \frac{\tilde{r}_+^{2\Delta}\sin(\pi\Delta)}{2\left(2^\Delta\pi\right)^2}\left(\frac{r_{+,1}^2 - r_{-,1}^2}{\tilde{r}_+^2}\right)^{\frac{\Delta-1}{2}}\left(\frac{r_{+,2}^2 - r_{-,2}^2}{\tilde{r}_+^2}\right)^{\frac{\Delta-1}{2}} = \frac{\tilde{r}_+^2(r_{+,1}^2 - r_{-,1}^2)^{\frac{\Delta-1}{2}}(r_{+,2}^2 - r_{-,2}^2)^{\frac{\Delta-1}{2}}\sin(\pi\Delta)}{2\left(2^\Delta\pi\right)^2}. \tag{3.130}$$

The limits of the $\tilde{x}$ integral above are set by the theta function $\theta\left(\frac{\tilde{U}}{\tilde{U}_1} - \cosh\left(\tilde{r}_+\delta\tilde{x}\right)\right)$.

We can use the above result to calculate the stress tensor:

$$\langle \tilde{T}_{kk} \rangle = \lim_{\tilde{U}'\to\tilde{U}} \partial_{\tilde{U}'}\partial_{\tilde{U}}\tilde{G}_h(\tilde{U},\tilde{U}'). \tag{3.131}$$

If the background was exactly planar BTZ, then the shift of $\tilde{V}$ coordinate at $\tilde{U} = +\infty$

would be

$$\Delta\tilde{V}(\tilde{x}) = 2\pi G_N \int_{-\infty}^{+\infty} \mathrm{d}\tilde{x}' \tilde{H}\left(\tilde{x}-\tilde{x}'\right)\left(\int_{-\infty}^{\infty} \mathrm{d}\tilde{U}\langle \tilde{T}_{kk}\rangle\right)(\tilde{x}'), \tag{3.132}$$

where $\tilde{H}(\tilde{x}-\tilde{x}')$ is the Green's function (3.87) for non-compact $\tilde{x}$ and $\tilde{x}'$ when $\tilde{r}_- = 0$,

$$H\left(\tilde{x}-\tilde{x}'\right) = \tilde{r}_+ e^{-\tilde{r}_+|\tilde{x}'-\tilde{x}|}. \tag{3.133}$$

From our arguments above, using this result with (3.113) also gives the correct result in our three-boundary wormhole up to two sorts of corrections. The first are due to errors in (3.113) associated with the finite-but-small thickness of the causal shadow, and the second comes from neglecting the sum over non-trivial images of q_∂. But both sorts of corrections are exponentially small in the hot limit as discussed above. Thus to good approximation in the coordinates related to the i^{th} boundary we find the shift ΔV_i to be

$$\Delta V_i(x_i) = e^{-r_{-,i}x_i}\Delta\tilde{V}(\tilde{x}). \tag{3.134}$$

To put this all together, recall that we are most interested in the region near $\tilde{x} = 0$ where the separation between the bifurcation surfaces is exponentially small. There $V_i \approx \tilde{V}$, and the three coordinate systems are all associated with the same frame of reference. In particular, both bifurcation surfaces will have $U_1 + V_1 \approx$ *constant* and also $U_2 + V_2 \approx$ *constant*. Thus the exponentially small separation is also associated with exponentially small sized $\Delta\tilde{V}_{CS} \approx \Delta V_{1,CS} \approx \Delta V_{2,CS}$ of the causal shadow in this region.

On the other hand, near $x_i = 0$ the time advance ΔV_i is *not* exponentially suppressed at large ℓ_i and $\tilde{\ell}_i$. Instead, it has at most a polynomial suppression. Thus at large $\ell_i, \tilde{\ell}_i$ we find $\Delta V_i \gg \Delta V_{i,CS}$ near $\tilde{x} = 0$ and the wormhole becomes traversable in this region.

As a consistency check, we now show that the physical quantity ΔV_i does not depend on the fictitious parameter $\tilde{r}_+$ that we have been using to simplify the calculations. Our starting point is (3.129). We write $\tilde{G}_h \equiv F + F'$ where F is the term explicitly shown in (3.129)

$$F(\tilde{U},\tilde{U}') = \tilde{C}_0 \int d\tilde{x}_1 \int_{\tilde{U}_0}^{\tilde{U}} \frac{d\tilde{U}_1}{\tilde{r}_+\tilde{U}_1}\tilde{h}\left(\frac{\log\tilde{U}_1}{\tilde{r}_+},\tilde{x}_1\right)\left[\left(\tilde{U}_1\tilde{U}' + \cosh\left(\tilde{r}_+\delta\tilde{x}\right)\right)\left(\frac{\tilde{U}}{\tilde{U}_1} - \cosh\left(\tilde{r}_+\delta\tilde{x}\right)\right)\right]^{-\Delta} \tag{3.135}$$

and F' is the term with $\tilde{U}$ and $\tilde{U}'$ exchanged. Using this symmetry we may write $\langle\tilde{T}_{kk}\rangle$ in the form

$$\langle\tilde{T}_{kk}\rangle = 2\lim_{\tilde{U}'\to\tilde{U}} \partial_{\tilde{U}'}\partial_{\tilde{U}} F(\tilde{U},\tilde{U}'). \tag{3.136}$$

Next, we change the integration variables to make the dependence on $\tilde{r}_+$ clear. First we define a new integration variable $y \equiv \cosh(\tilde{r}_+ \delta\tilde{x}) = \cosh[\tilde{r}_+(\tilde{x} - \tilde{x}_1)]$ to write F as

$$F(\tilde{U}, \tilde{U}') = \frac{2\tilde{C}_0}{\tilde{r}_+^2} \int_{\tilde{U}_0}^{\tilde{U}} \frac{d\tilde{U}_1}{\tilde{U}_1} \int_1^{\tilde{U}/\tilde{U}_1} \frac{dy}{\sqrt{y^2-1}} \tilde{h}\left(\frac{\log \tilde{U}_1}{\tilde{r}_+}, \tilde{x}_1\right) \left[\left(\tilde{U}_1\tilde{U}' + y\right)\left(\frac{\tilde{U}}{\tilde{U}_1} - y\right)\right]^{-\Delta}, \tag{3.137}$$

where the limits of the y integral are determined by the theta function $\theta\left(\frac{\tilde{U}}{\tilde{U}_1} - \cosh\left(\tilde{r}_+\delta\tilde{x}\right)\right)$, and the argument $\tilde{x}_1$ in the function $\tilde{h}$ should be implicitly treated as a function of y.

As we can see from (3.130), all the $\tilde{r}_+$ dependence in the prefactor $\frac{2\tilde{C}_0}{\tilde{r}_+^2}$ cancels out. Recall also the relations (3.115)

$$\tilde{r}_+\tilde{x} = r_{+,i}x_i, \quad \tilde{r}_+\tilde{t} = \kappa_i t_i - r_{-,i}x_i, \tag{3.138}$$

so that on the horizon $V = 0$ we have

$$\tilde{U} = e^{\tilde{r}_+\tilde{t}} = e^{\kappa_i t_i - r_{-,i}x_i}. \tag{3.139}$$

Similar relations hold for $\tilde{U}, \tilde{U}'$ and $\tilde{U}_0$ in the integration limits, and they can be expressed in terms of purely boundary quantities. Furthermore, we should avoid introducing any $\tilde{r}_+$ dependence in $\tilde{h}$ by hand. This means that, when choosing the form of $\tilde{h}$, the argument $\tilde{t}_1$ and $\tilde{x}_1$ in $\tilde{h}$ should both come with a factor of $\tilde{r}_+$, since the combination $\tilde{r}_+\tilde{t}_1$ and $\tilde{r}_+\tilde{x}_1$ can be converted by (3.138) to something that only involves parameters and coordinates related to some boundary. In terms of the new variable y, this means that we must have the combination $(\tilde{r}_+\tilde{x} - \cosh^{-1} y)$ independent of $\tilde{r}_+$. Therefore, F is also independent of $\tilde{r}_+$.

The physical observable ΔV_i on one boundary is

$$\Delta V_i(x_i) = e^{-r_{-,i}x_i}\, 2\pi G_N \int_{-\infty}^{+\infty} \mathrm{d}\tilde{x}' \tilde{r}_+ e^{-\tilde{r}_+|\tilde{x}'-\tilde{x}|} \left(\int_{-\infty}^{\infty} \mathrm{d}\tilde{U} \left\langle \tilde{T}_{kk} \right\rangle\right)(\tilde{x}')\,. \tag{3.140}$$

No dependence on $\tilde{r}_+$ is introduced in passing from F to $\int \mathrm{d}\tilde{U}\langle\tilde{T}_{kk}\rangle$ and, from our previous argument, $\int \mathrm{d}\tilde{U}\langle\tilde{T}_{kk}\rangle$ as a function of $\tilde{x}'$ should only depend on the combination $\tilde{r}_+\tilde{x}'$. As we can see, all other parts involving tilded coordinates in (3.140) all come with a factor of $\tilde{r}_+$, so the physical quantity ΔV_i will not have any $\tilde{r}_+$ dependence.

3.4.4 Numerical results

We now present some numerical results in order to illustrate our construction. Here we will take the boundary coupling to be turned on at $\tilde{t}_0 = 0$ and never shut off. We will

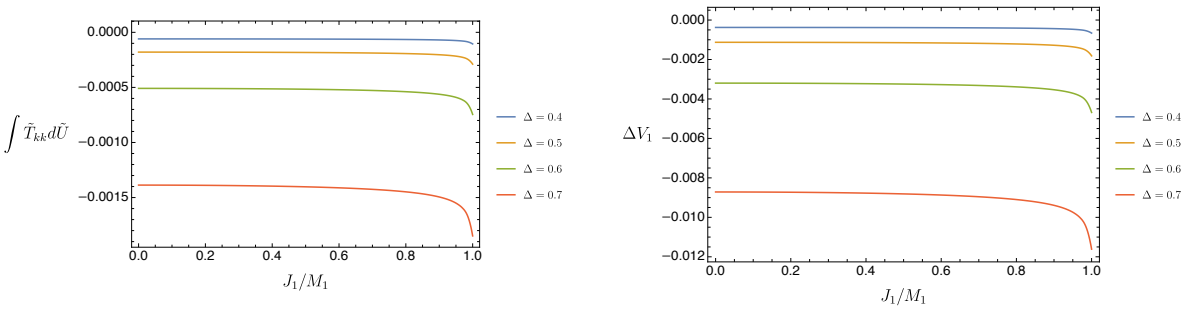

Figure 3.9: For the case of constant coupling, the averaged null energy $\int \tilde{T}_{kk} d\tilde{U}$ (left) and the horizon shift ΔV_1 at $x_1 = 0$ (right). In both panels, we choose $h = 1$, $\lambda = 1$, $G_N = 1$, $r_{+,2} = 100$, $r_{-,2} = 20$ and $r_{+,1} = 100$.

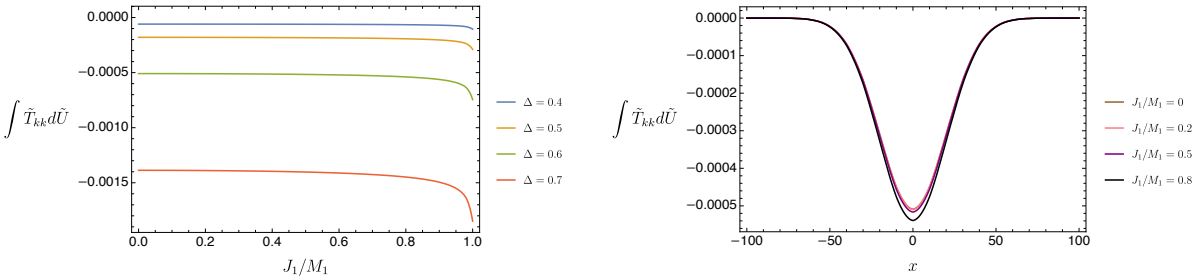

Figure 3.10: For the case of Gaussian coupling, the averaged null energy $\int \tilde{T}_{kk} d\tilde{U}$ at $x_1 = 0$ (left) and its profile for general x_1 (right). In both panels, we choose $h = 1$, $\lambda = 1$, $G_N = 1$ $r_{+,2} = 100$, $r_{-,2} = 20$ and $r_{+,1} = 100$, $\sigma = 0.2$ and $x_0 = 0$. In the right panel we also choose $\Delta = 0.6$.

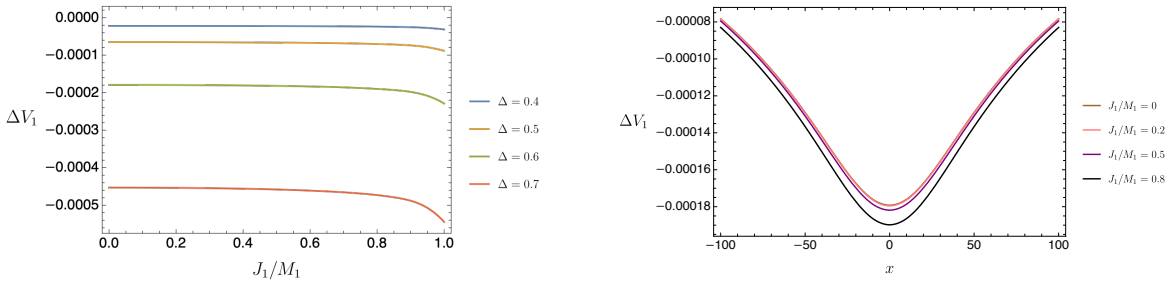

Figure 3.11: For the case of Gaussian coupling, the shift of horizon ΔV_1 at $x_1 = 0$ (left) and its profile for general x_1 (right). In both panels, we choose $h = 1$, $\lambda = 1$, $G_N = 1$ $r_{+,2} = 100$, $r_{-,2} = 20$ and $r_{+,1} = 100$, $\sigma = 0.2$ and $\tilde{x}_0 = 0$. In the right panel we also choose $\Delta = 0.6$.

consider two types of boundary coupling: 1) for every $\tilde{t} > 0$ the coupling is constant, as in (3.122) and 2) for every $\tilde{t} > 0$ we take the coupling to be a Gaussian centered at some point, as in (3.123).

We also take $h = 1$ and $\lambda = 1$ in the boundary coupling, and $G_N = 1$ for simplicity. Furthermore, without loss of generality, we only consider a subspace of the wormhole parameter space defined by $r_{+,2} = 100$, $r_{-,2} = 20$ and $r_{+,1} = 100$. We then study the dependence of various quantities on the remaining parameters $r_{-,1}$ (or equivalently the ratio between angular momentum and mass J_1/M_1 on boundary 1) and the scaling dimension Δ.

The quantities studied here are the averaged null energy $\int \tilde{T}_{kk} d\tilde{U}$ and the shift of the horizon ΔV_1 as measured on boundary 1. Note that here $\int \tilde{T}_{kk} d\tilde{U}$ is not a physical quantity since we could choose any kind of "tilded coordinates", but we show it here because its negativity is important for traversability. For convenience we choose $\tilde{r}_+ = 1$.

Results for the case of constant coupling are shown in figure 3.9. There we show $\int \tilde{T}_{kk} d\tilde{U}$ and ΔV_1 at $x_1 = 0$ (or equivalently $\tilde{x} = 0$) for different Δ and J_1/M_1. As we can see, both quantities are negative and diverge near extremality.

For Gaussian coupling, we choose $\sigma = 0.2$ and $\tilde{x}_0 = 0$. In figure 3.10, we show $\int \tilde{T}_{kk} d\tilde{U}$ at $x_1 = 0$ (or equivalently $\tilde{x} = 0$) and its angular dependence for some choices of parameters, while results about ΔV_1 are shown in figure 3.11.

3.5 Discussion

This chapter extended the Gao-Jafferis-Wall traversability protocol [55] to multi-boundary wormholes. The main physical difficulty in achieving traversability in this case is the existence of the causal shadow region between the horizons, and the main technical complication in the analysis involves calculating the image sum in the Green's function. Our main result is that, in the hot limit, both of these difficulties can be circumvented and traverseability can be demonstrated for appropriate couplings. As shown in section 3.2, this is because for any pair of horizons there is a region whose extent along the horizons is large in comparison with the AdS length where the horizons are exponentially close to each other. The analysis in such regions thus reduces to that of [55]. In particular, in this limit the distance between the global AdS_3 images of appropriate bulk points bceomes large, which exponentially suppresses all but one of the corresponding contributions to the Green's function relative to the largest such contribution. This greatly simplifies the calculation of the Green's function required to calculate the average null energy along the

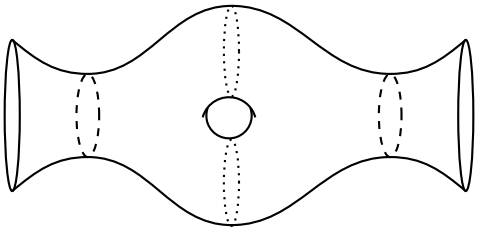

Figure 3.12: A Cauchy slice of the $(2,1)$ geometry showing the horizons (dashed lines) and the two extremal surfaces (dotted lines) in the causal shadow region. In the hot limit, the length of both types of surfaces have to be taken to be large so that, by the Gauss-Bonnet theorem, there will be a large region where they are arbitrarily close to each other.

horizon. In a dual field theory description, the essential point is that the CFT state in this region is approximately given by the TFD state [161].

Although we presented explicit calculations only for the three-boundary wormhole geometry, our work can be generalized to general n-boundary genus g wormholes (i.e. to (n,g) geometries). The one subtlety in doing so is that, in addition to taking a hot limit for the horizons, one must also take similar limits of certain internal moduli in order to make the causal shadow exponentially small in certain regions. See figure 3.12 for the case $n=2$, $g=1$, but similar issues arise even for $g=0$ when $n>3$. Indeed, one can view this as a result of the fact that a general (n,g) geometry can be made by sewing together copies of $(3,0)$ "pair of pants" geometries, but that in doing so some of the minimal circles that would have defined horizons in some given $(3,0)$ geometry become cycles inside the causal shadow of the final (n,g) geometry. Thus, the desired hot limit involves not only taking limits of the parameters that define the final (n,g) horizons, but also requires us to take limits of the parameters associated with the would-be $(3,0)$ horizons that are now inside the causal shadow. That this is possible in general was shown in [161] for the static case, but those arguments can be generalized to allow rotation just as in section 3.2 above. Thus the traversability analysis reduces to exactly the same one we used for the case without genus, and once again the CFT dual to the bulk region where the horizons are exponentially close together is well-approximated by the TFD state.

In the extremal limit, we showed in appendix B.2 that the minimal distance d_{ij} between the horizons diverges logarithmically. However, from (3.129) and (3.132), we see that the time advance ΔV induced by the double-trace deformation diverges polynomially, which is also illustrated in figures 3.9 and 3.11. For this reason, we expect that the wormhole is still traversable in the extremal limit even though, as discussed in section 3.3, the perturbative

analysis that allowed us to calculate ΔV will no longer be valid[33].

Recall that, in the ER=EPR proposal [49], entanglement between two (non-interacting) quantum systems is geometrically realized by a non-traversable wormhole (i.e. Einstein-Rosen bridge) connecting them. When the two systems are allowed to dynamically interact with each other via a quantum interaction like the double-trace deformation, a quantum teleportation protocol becomes possible and quantum information can be teleported between them through the wormhole that now becomes traversable. As pointed out in [55], this is distinct from the standard quantum teleportation protocol where only classical interactions are allowed between the two entangled systems (though see [155] for connections with standard quantum teleportation). On the one hand, this provided a concrete mechanism for recovery of quantum information via the Hayden-Preskill protocol [180] from the Hawking radiation of old black holes [152]. One the other hand, it inspired a number of experimental proposals (e.g. [157, 160]) for quantum teleportation via quantum interactions between two entangled systems[34]. Looked at from this perspective, and although our construction holds in the limit where the mulitpartite entanglement is ignored, our work is a first step toward a generalization of the quantum teleportation protocol to quantum systems with multipartite entanglement. Since the CFT state dual to a general (n, g) geometry is not known for general values of the moduli parameters, one can focus on the hot limit where locally the entanglement is mainly bipartite and is approximately a TFD state. It would be interesting to realize such a quantum state in the lab and perform the quantum teleportation protocol on it. As discussed in this work, the main new features in this case are the causal shadow region as well as the non-trivial angular dependence. It would be interesting to understand how these features are realized in an experimental set-up of quantum teleportation in the case of quantum circuits with multipartite entanglement. We expect that, in this case, the traversability protocol will occur on a mixed TFD state and that the "size" of the causal shadow region will provide an upper bound on the fidelity of the teleported state. See also [182] for a three-mouth traversable wormhole where multipartite entanglement may play a larger role.

As discussed in [152], the experience of an observer passing through a two-sided traversable wormhole is that of a smooth free fall through a low-curvature spacetime. For an observer entering a multi-boundary wormhole, the experience will be similarly pleasant only for particular angular domains. Entering the wormhole from other directions will require the observer to become trapped inside the black hole and to reach the singularity. One should thus be sure of the accuracy of one's trajectory when entering such a wormhole.

[33] For further discussion on traversable wormholes in the extremal limit, see [179].

[34] The proposal [157] was experimentally realized in [181] using an ion trap quantum computer.

There are several directions for future investigations. First, it would be interesting to extend this work to higher dimensions, where gravity is more interesting than in three dimensions. In addition, as discussed above, this work can be interpreted as a quantum teleportation circuit with multipartite entanglement as a resource. Therefore, one can extend the analysis of [157, 160, 183, 184] to this case and characterize how multipartite entanglement affects the properties and conditions of teleportation.

Chapter 4

Optomechanical Quantum Cavendish Experiment

4.1 Introduction

One of the biggest difficulties in constructing a theory of quantum gravity is the lack of experimental data. Unavailability of clean data from regimes where both quantum and gravitational effects are present have cast a long shadow on the fundamental conceptual problems that a theory of quantum gravity is expected to solve [185, 186]. Although theories of both regimes have been successfully tested to extremely high degrees in their respective domains of validity (i.e. large distances and massive bodies for general relativity versus short distances and small masses for quantum mechanics), the disparities between them, which stem from the weakness of gravity and decoherence of quantum states, have led to the yet-unsurmounted task of designing experiments that can access regimes where both theories predict effects of comparable degrees of observability. These experiments are of two types: 1) those where the goal is to construct a measurement apparatus with increased sensitivity to provide information about cosmological and astrophysical phenomena, or 2) experiments where both the source of observations and the measurement apparatus need to be constructed. The first type include observations of the primordial cosmic microwave background (CMB) for information about the very early universe (i.e. a rare example of a natural quantum gravity regime), and sensitive detection of gravitational waves from black holes mergers as a possible source of information about the quantum degrees of freedom inside black holes [187]. The second type was first proposed by Feynman [188], where he suggested putting a massive object in superposition to test whether its gravitational field

can also be put in superposition (i.e. is quantum in nature) or whether a gravity-induced collapse of the wavefunction would prevent this from happening.

While a direct detection of the graviton (i.e. the quantum particle that mediates the force of gravity) remains out of technological reach, there has been several proposals of low-energy table-top experiments aiming at testing the effects of gravity in quantum regimes. Milestone experiments include observing gravity-induced phase shifts in the wavefunction of neutrons in a vertical interferometer [189], measuring the gravitational acceleration using free-falling atoms [190], and observing quantum bound states of neutrons induced by Earth's gravitational field [191]. However, classical (Newtonian) gravity is sufficient to interpret these experiments. Recently, several experimental proposals were put forward to prove the quantum nature of gravity in table-top experiments. For example, the set-ups of [192, 193, 194] aim at generating and detecting gravity-induced entanglement between two masses, which is argued to be a witness to the quantum nature of gravity. Other proposals were given that aim to generate a superposition state of the gravitational field of test masses [195, 196, 197]. While these proposals do not probe Planck scale physics, they are important in expanding our experimental tools to regimes where gravity exhibits quantum behaviour.

Optomechanics is the experimental field of using light to prepare quantum states of mechanical oscillators. Advances in optomechanics [198] and atom interferometry [199] have made the possibility of measuring the effects of gravity in table-top quantum systems closer than ever. Proposals to observe the effects predicted by models of gravity that modify quantum mechanics, such as gravitational decoherence models [200, 201, 202], in optomechanical settings have been considered before [203].

In this chapter, we propose an experiment that probe the mutual gravitational interaction between two quantum systems. In particular, we investigate the question: given the gravitational interaction between two quantized systems in superposition, how can we experimentally observe the effects of this interaction? To this end we propose an optomechanical set-up to observe the effect of the gravitational interaction between two quantum micro-mechanical oscillators. A set-up involving superposing mirrors of order 10^{14} atoms was proposed in [202], and its application in observing the effects of gravitational decoherence models was considered in [204]. Here, we assume that the (quantum) gravitational interaction term is given by $G_N Mm/|\hat{r}_1 - \hat{r}_2|$, where $\hat{r}_1$ and $\hat{r}_2$ are position operators of the gravitating masses, and perturbatively calculate its effect on the visibility pattern of interfering photons in an optomechanical set-up. We find that the gravitational coupling leads to a shift in the period and magnitude of the visibility of photons whose observability is within reach of today's technologies.

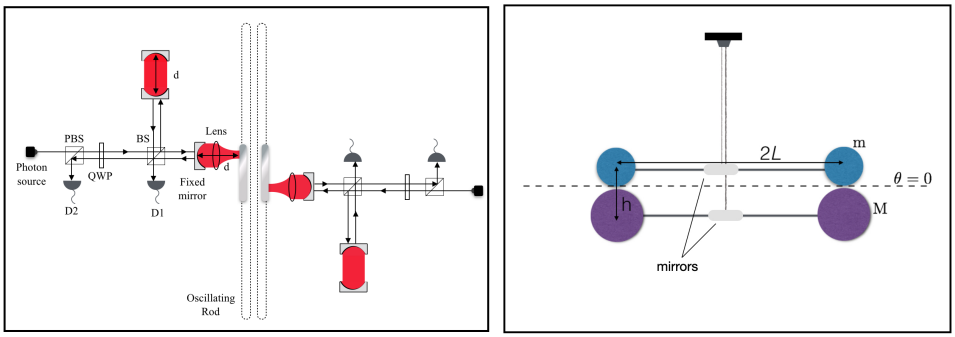

(a) upper-view of the set-up (b) front-view of the oscillators

Figure 4.1: The proposed set-up consists of two freely-moving angular oscillators suspended with vertical displacement h between them, and moving angularly in the horizontal plane to which they are fixed, as shown in (b). At the centre of each oscillator is a mirror that forms the oscillating part of a cavity system, whose other part is a fixed mirror at distance d away. A focusing lens is used to reduce leakage of cavity photons due to reflections from angularly oscillating mirrors. Photons with high radiation pressure are put in a superposition of either entering the cavity with the movable end mirror or an empty cavity with the same unperturbed length. The beams exiting each cavity are then recombined and the resulting visibility pattern analysed, as in shown in (a).

The chapter is organized as follows: In section 4.2, we discuss the set-up to be used to search for the model's signatures, the parameters that will optimize between their strengths and experimental feasibility, as well as the nature and magnitude of the signatures. In section 4.3, we discuss the requirements to deal with environmental decoherence and systematic errors, comment on the gravity-induced entanglement between the oscillators, and sum up our conclusions.

4.2 Experimental proposal

Figure 4.1 shows the experimental set-up. It consists of a mechanical component (figure 4.1b) formed by two oscillating rods with masses $2M$ and $2m$, as well as an optical component (figure 4.1a). For the mechanical component, two micro-rods of length $2L$ each are suspended from their centre with a relative vertical separation h. Masses are fixed at the end of each rod and mirrors are attached to its centre. Each oscillating mirror will form one side of a high-finesse optical cavity.

The optical component of the experiment has two similar parts, one for each of the oscillating mirrors. Each part follows the scheme of [205], which makes use of a Michelson interferometer to prepare a microscopic oscillator in a superposed state. For each part, an input pulse will be generated using a high-radiation pressure photon source. The input pulse will be split using a beam splitter into two paths, one going into the cavity with the movable end mirror attached to the oscillating rod while the other passes through an empty cavity. A lens will be placed in the oscillator cavity to focus the incoming beam onto an edge of the mirror, so that the time needed to cross the length of the cavity is much smaller than the period of the rod. Individually, the visibility pattern of the photon from each part of the set-up can reveal that the associated mirror is in a superposed state, as explained in [205]. However, the gravitational interaction between the two oscillating rods will lead to a shift in the visibility patterns observed.

4.2.1 The cavity Hamiltonian

The Hamiltonian describing the interaction between the cavity modes with the mirrors is given by [206]

$$\begin{aligned} H_1 = {} & \hbar\omega_c(c_1^\dagger c_1 + c_2^\dagger c_2) + \hbar\Omega_a a^\dagger a - \Lambda_m \hbar\Omega_a c_1^\dagger c_1 (a^\dagger + a) \\ & + \hbar\omega_d(d_1^\dagger d_1 + d_2^\dagger d_2) + \hbar\Omega_b b^\dagger b - \Lambda_M \hbar\Omega_b d_1^\dagger d_1 (b^\dagger + b) \end{aligned} \tag{4.1}$$

where a and $a^\dagger$ (respectively b and $b^\dagger$) are the creation and annihilation operators of the mechanical modes of rod m (M), c_1 and $c_1^\dagger$ (d_1 and $d_1^\dagger$) are the creation and annihilation operators of photons in the path entering the cavity containing the mirror attached on rod m (M) while c_2 and $c_2^\dagger$ (d_2 and $d_2^\dagger$) are those of photons in the path not entering the oscillator cavity. In addition, ω_c and ω_d are the frequencies of the two input pulses, Ω_a and Ω_b are the natural frequencies of the two rods of masses m and M, respectively, and

$$\Lambda_m = \frac{\omega_c}{2d\,\Omega_a}\sqrt{\frac{\hbar}{m\Omega_a}} \quad \text{and} \quad \Lambda_M = \frac{\omega_d}{2d\,\Omega_b}\sqrt{\frac{\hbar}{M\Omega_b}} \tag{4.2}$$

are the optomechanical coupling constants [205]. Note that the coupling between the mechanical oscillator and cavity photons (third and sixth terms in (4.1)) represent external and parametric driving of the oscillator by the cavity photons so that cavity photons can create phonon excitations in the oscillator. The rods are assumed initially to be in coherent oscillatory states

$$|\beta_j\rangle = \sum_{n=0}^{\infty} \frac{\beta_j^n}{\sqrt{n!}} |n\rangle\,, \quad j \in \{m, M\}, \tag{4.3}$$

where $|n\rangle$ are the Fock eigenstates of the harmonic oscillator. The initial state of the total system is

$$|\psi(0)\rangle = \frac{1}{\sqrt{2}}\left(|0,1\rangle_c + |1,0\rangle_c\right)|\beta_m\rangle \otimes \frac{1}{\sqrt{2}}\left(|0,1\rangle_d + |1,0\rangle_d\right)|\beta_M\rangle \tag{4.4}$$

where $|1,0\rangle_\chi = \chi_1^\dagger|0\rangle$, $|0,1\rangle_\chi = \chi_2^\dagger|0\rangle$ for $\chi = c,d$ and where $|0\rangle$ is the vacuum state of the cavity modes. The evolution of the combined oscillator-cavity system was analyzed in [207], where it was found that, under the action of H_1 (without gravitational interaction), the state $|\psi(0)\rangle$ evolves according to

$$\begin{aligned}|\psi(t)\rangle &= e^{-iH_1 t}|\psi(0)\rangle \\ &= \frac{e^{-i\omega_c t}}{\sqrt{2}}\left(|0,1\rangle_c|\Phi_{0,m}(t)\rangle + e^{i\phi_m(t)}|1,0\rangle_c|\Phi_{1,m}(t)\rangle\right) \\ &\otimes \frac{e^{-i\omega_d t}}{\sqrt{2}}\left(|0,1\rangle_d|\Phi_{0,M}(t)\rangle + e^{i\phi_M(t)}|1,0\rangle_d|\Phi_{1,M}(t)\rangle\right)\end{aligned} \tag{4.5}$$

where

$$\begin{aligned}\Phi_{0,j}(t) &= \beta_j e^{-i\Omega_k t}, \\ \Phi_{1,j}(t) &= \beta_j e^{-i\Omega_k t} + \Lambda_j(1 - e^{-i\Omega_k t}), \\ \phi_j(t) &= \Lambda_j^2(\Omega_k t - \sin\Omega_k t) + \Lambda_j \mathrm{Im}[\beta_j(1 - e^{-i\Omega_k t})],\end{aligned} \tag{4.6}$$

and $(j,k) \in \{(m,a),(M,b)\}$. The interferometric visibility pattern is directly measurable from the statistics of photon detection and, therefore, it provides an important source of information about the cavity system. The visibility is given by twice the absolute value of one of the off-diagonal terms in the photon density matrix so that, for instance, if ρ_c is the reduced density matrix of the cavity photons coupled to rod m then $\mathcal{V}_{0,c}(t) = 2\,|\mathrm{Tr}[\rho_{0,c}(t)\,|0,1\rangle_c\,\langle 1,0|_c]|$. If the system evolves only according to H_1, then the visibility pattern of the photons in the two cavity systems will be

$$\begin{aligned}\mathcal{V}_{0,c}(t) &= e^{-\Lambda_m^2(1-\cos\Omega_a t)}, \\ \mathcal{V}_{0,d}(t) &= e^{-\Lambda_M^2(1-\cos\Omega_b t)}.\end{aligned} \tag{4.7}$$

The visibility is a measure of the distinguishability of photons in the two interfering paths. The result (4.7) shows the independence of each cavity system from the other, and that

the timescale of oscillation of the visibility pattern is set by the frequency of the oscillating rod. At the beginning, the photons are maximally indistinguishable (i.e. the visibility is maximum). The minimum visibility point occurs when the oscillator is at its maximum extension. At the end of each period, the visibility returns to its maximum value. As will be shown below, this behaviour is changed when the gravitational interaction between the rods and environmental decoherence are taken into account.

4.2.2 The gravitational interaction

Our set-up is designed so as to maximize the effect of the gravitational interaction between the two oscillators. Below, we will derive the total Hamiltonian of the system. First, note that two classical harmonic oscillators will couple via gravity according to

$$H = \frac{p_m^2}{2m} + \frac{1}{2} I_m \Omega_a^2 \theta_m^2 + \frac{p_M^2}{2M} + \frac{1}{2} I_M \Omega_b^2 \theta_M^2 + H_g \tag{4.8}$$

where $I_m = 2mL^2$ and $I_M = 2ML^2$ are the two moments of inertia for the two rods. For two angular oscillators with masses at each end of a rod of length L and suspended with vertical displacement h, the classical gravitational interaction will be

$$\begin{aligned} H_g &= 2\frac{-G_N M m}{\left(h^2 + (2L\sin(\frac{\theta_M - \theta_m}{2}))^2\right)^{1/2}} \\ &\approx 2\frac{-G_N M m}{h\left(1 + (L(\theta_M - \theta_m)/h)^2\right)^{1/2}} \\ &\approx 2\frac{-G_N M m}{h}\left(1 - \frac{1}{2}(\frac{L(\theta_M - \theta_m)}{h})^2\right) \\ &= \frac{-2G_N M m}{h} + \frac{G_N M m}{h^3}(L(\theta_M - \theta_m))^2 \\ &= \frac{-2G_N M m}{h} + \frac{G_N M m L^2}{h^3}\left(\theta_M^2 + \theta_m^2 - \theta_M\theta_m - \theta_m\theta_M\right). \end{aligned} \tag{4.9}$$

Therefore, up to a constant term, the total Hamiltonian can be written as

$$H = \frac{p_m^2}{2m} + \frac{1}{2} m\omega_a^2 \theta_m^2 + \frac{p_M^2}{2M} + \frac{1}{2} M\omega_b^2 \theta_M^2 - \frac{2G_N M m L^2}{h^3}\theta_m\theta_M \tag{4.10}$$

where $\omega_a = \sqrt{\Omega_a^2 + \frac{G_N M}{h^3}}$ and $\omega_b = \sqrt{\Omega_b^2 + \frac{G_N m}{h^3}}$. The frequency of a photon inside a cavity of length d is

$$\omega_c = 2\pi\frac{n}{2d} = \frac{n\pi}{d} \tag{4.11}$$

where $n = 1, 2, 3, \ldots$. When it couples to an angular oscillator with displacement θ, the length of the cavity varies $d \to d + \delta$ for $\delta << d$, so that[35]

$$\omega_c = \frac{n\pi}{d+\delta} = \frac{n\pi}{d(1+\delta/d)} \approx \frac{n\pi}{d}(1 - \delta/d). \tag{4.12}$$

In our case, $\delta = L\sin\theta \approx L\theta$. So,

$$\omega_c \to \omega_c - \omega_c \frac{L\theta}{d}. \tag{4.13}$$

Introducing the annihilation operators for the two oscillators

$$a = \sqrt{\frac{I_m\omega_a}{2\hbar}}\left(\theta_m + \frac{i}{I_m\omega_a}p_m\right), \tag{4.14}$$

$$b = \sqrt{\frac{I_M\omega_b}{2\hbar}}\left(\theta_M + \frac{i}{I_M\omega_b}p_M\right) \tag{4.15}$$

and substituting back in the total Hamiltonian to rewrite it in terms of the creation/annihilation operators, including the photon cavity terms gives the quantized Hamiltonian of the total system as

$$\begin{aligned} H = {} & \hbar\omega_c(c_1^\dagger c_1 + c_2^\dagger c_2) + \hbar\omega_a a^\dagger a - \lambda_m\hbar\omega_a c_1^\dagger c_1(a^\dagger + a) \\ & + \hbar\omega_d(d_1^\dagger d_1 + d_2^\dagger d_2) + \hbar\omega_b b^\dagger b - \lambda_M\hbar\omega_b d_1^\dagger d_1(b^\dagger + b) \\ & + \hbar\gamma(a^\dagger + a)(b^\dagger + b) \end{aligned} \tag{4.16}$$

where

$$\gamma := -\frac{G_N}{2h^3}\sqrt{\frac{Mm}{\omega_a\omega_b}} \tag{4.17}$$

is the gravitational coupling constant between the two oscillators. Below, we will denote

$$H_g := \hbar\gamma(a^\dagger + a)(b^\dagger + b), \tag{4.18}$$

and H_0 is the first two lines of (4.16). We note also that the frequencies of the oscillators and the optomechanical coupling constant are modified from the old Hamiltonian in (4.1) due to the gravitational interaction according to

$$\Omega_a \to \omega_a = \sqrt{\Omega_a^2 + \frac{G_N M}{h^3}}, \qquad \Omega_b \to \omega_b = \sqrt{\Omega_b^2 + \frac{G_N m}{h^3}}, \tag{4.19}$$

$$\Lambda_m \to \lambda_m = \frac{\omega_c}{2\omega_a d}\sqrt{\frac{\hbar}{m\omega_a}}, \qquad \Lambda_M \to \lambda_M = \frac{\omega_d}{2\omega_b d}\sqrt{\frac{\hbar}{M\omega_b}}. \tag{4.20}$$

[35]The linear expansion corresponds to the adiabatic approximation of the oscillator-cavity system in which phonons of the oscillator cannot excite photons in the cavity.

4.2.3 The shift in visibility

The visibility pattern of photons in the gravitationally coupled system will be different from that of the uncoupled system given in (4.7). To calculate this shift, we switch to the interaction picture in which the density matrix of the total system is

$$\rho_I(t) = U(t)\rho_I(0)U^\dagger(t) \tag{4.21}$$

where $\rho_I(0) = |\psi(0)\rangle \langle\psi(0)|$, and

$$U(t) = \mathcal{T} \exp\left[-\frac{i}{\hbar}\int_0^t dt' H_I(t')\right], \tag{4.22}$$

with $\mathcal{T}$ being the time-ordering operator. To derive the form of the interaction Hamiltonian $H_I(t) = e^{iH_0t/\hbar}H_g e^{-iH_0t/\hbar}$, recall from the BHC formula that, given operators A and B, we have

$$e^A B e^{-A} = B + [A, B] + \frac{1}{2}[A, [A, B]] + \ldots. \tag{4.23}$$

The operator $e^{-iH_0t/\hbar}$ was calculated to be [208]

$$\begin{aligned} e^{-iH_0t/\hbar} &= e^{-i\omega_c t(c_1^+c_1 + c_2^+c_2)} e^{i(\lambda_m c_1^+c_1)^2(\omega_a t - \sin(\omega_a t))} \\ &\quad \times e^{\lambda_m c_1^+c_1\left(a^+\alpha - a\alpha^*\right)} e^{-i\omega_a t a^+a} \times [M], \end{aligned} \tag{4.24}$$

where $\alpha = (1 - e^{-i\omega_a t})$, and $[M]$ here and below denotes the same part of the term as on its left but under the isomorphic transformations

$$\begin{gathered} (.)_{a,c,m} \to (.)_{b,d,M}, \\ a, c \to b, d. \end{gathered}$$

Using the BHC formula, the interaction Hamiltonian is

$$\begin{aligned} H_I(t) &= e^{iH_0t/\hbar}H_g e^{-iH_0t/\hbar} \\ &= e^{iH_0t/\hbar}\hbar\gamma(a^\dagger + a)(b^\dagger + b)e^{-iH_0t/\hbar} \\ &= \hbar\gamma e^{i\omega_a t a^\dagger a} e^{\lambda_m c_1^\dagger c_1(a\alpha^* - a^\dagger\alpha)}(a^\dagger + a) \\ &\quad e^{-\lambda_m c_1^\dagger c_1(a\alpha^* - a^\dagger\alpha)} e^{-i\omega_a t a^\dagger a} \times [M] \\ &= \hbar\gamma e^{i\omega_a t a^\dagger a}(a^\dagger + a + \lambda_m c_1^\dagger c_1(\alpha + \alpha^*))e^{-i\omega_a t a^\dagger a} \times [M] \\ &= \hbar\gamma(a^\dagger e^{i\omega_a t} + a e^{-i\omega_a t} + \lambda_m c_1^\dagger c_1(\alpha + \alpha^*)) \times [M] \\ &= \hbar\gamma(a^\dagger e^{i\omega_a t} + a e^{-i\omega_a t} + 2\lambda_m c_1^\dagger c_1(1 - \cos\omega_a t)) \times [M] \\ &= \hbar\gamma(a^\dagger e^{i\omega_a t} + a e^{-i\omega_a t} + 2\lambda_m c_1^\dagger c_1(1 - \cos\omega_a t)) \\ &\quad \times (b^\dagger e^{i\omega_b t} + b e^{-i\omega_b t} + 2\lambda_M d_1^\dagger d_1(1 - \cos\omega_b t)). \end{aligned} \tag{4.25}$$

The expectation value of any operator $\mathcal{O}$ is independent of the picture used to calculate it. In the interaction picture, this is equal to

$$\begin{aligned}\langle \mathcal{O}(t)\rangle &= \mathrm{Tr}[\rho_I(t)\mathcal{O}_I(t)] \\ &= \mathrm{Tr}[U(t)\rho_I(0)U^\dagger(t)e^{iH_0t/\hbar}\mathcal{O}_S e^{-iH_0t/\hbar}] \\ &= \mathrm{Tr}[e^{-iH_0t/\hbar}U(t)\rho_I(0)U^\dagger(t)e^{iH_0t/\hbar}\mathcal{O}_S] \end{aligned} \tag{4.26}$$

where $\mathcal{O}_S$ is the operator in the Schrodinger picture.

The visibility of photons in the cavity of rod m due to the full Hamiltonian is therefore

$$\mathcal{V}_{1,c}(t) = 2\left|\mathrm{Tr}[\rho_{1,c}(t)\left|0,1\right\rangle_c\left\langle 1,0\right|_c]\right|, \tag{4.27}$$

where

$$\rho_{1,c}(t) = \mathrm{Tr}_{m,M,d}\left[e^{-iH_0t/\hbar}U(t)\rho_I(0)U^\dagger(t)e^{iH_0t/\hbar}\right] \tag{4.28}$$

is the partial state of the photons in the cavity of rod m in the Schrodinger picture after tracing out the two oscillators and the photons in the cavity of rod M. To calculate the visibility from (4.28), we need to determine the action of $e^{-iH_0t\hbar}U(t)$ on $\rho_I(0)$. First, note that

$$\begin{aligned} e^{-iH_0t/\hbar}a^\dagger &= e^{-iH_0t/\hbar}a^\dagger e^{iH_0t/\hbar}e^{-iH_0t/\hbar} \\ &= e^{-\lambda_m c_1^\dagger c_1(a\alpha^*-a^\dagger\alpha)}e^{-i\omega_a t a^\dagger a}a^\dagger e^{i\omega_a t a^\dagger a}e^{\lambda_m c_1^\dagger c_1(a\alpha^*-a^\dagger\alpha)}e^{-iH_0t/\hbar} \\ &= e^{-\lambda_m c_1^\dagger c_1(a\alpha^*-a^\dagger\alpha)}a^\dagger e^{-i\omega_a t}e^{\lambda_m c_1^\dagger c_1(a\alpha^*-a^\dagger\alpha)}e^{-iH_0t/\hbar} \\ &= (a^\dagger - \lambda_m c_1^\dagger c_1\alpha^*)e^{-i\omega_a t}e^{-iH_0t/\hbar} \end{aligned} \tag{4.29}$$

and, similarly

$$e^{-iH_0t/\hbar}a = (a - \lambda_m c_1^\dagger c_1\alpha)e^{i\omega_a t}e^{-iH_0t/\hbar}. \tag{4.30}$$

This allows us to write, using the BHC formula, up to first-order in γ

$$
\begin{aligned}
e^{-iH_0t/\hbar}U(t) &\approx e^{-iH_0t/\hbar}\left(1-\frac{i}{\hbar}\int_0^t dt' H_I(t')\right)\\
&= e^{-iH_0t/\hbar}\left(1-i\gamma\int_0^t dt'(a^\dagger e^{i\omega_a t'}+ae^{-i\omega_a t'}+2\lambda_m c_1^\dagger c_1(1-\cos\omega_a t'))\times[M]\right)\\
&= e^{-iH_0t/\hbar}-\frac{i\gamma}{\hbar}\int_0^t dt'\Big((a^\dagger-\lambda_m c_1^\dagger c_1\alpha^*)e^{i\omega_a(t'-t)}+(a-\lambda_m c_1^\dagger c_1\alpha)e^{-i\omega_a(t'-t)}\\
&+2\lambda_m c_1^\dagger c_1(1-\cos\omega_a t')\Big)\times[M]e^{-iH_0t/\hbar}\\
&= 1-\frac{i\gamma}{\hbar}\int_0^t dt'\Big(a^\dagger e^{i\omega_a(t'-t)}+ae^{-i\omega_a(t'-t)}\\
&+\lambda_m c_1^\dagger c_1(2-2\cos\omega_a t'-\alpha^* e^{i\omega_a(t'-t)}-\alpha e^{-i\omega_a(t'-t)})\Big)\times[M]e^{-iH_0t/\hbar}\\
&= 1-\frac{i\gamma}{\hbar}\int_0^t dt'\Big(a^\dagger e^{i\omega_a(t'-t)}+ae^{-i\omega_a(t'-t)}\\
&+\lambda_m c_1^\dagger c_1(2-2\cos\omega_a t'-2\cos\omega_a(t'-t)+2\cos\omega_a t')\Big)\times[M]e^{-iH_0t/\hbar}\\
&= 1-\frac{i\gamma}{\hbar}\int_0^t dt'\Big(a^\dagger e^{i\omega_a(t'-t)}+ae^{-i\omega_a(t'-t)}+2\lambda_m c_1^\dagger c_1(1-\cos\omega_a(t'-t))\Big)\times[M]e^{-iH_0t/\hbar}.
\end{aligned}
\tag{4.31}
$$

Using this relation, we can calculate the action of this operator on the initial state $|\psi(0)\rangle_I$ of the total system given in (4.5) perturbatively to be

$$
\begin{aligned}
e^{-iH_0t/\hbar}U(t)\,|\psi(0)\rangle_I &= |\psi(t)\rangle-\frac{i\gamma}{\hbar}\int_0^t dt'(a^\dagger e^{i\omega_a(t'-t)}+ae^{-i\omega_a(t'-t)}\\
&+2\lambda_m c_1^\dagger c_1(1-\cos\omega_a(t'-t)))\times[M]\,|\psi(t)\rangle\\
&= |\psi(t)\rangle-\frac{i\gamma}{\hbar}\int_0^t dt'(a^\dagger e^{i\omega_a(t'-t)}+ae^{-i\omega_a(t'-t)}+2\lambda_m c_1^\dagger c_1(1-\cos\omega_a(t'-t)))\\
&(b^\dagger e^{i\omega_b(t'-t)}+be^{-i\omega_b(t'-t)}+2\lambda_M d_1^\dagger d_1(1-\cos\omega_b(t'-t)))\,|\psi(t)\rangle
\end{aligned}
$$

$$
\begin{aligned}
&= \frac{e^{-i\omega_c t - i\omega_d t}}{2}\,[\,\left(1 - \frac{i\gamma}{\hbar}\int_0^t dt'(a^\dagger e^{i\omega_a(t'-t)} + \Phi_{0,m}(t)e^{-i\omega_a(t'-t)})\right.\\
&\left.(b^\dagger e^{i\omega_b(t'-t)} + \Phi_{0,M}(t)e^{-i\omega_b(t'-t)})\right)\\
&|0,1\rangle_c\,|0,1\rangle_d\,|\Phi_{0,m}\rangle\,|\Phi_{0,M}\rangle\\
&+\left(1 - \frac{i\gamma}{\hbar}\int_0^t dt'(a^\dagger e^{i\omega_a(t'-t)} + \Phi_{0,m}(t)e^{-i\omega_a(t'-t)})\right.\\
&\left.(b^\dagger e^{i\omega_b(t'-t)} + \Phi_{1,M}(t)e^{-i\omega_b(t'-t)} + 2\lambda_M(1-\cos\omega_b(t'-t)))\right)\\
&e^{i\phi_M(t)}\,|0,1\rangle_c\,|1,0\rangle_d\,|\Phi_{0,m}\rangle\,|\Phi_{1,M}\rangle\\
&+\left(1 - \frac{i\gamma}{\hbar}\int_0^t dt'(a^\dagger e^{i\omega_a(t'-t)} + \Phi_{1,m}(t) + 2\lambda_m(1-\cos\omega_a(t'-t)))\right.\\
&\left.(b^\dagger e^{i\omega_b(t'-t)} + \Phi_{0,M}(t)e^{-i\omega_b(t'-t)})\right)\\
&e^{i\phi_m(t)}\,|1,0\rangle_c\,|0,1\rangle_d\,|\Phi_{1,m}\rangle\,|\Phi_{0,M}\rangle\\
&+\left(1 - \frac{i\gamma}{\hbar}\int_0^t dt'(a^\dagger e^{i\omega_a(t'-t)} + \Phi_{1,m}(t)e^{-i\omega_a(t'-t)+2\lambda_m(1-\cos\omega_a(t'-t))})\right.\\
&\left.(b^\dagger e^{i\omega_b(t'-t)} + \Phi_{1,M}(t)e^{-i\omega_b(t'-t)} + 2\lambda_M(1-\cos\omega_b(t'-t)))\right)\\
&e^{i\phi_m(t)}e^{i\phi_M(t)}\,|1,0\rangle_c\,|1,0\rangle_d\,|\Phi_{1,m}\rangle\,|\Phi_{1,M}\rangle].
\end{aligned}
\tag{4.32}
$$

Tracing out the two oscillators and the photons in the cavity of rod M from the density matrix formed by this state, keeping terms only to order $\mathcal{O}(\gamma)$, and calculating twice the absolute value of one of the off-diagonal terms gives the visibility (4.27) of photons in the cavity of rod m to be

$$
\begin{aligned}
\mathcal{V}_{1,c}(t) &\approx e^{-\lambda_m^2(1-\cos\omega_a t)} \times \left|1 + i2\gamma\int_0^t dt'\lambda_m(1-\cos\omega_a(t'-t)) \times (2\beta_M\cos\omega_b t' + \lambda_M(1-\cos\omega_b t'))\right|\\
&= e^{-\lambda_m^2(1-\cos\omega_a t)} \times \left|1 + i2\gamma\lambda_m[(2\beta_M - \lambda_M)(\frac{\sin\omega_b t}{\omega_b} - \frac{\omega_a\sin\omega_a t - \omega_b\sin\omega_b t}{\omega_a^2-\omega_b^2}) + \lambda_M(t - \frac{\sin\omega_a t}{\omega_a})]\right|.
\end{aligned}
\tag{4.33}
$$

Quantum optomechanics allows coherent quantum control over mechanical objects ranging from nano-sized devices of 10^{-20} kg, to micro-mechanical structures of masses 10^{-11} kg, up to centimeter-sized suspended mirrors of several kilograms in mass for gravitational wave detectors [198]. Early breakthroughs in quantum optomechanics were with 10^{-16} kg masses [209, 210], followed recently by room-temperature regimes with masses around 10^{-12} kg [211], and proposals for future experiments reaching 10^{-6} kg masses [212].

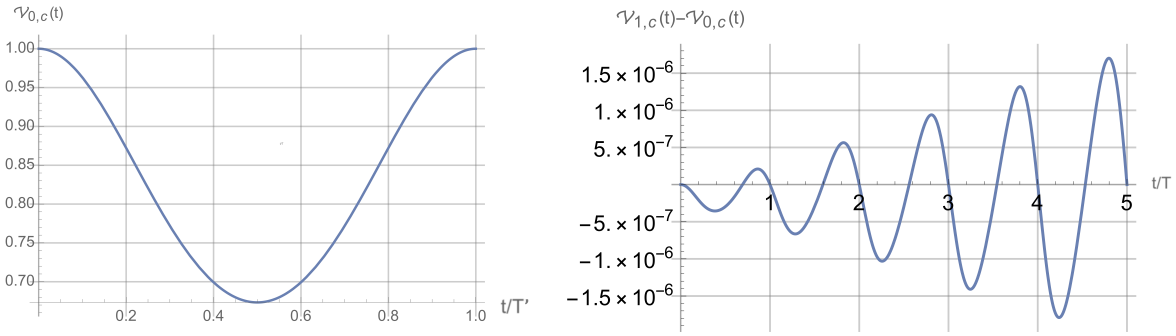

(a) (b)

Figure 4.2: (a) The visibility pattern of the photon field in the cavity system of rod m before coupling it to rod M, showing periodic behaviour whose period is determined by that of the oscillator $T' = 2\pi/\Omega_a$ and the strength of its drop at every period depends on the optomechanical coupling between the rod and the photon field. (b) The shift in the magnitude of visibility from the case with no gravitational coupling as a function of time due to the combined effect of the modified period of the oscillator, $2\pi/\Omega_a \to 2\pi/\omega_a = T$, and the action of the coupled Hamiltonian on the state of the system, as calculated perturbatively in (4.33).

We assume the masses attached to the end of the rods to be micro-mechanical structures with masses $M = m = 10^{-13}$ kg and to be separated by a vertical distance $h = 10^{-8}$ m, each mounted on an oscillator with frequencies $\Omega_a = 3 \times 10^3$ Hz, and $\Omega_b = \alpha\Omega_a$ for $\alpha = 0.9$. The oscillators are assumed to be cooled down to near their ground states so that $\beta_M = \beta_m = 1$. We propose to use light of frequency $\omega_c = \omega_d = 450 \times 10^{12}$ Hz in both cavities, each with cavity length $d = 10$ cm.

The pre-coupling visibility pattern $\mathcal{V}_{0,c}(t)$ and the shift in visibility induced by the gravitational interaction $\mathcal{V}_{1,c}(t) - \mathcal{V}_{0,c}(t)$ for photons of the cavity system of m are both shown in figure 4.2. In figure 4.2a, we see that the visibility pattern of cavity photons in the non-interacting system has the same period $2\pi/\Omega_a$ as the oscillator, and at half that period it reaches its minimum point at $e^{-2\Lambda_m^2}$. The drop in visibility in the middle of the period is because oscillations of the rod contain which-path information about the position of the superposed photons, dependent on the coupling strength λ_m between the photon field and the oscillator. When the oscillator returns to its original position after a full period of oscillation, this which-path information is deleted and the visibility is restored to its original value.

Figure 4.2b shows the shift in visibility as a function of time when the two oscillators are

coupled to each other via gravity. The sources of this shift are twofold. The first is due to the difference in frequencies between the coupled oscillators and their idealized uncoupled state. This is observable as a shift in the frequency of the visibility pattern of photons of magnitude $\omega_k - \Omega_k \approx \frac{G_N M m}{2jh^3\Omega_k} \sim \mathcal{O}(\gamma)$, for $(j,k) \in \{(m,a),(M,b)\}$. The second kind of shift is due to the second term in (4.33), which oscillates around $(\gamma\lambda_m\lambda_M)^2 t^2 \sim \mathcal{O}(\gamma^2)$ and is observable as a growing variation in the shape of the visibility pattern from the one in $\mathcal{V}_{0,c}(t)$. Recall also that λ_M is the coupling parameter between the mirror in the cavity of rod M and its cavity mode. From (4.33), we see that when this coupling is turned off ($\lambda_M = 0$), the shift in visibility is still that of figure 4.2b for small times. However the effect of the coupling is an increase in the shift with time due to the $\lambda_M(t - \frac{\sin(\omega_a t)}{\omega_a})$ term in (4.33). The linear behaviour of the shift in visibility with t is predicted from perturbation theory for time scales below $\gamma^{-1} \sim 853$ s for the parameters used above. Maintaining the coherence of the state for long enough times will therefore lead to more observable effects.

4.3 Discussion

4.3.1 Decoherence and systematic errors

In practice, due to environmental effects, an oscillator will be in a thermal mixture of coherent states $|\beta\rangle\langle\beta|$[36]

$$\frac{1}{\pi\bar{n}} \int d^2\beta e^{-|\beta|^2/\bar{n}} |\beta\rangle\langle\beta| \tag{4.34}$$

where $\bar{n} = (e^{\hbar\omega_a/k_B T} - 1)^{-1}$ is the mean thermal number of phonon excitations at temperature T and oscillator frequency ω_a. This will modify the visibility according to [205]

$$e^{-\lambda_m^2(1-\cos\omega_a t)} \to e^{-\lambda_m^2(2\bar{n}+1)(1-\cos\omega_a t)} \tag{4.35}$$

which causes a fast decay in visibility that is revived only after a full period. Note that $\bar{n}$ depends on the ratio between the frequency of the oscillator ω_a and the average frequency of thermal excitations $k_B T/\hbar$ (i.e. $\bar{n}$ decreases when this ratio increases, as expected). The width of the visibility's revived peak scales according to $\sim \frac{1}{\lambda_m\sqrt{\frac{4k_B T}{\hbar\omega_a}+2}}$. Increasing this width constitutes one of the main experimental challenges to realize this proposal, and requires a method to cool down the centre of mass mode of the oscillator to very near

[36]Note that, in general, β is a complex number. So, if we write $\beta = |\beta|e^{i\theta}$, then $d^2\beta = d|\beta|d\theta$. Furthermore, $|\beta|^2 = n$ is the average phonon number of the oscillator.

their ground state [213]. Another experimental challenge is due to decoherence from the mechanical damping of the oscillator and from dephasing with the environment, which lowers the revived peak of visibility. In order to observe the shift in the period of the oscillators, we need at least to be able to resolve one full period of the oscillation. If the environment is modelled as an Ohmic thermal bath of harmonic oscillators and the damping rate of oscillators is Γ_a, then the dephasing rate due to the environment at temperature T is $\Gamma_D = \Gamma_a k_B T m (\Delta x)^2/\hbar^2$, where $\Delta x \sim \sqrt{\frac{\hbar}{m\omega_a}}$ is the uncertainty in position of the oscillator [202, 214]. The condition for observing the shift in the period mentioned above is then $\Gamma_D \lesssim \omega_a$, which corresponds to

$$Q \gtrsim \frac{k_B T}{\hbar \omega_a} \sim \bar{n} \tag{4.36}$$

where $Q := \omega_a/\Gamma_a$ is the quality factor of the oscillator. Values of $Q \sim 10^7$ have been achieved for suspended nanoparticles [215], which corresponds to having $T \lesssim 0.23$ K for the parameters of the set-up considered here.

Another source of systematic errors in the set-up proposed is the effect of gravitational interaction with surrounding objects in the laboratory. If the rods are in a plane at half the height of a cylinder with all surrounding objects having a mass distribution of cylindrical symmetry, then the overall contribution would be a constant to the Hamiltonian that does not affect the dynamics described above. Earth's gravity would give an overall phase to the states of the oscillators that does not affect the photons visibility patterns. If we suppose that an inhomogeneity in the mass distribution surrounding the oscillators was due to a mass $\mathcal{M}$ located at distance $\vec{R}$ from the centre of the two rods, then this adds terms of the form $\frac{2G_N \mathcal{M} m}{|\vec{R}-\vec{r}_a|} + \frac{2G_N \mathcal{M} M}{|\vec{R}-\vec{r}_b|}$ to the classical Hamiltonian of the system, where $\vec{r}_a$ and $\vec{r}_b$ are the position vectors of the masses from the centre. Expanding these terms to first-order in distance and quantizing, this will add to the quantized Hamiltonian $-\frac{G_N \mathcal{M}}{R^2}\sqrt{\frac{\hbar m}{\omega_a}}(a^\dagger + a) - \frac{G_N \mathcal{M}}{R^2}\sqrt{\frac{\hbar M}{\omega_b}}(b^\dagger + b)$, up to constant terms. Comparing with terms proportional to $(a^\dagger + a)$ and $(b^\dagger + b)$ in (4.16), we see that the condition for this inhomogeneity to have negligible effects on the dynamics is to have $N_a \lambda_a \hbar \omega_a \gg \frac{G_N \mathcal{M}}{R^2}\sqrt{\frac{\hbar m}{\omega_a}}$, where N_a is the number of photons in the cavity associated with mass m, and N_b is the same number for mass M. For the parameters of our set-up, this correspond to $\frac{\mathcal{M}}{N_a R^2} \ll 2.2 \times 10^5 \text{kg.m}^{-2}$. Therefore, satisfying this condition means that the systematic errors due to surrounding mass distribution is negligible.[37]

[37] Environmental photons are also a major source of errors that we did not analyze in this work and can lead to more stringent conditions on the experimental parameters.

4.3.2 Entanglement generation

As mentioned in the introduction, the novel feature of our proposed scheme is the observation of effects arising from gravitationally interacting quantum systems (whereas most previous studies are for a quantum test mass in the background gravitational field of the Earth). It is also interesting to note that entanglement, albeit quite weak, is generated due to this gravitational interaction. Denoting for convenience the system associated with m system 1 (consisting of the oscillating mirror and the cavity modes) and that of M as system 2, we see that the initial state $|\psi(0)\rangle\langle\psi(0)|$ in (4.4) is separable between the two systems. Since the only coupling between systems 1 and 2 in the proposed scheme is gravity, any resulting entanglement between the two systems can be attributed to the gravitational interaction.

To quantify the amount of entanglement, we can use the linear entropy, defined as $S := 1-\mathrm{Tr}(\rho_1^2)$, where ρ_1 is the partial state of system 1. If we define $A := \frac{-1}{\gamma\hbar}\int_0^t dt' e^{-iH_0t/\hbar}H_I(t')e^{iH_0t/\hbar}$, then we note that it is Hermitian, and, from (4.29) and (4.30), it can be written as $A = \frac{-1}{\gamma\hbar}\int_0^t dt' H_I(t'-t)$. The density matrix of the two systems: system 1 for oscillator of mass m with its cavity photons and system 2 for oscillator of mass M with its cavity photons, can be written as a separable pure bi-partite state $\rho = \rho_1\otimes\rho_2 =: |\psi_1\rangle\langle\psi_1|\otimes|\psi_2\rangle\langle\psi_2|$ so that $|\psi_1\rangle|\psi_2\rangle = |\psi(t)\rangle$, as given in (4.5). Furthermore, let

$$A_1{}^2 := (\langle\psi_2|A|\psi_2\rangle)^2, \tag{4.37}$$

$$A^2{}_1 := \langle\psi_2|A^2|\psi_2\rangle. \tag{4.38}$$

If we use the BCH formula in (4.23) and calculate up to second-order in γ, then under the action of the unitary $U = e^{i\gamma A}$, the state in the Schrodinger picture evolves according to

$$\begin{aligned}\rho' &= U\rho U^\dagger \\ &= e^{i\gamma A}\rho e^{-i\gamma A} \\ &= \rho + i\gamma[A,\rho] + \frac{1}{2}[i\gamma A,[i\gamma A,\rho]] + \ldots \\ &= \rho + i\gamma[A,\rho] - \frac{\gamma^2}{2}(A^2\rho + \rho A^2 - 2A\rho A).\end{aligned} \tag{4.39}$$

Tracing out system 2 will give

$$\rho_1' = \rho_1 + i\gamma[A_1,\rho_1] - \frac{\gamma^2}{2}(A^2{}_1\rho_1 + \rho_1 A^2{}_1 - 2A_1\rho_1 A_1). \tag{4.40}$$

Squaring this and keeping terms only up to second-order in γ will give

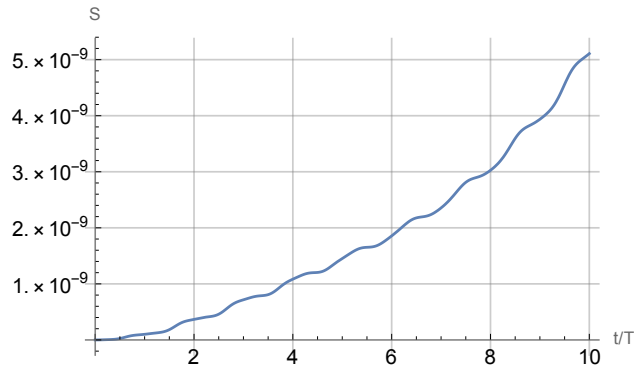

Figure 4.3: Plot of Linear Entropy, S, against t/T.

$$\rho_1'^2 = \rho_1^2 + i\gamma[A_1, \rho_1^2] - \frac{\gamma^2}{2}(2A_1\rho_1A_1\rho_1 + 2\rho_1A_1\rho_1A_1 - 2A_1\rho_1^2A_1 - 2\rho_1{A_1}^2\rho_1 + \rho_1{A^2}_1\rho_1 + \rho_1^2{A^2}_1 - 2\rho_1A_1\rho_1A_1 + {A^2}_1\rho_1^2 + \rho_1{A^2}_1\rho_1 - 2A_1\rho_1A_1\rho_1). \tag{4.41}$$

Finally, taking the trace of this gives

$$\begin{aligned}\operatorname{Tr}\rho_1'^2 &= 1 - \frac{\gamma^2}{2}(4\operatorname{Tr}({A^2}_1\rho_1) - 4\operatorname{Tr}({A_1}^2\rho_1)) \\ &= 1 - 2\gamma^2(\operatorname{Tr}({A^2}_1\rho_1) - \operatorname{Tr}({A_1}^2\rho_1))\end{aligned} \tag{4.42}$$

so that the linear entropy will now be

$$\begin{aligned}S &= 1 - \operatorname{Tr}\rho_1'^2 \\ &= 2\gamma^2(\operatorname{Tr}({A^2}_1\rho_1) - \operatorname{Tr}({A_1}^2\rho_1)).\end{aligned} \tag{4.43}$$

In figure 4.3, we plot the linear entropy for the set-up parameters considered here. Even though the amount of entanglement generated for the period shown is small, we observe an increase with time, similar to the shift in the visibility pattern. Since the visibility is related to how much which-path information the position of the oscillator can reveal, which in turn is dependent on the amount of entanglement between the oscillator and the cavity photons, the increase in the amount of entanglement due to gravity shown in figure 4.3 means that, by monogamy of entanglement, the correlations between the oscillator and the cavity photons will correspondingly decay. This causes the visibility pattern to have a growth term as given in (4.33). We expect that an exact calculation will give a linear entropy and visibility that are bounded from above.

Note that, in our calculation of linear entropy (i.e. entanglement between the two oscillators), we did not include the effects of the environment, which will lead to a reduction of this entanglement.

4.3.3 Summary

Reminiscent of the experiment done by Cavendish [216] using suspended masses to measure the gravitational interaction between them, a 'Quantum Cavendish Experiment' is one that uses suspended masses in a quantized state to detect and measure gravitational effects in quantum regimes so that the effects of Earth's gravity cancel out. Such types of experiments have been used before in sensitive verification of Newton's inverse-square law at scales below the dark energy length scale [217], and have been first incorporated in an optomechanical set-up to approach the quantum limit of mechanical sensing in [218]. Recently, such a set-up was used to measure the gravitational force of milli-gram masses [212] (see also [219]), and proposals have considered its application in testing gravitational decoherence models [220], and its implementation using optically levitated nano-dumbbells [221]. Quantization of suspended linearly moving mirrors whose dynamics is dominated by the radiation-pressure of cavity photons has been achieved with masses ranging from 40 kg [222] to milli-grams [223].

Our set-up requires forming coherent states of torsional mirrors of nanogram masses by cooling them to their ground states, surpassing the standard quantum limit of detection [224]. The suspended masses are coupled to a cavity field inside an optomechanical set-up, and the effect of the mutual gravitational interaction between the masses is calculated on the visibility pattern of cavity photons, whose observation is based on robust and well-tested experimental techniques.

We found that the effects on the visibility are of two types: a shift in the period of revival by an amount $\delta T = \frac{2\pi}{\Omega_a} - \frac{2\pi}{\omega_a}$, and a change in the shape of the visibility pattern from the functional form $e^{-\lambda_m^2(1-\cos\omega_a t)}$ that is of order $\mathcal{O}(\gamma^2)$ for time scale $t \lesssim \gamma^{-1}$. In practice, it is easier to detect δT, which corresponds to $\delta T \approx 0.78$ ns for the parameters used above, than the shift in vertical magnitude that is of order 10^{-6} in figure 4.2b.

To illustrate, suppose that the visibility at some time t is drawn from an a priori Gaussian distribution of variance σ^2. Then the error on the estimate of the visibility at time t obtained by averaging over N data points is $\sigma_{\text{error}} = \frac{\sigma}{\sqrt{N}}$. If $\sigma_{\text{error}} \sim 10^{-6}$ then $N \sim 10^{12}\sigma^2$, which is difficult to achieve. On the other hand, the accuracy of measuring δT is dependent only on the time resolution available.

Since our calculations assumed that the mechanical oscillators were in a state of superposition (i.e. their gravitational fields are in superposition), an observation of the shift in the period δT of the visibility pattern would amount to an indirect evidence that the gravitational field can exist in a state of superposition. On the other hand, this set-up can also be used to study the gravity-induced collapse models [200, 201, 202], which predicts that the wavefunction of the oscillators would collapse and that no shifts in the period δT of the visibility pattern can be observed.

We also calculated the effect of gravity-induced entanglement in the set-up, showing growth in the linear entropy between the two oscillators. Given the recent interest in observing entanglement due to gravity [192, 193, 194], it will be desirable to obtain an entanglement witness that can experimentally verify the entanglement generated for this scheme. One may also consider whether observable steady-state entanglement due to gravity may be obtained similar to other optomechanical settings, for example in [225].

Chapter 5

Measurement-Based Variational Quantum Eigensolvers

5.1 Introduction

Variational methods are crucial to investigate the physics of strongly correlated quantum systems. Numerical tools like the density matrix renormalization group [226, 227, 228, 229] have been applied to several problems including real-time dynamics [230], condensed matter physics [231], lattice gauge theories [232, 233, 234, 235], and quantum chemistry [236, 237]. Nevertheless, the classes of states that can be studied with classical computers is limited [238]. VQEs were proposed to overcome this problem using a closed feedback loop between a classical computer and a quantum processor [239, 240, 241, 242]. The classical algorithm optimizes a cost function – typically the expectation value of some operator – which is efficiently evaluated by the quantum hardware. The VQE provides an approximation to the (low-lying) eigenvalues of this operator and the corresponding eigenstates. VQEs are advantageous for a variety of applications [243, 242, 244, 245, 246, 247, 248] and have been experimentally demonstrated in fields including quantum chemistry [249, 250], particle physics [251, 252, 253, 254], and classical optimization [255, 256, 257].

Existing VQE protocols are based on the circuit model, where gates are sequentially applied on an initial state [239]. These gates involve variational parameters whose optimization allows the resulting output state to approximate the desired target state (e.g. the ground state of some Hamiltonian). This chapter describes a proposal for a new approach to VQE protocols, based on the measurement-based model of quantum computation (MBQC) [258, 259, 260, 261, 262, 263]. In MBQC, an entangled state is prepared and the

computation is realized by performing single-qubit measurements. While the circuit-based and measurement-based models both allow for universal quantum computation and have equivalent scaling of resources [261], they are intrinsically different. The circuit-based model is limited by the circuit size and the gates that can be performed, while MBQC is limited by the size of the entangled state one can prepare. Moreover, for certain applications, the required coherence times [264, 265] and error thresholds [261, 264, 266, 265] are much less demanding for MBQC.

In this chapter, we develop a new variational technique based on MBQC, that we call measurement-based VQE (MB-VQE). Our protocols determine the ground state of a target Hamiltonian, which is a prototypical task for VQEs with wide-ranging applications [240, 249, 246, 248, 267, 252, 247]. The underlying idea behind MB-VQE is to use a tailored entangled state called the 'custom state' that encodes some ansatz state and allows for exploring an appropriate corner of the system's Hilbert space (see figure 5.1a). This custom state includes auxiliary qubits which, once measured, modify the ansatz state into some output state. The choices of the measurement bases, and the corresponding variational changes to the state, are controlled by a classical optimization algorithm. This approach differs conceptually and practically from standard VQE schemes since MB-VQE shifts the challenge from performing multi-qubit gates to creating an entangled initial state, which can provide advantages for certain applications.

The chapter is organized as follows:

In section 5.2, we start by giving a brief review of MBQC. Then, we present the framework for the MB-VQE developed for two specific schemes that are suited to different problem classes.

In section 5.3, we introduce the first scheme: a direct translation of circuit-based VQEs to MB-VQEs (see figure 5.1b). Here, the variational state family is the same for the circuit- and the measurement-based approaches, but the implementation differs as the MB-VQE requires different resources and is manipulated by single-qubit measurements only. We exemplify this direct translation for the Schwinger model [268] and highlight the different hardware requirements and the scaling of resources. As explained below, a translation to MB-VQE is advantageous for circuits containing a large fraction of so-called Clifford gates[38], as these are absorbed into the custom state.

In section 5.4, we introduce the second scheme: a novel method to construct variational state families, illustrated using the toric code model with local perturbations [270]. As

[38]Intuitively, Clifford gates are defined as gates that transform Pauli strings into other Pauli strings. See [269] for a more precise definition.

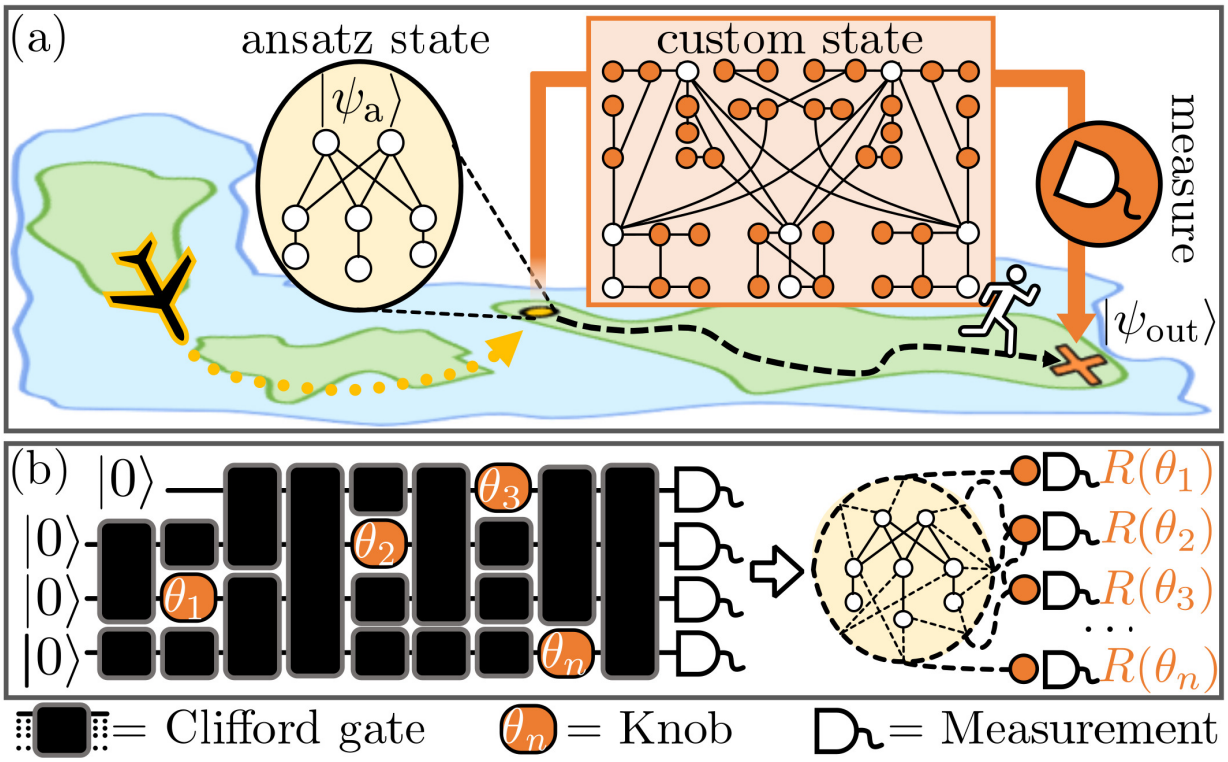

Figure 5.1: **MB-VQE schemes.** *(a)* Variation of a problem-specific ansatz state by 'edge-modification', explained in section 5.4. An ansatz state $|\psi_a\rangle$ starts the MB-VQE in a suitable corner of the Hilbert space (choice of green island). Next, the MB-VQE algorithm explores the neighbourhood (runner on black arrow). The variational optimization exploits a custom state that is obtained by decorating the edges of the ansatz state with auxiliary qubits (orange circles). Their measurement in rotated bases $R(\vec{\theta})$ with variational parameters $\vec{\theta}$ transforms the ansatz state $|\psi_a\rangle$ into the output state $|\psi_{out}\rangle$. *(b)* Direct translation of a VQE circuit into a MB-VQE, as explained in section 5.3. Left: a VQE circuit consisting of Clifford gates (black) and single-qubit parametric gates ('knobs'). Right: the corresponding MB-VQE, where the Clifford part of the circuit has been performed beforehand. The custom state consists of output (white circles) and auxiliary (orange circles) qubits only; the latter are measured in rotated bases and are related to the 'knobs' in the circuit.

figure 5.1a shows, we start from an ansatz state $|\psi_{\mathrm{a}}\rangle$ in an appropriate corner of the Hilbert space. To explore this neighbourhood using a classical optimization algorithm, we introduce a custom state and apply measurement-based modifications of $|\psi_{\mathrm{a}}\rangle$ that have no direct analogue in the circuit-model. The resulting variational family is not efficiently accessible with known classical methods and is more costly to access with circuit-based VQEs.

Finally, we summarize our results and discuss their implications in section 5.5.

5.2 General framework

5.2.1 Measurement-based quantum computing

Here, we provide a brief review of MBQC, based on [261]. In particular, we review how a universal set of gates can be realized in the MBQC framework.

The main resource of MBQC are so-called graph states [271, 272]. A graph state $|G\rangle$, associated with a graph $G = (V, E)$, is a stabilizer state (an eigenstate with $+1$ eigenvalue) of the operators

$$\hat{K}_a = \hat{X}_a \prod_{b \in V} \left(\hat{Z}_b\right)^{\Gamma_{ab}}, \tag{5.1}$$

where $a \in V$ and Γ_{ab} is the adjacency matrix of the graph G, and $\hat{X}$, $\hat{Y}$, and $\hat{Z}$ are the Pauli operators. When the graph G is a connected subset $\mathcal{C}$ of a simple cubic lattice $\mathbb{Z}^d$, $d \geq 1$, the graph state $|G\rangle$ is called a cluster state $|\mathcal{C}\rangle$. Therefore, the cluster state is defined by the condition

$$\hat{K}_a |\mathcal{C}\rangle = |\mathcal{C}\rangle\,, \quad \forall a \in V. \tag{5.2}$$

A simple way to realize this state is as follows: start with the product state

$$|+\rangle_{\mathcal{C}} = \bigotimes_{a \in V} |+\rangle_a\,, \tag{5.3}$$

then apply the sequence of unitary two-qubit operations

$$\hat{S}_{\mathcal{C}} = \prod_{(a,b) \in E} \hat{S}_{ab} \tag{5.4}$$

where

$$\hat{S}_{ab} = \frac{1}{2}\left(\hat{\mathbb{1}} + \hat{Z}_a + \hat{Z}_b - \hat{Z}_a \otimes \hat{Z}_b\right). \tag{5.5}$$

Therefore,

$$|\mathcal{C}\rangle = \hat{S}_{\mathcal{C}} |+\rangle_{\mathcal{C}} . \tag{5.6}$$

It is easy to verify that this equation satisfy the condition (5.2). MBQC starts with the preparation of the cluster state, followed by single-qubit measurements in a certain order either in the eigenbasis of the Pauli operators $\hat{X}$, $\hat{Y}$, $\hat{Z}$, or in the rotated basis $R(\theta) \equiv \{(|0\rangle \pm e^{i\theta} |1\rangle)/\sqrt{2}\}$. Depending on the measurement outcomes, the system is probabilistically projected into different states. To make the computation deterministic, so-called byproduct operators and adaptive measurements are required [261]. The former applies $\hat{X}$ and $\hat{Z}$ operators to the output qubits depending on the measurement results, while the latter involves adapting the measurement bases $R(\theta)$ based on earlier measurement outcomes. Consequently, adaptive measurements must be performed in a specific order.

In the following, we will give the procedure to implement a general one-qubit rotation gate and a CX (i.e. $CNOT$) gate. We denote the measurement result on qubit a as $(-1)^{s_a}$, where $s_a \in \{0, 1\}$. A generic single-qubit unitary gate (up to an overall phase factor) can be written as

$$\hat{U}(\theta_1, \theta_2, \theta_3) = \hat{U}_x(\theta_3)\hat{U}_z(\theta_2)\hat{U}_x(\theta_1), \tag{5.7}$$

which corresponds to a rotation with an arbitrary angle around an arbitrary axis, where $\hat{U}_x(\theta) = \exp\left(-i\theta\hat{X}/2\right)$ and $\hat{U}_z(\theta) = \exp\left(-i\theta\hat{Z}/2\right)$. The cluster state required to implement the general rotation gate $\hat{U}(\theta_1, \theta_2, \theta_3)$ consists of 5 qubits, and the measurement pattern realizing this gate is shown in figure 5.2a, where qubit 1 is the input state $|\psi_{\text{in}}\rangle$ and is measured in $\hat{X}$ basis, qubits 2, 3, and 4 are measured in the bases $R(-(-1)^{s_1}\theta_1)$, $R(-(-1)^{s_2}\theta_2)$, and $R(-(-1)^{s_1+s_3}\theta_3)$, respectively, and qubit 5 is the output qubit. Measuring the qubits in this order results in the final state of the output qubit being

$$|\psi_{\text{out}}\rangle = \hat{U}_{\Sigma,r}\hat{U}(\theta_1, \theta_2, \theta_3) |\psi_{\text{in}}\rangle , \tag{5.8}$$

where the byproduct operator $\hat{U}_{\Sigma,r}$ is

$$\hat{U}_{\Sigma,r} = \hat{X}^{s_2+s_4}\hat{Z}^{s_1+s_3}. \tag{5.9}$$

This is an example of MBQC with adaptive measurements, since the measurement bases of qubits 2, 3, and 4 depend on previous results and must be performed in a specific order. By contrast, a CX gate acting on two qubits corresponds to a non-adaptive measurement pattern. In this case, the cluster state consists of 15 qubits and the measurements can be performed in any order or simultaneously, as shown in figure 5.2b. The byproduct operators for the CX gate are

$$\begin{aligned}\hat{U}_{\Sigma,CX} =& \hat{X}_7^{s_2+s_3+s_5+s_6}\hat{Z}_7^{s_1+s_3+s_4+s_5+s_8+s_9+s_{11}+1} \\ & \hat{X}_{15}^{s_2+s_3+s_8+s_{10}+s_{12}+s_{14}}\hat{Z}_{15}^{s_9+s_{11}+s_{13}},\end{aligned} \tag{5.10}$$

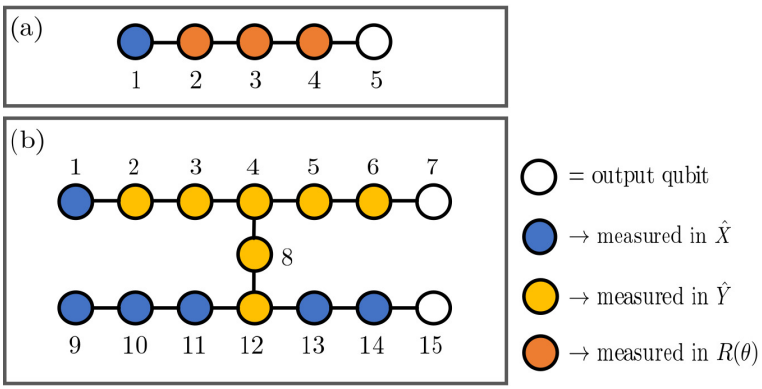

Figure 5.2: **Set of gates in MBQC.** *(a)* Measurement pattern for a general single-qubit unitary operation $\hat{U}(\theta_1, \theta_2, \theta_3)$. Qubit 1 is the input qubit. *(b)* Measurement pattern for the CX gate. Qubits 1 and 9 are the input qubits (control and target qubits, respectively).

and the output qubits are qubits 7 (control qubit) and 15 (target qubit).

While figure 5.2 shows how to implement individual gates in the MBQC formalism, one can implement a sequence of gates by concatenating the corresponding measurement patterns. To illustrate this, assume that $\hat{A}$ and $\hat{B}$ are two gates, corresponding to two cluster states with input, output and auxiliary qubits. In order to perform the gate $\hat{B}\hat{A}$ in the MBQC framework, we combine the measurement patterns of $\hat{A}$ and $\hat{B}$ such that the input qubits of $\hat{B}$ are the same as the output qubits of $\hat{A}$. As a result, $\hat{B}\hat{A}$ has the same input qubits as $\hat{A}$ and the same output qubits as $\hat{B}$. Let $\hat{U}_{\Sigma,A}$ and $\hat{U}_{\Sigma,B}$ be the respective byproduct operators and assume that $\hat{B}$ is a Clifford gate. Then, the overall byproduct operator is $\hat{U}_\Sigma = \hat{U}_{\Sigma,B}\hat{U}'_{\Sigma,A}$, where

$$\hat{U}_{\Sigma,B}\hat{B}\hat{U}_{\Sigma,A}\hat{A} = \hat{U}_{\Sigma,B}\hat{U}'_{\Sigma,A}\hat{B}\hat{A}, \tag{5.11a}$$

$$\hat{U}'_{\Sigma,A} = \hat{B}\hat{U}_{\Sigma,A}\hat{B}^\dagger. \tag{5.11b}$$

If instead $\hat{B}$ is a rotation gate as in (5.7), the overall byproduct operator is $\hat{U}_\Sigma = \hat{U}_{\Sigma,B}\hat{U}_{\Sigma,A}$, and

$$\hat{U}_{\Sigma,B}\hat{B}\hat{U}_{\Sigma,A}\hat{A} = \hat{U}_{\Sigma,B}\hat{U}_{\Sigma,A}\hat{B}'\hat{A}, \tag{5.12a}$$

$$\hat{B}' = \hat{U}^{-1}_{\Sigma,A}\hat{B}\hat{U}_{\Sigma,A}. \tag{5.12b}$$

This modification of $\hat{B}$ affects the bases of the rotated measurements, which have to be fixed following the protocol in [261]. With this, MBQC can simulate any sequence of CX and single-qubit gates, which is equivalent to universal quantum computation [273].

An advantage of MBQC is the possibility to simultaneously perform all non-adaptive measurements at a single time step (see figure 5.1b). This corresponds to the Clifford part of a circuit and includes single- and many-qubit gates [261]. This is independent of the position of the gates in the circuit, and reduces the required overhead and coherence time. Remarkably, this can be either done directly on the cluster state in the quantum hardware, or on a classical computer before the experiment. In the latter case, the Clifford part of the circuit can be efficiently performed on a classical computer using the Gottesman-Knill theorem [274], which transforms the initial cluster state into a new graph state that is local-Clifford equivalent to the quantum state obtained after all non-adaptive measurements are performed [275]. This state can be directly prepared and used for the MBQC to perform the remaining rotation gates, and it usually have dramatically fewer auxiliary qubits compared to the initial cluster state.

5.2.2 Measurement-based VQE

First, we explain how VQE algorithms work [240]. For the prototypical task of finding the ground state of some Hamiltonian H, the VQE algorithm generally works as follows

1. Prepare the variational state $|\psi(\vec{\theta})\rangle$ on the quantum computer, where $\vec{\theta}$ set the values of adjustable gates or experimental parameters.
2. Measure $\langle\psi(\vec{\theta})|H|\psi(\vec{\theta})\rangle$ from the quantum hardware.
3. The value of $\langle\psi(\vec{\theta})|H|\psi(\vec{\theta})\rangle$ is sent to a classical optimizer that updates the parameters $\vec{\theta}$ to decrease the energy of the variational state.
4. Iterate over this process until convergence in the value of energy is achieved, at which point $|\psi(\vec{\theta})\rangle$ is the ground state of the Hamiltonian H.

That convergence to the ground state is possible rests on the variational theorem of quantum mechanics, which states that, for any real-valued parameters $\vec{\theta}$, $\langle\psi(\vec{\theta})|H|\psi(\vec{\theta})\rangle \geq E_{gs}$, where E_{gs} is the ground state energy of the Hamiltonian [240]. This implies that there exists some optimal $\vec{\theta}^*$ such that $|\psi(\vec{\theta}^*)\rangle$ is (sufficiently close to) the ground state of the Hamiltonian. However, it is crucial that the variational state family $|\psi(\vec{\theta})\rangle$ is chosen to be suitable for the problem. For example, the VQE algorithm will not work if $|\psi(\vec{\theta})\rangle$ is chosen to respect some symmetry that the ground state of the Hamiltonian is known not to have. Furthermore, for the quantum computation to have an advantage, we need $|\psi(\vec{\theta})\rangle$ to be difficult to simulate classically.

We now explain how MBQC is used to design a MB-VQE. While the classical part of the feedback loop is left untouched (though note that the best optimization algorithm [276, 277, 278, 279, 280, 281] is problem-dependent [252, 282]), the MB-VQE is based on the creation and partial measurement of a tailored graph state rather than the application of a sequence of gates to create the variational state $|\psi(\vec{\theta})\rangle$. Specifically, the quantum part of a MB-VQE comprises an ansatz state $|\psi_{\mathrm{a}}\rangle$ that is transformed into a 'custom state', and a measurement prescription. As schematically represented in figure 5.1a, $|\psi_{\mathrm{a}}\rangle$ is a graph state from which we start exploring the variational class of families attainable by the MB-VQE. The custom state is then created by expanding $|\psi_{\mathrm{a}}\rangle$ into a bigger graph state. This is done by edge-modification, i.e. by adding new vertices and connecting them to pre-existing sites in the ansatz state. According to a measurement prescription defined below, which is the same at every iteration of the algorithm, the auxiliary qubits of the custom state are then measured in rotated bases $R(\vec{\theta})$, with $\vec{\theta}$ being the variational parameters over which the optimization occurs. After the variational measurements of the auxiliary qubits, the remaining qubits will constitute the output state $|\psi_{\mathrm{out}}\rangle = |\psi(\vec{\theta})\rangle$ of the MB-VQE algorithm (see figure 5.1a). The cost function to be fed into the classical side of the MB-VQE is then measured from $|\psi_{\mathrm{out}}\rangle$ (i.e. its energy), and the variational parameters $\vec{\theta}$ are updated by the optimization algorithm. This process is repeated until convergence in the value of energy is achieved.

Just like the circuit-based VQE, the custom state determines the success of our MB-VQE. Generally, the more auxiliary qubits are measured in rotated bases $R(\vec{\theta})$, the bigger the available class of variational states that can be explored. However, an excessive number of parameters $\vec{\theta}$ will make the algorithm's convergence rate slower and the experimental implementation harder. Therefore, it is important to tailor the custom state to the considered problem. As will be described below, the expansion of the ansatz state through edge-modification, with the subsequent measurement of the auxiliary qubits, allows for remarkable control over the desired ansatz state's transformations. Not only can one apply gates – just like in a circuit-based VQE – by following MBQC prescriptions (see the Schwinger model example in section 5.3), one can also identify completely new patterns of auxiliary qubits, that transform the ansatz state in a way that would be expensive to simulate with the circuit formalism (see the toric code example in section 5.4). For instance, a single auxiliary qubit measured in $R(\theta)$ and connected to an arbitrary number of output qubits $\{1, 2, 3, \dots\}$, acts $e^{i\frac{\theta}{2}\hat{Z}_1\otimes\hat{Z}_2\otimes\hat{Z}_3\otimes\cdots}$ onto them [260]. In a circuit, the same operation requires a linear number of two-qubit gates[39].

[39] A simple way to get the same operation within the circuit framework is to use an ancilla qubit in place of the auxiliary qubit in the graph, and act with CX gates between the ancilla and the output qubits.

5.3 From circuit-based to measurement-based VQE

Since MBQC can simulate a universal set of gates [261], one can create a MB-VQE by directly translating the circuit-based VQE into its corresponding custom state and sequence of measurements. As we discuss below, this strategy is advantageous if the number of parametric adaptive measurements (i.e. the knobs in figure 5.1b) in the resulting MB-VQE scheme is small.

As an example, we determine the ground state energy of the so-called Schwinger model [268], a testbed used for benchmarking quantum simulations in high energy physics [251, 283, 233]. The Schwinger model describes quantum electrodynamics on a one-dimensional lattice and can be cast in the form of a spin model with long range interactions [284, 285, 286],

$$\begin{aligned}\hat{H} = &\frac{J}{2}\sum_{n=1}^{S-2}\sum_{k=n+1}^{S-1}(S-k)\hat{Z}_n\hat{Z}_k - \frac{J}{2}\sum_{n=1}^{S-1} n\mathrm{mod}2\sum_{k=1}^{n}\hat{Z}_k \\ &+ w\sum_{n=1}^{S-1}\left(\hat{\sigma}_n^+\hat{\sigma}_{n+1}^- + \mathrm{H.C.}\right) + \frac{\mu}{2}\sum_{n=1}^{S}(-1)^n\hat{Z}_n,\end{aligned} \tag{5.13}$$

where S is the number of fermions, μ their mass, $w = \frac{1}{2a}$, and $J = \frac{g^2a}{2}$. Here, a and g are the lattice spacing and the coupling strength, respectively, and $\hat{\sigma}_n^\pm = (\hat{X}_n \pm i\hat{Y}_n)/2$.

For the VQE protocol, we assume the typical situation where parametric single-qubit gates and fixed entangling gates (CXs) are used to create the variational state [287, 249]. We consider a generic VQE circuit, in which a sequence of 'layers' is applied [240], each containing local rotations and entangling gates. As shown in figure 5.3a for $S = 4$, we choose each layer to consist of the gates

$$\prod_{n=1}^{S/2-1} CX_{2n,2n+1}\prod_{n=1}^{S/2} CX_{2n-1,2n}\prod_{n=1}^{S}\hat{U}_{x,n}(\theta_{x,n})\hat{U}_{z,n}(\theta_{z,n}), \tag{5.14}$$

where $\hat{U}_{\nu,n}(\theta_{\nu,n}) = \exp\left(i\theta_{\nu,n}\hat{V}_n/2\right)$, and $(\nu,\hat{V}) = (x,\hat{X})$ or $(\nu,\hat{V}) = (z,\hat{Z})$. The circuit for the VQE is created by concatenating K layers, where K is big enough to sufficiently explore the relevant subsector of the considered Hilbert space. As described in section 5.2, the MB-VQE custom state corresponding to a K-layer circuit is obtained by joining the measurement patterns of the gates in (5.14), and performing all non-adaptive measurements classically, which effectively removes the Clifford parts of the circuit. The resulting custom state is shown in figure 5.3b. As ansatz state, we use $|\psi_\mathrm{a}\rangle = \bigotimes_{n=1}^{S}|+\rangle$.

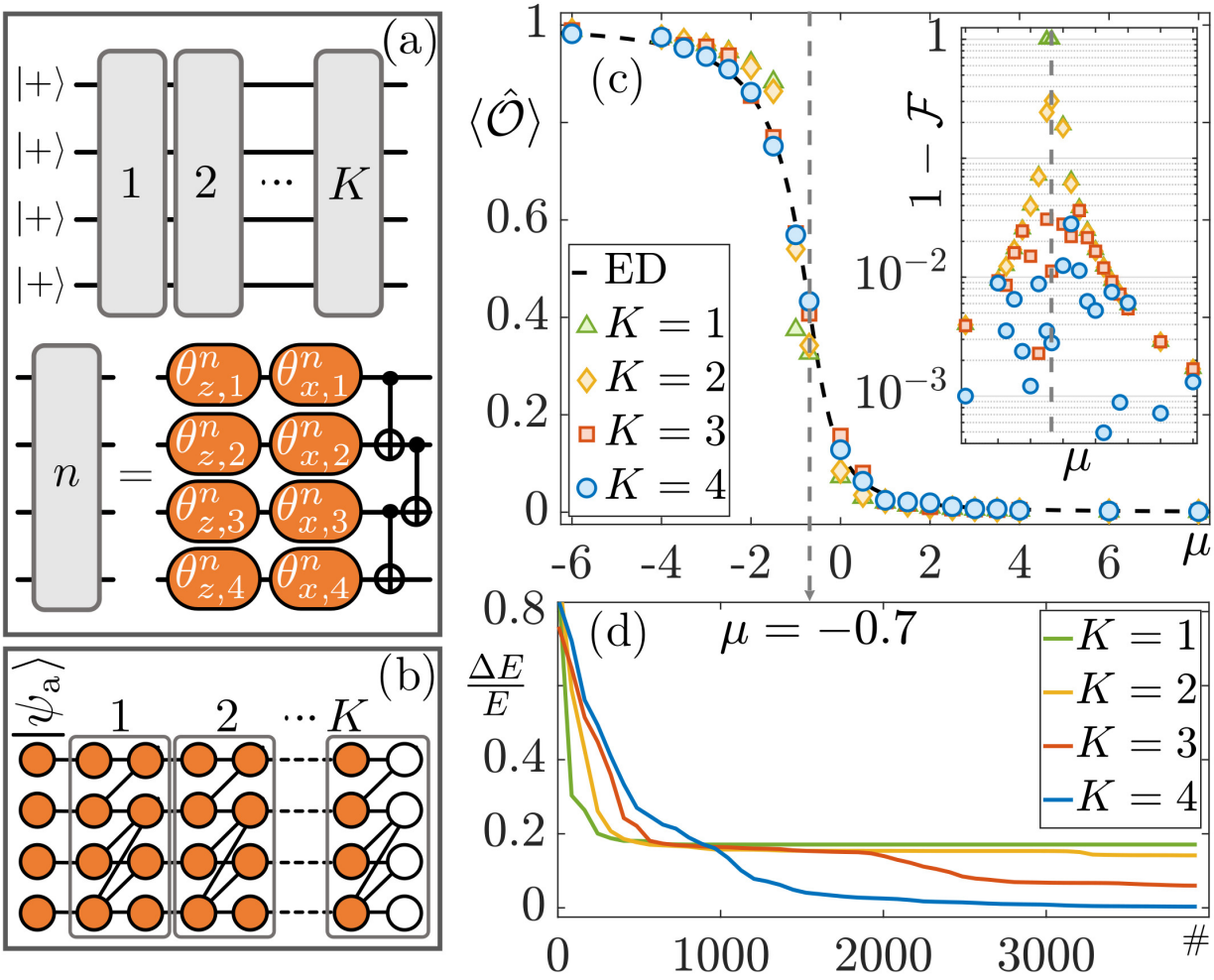

Figure 5.3: **Schwinger model.** *(a)* Ansatz state and VQE circuit for $S = 4$ qubits and K layers. Each layer consists of CX gates and local rotations (orange) parametrized by angles $\theta^n_{\nu,i}$ (with rotation axis $\nu = x, z$; $i = 1, \ldots, 4$). *(b)* MB-VQE custom state for K layers. White circles are output qubits. Auxiliary qubits (orange) are measured in rotated bases $R(\theta)$. *(c)* The order parameter $\langle\hat{\mathcal{O}}\rangle$ vs fermion mass μ plot. The dashed line and dots represent exact diagonalization (ED) and MB-VQE results, respectively, with the number of layers K used indicated in the legend. The inset shows the infidelity $1 - \mathcal{F}$ between the output state and the true ground state. *(d)* Relative energy difference $\Delta E/E$ between the output state of MB-VQE algorithm and the true ground state for $\mu = -0.7$, versus the number of iterations in the optimization procedure. The variational parameters are initialized at zero, and $J = \omega = 1$ in (5.13).

The MB-VQE simulation results are shown in figure 5.3c for $S = 4$ and different values of K. We plot the order parameter $\langle\hat{\mathcal{O}}\rangle = \frac{1}{2S(S-1)}\sum_{i,j<i}\langle(1+(-1)^i\hat{Z}_i)(1+(-1)^j\hat{Z}_j)\rangle$ against the fermion mass μ and correctly observe a second-order phase transition around $\mu = -0.7$ [288, 251, 289]. As expected, increasing K improves the ground state approximation, as demonstrated by the inset in figure 5.3c and by figure 5.3d. The points near the phase transition require $K \gtrsim 3$ layers ($\gtrsim 28$ qubits), whereas $K = 1$ layer (12 qubits) suffices for the easiest points. Note that allowing different gates as resources in (5.14) generally leads to different convergence rates, as demonstrated by the results in [251].

Perfect platforms provided, both the circuit-based VQE and the MB-VQE give the same result. However, the quantum hardware requirements are different for the two methods. The circuit-based VQE requires S qubits, $2KS$ single-qubit operations, and $K(S-1)$ entangling gates. For the corresponding MB-VQE, a custom state of $S(2K+1)$ qubits and $2KS$ single-qubit operations (measurements) are required. Generally, translating a circuit-based VQE into its corresponding MB-VQE is advantageous whenever the circuit involves a large Clifford part compared to the number of adaptive measurements (i.e. knobs). In this case, MB-VQE avoids the requirement of performing long gate sequences, which is currently challenging due to error accumulation in circuit-based quantum computation. This is especially interesting for platforms where entangling gates are hard to realize (e.g. photonic setups) or in systems with limited coherence times.

5.4 MB-VQE by edge-modification

MB-VQEs are advantageous whenever a perturbation $\hat{H}_\mathrm{p}$ is added to a Hamiltonian $\hat{H}_0$ whose ground state, used as ansatz state $|\psi_\mathrm{a}\rangle$ below, is a stabilizer state (equivalent to a graph state up to local Clifford operations [275]). Here, we illustrate the idea of MB-VQE through edge-modification (first outlined in section 5.2) through the example of a perturbed toric code model. First, we will provide a brief review of the perturbed toric code model and the notation used to describe it. Then, we will present the MB-VQE algorithm used to find its ground state.

5.4.1 Toric code and logical states

The toric code is a quantum error-correcting code defined on a two-dimensional rectangular lattice with periodic boundary conditions [290] (see figure 5.4). On the lattice, the number of columns (rows) of independent vertices is N_x (N_y) and edges represent qubits. The

toric code state is a stabilizer state of so-called star $\hat{A}_s$ and plaquette $\hat{B}_p$ operators. For any vertex s in the lattice, $\hat{A}_s$ acts with $\hat{Z}$ on the four incident edges, while $\hat{B}_p$ acts with $\hat{X}$ on the four edges in the p^{th} plaquette[40]. The toric code Hamiltonian is then $\hat{H}_0 = -\sum_s \hat{A}_s - \sum_p \hat{B}_p$, and the ground state is stabilized by the plaquette $\hat{B}_p$ and star $\hat{A}_s$ operator. Since $\prod_s \hat{A}_s = \prod_p \hat{B}_p = 1$, the toric code has $2N_xN_y - 2$ independent stabilizers (i.e. there are two more degrees of freedom than independent stabilizers), and $\hat{H}_0$ has four degenerate ground states $|r,t\rangle_L$ $(r,t = 0,1)$, called logical states. To explicitly write down these logical states, we add two extra stabilizers to the set of operators $\hat{A}_s$ and $\hat{B}_p$. There are two common choices for the pair of extra stabilizers to be added, which are called logical-X ($\hat{X}_{L,1}$ and $\hat{X}_{L,2}$) and logical-Z ($\hat{Z}_{L,1}$ and $\hat{Z}_{L,2}$) operators, and are shown in figures 5.4b and 5.4c, respectively. Explicitly, $\hat{Z}_{L,1}$ ($\hat{Z}_{L,2}$) acts with $\hat{Z}$ on all horizontal (vertical) edges of an arbitrarily chosen column (row). Similarly, $\hat{X}_{L,1}$ ($\hat{X}_{L,2}$) acts with $\hat{X}$ on all horizontal (vertical) edges of an arbitrarily chosen row (column). Here, we choose the logical operators to act on the first row and column of the toric code lattice. Both logical-X and logical-Z operators commute with all the other plaquette $\hat{B}_p$ and star $\hat{A}_s$ operators, but do not generally commute between themselves. The logical state $|r,t\rangle_L$ can then be defined as the unique ground state of $\hat{H}_0 - (-1)^r\hat{Z}_{L,1} - (-1)^t\hat{Z}_{L,2}$ $(r,t = 0,1)$.

The perturbation added to the toric code Hamiltonian is

$$\hat{H}_{\text{p}} = \sum_{n=1}^{2N_xN_y} \lambda_n \hat{Z}_n, \tag{5.15}$$

which corresponds to an inhomogeneous magnetic field. The task for the MB-VQE algorithm is to find the ground state of $\hat{H}_0 + \hat{H}_{\text{p}}$ for different choices of the perturbation parameters $\{\lambda_n\}$ and, for simplicity, we choose $N_x = N_y = 2$. As ansatz state for the MB-VQE, we choose the highly entangled graph state $|\psi_{\text{a}}\rangle = |0,0\rangle_L$[41], that approximates the ground state of $\hat{H}_0 + \hat{H}_{\text{p}}$ for small positive values of λ_n. The graph state representation of $|0,0\rangle_L$ can be determined efficiently classically [275] and is shown in figure 5.6b.

5.4.2 Algorithm and results

The quantum part of MB-VQE involves preparing the variational state at every iteration by applying projective measurements on a custom state that is created from the ansatz state.

[40] Note that this is opposite to the choice given in [290], where $\hat{Z}$ and $\hat{X}$ operators are exchanged. However, the two are equivalent by a Fourier transform.

[41] Note that, for general perturbations, the ansatz state will be a superposition of different logical states $\sum_{r,t} c_{r,t}|r,t\rangle_L$, with $\sum_{r,t}|c_{r,t}|^2 = 1$ $(r,t = 0,1)$.

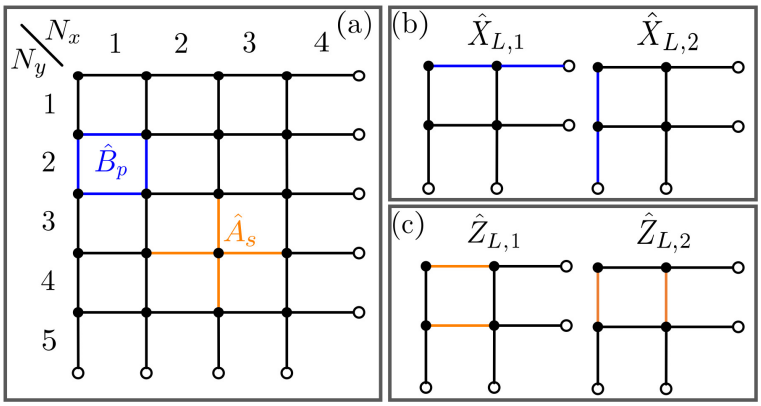

Figure 5.4: **Toric code notation.** *(a)* Toric code for $N_x = 4$ and $N_y = 5$. Qubits exist on the edges of the lattice, and two of the generators $\hat{A}_s$ and $\hat{B}_p$ are explicitly represented. Since the lattice lies on a torus, periodic boundary conditions are enforced, as shown by empty dots. Schematic representations of the logical-X and logical-Z operators in the case $N_x = N_y = 2$ are given in *(b)* and *(c)*, respectively. In the whole figure, links colored in blue (orange) represent the action of the $\hat{X}$ ($\hat{Z}$) operator on the corresponding qubits.

Here, we explain how to modify the edges of the perturbed toric code ansatz state $|\psi_\mathrm{a}\rangle$ (see figure 5.6b) to obtain the custom state. The local perturbation term $\hat{H}_\mathrm{p}$ in (5.15) leads to a reduction in the amount of entanglement in the ground state, as can be understood by considering the ground state of $\hat{H}_\mathrm{p}$, which (for positive weights λ_n) is the tensor product state $\bigotimes_n |1\rangle_n$. Therefore, we need to modify the edges of $|\psi_\mathrm{a}\rangle$ in such a way that, after the measurement of the auxiliary qubits, we both fine-tune the amount of entanglement between connected vertices and transform the state of the output qubits. This can be done by following the protocol given in figure 5.5. The idea is to modify any edge connecting two output qubits by adding two auxiliary qubits in an arbitrary state (green circles in figure 5.5b), which are then measured in the $\hat{X}$ basis. If both these qubits are in the state $|+\rangle = (|0\rangle + |1\rangle)/\sqrt{2}$, their measurement leaves the output qubits unaffected. However, if both auxiliary qubits are either in $|0\rangle$ or $|1\rangle$, their measurement eliminates all pre-existing entanglement between the original output qubits.

While it is possible to directly prepare the custom state with auxiliary qubits in arbitrary states, this does not create a graph state, and as such there are no known methods to obtain a deterministic outcome after the measurement of all auxiliary qubits. A formal MBQC protocol can be obtained by following the measurement patterns presented in section 5.2.1 and [261]. Each of the auxiliary qubits to be used in the edge-modification is substituted with five qubits, to be measured in a specific order following the MBQC imple-

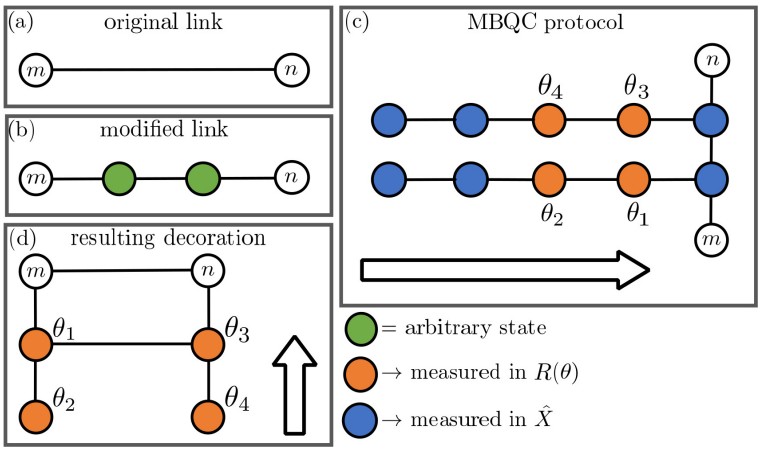

Figure 5.5: **Edge decoration.** Schematic description of the edge-modification technique used for the perturbed toric code MB-VQE. The edge connecting a linked pair (m, n) of vertices in $|\psi_{\mathrm{a}}\rangle$ (shown in *(a)*) is modified by adding two auxiliary qubits in an arbitrary state (shown in *(b)*). The corresponding MBQC procedure uses the measurement pattern presented in *(c)*. By classically removing Clifford operations, we reduce the number of auxiliary qubits to be added to four, as shown in *(d)* and figure 5.6a. The arrows represent the temporal order in which the auxiliary qubits have to be measured. In *(c)* and *(d)*, we explicitly indicate the angles θ_i $(i = 1, \ldots, 4)$ of the rotated bases in which the corresponding qubits are measured.

mentation of a general rotation gate (see figures 5.2a and 5.5c). In this case, an arbitrary state can be prepared with only two measurements in rotated bases[42] and, out of the ten auxiliary qubits in figure 5.5c, six can be eliminated by efficient classical computation [274]. The resulting graph state, presented in figure 5.5d, only contains four auxiliary qubits per edge of the ansatz state.

To better understand the effects of our edge-modification, we look at the state $|\psi_{n,m}\rangle$ of the two output qubits n and m after the auxiliary qubits are measured. With the

[42]For an arbitrary input state, we need three measurements in rotated bases to implement a general rotation gate (as shown in figure 5.2a). But, here, since we know that the 'input state' is fixed at $|+\rangle$, only two measurements in rotated bases suffice to implement a general rotation gate so that the auxiliary qubits shown in figure 5.5b can be in arbitrary states.

parameters θ_i $(i = 1, \ldots, 4)$ introduced in figure 5.5, we find[43]

$$
\begin{aligned}
|\psi_{n,m}\rangle = &\left[1 + \cos\theta_4 \sin\theta_1 \sin\theta_2 + \cos\theta_1 \cos\theta_3 \sin\theta_2 \sin\theta_4 + \cos\theta_2 \sin\theta_3 \sin\theta_4\right] |0\rangle_m |0\rangle_n \\
&+ \left[\cos^2\frac{\theta_4}{2} + \frac{1}{2}\left(-1 + \cos\theta_4\right) + \sin\theta_1 \sin\theta_2 + i \sin\theta_4 \left(\cos\theta_2 \cos\theta_3 - \cos\theta_1 \sin\theta_2 \sin\theta_3\right)\right] |0\rangle_m |1\rangle_n \\
&+ \left[\cos\theta_2 + \sin\theta_3 \sin\theta_4 + i \sin\theta_2 \left(\cos\theta_1 \cos\theta_4 - \cos\theta_3 \sin\theta_1 \sin\theta_4\right)\right] |1\rangle_m |0\rangle_n \\
&+ \left[-\cos\theta_2 \cos\theta_4 - i \cos\theta_1 \sin\theta_2 + \sin\theta_4 \left(-i \cos\theta_3 + \sin\theta_1 \sin\theta_2 \sin\theta_3\right)\right] |1\rangle_m |1\rangle_n,
\end{aligned}
\tag{5.16}
$$

which, for simplicity, is not normalized. From this equation, it is possible to see that for $\theta_i = 0$ $(\theta_i = \pi/2)$, $\forall i$, we get the initial graph state $|\psi_{n,m}\rangle = CZ|+\rangle_m|+\rangle_n$ (the separable state $|\psi_{n,m}\rangle = |+\rangle_m|+\rangle_n$). For arbitrary angles θ_i, the entanglement between the output qubits is generally reduced, and their wave vector rotated according to (5.16). By taking a deeper look on (5.16), it is possible to realize that the edge-modification technique presented here does not allow for reaching an arbitrary output state $|\psi_{n,m}\rangle$. For instance, there is no combination of the angles $\{\theta_1, \ldots, \theta_4\}$ such that $|\psi_{n,m}\rangle = |0\rangle_m|1\rangle_n$. This limitation can be lessened or even removed in several ways. For instance, adding a third qubit in an arbitrary state on the link connecting m and n allows for more control over the output state $|\psi_{n,m}\rangle$. Otherwise, after the auxiliary qubits are measured, one can rotate the states of the two output qubits by acting with single-qubit rotations onto them, as explained in section 5.2.1.

We remark that the number of auxiliary qubits can be further reduced by switching from a deterministic to a probabilistic protocol. While the edge-modification procedure presented in figure 5.5b does not resort to a graph state (i.e. it does not satisfy (5.2)), it can still be used for a MB-VQE. From one side, this saves half the auxiliary qubits that are needed for the creation of the custom state. On the other side, the loss of determinism in the outcome forces us to repeat each iteration of the MB-VQE algorithm until a specific measurement outcome is obtained. The number of extra repetitions that one must perform scales exponentially with the number of auxiliary qubits, making this probabilistic approach useful for toy examples only.

The edge-modification procedure outlined above is applied to the ansatz state of the perturbed toric code, which has a graph state representation shown in figure 5.6b, giving the custom state shown in figure 5.1a. The auxiliary qubits are then measured in rotated bases $R(\vec{\theta})$ that are controlled by the variational parameters of the algorithm. Depending

[43] We are assuming that all measurement outcomes in figure 5.5c were $+1$. This is possible because one can find a byproduct operator that ensures this output state (5.16) regardless of the actual individual measurement outcomes.

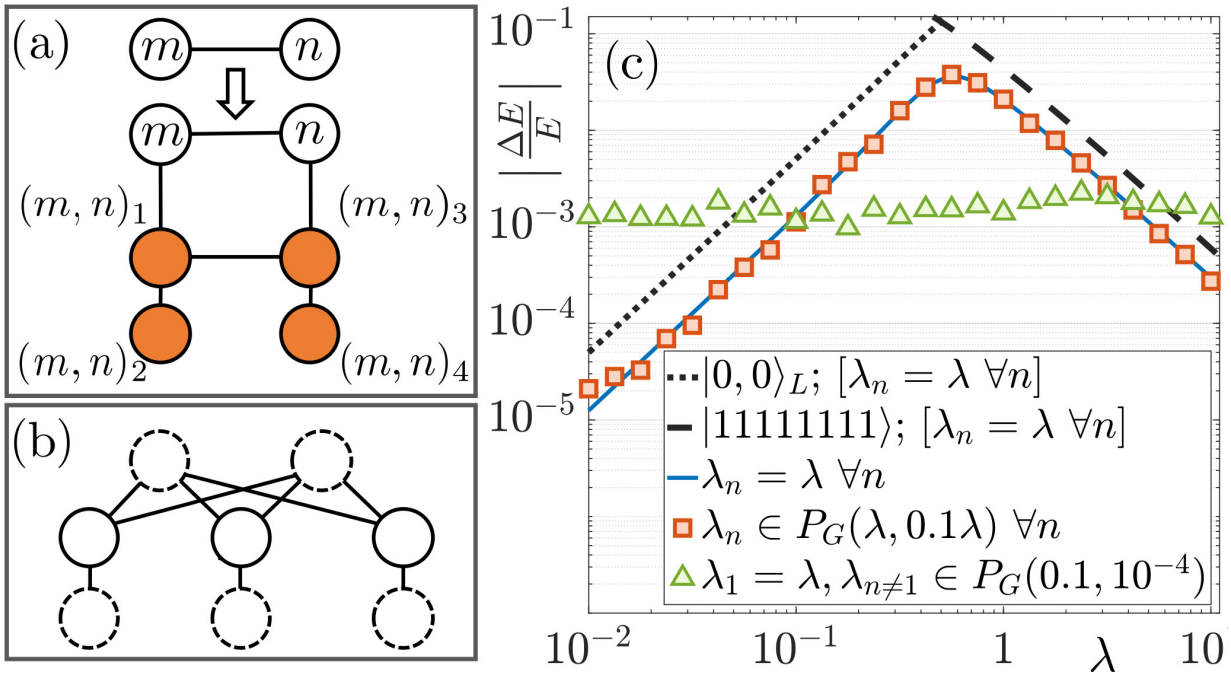

Figure 5.6: **Perturbed toric code.** *(a)* Edge-modification resource for the MB-VQE. Four auxiliary qubits (orange circles), labelled $(m,n)_i$ $(i = 1,\ldots,4)$, are added to two connected output qubits m and n (white circles). *(b)* Graph state representation of the ansatz state $|0,0\rangle_L$. Additional Hadamard gates are applied to qubits with dashed lines. *(c)* Relative difference between the MB-VQE results and the true ground state energy vs the perturbation strength. We let λ_n in (5.15) be equal on all qubits (solid blue line), or sampled from a normal distribution P_G of average λ and variance 0.1λ (red squares). Green triangles describe a perturbation acting strongly on λ_1 and weakly on the other qubits. Dotted and dashed lines are computed with respect to $|0,0\rangle_L$ (ansatz state) and $|1\rangle^{\otimes 2N_xN_y}$ (ground state of $\hat{H}_\mathrm{p}$) for $\lambda_n = \lambda\ \forall n$.

on $\vec{\theta}$, the entanglement between the qubits is modified, and the ansatz state is transformed into the output state $|\psi_{\text{out}}\rangle = |\psi(\vec{\theta})\rangle$.

Numerical results for the MB-VQE are shown in figure 5.6c. The relative energy difference between the MB-VQE results and the true ground state (calculated via exact diagonalization) is plotted against the perturbation strength. This is done with all λ_n in (5.15) equal to λ (solid blue line), with each λ_n drawn from a Gaussian distribution $P_G(\mu, \sigma^2)$ with mean $\mu = \lambda$ and variance $\sigma^2 = 0.1\lambda$ (orange squares), and with $\lambda_1 = \lambda$, λ_n randomly sampled from $P_G(\mu = 0.1, \sigma^2 = 10^{-4})$ for $n \neq 1$ (green triangles). A plot of the infidelity resembles figure 5.6c, with maximum infidelities for the blue curve, red squares and green triangles being 6.2×10^{-2}, 6.5×10^{-2}, and 9.4×10^{-3}, respectively. Figure 5.6c shows that the MB-VQE produces the ground state energy with high confidence when the perturbation strength is very small or very large. Notably, the MB-VQE outperforms the ansatz state (dotted black line) and the ground state of $\hat{H}_{\text{p}}$ in (5.15) (dashed black line) in all cases. If the perturbation only acts on one qubit, the chosen custom state allows the MB-VQE to find the exact ground state energy within machine precision. This is also the case if the perturbation acts on two disconnected qubits, provided we connect them and add auxiliary qubits as in figure 5.6a. This suggests that the outcome of the MB-VQE can be significantly improved by adding few extra auxiliary qubits.

5.5 Discussion

In this chapter, we merged the principles of measurement-based quantum computation and quantum-classical optimization to create a MB-VQE that finds the ground state of some target Hamiltonian. The framework rests on the creation of a custom state that consists of the ansatz state with additional auxiliary qubits that are measured in rotated bases controlled by the variational parameters of the algorithm. These measurements allow the variational state to explore the Hilbert space of the problem in search of the desired ground state. We presented two new types of variational schemes that are not restricted to our specific examples and can be combined and generalized to other cases. We first showed how to adapt any circuit-based VQE to become a MB-VQE, using the Schwinger model as example[44]. The second approach applies when the ansatz state is a stabilizer state, which

[44]Note that, while we have presented the Schwinger model MB-VQE as a translation of the circuit-based VQE that was studied in the literature before [251], it is also true that it falls under the principle of MB-VQE by edge-modification. Indeed, as explained in section 5.2, the principle of creating variational states through edge-modification underlies all MB-VQE methods.

allow us to efficiently determine its corresponding graph state [275], as in the perturbed toric code model.

Our scheme based on edge-modification provides a new way of thinking about state variations in VQEs. In particular, the effects resulting from measuring only one or few entangled auxiliary qubits can be challenging to describe with a simple circuit. The resulting state transformations do not necessarily correspond to unitary operations and can affect a large number of remaining qubits [260]. Accordingly, MB-VQEs can lead to schemes in which few auxiliary qubits suffice to reach the desired state, while many gates would be required in a circuit-based protocol. Just like circuit optimization in standard VQEs [291], tailored edge-modifications can lead to a leap for MB-VQEs, with the custom state optimized to the specific problem. The framework presented here provides a starting point for designing VQEs whose properties are different and complementary to the standard approach that is based on varying a state by applying gates.

Experimental proof-of-concept demonstrations of the idea of MB-VQE by edge-modification can be explored by considering the smallest instance of the planar code [290], with perturbation on a single qubit as a first step. In this scenario, the MB-VQE requires as few as eight entangled qubits instead of the 44 used above. Especially promising candidate systems include superconducting qubits and photonic platforms. The latter recently demonstrated the capability to entangle several thousands of qubits [292, 293], and to create tailored graph states [294, 295, 296, 297]. When designing custom states for future experiments, it will be important to understand the effects of decoherence and it will be interesting to investigate whether MB-VQEs retain the high robustness of MBQC against errors [264, 266, 265].

While the principles of MB-VQE outlined here are platform-agnostic, they open the door for complex quantum computations in systems where long gate sequences or the realization of entangling gates are challenging. In particular, MB-VQE offers new routes for experiments with photonic quantum systems, thus enlarging the toolbox of variational computations.

Chapter 6

Final Remarks

This thesis considered four different aspects of quantum information, AdS/CFT duality, and the interplay between them. In this final chapter, we reflect on the results presented in each of these aspects, summarize what they have taught us, and point out some directions for future investigations.

Chapter 2 made the first rigorous study of the holographic complexity conjectures for rotating black holes. This was lacking previously due to the difficulty in describing the null hypersurfaces in rotating spacetimes in a way that is amenable to the relevant calculations. Our first contribution was to point out that there exists a special class of spacetimes where these complications vanish: the odd-dimensional equal-spinning black holes. Based on this, we carried out a detailed study of two quantities: the complexity of formation and the late-time rate of growth of complexity for both the complexity=volume and complexity=action conjectures. We verified that the late-time rate of complexity growth is a constant and that the limit is approached from above for the CA conjecture and from below for the CV conjecture, which agrees with the behaviour found for charged black holes. However, we found that the complexity of formation for rotating black holes is different from charged ones. For charged black holes, it was found [69] that the complexity scales with the entropy for large black holes, $\Delta\mathcal{C} \sim Sf(\mu/T) + S\log(\mu/T)$. Using a combination of analytical and numerical arguments, we showed that, for rotating black holes, this relation instead becomes $\Delta\mathcal{C} \sim V^{(D-2)/(D-1)}f(\Omega_H/T) + S\log(\Omega_H/T)$. This distinction is possible only because, in general, the thermodynamic volume V and entropy S are independent functions but that, in the case of static black holes, they are not independent, $S \sim V^{(D-2)/(D-1)}$. Therefore, our results generalize the behaviour found for static black holes to the case when there is no time symmetry.

Our argument for the role of thermodynamic volume in holographic complexity is a bulk argument whose validity rests on the CV and CA conjectures. Although complexity is ultimately a CFT quantity, we have not presented a CFT argument for why thermodynamic volume is relevant for complexity. The role of thermodynamic volume in holography is not yet well understood (though see [113, 114, 115, 116, 117, 118, 119, 120] for progress in this direction). Our work provides a strong motivation to study this question in the future and provide a CFT argument to either verify our results or show their limitations. Another direction for future investigation is to go beyond the odd-dimensional equal-spinning class of black holes, though we expect this task to be formidable.

In chapter 3, we considered general traversable wormholes in AdS_3 spacetimes. Two-sided traversable wormholes were first considered in the seminal paper of Gao-Jafferis-Wall [55]. The difficulty in generalizing this protocol to multi-boundary wormholes is the existence of the causal shadow region between the horizons of any two asymptotic regions. Our first contribution was to point out that this difficulty can be overcome in the hot limit of multi-boundary wormholes where the temperature in all asymptotic regions is large. We explicitly showed in the three-boundary wormhole case that there exists a large region where the causal shadow between any two asymptotic regions is exponentially small in the hot limit. Furthermore, the local CFT state in these regions can be well approximated by the TFD state. Based on these two results, we showed how the Gao-Jafferis-Wall protocol can be applied to the case of multi-boundary wormholes to make them traversable. We also discussed how multi-boundary wormholes with non-trivial topologies can be made traversable.

It would be interesting to extend this work to higher dimensions where gravity is more interesting. Furthermore, since the CFT state dual to multi-boundary wormholes has multipartite entanglement, and since traversable wormholes are dual to quantum teleportation circuits, it would be interesting to investigate how multipartite entanglement can be used as a resource for quantum teleportation circuits, effectively extending the work presented in [157, 160, 183, 184] to understand how multipartite entanglement affects the properties and conditions of teleportation.

Chapter 4 considered the experimental question of detecting non-classical effects of gravity in quantum regimes. The difficulty in achieving this experimentally is that the gap between the smallest mass whose gravitational effects can be detected and the largest mass that can be put in a controlled quantum state is still quite large. To help overcome this gap, we proposed an experimental set-up that uses cavity optomechanics to prepare two quantum micro-mechanical oscillators in a superposition state and detect the effects of the gravitational interaction between them. The observable from which the effects of gravity can be studied is the visibility pattern of interfering photons in the cavity systems

of the set-up. We quantified the shift that the gravitational interaction would induce on the photons visibility pattern, and discussed the effects of errors in the set-up such as thermal phonons and the gravitational effects of surrounding mass distributions.

We have not given a detailed account on how the experimental proposal can be realized in the lab. We hope that experimentalists would take this question and improve on our proposal. Furthermore, although we have showed that the gravitational interaction induces entanglement between the two quantum micro-mechanical oscillators, we have not given an entanglement witness that can experimentally verify this in our set-up. It would be interesting to consider this in future investigations.

In chapter 5, we merged the principles of measurement-based quantum computation with variational quantum eigensolver algorithms to find the ground state of some target Hamiltonian. This problem has many applications in different fields and is expected to be the first practical application of near-term quantum devices. To do this, we first showed how any circuit-based VQE can be translated into a measurement-based VQE. That this is possible is expected since MBQC is known to be a universal quantum computer. Furthermore, we introduced a new class of variational state families that are unique to MBQC and have no immediate analogue in circuit-based VQEs. This second approach is suitable when the ansatz state is a stabilizer state. We illustrated these two schemes with two examples: the Schwinger model and the perturbed toric code model. These two approaches provide a starting point for designing VQEs whose properties are different and complementary to the standard approach that is based on varying a state by applying gates, and open the door for new applications of VQE algorithms.

There are two directions for future investigations. First, we have not presented an error analysis for our MB-VQE schemes. When designing variational states for MB-VQEs for future experiments, it will be important to understand the effects of decoherence and investigate whether MB-VQEs retain the high robustness of MBQC against errors [264, 266, 265]. Second, we have not discussed the details of experimental implementation for our schemes. It would be interesting to investigate this question in the future, particularly for photonic platforms that are more suitable for MBQC.

References

[1] A. Al Balushi, R. A. Hennigar, H. K. Kunduri and R. B. Mann, *Holographic complexity of rotating black holes*, 2010.11203.

[2] A. Al Balushi, R. A. Hennigar, H. K. Kunduri and R. B. Mann, *Holographic Complexity and Thermodynamic Volume*, *Phys. Rev. Lett.* **126** (2021) 101601, [2008.09138].

[3] A. Al Balushi and R. B. Mann, *Null hypersurfaces in Kerr–(A)dS spacetimes*, *Class. Quant. Grav.* **36** (2019) 245017, [1909.06419].

[4] M. T. N. Imseis, A. Al Balushi and R. B. Mann, *Null Hypersurfaces in Kerr-Newman-AdS Black Hole and Super-Entropic Black Hole Spacetimes*, *Class. Quant. Grav.* **38** (2021) 045018, [2007.04354].

[5] A. Al Balushi, Z. Wang and D. Marolf, *Traversability of Multi-Boundary Wormholes*, *JHEP* **04** (2021) 083, [2012.04635].

[6] A. Al Balushi, W. Cong and R. B. Mann, *Optomechanical quantum Cavendish experiment*, *Phys. Rev. A* **98** (2018) 043811, [1806.06008].

[7] R. R. Ferguson, L. Dellantonio, A. Al Balushi, K. Jansen, W. Dür and C. A. Muschik, *A measurement-based variational quantum eigensolver*, 2010.13940.

[8] Z.-W. Wang, A. Al Balushi, R. Mann and H.-M. Jiang, *Safe Trinification*, *Phys. Rev. D* **99** (2019) 115017, [1812.11085].

[9] S. W. Hawking, *Particle Creation by Black Holes*, *Commun. Math. Phys.* **43** (1975) 199–220.

[10] S. W. Hawking, *Breakdown of Predictability in Gravitational Collapse*, *Phys. Rev. D* **14** (1976) 2460–2473.

[11] J. D. Bekenstein, *Black holes and the second law*, *Lett. Nuovo Cim.* **4** (1972) 737–740.

[12] G. 't Hooft, *Dimensional reduction in quantum gravity*, *Conf. Proc. C* **930308** (1993) 284–296, [gr-qc/9310026].

[13] L. Susskind, *The World as a hologram*, *J. Math. Phys.* **36** (1995) 6377–6396, [hep-th/9409089].

[14] R. Bousso, *The Holographic principle*, *Rev. Mod. Phys.* **74** (2002) 825–874, [hep-th/0203101].

[15] J. Maldacena, *The large N Limit of superconformal field theories and supergravity*, *Advances in Theoretical and Mathematical Physics* **2** (1998) 231–252.

[16] S. S. Gubser, I. R. Klebanov and A. M. Polyakov, *Gauge theory correlators from noncritical string theory*, *Phys. Lett. B* **428** (1998) 105–114, [hep-th/9802109].

[17] E. Witten, *Anti-de Sitter space and holography*, *Adv. Theor. Math. Phys.* **2** (1998) 253–291, [hep-th/9802150].

[18] S. Ryu and T. Takayanagi, *Aspects of Holographic Entanglement Entropy*, *JHEP* **08** (2006) 045, [hep-th/0605073].

[19] D. Harlow, *Jerusalem Lectures on Black Holes and Quantum Information*, *Rev. Mod. Phys.* **88** (2016) 015002, [1409.1231].

[20] V. E. Hubeny, *The AdS/CFT Correspondence*, *Class. Quant. Grav.* **32** (2015) 124010, [1501.00007].

[21] M. Van Raamsdonk, *Lectures on Gravity and Entanglement*, in *Theoretical Advanced Study Institute in Elementary Particle Physics: New Frontiers in Fields and Strings*, pp. 297–351, 2017. 1609.00026. DOI.

[22] D. Harlow, *TASI Lectures on the Emergence of Bulk Physics in AdS/CFT*, *PoS* **TASI2017** (2018) 002, [1802.01040].

[23] G. Penington, *Entanglement Wedge Reconstruction and the Information Paradox*, *JHEP* **09** (2020) 002, [1905.08255].

[24] A. Almheiri, N. Engelhardt, D. Marolf and H. Maxfield, *The entropy of bulk quantum fields and the entanglement wedge of an evaporating black hole*, *JHEP* **12** (2019) 063, [1905.08762].

[25] A. Almheiri, R. Mahajan and J. E. Santos, *Entanglement islands in higher dimensions*, *SciPost Phys.* **9** (2020) 001, [1911.09666].

[26] D. N. Page, *Information in black hole radiation*, *Phys. Rev. Lett.* **71** (1993) 3743–3746, [hep-th/9306083].

[27] G. Penington, S. H. Shenker, D. Stanford and Z. Yang, *Replica wormholes and the black hole interior*, 1911.11977.

[28] A. Almheiri, T. Hartman, J. Maldacena, E. Shaghoulian and A. Tajdini, *Replica Wormholes and the Entropy of Hawking Radiation*, *JHEP* **05** (2020) 013, [1911.12333].

[29] A. Almheiri, T. Hartman, J. Maldacena, E. Shaghoulian and A. Tajdini, *The entropy of Hawking radiation*, 2006.06872.

[30] J. Maldacena, *Wilson loops in large N field theories*, *Phys. Rev. Lett.* **80** (1998) 4859–4862, [hep-th/9803002].

[31] M. Henningson and K. Skenderis, *The Holographic Weyl anomaly*, *JHEP* **07** (1998) 023, [hep-th/9806087].

[32] V. Balasubramanian and P. Kraus, *A Stress tensor for Anti-de Sitter gravity*, *Commun. Math. Phys.* **208** (1999) 413–428, [hep-th/9902121].

[33] T. J. Osborne and M. A. Nielsen, *Entanglement in a simple quantum phase transition*, *Phys. Rev. A* **66** (2002) 032110, [quant-ph/0202162].

[34] I. R. Klebanov, D. Kutasov and A. Murugan, *Entanglement as a probe of confinement*, *Nucl. Phys. B* **796** (2008) 274–293, [0709.2140].

[35] P. Calabrese and J. L. Cardy, *Evolution of entanglement entropy in one-dimensional systems*, *J. Stat. Mech.* **0504** (2005) P04010, [cond-mat/0503393].

[36] P. Calabrese and J. Cardy, *Entanglement entropy and conformal field theory*, *J. Phys. A* **42** (2009) 504005, [0905.4013].

[37] S. Ryu and T. Takayanagi, *Holographic derivation of entanglement entropy from AdS/CFT*, *Phys. Rev. Lett.* **96** (2006) 181602, [hep-th/0603001].

[38] V. E. Hubeny, M. Rangamani and T. Takayanagi, *A Covariant holographic entanglement entropy proposal*, *JHEP* **07** (2007) 062, [0705.0016].

[39] T. Faulkner, A. Lewkowycz and J. Maldacena, *Quantum corrections to holographic entanglement entropy*, *JHEP* **11** (2013) 074, [1307.2892].

[40] N. Engelhardt and A. C. Wall, *Quantum Extremal Surfaces: Holographic Entanglement Entropy beyond the Classical Regime*, *JHEP* **01** (2015) 073, [1408.3203].

[41] D. L. Jafferis, A. Lewkowycz, J. Maldacena and S. J. Suh, *Relative entropy equals bulk relative entropy*, *JHEP* **06** (2016) 004, [1512.06431].

[42] X. Dong, D. Harlow and A. C. Wall, *Reconstruction of Bulk Operators within the Entanglement Wedge in Gauge-Gravity Duality*, *Phys. Rev. Lett.* **117** (2016) 021601, [1601.05416].

[43] J. Cotler, P. Hayden, G. Penington, G. Salton, B. Swingle and M. Walter, *Entanglement Wedge Reconstruction via Universal Recovery Channels*, *Phys. Rev. X* **9** (2019) 031011, [1704.05839].

[44] A. Almheiri, X. Dong and D. Harlow, *Bulk Locality and Quantum Error Correction in AdS/CFT*, *JHEP* **04** (2015) 163, [1411.7041].

[45] D. Harlow, *The Ryu–Takayanagi Formula from Quantum Error Correction*, *Commun. Math. Phys.* **354** (2017) 865–912, [1607.03901].

[46] F. Pastawski, B. Yoshida, D. Harlow and J. Preskill, *Holographic quantum error-correcting codes: Toy models for the bulk/boundary correspondence*, *JHEP* **06** (2015) 149, [1503.06237].

[47] P. Hayden, S. Nezami, X.-L. Qi, N. Thomas, M. Walter and Z. Yang, *Holographic duality from random tensor networks*, *JHEP* **11** (2016) 009, [1601.01694].

[48] J. Maldacena, *Eternal black holes in anti-de Sitter*, *Journal of High Energy Physics* **2003** (2003) 021–021.

[49] J. Maldacena and L. Susskind, *Cool horizons for entangled black holes*, *Fortsch. Phys.* **61** (2013) 781–811, [1306.0533].

[50] G. T. Horowitz and J. Polchinski, *Gauge/gravity duality*, gr-qc/0602037.

[51] D. Marolf, *Unitarity and Holography in Gravitational Physics*, *Phys. Rev. D* **79** (2009) 044010, [0808.2842].

[52] L. Susskind, *Computational complexity and black hole horizons*, *Fortschritte der Physik* **64** (2016) 24–43.

[53] A. R. Brown, D. A. Roberts, L. Susskind, B. Swingle and Y. Zhao, *Holographic Complexity Equals Bulk Action?*, *Physical Review Letters* **116** (2016) .

[54] A. R. Brown, D. A. Roberts, L. Susskind, B. Swingle and Y. Zhao, *Complexity, action, and black holes*, *Physical Review D* **93** (2016) .

[55] P. Gao, D. L. Jafferis and A. C. Wall, *Traversable Wormholes via a Double Trace Deformation*, *JHEP* **12** (2017) 151, [1608.05687].

[56] S. Ryu and T. Takayanagi, *Aspects of holographic entanglement entropy*, *Journal of High Energy Physics* **2006** (2006) .

[57] H. Casini, M. Huerta and R. C. Myers, *Towards a derivation of holographic entanglement entropy*, *Journal of High Energy Physics* **2011** (2011) .

[58] L. Susskind, *Computational Complexity and Black Hole Horizons*, *Fortsch. Phys.* **64** (2016) 24–43, [1403.5695].

[59] D. Stanford and L. Susskind, *Complexity and shock wave geometries*, *Physical Review D - Particles, Fields, Gravitation and Cosmology* **90** (2014) .

[60] M. A. Nielsen, *A geometric approach to quantum circuit lower bounds*, 0502070.

[61] M. A. Nielsen, M. R. Dowling, M. Gu and A. C. Doherty, *Quantum computation as geometry*, *Science* **311** (2006) 1133–1135.

[62] M. R. Dowling and M. A. Nielsen, *The geometry of quantum computation*, 0701004.

[63] R. A. Jefferson and R. C. Myers, *Circuit complexity in quantum field theory*, *Journal of High Energy Physics* **2017** (2017) .

[64] S. Chapman, M. P. Heller, H. Marrochio and F. Pastawski, *Towards Complexity for Quantum Field Theory States*, *Physical Review Letters* **120** (2017) 121602, [1707.08582].

[65] M. Sinamuli and R. B. Mann, *Topological and time dependence of the action-complexity relation*, *Phys. Rev. D* **98** (2018) 026005, [1804.07333].

[66] R. Khan, C. Krishnan and S. Sharma, *Circuit complexity in fermionic field theory*, *Physical Review D* **98** (2018) .

[67] R. Q. Yang, *Complexity for quantum field theory states and applications to thermofield double states*, *Physical Review D* **97** (2018) .

[68] M. Sinamuli and R. B. Mann, *Holographic Complexity and Charged Scalar Fields*, *Phys. Rev.* **D99** (2019) 106013, [1902.01912].

[69] D. Carmi, S. Chapman, H. Marrochio, R. C. Myers and S. Sugishita, *On the time dependence of holographic complexity*, *Journal of High Energy Physics* **2017** (2017) .

[70] L. Lehner, R. C. Myers, E. Poisson and R. D. Sorkin, *Gravitational action with null boundaries*, *Physical Review D* **94** (2016) .

[71] T. Hartman and J. Maldacena, *Time Evolution of Entanglement Entropy from Black Hole Interiors*, *JHEP* **05** (2013) 014, [1303.1080].

[72] L. Susskind, *Entanglement is not enough*, *Fortsch. Phys.* **64** (2016) 49–71, [1411.0690].

[73] S. Lloyd, *Ultimate physical limits to computation*, *Nature* **406** (2000) 1047–1054.

[74] W. Cottrell and M. Montero, *Complexity is simple!*, *JHEP* **02** (2018) 039, [1710.01175].

[75] S. P. Jordan, *Fast quantum computation at arbitrarily low energy*, *Phys. Rev. A* **95** (2017) 032305, [1701.01175].

[76] H. Huang, X.-H. Feng and H. Lu, *Holographic Complexity and Two Identities of Action Growth*, *Phys. Lett. B* **769** (2017) 357–361, [1611.02321].

[77] P. A. Cano, R. A. Hennigar and H. Marrochio, *Complexity Growth Rate in Lovelock Gravity*, *Physical Review Letters* **121** (2018) .

[78] J. Jiang, *Action growth rate for a higher curvature gravitational theory*, *Phys. Rev. D* **98** (2018) 086018, [1810.00758].

[79] A. P. Reynolds and S. F. Ross, *Complexity of the AdS Soliton*, *Class. Quant. Grav.* **35** (2018) 095006, [1712.03732].

[80] Z. Fu, A. Maloney, D. Marolf, H. Maxfield and Z. Wang, *Holographic complexity is nonlocal*, *JHEP* **02** (2018) 072, [1801.01137].

[81] S. Andrews, R. A. Hennigar and H. K. Kunduri, *Chemistry and Complexity for Solitons in AdS_5*, 1912.07637.

[82] S. Chapman, H. Marrochio and R. C. Myers, *Holographic complexity in Vaidya spacetimes. Part I*, *JHEP* **06** (2018) 046, [1804.07410].

[83] S. Chapman, H. Marrochio and R. C. Myers, *Holographic complexity in Vaidya spacetimes. Part II*, *JHEP* **06** (2018) 114, [1805.07262].

[84] D. Carmi, R. C. Myers and P. Rath, *Comments on Holographic Complexity*, *JHEP* **03** (2017) 118, [1612.00433].

[85] Z.-Y. Fan and M. Guo, *Holographic complexity under a global quantum quench*, *Nucl. Phys. B* **950** (2020) 114818, [1811.01473].

[86] S. Chapman, D. Ge and G. Policastro, *Holographic Complexity for Defects Distinguishes Action from Volume*, *JHEP* **05** (2019) 049, [1811.12549].

[87] A. Bernamonti, F. Galli, J. Hernandez, R. C. Myers, S.-M. Ruan and J. Simn, *First Law of Holographic Complexity*, *Phys. Rev. Lett.* **123** (2019) 081601, [1903.04511].

[88] A. Bernamonti, F. Galli, J. Hernandez, R. C. Myers, S.-M. Ruan and J. Simn, *Aspects of The First Law of Complexity*, 2002.05779.

[89] S. W. Hawking, C. J. Hunter and M. M. Taylor-Robinson, *Rotation and the ads-cft correspondence*, *Phys. Rev. D* **59** (Feb, 1999) 064005.

[90] R. B. Mann, *Entropy of rotating Misner string space-times*, *Phys. Rev. D* **61** (2000) 084013, [hep-th/9904148].

[91] S. W. Hawking and H. S. Reall, *Charged and rotating AdS black holes and their CFT duals*, *Phys. Rev.* **D61** (2000) 024014, [hep-th/9908109].

[92] D. S. Berman and M. K. Parikh, *Holography and rotating AdS black holes*, *Phys. Lett.* **B463** (1999) 168–173, [hep-th/9907003].

[93] S. Das and R. B. Mann, *Conserved quantities in Kerr-anti-de Sitter space-times in various dimensions*, *JHEP* **08** (2000) 033, [hep-th/0008028].

[94] M. Guica, T. Hartman, W. Song and A. Strominger, *The Kerr/CFT Correspondence*, *Phys. Rev.* **D80** (2009) 124008, [0809.4266].

[95] I. Bredberg, C. Keeler, V. Lysov and A. Strominger, *Cargese Lectures on the Kerr/CFT Correspondence*, *Nucl. Phys. Proc. Suppl.* **216** (2011) 194–210, [1103.2355].

[96] G. Compere, *The Kerr/CFT correspondence and its extensions*, *Living Rev. Rel.* **15** (2012) 11, [1203.3561].

[97] R. G. Cai, S. M. Ruan, S. J. Wang, R. Q. Yang and R. H. Peng, *Action growth for AdS black holes*, *Journal of High Energy Physics* **2016** (2016) .

[98] K. Nagasaki, *Complexity growth of rotating black holes with a probe string*, *Phys. Rev.* **D98** (2018) 126014, [1807.01088].

[99] S. Chapman and H. Z. Chen, *Complexity for Charged Thermofield Double States*, 1910.07508.

[100] M. Brigante, H. Liu, R. C. Myers, S. Shenker and S. Yaida, *Viscosity Bound Violation in Higher Derivative Gravity*, *Phys. Rev. D* **77** (2008) 126006, [0712.0805].

[101] R. C. Myers, M. F. Paulos and A. Sinha, *Holographic studies of quasi-topological gravity*, *JHEP* **08** (2010) 035, [1004.2055].

[102] R. C. Myers and A. Sinha, *Holographic c-theorems in arbitrary dimensions*, *JHEP* **01** (2011) 125, [1011.5819].

[103] M. Mezei, *Entanglement entropy across a deformed sphere*, *Phys. Rev. D* **91** (2015) 045038, [1411.7011].

[104] P. Bueno, R. C. Myers and W. Witczak-Krempa, *Universality of corner entanglement in conformal field theories*, *Phys. Rev. Lett.* **115** (2015) 021602, [1505.04804].

[105] P. Bueno, P. A. Cano, R. A. Hennigar and R. B. Mann, *Universality of Squashed-Sphere Partition Functions*, *Phys. Rev. Lett.* **122** (2019) 071602, [1808.02052].

[106] D. Kastor, S. Ray and J. Traschen, *Enthalpy and the Mechanics of AdS Black Holes*, *Class. Quant. Grav.* **26** (2009) 195011, [0904.2765].

[107] M. Cvetic, G. Gibbons, D. Kubiznak and C. Pope, *Black Hole Enthalpy and an Entropy Inequality for the Thermodynamic Volume*, *Phys. Rev. D* **84** (2011) 024037, [1012.2888].

[108] A. B. Bordo, *Geometric and Thermodynamic Volume of Hairy Black Branes*, 2006.10880.

[109] J. Couch, W. Fischler and P. H. Nguyen, *Noether charge, black hole volume, and complexity*, *JHEP* **03** (2017) 119, [1610.02038].

[110] Z.-Y. Fan and M. Guo, *On the Noether charge and the gravity duals of quantum complexity*, *JHEP* **08** (2018) 031, [1805.03796].

[111] H.-S. Liu, H. L, L. Ma and W.-D. Tan, *Holographic Complexity Bounds*, *JHEP* **07** (2020) 090, [1910.10723].

[112] W. Sun and X.-H. Ge, *Complexity growth rate, grand potential and partition function*, 1912.00153.

[113] C. V. Johnson, *Holographic Heat Engines*, *Class. Quant. Grav.* **31** (2014) 205002, [1404.5982].

[114] D. Kastor, S. Ray and J. Traschen, *Chemical Potential in the First Law for Holographic Entanglement Entropy*, *JHEP* **11** (2014) 120, [1409.3521].

[115] A. Karch and B. Robinson, *Holographic Black Hole Chemistry*, *JHEP* **12** (2015) 073, [1510.02472].

[116] E. Caceres, P. H. Nguyen and J. F. Pedraza, *Holographic entanglement chemistry*, *Phys. Rev. D* **95** (2017) 106015, [1605.00595].

[117] M. Sinamuli and R. B. Mann, *Higher Order Corrections to Holographic Black Hole Chemistry*, *Phys. Rev. D* **96** (2017) 086008, [1706.04259].

[118] C. V. Johnson and F. Rosso, *Holographic Heat Engines, Entanglement Entropy, and Renormalization Group Flow*, *Class. Quant. Grav.* **36** (2019) 015019, [1806.05170].

[119] C. V. Johnson, V. L. Martin and A. Svesko, *Microscopic description of thermodynamic volume in extended black hole thermodynamics*, *Phys. Rev. D* **101** (2020) 086006, [1911.05286].

[120] F. Rosso and A. Svesko, *Novel Aspects of the Extended First Law of Entanglement*, 2003.10462.

[121] G. Gibbons, H. Lu, D. N. Page and C. Pope, *The General Kerr-de Sitter metrics in all dimensions*, *J. Geom. Phys.* **53** (2005) 49–73, [hep-th/0404008].

[122] H. K. Kunduri, J. Lucietti and H. S. Reall, *Gravitational perturbations of higher dimensional rotating black holes: Tensor perturbations*, *Phys. Rev.* **D74** (2006) 084021, [hep-th/0606076].

[123] G. Gibbons, M. Perry and C. Pope, *The First law of thermodynamics for Kerr-anti-de Sitter black holes*, *Class. Quant. Grav.* **22** (2005) 1503–1526, [hep-th/0408217].

[124] D. Kubiznak, R. B. Mann and M. Teo, *Black hole chemistry: thermodynamics with Lambda*, *Class. Quant. Grav.* **34** (2017) 063001, [1608.06147].

[125] F. Pretorius and W. Israel, *Quasi-spherical light cones of the Kerr geometry*, *Classical and Quantum Gravity* **15** (1998) 2289–2301.

[126] M. Banados, M. Henneaux, C. Teitelboim and J. Zanelli, *Geometry of the (2+1) black hole*, *Phys. Rev. D* **48** (1993) 1506–1525, [gr-qc/9302012].

[127] I. S. Booth, *Metric based Hamiltonians, null boundaries, and isolated horizons*, *Class. Quant. Grav.* **18** (2001) 4239–4264, [gr-qc/0105009].

[128] J. W. York, *Role of conformal three-geometry in the dynamics of gravitation*, *Physical Review Letters* **28** (1972) 1082–1085.

[129] G. W. Gibbons and S. W. Hawking, *Action integrals and partition functions in quantum gravity*, *Physical Review D* **15** (1977) 2752–2756.

[130] G. Hayward, *Gravitational action for spacetimes with nonsmooth boundaries*, *Physical Review D* **47** (1993) 3275–3280.

[131] I. Booth and R. B. Mann, *Static and infalling quasilocal energy of charged and naked black holes*, *Phys. Rev. D* **60** (1999) 124009.

[132] L. Susskind and Y. Zhao, *Switchbacks and the Bridge to Nowhere*, 1408.2823.

[133] K. Skenderis, *Lecture notes on holographic renormalization*, in *Classical and Quantum Gravity*, vol. 19, pp. 5849–5876, 2002. DOI.

[134] S. De Haro, K. Skenderis and S. N. Solodukhin, *Holographic reconstruction of spacetime and renormalization in the AdS/CFT correspondence*, *Communications in Mathematical Physics* **217** (2001) 595–622.

[135] C. Fefferman and C. R. Graham, *The ambient metric*, 0710.0919.

[136] K. Goto, H. Marrochio, R. C. Myers, L. Queimada and B. Yoshida, *Holographic Complexity Equals Which Action?*, *JHEP* **02** (2019) 160, [1901.00014].

[137] A. R. Brown, H. Gharibyan, H. W. Lin, L. Susskind, L. Thorlacius and Y. Zhao, *Complexity of Jackiw-Teitelboim gravity*, *Phys. Rev. D* **99** (2019) 046016, [1810.08741].

[138] Z.-Y. Fan and H.-Z. Liang, *Time dependence of complexity for Lovelock black holes*, *Phys. Rev. D* **100** (2019) 086016, [1908.09310].

[139] V. Balasubramanian, A. Kar and G. Srosi, *Holographic Probes of Inner Horizons*, *JHEP* **06** (2020) 054, [1911.12413].

[140] S. Hollands, R. M. Wald and J. Zahn, *Quantum instability of the Cauchy horizon in Reissner–Nordstrm–deSitter spacetime*, *Class. Quant. Grav.* **37** (2020) 115009, [1912.06047].

[141] S. A. Hartnoll, G. T. Horowitz, J. Kruthoff and J. E. Santos, *Gravitational duals to the grand canonical ensemble abhor Cauchy horizons*, 2006.10056.

[142] O. Coussaert and M. Henneaux, *Supersymmetry of the (2+1) black holes*, *Phys. Rev. Lett.* **72** (1994) 183–186, [hep-th/9310194].

[143] J. Jiang and M. Zhang, *Holographic Complexity in a Charged Supersymmetric Black Holes*, 2009.06830.

[144] A. R. Brown and L. Susskind, *Second law of quantum complexity*, *Phys. Rev. D* **97** (2018) 086015, [1701.01107].

[145] A. Einstein and N. Rosen, *The Particle Problem in the General Theory of Relativity*, *Phys. Rev.* **48** (1935) 73–77.

[146] J. L. Friedman, K. Schleich and D. M. Witt, *Topological censorship*, *Phys. Rev. Lett.* **71** (Sep, 1993) 1486–1489.

[147] G. Galloway, K. Schleich, D. Witt and E. Woolgar, *Topological censorship and higher genus black holes*, *Phys. Rev. D* **60** (1999) 104039, [gr-qc/9902061].

[148] E. Caceres, A. S. Misobuchi and M.-L. Xiao, *Rotating traversable wormholes in AdS*, *JHEP* **12** (2018) 005, [1807.07239].

[149] Z. Fu, B. Grado-White and D. Marolf, *A perturbative perspective on self-supporting wormholes*, *Class. Quant. Grav.* **36** (2019) 045006, [1807.07917].

[150] Z. Fu, B. Grado-White and D. Marolf, *Traversable Asymptotically Flat Wormholes with Short Transit Times*, *Class. Quant. Grav.* **36** (2019) 245018, [1908.03273].

[151] J. Maldacena, A. Milekhin and F. Popov, *Traversable wormholes in four dimensions*, 1807.04726.

[152] J. Maldacena, D. Stanford and Z. Yang, *Diving into traversable wormholes*, *Fortsch. Phys.* **65** (2017) 1700034, [1704.05333].

[153] J. Maldacena and X.-L. Qi, *Eternal traversable wormhole*, 1804.00491.

[154] G. T. Horowitz, D. Marolf, J. E. Santos and D. Wang, *Creating a Traversable Wormhole*, *Class. Quant. Grav.* **36** (2019) 205011, [1904.02187].

[155] L. Susskind and Y. Zhao, *Teleportation through the wormhole*, *Phys. Rev. D* **98** (2018) 046016, [1707.04354].

[156] R. van Breukelen and K. Papadodimas, *Quantum teleportation through time-shifted AdS wormholes*, *JHEP* **08** (2018) 142, [1708.09370].

[157] B. Yoshida and N. Y. Yao, *Disentangling Scrambling and Decoherence via Quantum Teleportation*, *Phys. Rev. X* **9** (2019) 011006, [1803.10772].

[158] D. Bak, C. Kim and S.-H. Yi, *Bulk view of teleportation and traversable wormholes*, *JHEP* **08** (2018) 140, [1805.12349].

[159] B. Freivogel, D. A. Galante, D. Nikolakopoulou and A. Rotundo, *Traversable wormholes in AdS and bounds on information transfer*, *JHEP* **01** (2020) 050, [1907.13140].

[160] A. R. Brown, H. Gharibyan, S. Leichenauer, H. W. Lin, S. Nezami, G. Salton et al., *Quantum Gravity in the Lab: Teleportation by Size and Traversable Wormholes*, 1911.06314.

[161] D. Marolf, H. Maxfield, A. Peach and S. F. Ross, *Hot multiboundary wormholes from bipartite entanglement*, *Class. Quant. Grav.* **32** (2015) 215006, [1506.04128].

[162] S. Aminneborg, I. Bengtsson, D. Brill, S. Holst and P. Peldan, *Black holes and wormholes in (2+1)-dimensions*, *Class. Quant. Grav.* **15** (1998) 627–644, [gr-qc/9707036].

[163] D. R. Brill, *Multi - black hole geometries in (2+1)-dimensional gravity*, *Phys. Rev. D* **53** (1996) 4133–4176, [gr-qc/9511022].

[164] D. Brill, *Black holes and wormholes in (2+1)-dimensions*, *Lect. Notes Phys.* **537** (2000) 143, [gr-qc/9904083].

[165] H. Maxfield, *Entanglement entropy in three dimensional gravity*, *JHEP* **04** (2015) 031, [1412.0687].

[166] S. Aminneborg, I. Bengtsson and S. Holst, *A Spinning anti-de Sitter wormhole*, *Class. Quant. Grav.* **16** (1999) 363–382, [gr-qc/9805028].

[167] K. Krasnov, *Analytic continuation for asymptotically AdS 3-D gravity*, *Class. Quant. Grav.* **19** (2002) 2399–2424, [gr-qc/0111049].

[168] E. Caceres, A. Kundu, A. K. Patra and S. Shashi, *A Killing Vector Treatment of Multiboundary Wormholes*, *JHEP* **02** (2020) 149, [1912.08793].

[169] M. Banados, C. Teitelboim and J. Zanelli, *The Black hole in three-dimensional space-time*, *Phys. Rev. Lett.* **69** (1992) 1849–1851, [hep-th/9204099].

[170] M. Headrick, V. E. Hubeny, A. Lawrence and M. Rangamani, *Causality & holographic entanglement entropy*, *JHEP* **12** (2014) 162, [1408.6300].

[171] V. Balasubramanian, P. Hayden, A. Maloney, D. Marolf and S. F. Ross, *Multiboundary Wormholes and Holographic Entanglement*, *Class. Quant. Grav.* **31** (2014) 185015, [1406.2663].

[172] H. Maxfield, S. Ross and B. Way, *Holographic partition functions and phases for higher genus Riemann surfaces*, *Class. Quant. Grav.* **33** (2016) 125018, [1601.00980].

[173] S. Hawking and D. N. Page, *Thermodynamics of Black Holes in anti-De Sitter Space*, *Commun. Math. Phys.* **87** (1983) 577.

[174] J. M. Maldacena, *Eternal black holes in anti-de Sitter*, *JHEP* **04** (2003) 021, [hep-th/0106112].

[175] X. Dong, S. Maguire, A. Maloney and H. Maxfield, *Phase transitions in 3D gravity and fractal dimension*, *JHEP* **05** (2018) 080, [1802.07275].

[176] T. Banks, M. R. Douglas, G. T. Horowitz and E. J. Martinec, *AdS dynamics from conformal field theory*, hep-th/9808016.

[177] D. Harlow and D. Stanford, *Operator Dictionaries and Wave Functions in AdS/CFT and dS/CFT*, 1104.2621.

[178] J. Louko, D. Marolf and S. F. Ross, *On geodesic propagators and black hole holography*, *Phys. Rev. D* **62** (2000) 044041, [hep-th/0002111].

[179] S. Fallows and S. F. Ross, *Making near-extremal wormholes traversable*, 2008.07946.

[180] P. Hayden and J. Preskill, *Black holes as mirrors: Quantum information in random subsystems*, *JHEP* **09** (2007) 120, [0708.4025].

[181] K. Landsman, C. Figgatt, T. Schuster, N. Linke, B. Yoshida, N. Yao et al., *Verified Quantum Information Scrambling*, *Nature* **567** (2019) 61–65, [1806.02807].

[182] R. Emparan, B. Grado-White, D. Marolf and M. Tomasevic, *Multi-mouth Traversable Wormholes*, 2012.07821.

[183] S. Nezami, H. W. Lin, A. R. Brown, H. Gharibyan, S. Leichenauer, G. Salton et al., *Quantum Gravity in the Lab: Teleportation by Size and Traversable Wormholes, Part II*, 2102.01064.

[184] T. Schuster, B. Kobrin, P. Gao, I. Cong, E. T. Khabiboulline, N. M. Linke et al., *Many-body quantum teleportation via operator spreading in the traversable wormhole protocol*, 2102.00010.

[185] C. Kiefer, *Quantum gravity: general introduction and recent developments*, *Annalen der Physik* **15** (2006) 129–148, [0508120].

[186] R. P. Woodard, *How Far Are We from the Quantum Theory of Gravity?*, *Quantum* **126002** (2009) 106, [0907.4238].

[187] C. Barceló, R. Carballo-Rubio and L. J. Garay, *Gravitational wave echoes from macroscopic quantum gravity effects*, *Journal of High Energy Physics* **2017** (2017) .

[188] R. Feynman, *The Role of Gravitation in Physics: Report from the Chapel Hill Conference Proceedings*. 1957.

[189] R. Colella, A. W. Overhauser and S. A. Werner, *Observation of gravitationally induced quantum interference*, *Phys. Rev. Lett.* **34** (Jun, 1975) 1472–1474.

[190] A. Peters, K. Y. Chung and S. Chu, *Measurement of gravitational acceleration by dropping atoms*, *Nature* **400** (1999) 849–852.

[191] V. V. Nesvizhevsky, H. G. Börner, A. K. Petukhov, H. Abele, S. Baeßler, F. J. Rueß et al., *Quantum states of neutrons in the earth's gravitational field*, *Nature* **415** (2002) 297–299.

[192] C. Marletto and V. Vedral, *Gravitationally Induced Entanglement between Two Massive Particles is Sufficient Evidence of Quantum Effects in Gravity*, *Physical Review Letters* **119** (2017) , [1707.06036].

[193] S. Bose, A. Mazumdar, G. W. Morley, H. Ulbricht, M. Toroš, M. Paternostro et al., *Spin Entanglement Witness for Quantum Gravity*, *Physical Review Letters* **119** (2017) , [1707.06050].

[194] T. Krisnanda, G. Y. Tham, M. Paternostro and T. Paterek, *Observable quantum entanglement due to gravity*, *npj Quantum Information* **6** (2020) 12, [1906.08808].

[195] M. Bahrami, A. Bassi, S. McMillen, M. Paternostro and H. Ulbricht, *Is Gravity Quantum?*, 1507.05733.

[196] M. Carlesso, A. Bassi, M. Paternostro and H. Ulbricht, *Testing the gravitational field generated by a quantum superposition*, *New J. Phys.* **21** (2019) 093052, [1906.04513].

[197] C. Anastopoulos and B.-L. Hu, *Probing a Gravitational Cat State*, *Class. Quant. Grav.* **32** (2015) 165022, [1504.03103].

[198] M. Aspelmeyer, T. J. Kippenberg and F. Marquardt, *Cavity optomechanics*, *Reviews of Modern Physics* **86** (2014) 1391–1452, [0712.1618].

[199] P. Asenbaum, C. Overstreet, T. Kovachy, D. D. Brown, J. M. Hogan and M. A. Kasevich, *Phase Shift in an Atom Interferometer due to Spacetime Curvature across its Wave Function*, *Physical Review Letters* **118** (2017) , [1610.03832].

[200] L. Diósi, *Gravitation and quantum-mechanical localization of macro-objects*, *Physics Letters A* **105** (1984) 199–202, [1412.0201].

[201] R. Penrose, *On Gravity's role in Quantum State Reduction*, *General Relativity and Gravitation* **28** (1996) 581–600.

[202] W. Marshall, C. Simon, R. Penrose and D. Bouwmeester, *Towards quantum superpositions of a mirror*, *Physical Review Letters* **91** (2003) , [0210001].

[203] Y. Chen, *Macroscopic Quantum Mechanics: Theory and Experimental Concepts of Optomechanics*, *J. Phys. B* **46** (2013) 104001, [1302.1924].

[204] S. L. Adler, A. Bassi and E. Ippoliti, *Towards quantum superpositions of a mirror: An exact open systems analysis - Calculational details*, *Journal of Physics A: Mathematical and General* **38** (2005) 2715–2727, [0407084].

[205] D. Kleckner, I. Pikovski, E. Jeffrey, L. Ament, E. Eliel, J. Van Den Brink et al., *Creating and verifying a quantum superposition in a micro-optomechanical system*, *New Journal of Physics* **10** (2008) , [0807.1834].

[206] C. K. Law, *Interaction between a moving mirror and radiation pressure: A Hamiltonian formulation*, *Physical Review A* **51** (1995) 2537–2541.

[207] S. Mancini, V. I. Man'ko and P. Tombesi, *Ponderomotive control of quantum macroscopic coherence*, *Physical Review A - Atomic, Molecular, and Optical Physics* **55** (1997) 3042–3050, [9612005].

[208] S. Bose, K. Jacobs and P. L. Knight, *Preparation of nonclassical states in cavities with a moving mirror*, *Physical Review A - Atomic, Molecular, and Optical Physics* **56** (1997) 4175–4186, [9708002].

[209] J. D. Teufel, T. Donner, D. Li, J. W. Harlow, M. S. Allman, K. Cicak et al., *Sideband cooling of micromechanical motion to the quantum ground state*, *Nature* **475** (2011) 359–363, [1103.2144].

[210] J. Chan, T. P. Alegre, A. H. Safavi-Naeini, J. T. Hill, A. Krause, S. Gröblacher et al., *Laser cooling of a nanomechanical oscillator into its quantum ground state*, *Nature* **478** (2011) 89–92, [1106.3614].

[211] R. A. Norte, J. P. Moura and S. Gröblacher, *Mechanical Resonators for Quantum Optomechanics Experiments at Room Temperature*, *Physical Review Letters* **116** (2016) , [1511.06235].

[212] J. Schmole, M. Dragosits, H. Hepach and M. Aspelmeyer, *A micromechanical proof-of-principle experiment for measuring the gravitational force of milligram masses*, *Classical and Quantum Gravity* **33** (2016) 125031.

[213] M. Bhattacharya and P. Meystre, *Trapping and cooling a mirror to its quantum mechanical ground state*, *Physical Review Letters* **99** (2007) , [0704.2425].

[214] E. Joos, H. D. Zeh, C. Kiefer, D. J. W. Giulini, J. Kupsch and I.-O. Stamatescu, *Decoherence and the Appearance of a Classical World in Quantum Theory*. Springer, 2003.

[215] J. Gieseler, B. Deutsch, R. Quidant and L. Novotny, *Subkelvin parametric feedback cooling of a laser-trapped nanoparticle*, *Physical Review Letters* **109** (2012) , [1202.6435].

[216] H. Cavendish, *Experiments to determine the density of the earth. by henry cavendish, esq. f. r. s. and a. s.*, *Philosophical Transactions of the Royal Society of London* **88** (1798) 469–526.

[217] D. J. Kapner, T. S. Cook, E. G. Adelberger, J. H. Gundlach, B. R. Heckel, C. D. Hoyle et al., *Tests of the gravitational inverse-square law below the dark-energy length scale*, *Physical Review Letters* **98** (2007) , [0611184].

[218] P. H. Kim, B. D. Hauer, C. Doolin, F. Souris and J. P. Davis, *Approaching the standard quantum limit of mechanical torque sensing*, *Nature Communications* **7** (2016) , [1607.00069].

[219] T. Westphal, H. Hepach, J. Pfaff and M. Aspelmeyer, *Measurement of gravitational coupling between millimetre-sized masses*, *Nature* **591** (2021) 225–228, [2009.09546].

[220] M. Carlesso, M. Paternostro, H. Ulbricht and A. Bassi, *When Cavendish meets Feynman: A quantum torsion balance for testing the quantumness of gravity*, 1710.08695.

[221] J. Ahn, Z. Xu, J. Bang, Y.-H. Deng, T. M. Hoang, Q. Han et al., *Optically Levitated Nanodumbbell Torsion Balance and GHz Nanomechanical Rotor*, 1804.06570.

[222] G. M. Harry, *Advanced LIGO: The next generation of gravitational wave detectors*, *Classical and Quantum Gravity* **27** (2010) .

[223] N. Matsumoto, K. Komori, Y. Michimura, G. Hayase, Y. Aso and K. Tsubono, *5-mg suspended mirror driven by measurement-induced backaction*, *Physical Review A - Atomic, Molecular, and Optical Physics* **92** (2015) , [1312.5031].

[224] Y. Enomoto, K. Nagano and S. Kawamura, *Standard quantum limit of angular motion of a suspended mirror and homodyne detection of a ponderomotively squeezed vacuum field*, *Physical Review A* **94** (2016) , [1602.05344].

[225] M. J. Hartmann and M. B. Plenio, *Steady state entanglement in the mechanical vibrations of two dielectric membranes*, *Phys. Rev. Lett.* **101** (Nov, 2008) 200503.

[226] D. Perez-Garcia, F. Verstraete, M. Wolf and J. Cirac, *Matrix product state representations*, *Quant. Inf. Comput.* **7** (2007) 401.

[227] J. Haegeman, T. J. Osborne and F. Verstraete, *Post-matrix product state methods: To tangent space and beyond*, *Phys. Rev. B* **88** (Aug, 2013) 075133.

[228] R. Orús, *Advances on tensor network theory: symmetries, fermions, entanglement, and holography*, *Eur. Phys. J. B* **87** (2014) 280.

[229] G. Evenbly and G. Vidal, *Tensor network renormalization*, *Phys. Rev. Lett.* **115** (Oct, 2015) 180405.

[230] F. Güttge, F. B. Anders, U. Schollwöck, E. Eidelstein and A. Schiller, *Hybrid nrg-dmrg approach to real-time dynamics of quantum impurity systems*, *Phys. Rev. B* **87** (Mar, 2013) 115115.

[231] Y.-C. He, M. P. Zaletel, M. Oshikawa and F. Pollmann, *Signatures of dirac cones in a dmrg study of the kagome heisenberg model*, *Phys. Rev. X* **7** (Jul, 2017) 031020.

[232] M. C. Banuls, K. Cichy, J. I. Cirac, K. Jansen and H. Saito, *Matrix Product States for Lattice Field Theories*, *PoS* **LATTICE 2013** (2014) 332.

[233] M. C. Bañuls and K. Cichy, *Review on novel methods for lattice gauge theories*, *Rep. Prog. Phys.* **83** (2020) 024401.

[234] M. Dalmonte and S. Montangero, *Lattice gauge theory simulations in the quantum information era*, *Contemp. Phys.* **57** (2016) 388–412.

[235] J. Bender, P. Emonts, E. Zohar and J. I. Cirac, *Real-time dynamics in 2+ 1d compact qed using complex periodic gaussian states*, 2006.10038.

[236] G. K.-L. Chan, J. J. Dorando, D. Ghosh, J. Hachmann, E. Neuscamman, H. Wang et al., *An introduction to the density matrix renormalization group ansatz in quantum chemistry*, in *Frontiers in quantum systems in chemistry and physics* (S. Wilson, P. J. Grout, J. Maru-ani, G. Delgado-Barrio and P. Piecuch, eds.), vol. 18 of *Progress in Theoretical Chemistry and Physics*, pp. 49–65. Springer, 2008.

[237] C. Krumnow, L. Veis, O. Legeza and J. Eisert, *Fermionic orbital optimization in tensor network states*, *Phys. Rev. Lett.* **117** (Nov, 2016) 210402.

[238] G. Ortiz, J. E. Gubernatis, E. Knill and R. Laflamme, *Quantum algorithms for fermionic simulations*, *Phys. Rev. A* **64** (Jul, 2001) 022319.

[239] A. Peruzzo, J. McClean, P. Shadbolt, M.-H. Yung, X.-Q. Zhou, P. J. Love et al., *A variational eigenvalue solver on a photonic quantum processor*, *Nat Commun.* **5** (2014) 4213.

[240] J. R. McClean, J. Romero, R. Babbush and A. Aspuru-Guzik, *The theory of variational hybrid quantum-classical algorithms*, *New J. Phys.* **18** (2016) 023023.

[241] E. Farhi, J. Goldstone and S. Gutmann, *A quantum approximate optimization algorithm*, *MIT-CTP/4610* (2014) .

[242] J. Preskill, *Quantum computing in the nisq era and beyond*, *Quantum* **2** (2018) 79.

[243] O. Shehab, I. H. Kim, N. H. Nguyen, K. Landsman, C. H. Alderete, D. Zhu et al., *Noise reduction using past causal cones in variational quantum algorithms*, 1906.00476.

[244] M. C. Bañuls, R. Blatt, J. Catani, A. Celi, J. I. Cirac, M. Dalmonte et al., *Simulating lattice gauge theories within quantum technologies*, *Eur. Phys. J. D* **74** (2020) 1–42.

[245] R. Kaubruegger, P. Silvi, C. Kokail, R. van Bijnen, A. M. Rey, J. Ye et al., *Variational spin-squeezing algorithms on programmable quantum sensors*, *Phys. Rev. Lett.* **123** (2019) 260505.

[246] E. F. Dumitrescu, A. J. McCaskey, G. Hagen, G. R. Jansen, T. D. Morris, T. Papenbrock et al., *Cloud quantum computing of an atomic nucleus*, *Phys. Rev. Lett.* **120** (May, 2018) 210501.

[247] J. F. Haase, L. Dellantonio, A. Celi, D. Paulson, A. Kan, K. Jansen et al., *A resource efficient approach for quantum and classical simulations of gauge theories in particle physics*, 2006.14160.

[248] B. Bauer, D. Wecker, A. J. Millis, M. B. Hastings and M. Troyer, *Hybrid quantum-classical approach to correlated materials*, *Phys. Rev. X* **6** (Sep, 2016) 031045.

[249] S. McArdle, S. Endo, A. Aspuru-Guzik, S. C. Benjamin and X. Yuan, *Quantum computational chemistry*, *Rev. Mod. Phys.* **92** (Mar, 2020) 015003.

[250] P. J. J. O'Malley, R. Babbush, I. D. Kivlichan, J. Romero, J. R. McClean, R. Barends et al., *Scalable quantum simulation of molecular energies*, *Phys. Rev. X* **6** (Jul, 2016) 031007.

[251] C. Kokail, C. Maier, R. van Bijnen, T. Brydges, M. K. Joshi, P. Jurcevic et al., *Self-verifying variational quantum simulation of lattice models*, *Nature* **569** (2019) 355–360.

[252] D. Paulson, L. Dellantonio, J. F. Haase, A. Celi, A. Kan, A. Jena et al., *Towards simulating 2d effects in lattice gauge theories on a quantum computer*, *arXiv preprint arXiv:2008.09252* (2020) .

[253] O. Shehab, K. Landsman, Y. Nam, D. Zhu, N. M. Linke, M. Keesan et al., *Toward convergence of effective-field-theory simulations on digital quantum computers*, *Phys. Rev. A* **100** (Dec, 2019) 062319.

[254] H.-H. Lu, N. Klco, J. M. Lukens, T. D. Morris, A. Bansal, A. Ekström et al., *Simulations of subatomic many-body physics on a quantum frequency processor*, *Phys. Rev. A* **100** (Jul, 2019) 012320.

[255] A. Borle, V. E. Elfving and S. J. Lomonaco, *Quantum approximate optimization for hard problems in linear algebra*, 2006.15438.

[256] C. Bravo-Prieto, R. LaRose, M. Cerezo, Y. Subasi, L. Cincio and P. Coles, *Variational quantum linear solver: A hybrid algorithm for linear systems*, *Bulletin of the American Physical Society* **65** (2020) .

[257] O. Kyriienko, A. E. Paine and V. E. Elfving, *Solving nonlinear differential equations with differentiable quantum circuits*, 2020.

[258] R. Raussendorf and H. J. Briegel, *A one-way quantum computer*, *Phys. Rev. Lett.* **86** (May, 2001) 5188–5191.

[259] H. J. Briegel, D. E. Browne, W. Dür, R. Raussendorf and M. Van den Nest, *Measurement-based quantum computation*, *Nature Phys.* **5** (2009) 19–26.

[260] D. E. Browne and H. J. Briegel, *One-way quantum computation - a tutorial introduction*, 0603226.

[261] R. Raussendorf, D. E. Browne and H. J. Briegel, *Measurement-based quantum computation on cluster states*, *Phys. Rev. A* **68** (Aug, 2003) 022312.

[262] P. Walther, K. J. Resch, T. Rudolph, E. Schenck, H. Weinfurter, V. Vedral et al., *Experimental one-way quantum computing*, *Nature* **434** (2005) 169–176.

[263] M. V. Larsen, X. Guo, C. R. Breum, J. S. Neergaard-Nielsen and U. L. Andersen, *Deterministic multi-mode gates on a scalable photonic quantum computing platform*, 2010.14422.

[264] M. Zwerger, H. Briegel and W. Dr, *Measurement-based quantum communication*, *App. Phys. B* **122** (06, 2015) 50.

[265] M. Zwerger, H. Briegel and W. Dür, *Hybrid architecture for encoded measurement-based quantum computation*, *Sci Rep* **4** (2014) 5364.

[266] M. Zwerger, H. J. Briegel and W. Dür, *Universal and optimal error thresholds for measurement-based entanglement purification*, *Phys. Rev. Lett.* **110** (Jun, 2013) 260503.

[267] N. Moll, P. Barkoutsos, L. S. Bishop, J. M. Chow, A. Cross, D. J. Egger et al., *Quantum optimization using variational algorithms on near-term quantum devices*, *Quantum Science and Technology* **3** (jun, 2018) 030503.

[268] J. Schwinger, *The theory of quantized fields. i*, *Phys. Rev.* **82** (1951) 914.

[269] D. Gottesman, *Theory of fault-tolerant quantum computation*, *Phys. Rev. A* **57** (Jan, 1998) 127–137.

[270] R. Hübener, C. Kruszynska, L. Hartmann, W. Dür, M. B. Plenio and J. Eisert, *Tensor network methods with graph enhancement*, *Phys. Rev. B* **84** (Sep, 2011) 125103.

[271] M. Hein, J. Eisert and H. J. Briegel, *Multiparty entanglement in graph states*, *Phys. Rev. A* **69** (2004) 062311.

[272] M. Hein, W. Dür, J. Eisert, R. Raussendorf, M. Nest and H.-J. Briegel, *Entanglement in graph states and its applications*, *Proc. of the Int. School of Physics Enrico Fermi on Quantum Computers, Algorithms and Chaos* (2006) .

[273] M. A. Nielsen and I. L. Chuang, *Quantum Computation and Quantum Information: 10th Anniversary Edition*. Cambridge University Press, USA, 10th ed., 2011.

[274] S. Aaronson and D. Gottesman, *Improved simulation of stabilizer circuits*, *Phys. Rev. A* **70** (Nov, 2004) 052328.

[275] M. Van den Nest, J. Dehaene and B. De Moor, *Graphical description of the action of local clifford transformations on graph states*, *Phys. Rev. A* **69** (Feb, 2004) 022316.

[276] D. P. Kingma and J. Ba, *Adam: A method for stochastic optimization*, 1412.6980.

[277] S. Ruder, *An overview of gradient descent optimization algorithms*, 1609.04747.

[278] J. Stokes, J. Izaac, N. Killoran and G. Carleo, *Quantum Natural Gradient*, *Quantum* **4** (May, 2020) 269.

[279] C. Audet and J. E. Dennis, *Mesh adaptive direct search algorithms for constrained optimization*, *SIAM Journal on Optimization* **17** (2006) 188–217.

[280] C. E. Rasmussen, *Gaussian processes in machine learning*, in *Summer School on Machine Learning*, pp. 63–71, Springer, 2003.

[281] P. I. Frazier, *A tutorial on bayesian optimization*, 1807.02811.

[282] M. Cerezo et al., *Variational Quantum Algorithms*, 2012.09265.

[283] N. Klco, E. F. Dumitrescu, A. J. McCaskey, T. D. Morris, R. C. Pooser, M. Sanz et al., *Quantum-classical computation of schwinger model dynamics using quantum computers*, *Phys. Rev. A* **98** (Sep, 2018) 032331.

[284] C. J. Hamer, Z. Weihong and J. Oitmaa, *Series expansions for the massive schwinger model in hamiltonian lattice theory*, *Phys. Rev. D* **56** (Jul, 1997) 55–67.

[285] E. A. Martinez, C. A. Muschik, P. Schindler, D. Nigg, A. Erhard, M. Heyl et al., *Real-time dynamics of lattice gauge theories with a few-qubit quantum computer*, *Nature* **534** (2016) 516–519.

[286] C. Muschik, M. Heyl, E. Martinez, T. Monz, P. Schindler, B. Vogell et al., *U(1) wilson lattice gauge theories in digital quantum simulators*, *New Journal of Physics* **19** (oct, 2017) 103020.

[287] F. Arute, K. Arya, R. Babbush, D. Bacon, J. C. Bardin, R. Barends et al., *Hartree-fock on a superconducting qubit quantum computer*, *Science* **369** (2020) 1084–1089.

[288] S. R. Coleman, *More About the Massive Schwinger Model*, *Annals Phys.* **101** (1976) 239.

[289] D. Yang, G. S. Giri, M. Johanning, C. Wunderlich, P. Zoller and P. Hauke, *Analog quantum simulation of* $(1+1)$*-dimensional lattice qed with trapped ions*, *Phys. Rev. A* **94** (Nov, 2016) 052321.

[290] A. Y. Kitaev, *Fault-tolerant quantum computation by anyons*, *Ann. Phys.* **303** (2003) 2–30.

[291] L. Funcke, T. Hartung, K. Jansen, S. Khn and P. Stornati, *Dimensional expressivity analysis of parametric quantum circuits*, 2011.03532.

[292] W. Asavanant, Y. Shiozawa, S. Yokoyama, B. Charoensombutamon, H. Emura, R. N. Alexander et al., *Generation of time-domain-multiplexed two-dimensional cluster state*, *Science* **366** (2019) 373–376.

[293] M. V. Larsen, X. Guo, C. R. Breum, J. S. Neergaard-Nielsen and U. L. Andersen, *Deterministic generation of a two-dimensional cluster state*, *Science* **366** (2019) 369–372.

[294] K. Tiurev, P. L. Mirambell, M. B. Lauritzen, M. H. Appel, A. Tiranov, P. Lodahl et al., *Fidelity of time-bin entangled multi-photon states from a quantum emitter*, 2007.09298.

[295] K. Tiurev, M. H. Appel, P. L. Mirambell, M. B. Lauritzen, A. Tiranov, P. Lodahl et al., *High-fidelity multi-photon-entangled cluster state with solid-state quantum emitters in photonic nanostructures*, 2007.09295.

[296] I. Schwartz, D. Cogan, E. R. Schmidgall, Y. Don, L. Gantz, O. Kenneth et al., *Deterministic generation of a cluster state of entangled photons*, *Science* **354** (2016) 434–437.

[297] T. Bastin, C. Thiel, J. von Zanthier, L. Lamata, E. Solano and G. S. Agarwal, *Operational determination of multiqubit entanglement classes via tuning of local operations*, *Phys. Rev. Lett.* **102** (Feb, 2009) 053601.

[298] J. Winicour, *Characteristic Evolution and Matching*, *Living Rev. Rel.* **8** (2005) 10, [gr-qc/0508097].

[299] V. Perlick, *Gravitational lensing from a spacetime perspective*, *Living Rev. Rel.* **7** (2004) 9.

[300] B. Carter, *Hamilton-Jacobi and Schrodinger separable solutions of Einstein's equations*, *Commun. Math. Phys.* **10** (1968) 280–310.

[301] M. M. Caldarelli, G. Cognola and D. Klemm, *Thermodynamics of Kerr-Newman-AdS black holes and conformal field theories*, *Class. Quant. Grav.* **17** (2000) 399–420, [hep-th/9908022].

[302] A. G. Agnese and M. La Camera, *Kerr - AdS and Kerr - dS solutions revisited*, *Phys. Rev.* **D61** (2000) 087502, [gr-qc/9907030].

[303] G. W. Gibbons and M. S. Volkov, *Zero mass limit of Kerr spacetime is a wormhole*, *Physical Review D* (2017) .

[304] K. S. Thorne, R. H. Price, D. A. Macdonald and S. Detweiler, *Black Holes: The Membrane Paradigm* , *Physics Today* (1988) .

APPENDICES

Appendix A

Appendices to chapter 2

A.1 Fefferman-Graham form of the metric

In computing the complexity of formation, it is important to justify equating the cutoffs at large distance $r_{\max}$ in both AdS and the black hole spacetimes. To see that this is the case, here we case the metric into the Fefferman-Graham form which will then allow us to directly compare the differences in the fall off of the metric components.

We define a new coordinate ρ according to the relation

$$g^2 dr^2 = \frac{\ell^2}{\rho^2} d\rho^2 \,. \tag{A.1}$$

Directly solving this relation to obtain r as a function of ρ yields

$$r = \rho - \frac{\ell^2}{4\rho} + \frac{\ell^2 M \Xi}{(2N+2)\rho^{2N+1}} + \mathcal{O}\left(\rho^{-(2N+3)}\right) \,. \tag{A.2}$$

In terms of the coordinate ρ the metric now reads

$$ds^2 = \frac{\ell^2 d\rho^2}{\rho^2} + \gamma_{\mu\nu} dx^\mu dx^\nu \,, \tag{A.3}$$

with the metric $\gamma_{\mu\nu}$ approaching the metric on the boundary as $\rho \to \infty$, along with the relevant corrections to this from the bulk. The specific form of this metric can be easily worked out, but its exact form is not necessary here.

With this expansion at hand it is now possible to directly compare the behaviour of r for the global AdS metric with that for the black hole metric. The result is, placing a UV cutoff at $\rho = \ell^2/\delta$,

$$r_{\max} - r_{\max}^{\text{AdS}} = \frac{M\Xi}{(2N+2)\ell^{4N}}\delta^{2N+1}. \tag{A.4}$$

Thus, for all positive N the difference in the cutoffs tends to zero in the limit where $\delta \to 0$. This justifies working directly with a cutoff $r_{\max}$ in both the AdS and black hole geometries.

A.2 Vanishing contribution of the GHY term

We will show that the GHY term (2.83) in the action does not contribute to the complexity of formation $\Delta\mathcal{C}_{\mathcal{A}}$ and is canceled by the contribution from vacuum AdS$_D$. First, note that the GHY term for vacuum AdS$_D$ is given by replacing $g(r)^{-2} \to f_0(r)$ in (2.83), where $f_0(r)$ is the blackening factor of vaccum AdS$_D$. At $r \to \infty$, the difference $I_{\text{GHY}} - I_{\text{GHY}}^{\text{AdS}}$ depends only on the tortoise coordinates. Using (A.4), it is straightforward to show that

$$\begin{aligned}(r^*_\infty - r^*(r_{\max})) - (r^*_{0\infty} - r^*_0(r^{\text{AdS}}_{\max})) &= \int_{r_{\max}}^{\infty} \frac{f(r)}{g(r)}\,dr - \int_{r^{\text{AdS}}_{\max}}^{\infty} \frac{1}{f_0(r)}\,dr \\ &= \int_{r^{\text{AdS}}_{\max}+\mathcal{O}(\delta^{2N+1})}^{\infty} \frac{f(r)}{g(r)}\,dr - \int_{r^{\text{AdS}}_{\max}}^{\infty} \frac{1}{f_0(r)}dr \\ &= \mathcal{O}(\delta^{2N+3}).\end{aligned} \tag{A.5}$$

Furthermore, the factor multiplying this term is of order $\mathcal{O}(1/\delta^{2N+2})$. Therefore,

$$I_{\text{GHY}} - I_{\text{GHY}}^{\text{AdS}} = \mathcal{O}(\delta) \tag{A.6}$$

which vanish in the limit $\delta \to 0$.

A.3 Complexity of formation in the static limit

Here, we consider, in arbitrary dimensions, the behaviour of the complexity of formation in the limit where $r_-/r_+ \to 0$. We compare the result with the analogous limit for charged black holes, and compare both with the results for the Schwarzschild-AdS black hole.

A.3.1 Complexity of formation for Schwarzschild-AdS

The Schwarzschild-AdS metric in D spacetime dimensions reads

$$ds^2 = -f_{\rm Schw}(r)dt^2 + \frac{dr^2}{f_{\rm Schw}(r)} + r^2 d\Omega_{D-2}^2 \tag{A.7}$$

where

$$f_{\rm Schw}(r) = k + \frac{r^2}{\ell^2} - \frac{2M}{r^{D-3}}\,. \tag{A.8}$$

(In the remainder of this section of the appendix we will drop the "Schw" subscript, but will re-introduce it in later sections when confusion could arise.) Here we will consider the complexity of formation for this geometry focusing on the $k = 0, +1$ cases, essentially reviewing the discussion of [64] but with a slightly different emphasis to allow straightforward comparison with our results for the rotating black holes.[45]

The calculation of the action on the WDW patch consists of a bulk term and a GHY term at the past/future singularities. Additional contributions vanish when the result is regularized by subtracting the contribution of two copies of global AdS. The calculation is carried out by focusing on a single quadrant of the WDW patch, then multiplying by a factor of four to obtain the full answer. Let us consider each of these contributions in turn.

Consider first the GHY term on the future singularity. It is straightforward to show that in this case the extrinsic curvature takes the form

$$K = -\frac{1}{2\sqrt{-f_{\rm Schw}(\epsilon)}}\left[f'_{\rm Schw}(\epsilon) + \frac{2(D-2)f_{\rm Schw}(\epsilon)}{r}\right]\,. \tag{A.9}$$

The spacetime has a four-fold reflection symmetry along the lines $t = 0$, and so the computation can be performed by focussing on one quadrant of the diagram and then multiplying by four. Focusing on the top-right quadrant of the Penrose diagram, the integration for t is carried out between $t = 0$ and $t = r^*_{\rm Schw,\infty} - r^*_{\rm Schw}(\epsilon)$, where the latter corresponds to the future right boundary of the WDW patch. The idea is to send ϵ to zero at the end of the computation, yielding for the GHY term

$$\begin{aligned} I^{\rm quadrant}_{\rm GHY} &= \frac{(D-1)M\Omega_{D-2}}{8\pi G_N}\left[r^*_{\rm Schw,\infty} - r^*_{\rm Schw}(0)\right] \\ &= \frac{(D-1)\Omega_{D-2}r_+^{D-3}(k + r_+^2/\ell^2)}{16\pi G_N}\left[r^*_{\rm Schw,\infty} - r^*_{\rm Schw}(0)\right]\,, \end{aligned} \tag{A.10}$$

[45] We avoid the case of hyperbolic black holes (i.e. $k = -1$) here as the causal structure in that case is different and does not offer any useful insight for our interests here.

where in the second equality we replaced the mass in terms of r_+. This term must be multiplied by a factor of 4 to account for the GHY contributions in each quadrant. Generally we will set $r^*_{\text{Schw},\infty} = 0$ by suitable choice of integration constant.

Next consider the bulk in the upper right quadrant, which takes the form

$$I_{\text{Bulk}}^{\text{Schw,quadrant}} = \frac{\Omega_{D-2}}{8\pi G_N}\int_0^{r_{\max}} \left[\frac{d\mathcal{I}_{\text{Schw}}}{dr}\left(r^*_{\text{Schw},\infty} - r^*_{\text{Schw}}(0)\right)\right] dr\,. \tag{A.11}$$

where

$$\mathcal{I}_{\text{Schw}} = -\frac{r^{D-1}}{\ell^2}\,. \tag{A.12}$$

Note that, just as in the main text, we have cut the integration off at $r = r_{\max}$ since the integral diverges otherwise. We will send $r_{\max} \to \infty$ after subtracting the contributions of the AdS vacuum, which will render the integral convergent. It is generally hard to evaluate the tortoise coordinate, and so a simpler form for the bulk integral is obtained using integration by parts:

$$I_{\text{Bulk}}^{\text{Schw,quadrant}} = \frac{\Omega_{D-2}}{8\pi G_N}\int_0^{r_{\max}} \frac{\mathcal{I}_{\text{Schw}}}{f_{\text{Schw}}(r)} dr\,. \tag{A.13}$$

This can be further simplified by isolating and separately dealing with the pole contribution at the black hole horizon. Doing this, writing

$$f_{\text{Schw}}(r) = F_{\text{Schw}}(r)(r^2 - r_+^2)\,, \tag{A.14}$$

we obtain

$$\begin{aligned} I_{\text{Bulk}}^{\text{Schw,quadrant}} &= \frac{\Omega_{D-2}}{8\pi G_N}\left[\frac{\mathcal{I}_{\text{Schw}}(r_+)}{2r_+F_{\text{Schw}}(r_+)}\log\frac{|r-r_+|}{r+r_+}\bigg|_0^\infty + \int_0^{r_{\max}}\left(\frac{\mathcal{I}_{\text{Schw}}(r)}{F_{\text{Schw}}(r)(r^2-r_+^2)}\right.\right. \\ &\quad \left.\left. - \frac{\mathcal{I}_{\text{Schw}}(r_+)}{F_{\text{Schw}}(r_+)(r^2-r_+^2)}\right)dr\right] \\ &= \frac{\Omega_{D-2}}{8\pi G_N}\left[\int_0^{r_{\max}}\left(\frac{\mathcal{I}_{\text{Schw}}(r)}{F_{\text{Schw}}(r)(r^2-r_+^2)} - \frac{\mathcal{I}_{\text{Schw}}(r_+)}{F_{\text{Schw}}(r_+)(r^2-r_+^2)}\right)dr\right]. \end{aligned} \tag{A.15}$$

In the first term involving the logarithm, we have extended the integration to infinity since that term is convergent. The remaining integral is completely well-behaved at the horizon and can easily be evaluated numerically. (It can be evaluated analytically in certain dimensions, or in the case of planar $k = 0$ black holes [64].)

The complexity of formation is then written as four times the sum of the GHY and bulk terms studied above, along with a subtraction of two copies of global AdS. The final result is

$$\pi\Delta\mathcal{C}^{\rm Schw}_{\rm form} = -\frac{(D-1)\Omega_{D-2}r_+^{D-3}(k+r_+^2/\ell^2)}{4\pi G_N}r^*_{\rm Schw}(0) + \frac{\Omega_{D-2}}{2\pi G_N}\left[\int_0^\infty\left(\frac{\mathcal{I}_{\rm Schw}(r)}{F_{\rm Schw}(r)(r^2-r_+^2)}-\frac{\mathcal{I}_{\rm Schw}(r_+)}{F_{\rm Schw}(r_+)(r^2-r_+^2)}-\frac{\mathcal{I}_0(r)}{f_0(r)}\right)dr\right]. \tag{A.16}$$

Here we have explicitly set $r^*_{\rm Schw,\infty}=0$, which we will do also throughout the remainder of this appendix.

A.3.2 Charged black holes & the neutral limit

Let us consider here the complexity of formation for charged black holes, as it will be insightful to compare the results for charged solutions with the results for the rotating solutions studied in this thesis. The charged solutions are given by the following metrics

$$ds^2 = -f_Q(r)dt^2+\frac{dr^2}{f_Q(r)}+r^2d\Omega^2_{D-2} \tag{A.17}$$

where

$$f_Q(r) = k+\frac{r^2}{\ell^2}-\frac{2M}{r^{D-3}}+\frac{q^2}{r^{2(D-3)}}\,. \tag{A.18}$$

We will be concerned here with the planar and spherical solutions, i.e. the $k=0,1$ ones.

Our objective is to understand how the complexity of formation for these solutions behave in the limit $q\to 0$. The causal structure of the charged black holes is qualitatively identical to the equal-spinning rotating holes considered in this work — see [69] for a full discussion. Since here we are only interested in the neutral limit, we will not consider the counterterm for null boundaries, as its contribution is subleading and vanishing in that limit. Moreover, just as for the rotating solutions, a GHY term at large distances is unimportant as it cancels when the subtraction relative to global AdS is performed. Therefore the complexity of formation consists of two ingredients: the bulk action and two corner terms where the past/future sheets of the WDW meet.

Let us consider first the corner terms. The analysis is qualitatively similar to that performed already in the rotating case (and we refer the reader to [69] for a full discussion

of these terms in the charged case), leading to the final result:

$$I^Q_{\rm jnt} = -\frac{\Omega_{D-2}}{8\pi G_N} r_{m_0}^{D-2} \log \frac{|f_Q(r_{m_0})|}{\alpha^2}\,, \tag{A.19}$$

where we have included a constant α that keeps track of the parameterization of the null geodesics normal to the sheets of the WDW patch. This accounts for the contribution of the future joint, the joint term at the past meeting point is identical and so the above should be multiplied by two when including it in the complexity of formation.

The parameter r_{m_0} appearing in the above is the value of the radial coordinate where the sheets of the WDW patch meet. It is obtained by solving the condition

$$r^*_\infty - r^*(r_{m_0}) = 0 \tag{A.20}$$

where r^* is the tortoise coordinate for the charged black hole. Here, introducing

$$f_Q(r) = F_Q(r)(r^2 - r_+^2)(r^2 - r_-^2), \tag{A.21}$$

to allow the problematic pieces at the horizons to be isolated and treated separately, we find it has the form

$$r^*(r) = \frac{1}{2r_+ F_Q(r_+)(r_+^2 - r_-^2)} \log \frac{|r - r_+|}{r + r_+} - \frac{1}{2r_- F_Q(r_-)(r_+^2 - r_-^2)} \log \frac{|r - r_-|}{r + r_-} + \mathcal{R}_Q(r) \tag{A.22}$$

where in the above we have chosen an integration constant such that $r^*_\infty = 0$ and have introduced

$$\begin{aligned} \mathcal{R}_Q(r) = \int_\infty^r \Bigg[&\frac{1}{F_Q(r')(r'^2 - r_+^2)(r'^2 - r_-^2)} - \frac{1}{F_Q(r_+)(r'^2 - r_+^2)(r_+^2 - r_-^2)} \\ &+ \frac{1}{F_Q(r_-)(r'^2 - r_-^2)(r_+^2 - r_-^2)} \Bigg] dr' \,. \end{aligned} \tag{A.23}$$

Consider next the bulk contribution. After some manipulation, the bulk action for charged black holes can be written in the form[46]

$$\Delta I^Q_{\rm Bulk} = \frac{\Omega}{2\pi G_N} \int_{r_{m_0}}^\infty \left[\frac{\mathcal{I}_Q(r)}{f_Q(r)} - \frac{\mathcal{I}_0(r)}{f_0(r)} \right] dr - \frac{\Omega}{2\pi G_N} \int_0^{r_{m_0}} \frac{\mathcal{I}_0(r)}{f_0(r)} dr \tag{A.24}$$

[46] Unlike the other solutions in this manuscript, the charged solutions are, of course, not vacuum. We follow here exactly the conventions of [69] for the electromagnetic terms in the action.

where

$$\mathcal{I}_Q(r) = -\frac{r^{D-1}}{\ell^2} - \frac{q^2}{r^{D-3}} \tag{A.25}$$

and the subscript "0" denotes this quantity and the metric for the AdS vacuum. Note that since the AdS contribution has been subtracted here, making the integral convergent, we have taken the limit of integration to infinity. The bulk term can be massaged in a manner similar to the tortoise coordinate we considered early in the manuscript. We first write the metric function as

$$f_Q(r) = F_Q(r)(r^2 - r_+^2)(r^2 - r_-^2)\,, \tag{A.26}$$

as before. Then, the integrand of the bulk term can be split up according to

$$\begin{aligned}\frac{\mathcal{I}_Q(r)}{f(r)} = \Bigg[&\frac{\mathcal{I}_Q(r)}{F_Q(r)(r^2 - r_+^2)(r^2 - r_-^2)} - \frac{\mathcal{I}_Q(r_+)}{F_Q(r_+)(r^2 - r_+^2)(r_+^2 - r_-^2)} + \frac{\mathcal{I}_Q(r_-)}{F_Q(r_-)(r^2 - r_-^2)(r_+^2 - r_-^2)}\Bigg] \\ &+ \frac{\mathcal{I}_Q(r_+)}{F_Q(r_+)(r^2 - r_+^2)(r_+^2 - r_-^2)} - \frac{\mathcal{I}_Q(r_-)}{F_Q(r_-)(r^2 - r_-^2)(r_+^2 - r_-^2)}\,.\end{aligned} \tag{A.27}$$

This decomposition of the integral allows us to isolate the contributions at the horizons which require special care. We can integrate these terms explicitly, and then arrive at the following expression for the bulk:

$$\begin{aligned}\Delta I^Q_{\rm Bulk} = \frac{\Omega}{2\pi G_N}\Bigg[&-\frac{\mathcal{I}_Q(r_+)}{2r_+F_Q(r_+)(r_+^2 - r_-^2)}\log\frac{|r_{m_0} - r_+|}{r_{m_0} + r_+} \\ &+\frac{\mathcal{I}_Q(r_-)}{2r_-F_Q(r_-)(r_+^2 - r_-^2)}\log\frac{|r_{m_0} - r_-|}{r_{m_0} + r_-}\Bigg] + \mathfrak{I}_Q(r_{m_0})\end{aligned} \tag{A.28}$$

where we have defined

$$\begin{aligned}\mathfrak{I}_Q(r_{m_0}) = \frac{\Omega}{2\pi G_N}\int_{r_{m_0}}^{\infty}\Bigg[&\frac{\mathcal{I}_Q(r)}{F_Q(r)(r^2 - r_+^2)(r^2 - r_-^2)} - \frac{\mathcal{I}_Q(r_+)}{F_Q(r_+)(r^2 - r_+^2)(r_+^2 - r_-^2)} \\ &+ \frac{\mathcal{I}_Q(r_-)}{F_Q(r_-)(r^2 - r_-^2)(r_+^2 - r_-^2)} - \frac{\mathcal{I}_0}{f_0(r)}\Bigg]dr - \frac{\Omega}{2\pi G_N}\int_0^{r_{m_0}}\frac{\mathcal{I}_0(r)}{f_0(r)}dr.\end{aligned} \tag{A.29}$$

This term is convergent and completely regular, requiring no special treatment at the horizons. It can be straightforwardly integrated numerically (or analytically in certain special cases).

The complexity of formation then takes the final form

$$\pi\Delta\mathcal{C}^Q_{\rm form} = \Delta I^Q_{\rm Bulk} + 2I^Q_{\rm jnt}\,. \tag{A.30}$$

We want to understand how this quantity behaves in the limit $r_-/r_+ \to 0$. For this we must first understand the asymptotic behaviour of r_{m_0} in this limit. In general dimensions, writing $r_{m_0} = y r_+(1+\epsilon)$ we find that

$$r^*(r) \sim -\frac{y^{D-2} r_+ \ell^2}{(D-3)(k\ell^2 + r_+^2)} \log\frac{\epsilon}{2} + r^*_{\rm Schw}(0) \tag{A.31}$$

where $y = r_-/r_+$ and $r^*_{\rm Schw}(0)$ is the value of the tortoise coordinate for the static solution at the origin (recall that we have set the integration constant so that $r^*_\infty = 0$). Explicitly, this term takes the form

$$r^*_{\rm Schw}(0) = \int_0^\infty \frac{f_{\rm Schw}(r) - F_{\rm Schw}(r_+)(r^2 - r_+^2)}{f_{\rm Schw}(r) F_{\rm Schw}(r_+)(r^2 - r_+^2)}\, dr\,, \quad F_{\rm Schw}(r) \equiv \frac{f_{\rm Schw}(r)}{r^2 - r_+^2}\,. \tag{A.32}$$

We then deduce the asymptotic form of the meeting location[47]

$$r_{m_0} = y r_+ \left[1 + 2\exp\left(\frac{(D-3)(k\ell^2 + r_+^2) r^*_{\rm Schw}(0)}{r_+ \ell^2 y^{D-2}}\right)\right]\,. \tag{A.33}$$

Using this asymptotic result along with the fact that near the inner horizon we have $|f_Q(r)| \approx |f_Q'(r_-)|(r - r_-)$ it is rather straightforward to show that

$$\lim_{y\to 0} 2I^Q_{\rm jnt} = -\frac{(D-3)\Omega_{D-2}}{4\pi\ell^2 G_N} r_+^{D-3}(k\ell^2 + r_+^2) r^*_{\rm Schw}(0)\,. \tag{A.34}$$

Comparing with the results for the neutral (A.10) case we see that

$$\frac{\lim_{y\to 0} 2I^Q_{\rm jnt}}{I^{\rm Schw}_{\rm GHY}} = \frac{D-3}{D-1}\,. \tag{A.35}$$

Note that this limit is independent of the parametrization of the null normals to the WDW patch, as indicated by the absence of α in the final expression.[48]

[47] The factor of 2 in front of the exponential differs from [69], where this factor is unity. The difference comes from the fact that we defined $f(r) = F(r)(r^2 - r_+^2)(r^2 - r_-^2)$ whereas those authors defined $f(r) = F(r)(r - r_+)(r - r_-)$. The prefactor of the exponential is completely unimportant for the $y \to 0$ limit, and the same results are obtained for $r_{m_0} = y r_+(1 + A\epsilon)$ for any choice of parameter A. It is the argument of the exponential that is important.

[48] As we mentioned earlier, inclusion of the counterterm for null boundaries changes the structure of the joint term, but this addition has no effect on the $y \to 0$ limit. For this reason, to keep the complexity of the expressions at a minimum, we did not include that term in the analysis presented here.

The limit of the bulk term is more difficult. It is easy to deal with the logarithm terms in this limit — one of them simply vanishes, while the other yields a finite result. We have:

$$\lim_{y\to 0}\Delta I^{Q}_{\rm Bulk}=-\frac{\Omega_{D-2}r_+^{D-3}(r_+^2+k\ell^2)r^*_{\rm Schw}(0)}{2\pi\ell^2 G_N}+\mathfrak{I}_Q(0)\,. \tag{A.36}$$

Determining the value of $\mathfrak{I}_Q(0)$ is the tricky part. However, after careful examination of (A.29) it can be shown that this term can be expressed as

$$\mathfrak{I}_Q(0)=\frac{\Omega_{D-2}}{2\pi G_N}\left[\int_0^\infty\left(\frac{\mathcal{I}_{\rm Schw}(r)}{F_{\rm Schw}(r)(r^2-r_+^2)}-\frac{\mathcal{I}_{\rm Schw}(r_+)}{F_{\rm Schw}(r_+)(r^2-r_+^2)}-\frac{\mathcal{I}_0(r)}{f_0(r)}\right)dr\right]=\Delta I^{\rm Schw}_{\rm Bulk}\,. \tag{A.37}$$

Thus, we conclude that the limit of the bulk action is

$$\lim_{y\to 0}\Delta I^{Q}_{\rm Bulk}=\frac{2I^{\rm Schw}_{\rm GHY}}{D-1}+\Delta I^{\rm Schw}_{\rm Bulk}\,. \tag{A.38}$$

It can be further shown that

$$\Delta I^{\rm Schw}_{\rm Bulk}=\frac{\Omega_{D-2}r_+^{D-1}r^*_{\rm Schw}(0)}{2\pi\ell^2G_N}=-\frac{2I^{\rm Schw}_{\rm GHY}}{D-1}\quad\text{when}\quad k=0\,. \tag{A.39}$$

The conclusion is that, when $k=0$, the limit of the bulk part of the action $\Delta I^{Q}_{\rm Bulk}$ vanishes in all dimensions. This is consistent with the analysis of [69] where the $D=5$ case was studied. However, the bulk term $\Delta I^{Q}_{\rm Bulk}$ *does not* vanish when $k=1$, as the equation just above does not hold in that case. However, the way in which the particular terms combine yields in general

$$\lim_{y\to 0}\pi\Delta\mathcal{C}^{Q}_{\rm form}=\frac{D-3}{D-1}I^{\rm Schw}_{\rm GHY}+\frac{2}{D-1}I^{\rm Schw}_{\rm GHY}+\Delta I^{\rm Schw}_{\rm Bulk}=I^{\rm Schw}_{\rm GHY}+\Delta I^{\rm Schw}_{\rm Bulk}=\pi\Delta C^{\rm Schw}_{\rm form}\,. \tag{A.40}$$

Thus, in the charged case the $y\to 0$ limit of the complexity of formation matches the complexity of formation for the Schwarzschild AdS solution, irrespective of the horizon topology. However, note the non-trivial way in which this limit is achieved, with the corner term producing one fraction of the GHY term and the bulk action for the charged solution producing the other fraction of the GHY term while at the same time giving the full Schwarzschild-AdS bulk contribution.

A.3.3 Rotating black holes & the static limit

Let us finally consider in detail the static limit of the rotating black holes that have been our focus here in this work. We are interested once again in determining the limit of the

bulk and joint terms in the action in the limit $y \equiv r_-/r_+ \to 0$. We work in general (odd) dimensions.

Consider first the joint term. The relevant part of this term is

$$I_{\rm jnt} = -\frac{\Omega_{2N+1}}{4\pi G_N}(r_{m_0})^{2N} h(r_{m_0}) \log|f(r_{m_0})^2| \,. \tag{A.41}$$

Here we have neglected the term $\ell_{\rm ct}^2\Theta^2/\alpha^2$ inside the logarithm for simplicity of presentation as it will have no effect on our discussion as it is subleading. Note also that here we have included the overall factor of 2 to account for both the past and future joints. Our objective is to understand the behaviour of this term as $r_-/r_+ \to 0$.

In order to understand the behaviour of this corner term as $y \to 0$ we need to understand the behaviour of r_{m_0}. Working in the limit of small y, and writing $r = yr_+(1+\epsilon)$, it is easy to show that the tortoise coordinate (2.42) behaves as

$$r^* = -\frac{r_+ \ell y^{N+1}}{2\sqrt{\ell^2 + r_+^2}} \log\frac{\epsilon}{2} + r^*_{\rm Schw}(0) \,. \tag{A.42}$$

where $r^*_{\rm Schw}(0)$ is the value of the Schwarzschild-AdS tortoise coordinate at the origin — see (A.32). In deriving this expression it is useful to note that

$$G(r_-) \sim \frac{\ell^2 r_+^4 y^{2N+2}}{\ell^2 + r_+^2} \quad \text{and} \quad h(r_-) \sim \frac{r_+\sqrt{r_+^2+\ell^2}}{\ell y^{N-1}} \,, \tag{A.43}$$

as $y \to 0$. We can then deduce that the meeting point behaves as

$$r_{m_0} = r_+ y \left[1 + 2\exp\left(\frac{2r^*_{\rm Schw}(0)\sqrt{\ell^2+r_+^2}}{r_+\ell y^{N+1}}\right)\right] \tag{A.44}$$

in the limit $y \to 0$.

Near the inner horizon we can expand

$$f^2(r_{m_0}) \approx (f^2)'(r_-)(r_{m_0} - r_-) \,. \tag{A.45}$$

Subsituting this into (A.41) and taking the limit $y \to 0$, we obtain the following result:

$$\lim_{y\to 0} I_{\rm jnt} = -\frac{\Omega_{2N+1}}{2\pi\ell^2 G_N} r_+^{2N}(\ell^2 + r_+^2) r^*_{\rm Schw}(0) \,. \tag{A.46}$$

Noting that $D = 2N + 3$ we see that

$$\lim_{y\to 0} I_{\rm jnt} = \frac{2I^{\rm Schw}_{\rm GHY}}{D-1} = \frac{I^{\rm Schw}_{\rm GHY}}{N+1}\,. \tag{A.47}$$

This limit is different in structure than the limit in the charged case.[49] The reason partly has to do with the behaviour of $h(r_{m_0})$ in the limit $y \to 0$ which approaches a constant — or blows up — rather than behaving $\sim y$ in this limit (as it would for the charged solution).

Next let us consider the behaviour of the bulk. Again, it is useful to split the bulk into pieces, isolating the parts that are divergent at the horizon. Doing this we can write the bulk term as

$$\begin{aligned}\Delta I_{\rm Bulk} = \frac{\Lambda\Omega_{2N+1}}{2(N+1)(2N+1)\pi G_N}\Bigg\{ &- \frac{r_+^{2N}G(r_+)h(r_+)}{2(r_+^2-r_-^2)}\log\frac{|r_{m_0}-r_+|}{r_{m_0}+r_+} + \frac{r_-^{2N}G(r_-)h(r_-)}{2(r_+^2-r_-^2)}\log\frac{|r_{m_0}-r_-|}{r_{m_0}+r_-}\\ &+ \int_{r_{m_0}}^{\infty}\left[\frac{r^{2N+1}G(r)h(r)}{(r^2-r_+^2)(r^2-r_-^2)} - \frac{r_+^{2N+1}G(r_+)h(r_+)}{(r^2-r_+^2)(r_+^2-r_-^2)} + \frac{r_-^{2N+1}G(r_-)h(r_-)}{(r^2-r_-^2)(r_+^2-r_-^2)} - \frac{r^{2N+2}}{r^2+\ell^2}\right]dr\\ &- \int_0^{r_{m_0}}\frac{r^{2N+2}}{r^2+\ell^2}dr\Bigg\}.\end{aligned} \tag{A.48}$$

Again, the last integral is convergent and its argument completely regular. As in the charged case, we can now easily study the limit of the logarithmic terms and then carefully consider the remaining integral. As before, the logarithmic term involving r_+ vanishes in this limit, and we must only consider the contribution from the logarithmic term involving r_-. However, here a crucial difference from the charged case arises. In the rotating case, we have

$$\frac{r_-^{2N}G(r_-)h(r_-)}{2(r_+^2-r_-^2)} \sim \mathcal{O}(y^{3N+3}) \tag{A.49}$$

from the limiting behaviour of $G(r_-)$ and $h(r_-)$ presented in (A.43) above. Meanwhile, the logarithm goes like

$$\log(r_{m_0}-r_-) \sim \mathcal{O}(y^{-(N+1)})\,, \tag{A.50}$$

based on the behaviour of r_{m_0} presented in (A.44). We therefore see that the logarithmic contributions to the bulk *vanishes* in the limit $y \to 0$! We then must only consider the remaining integral in the bulk. However, this term behaves just as it did in the charged case, producing the following final limit for the bulk term:

$$\Delta I_{\rm Bulk} = \frac{\Omega_{2N+1}}{2\pi G_N}\left[\int_0^{\infty}\left(\frac{\mathcal{I}_{\rm Schw}(r)}{F_{\rm Schw}(r)(r^2-r_+^2)} - \frac{\mathcal{I}_{\rm Schw}(r_+)}{F_{\rm Schw}(r_+)(r^2-r_+^2)} - \frac{\mathcal{I}_0(r)}{f_0(r)}\right)dr\right] = \Delta I^{\rm Schw}_{\rm Bulk}\,. \tag{A.51}$$

[49] Though note that for the special case of $D = 5$ (i.e. $N = 1$) the limit of the joint term matches in the two cases.

The combined joint and bulk terms give

$$\lim_{y\to 0}\pi\Delta\mathcal{C}_{\text{form}}=\frac{I^{\text{Schw}}_{\text{GHY}}}{N+1}+\Delta I^{\text{Schw}}_{\text{Bulk}}\neq\pi\Delta\mathcal{C}^{\text{Schw}}_{\text{form}} \tag{A.52}$$

which is the order of limits problem in the rotating case.

A.4 Alternate regularization of the WDW patch

Here we consider an alternate regularization of the WDW patch to examine the limiting behaviour of the complexity of formation as $y=r_-/r_+\to 0$. We do so by cutting off the future and past tips of the WDW patch at $r=r_{m_0}+\Delta r$ and introducing the appropriate GHY and joint terms to accommodate this (see figure A.1). This amounts to introducing two corner terms and one GHY term at the future tip of the WDW patch, and likewise at the past tip.

Consider first the GHY term on the right side of the future cutoff surface. This can be worked out to be

$$I^{F,R}_{\text{GHY}}=\frac{\Omega_{2N+1}}{16\pi G_N}{r_\Delta}^{2N+1}\left[(g^{-2})'(r_\Delta)+\frac{2(2N+1)}{r_\Delta g^2(r_\Delta)}\right]r^*(r_\Delta)\,. \tag{A.53}$$

where we have denoted $r_\Delta=r_{m_0}+\Delta r$. There are four contributions, all identical to this one, and so the final result for the GHY contribution is

$$I_{\text{GHY}}=\frac{\Omega_{2N+1}}{4\pi G_N}{r_\Delta}^{2N+1}\left[(g^{-2})'(r_\Delta)+\frac{2(2N+1)}{r_\Delta g^2(r_\Delta)}\right]r^*(r_\Delta)\,. \tag{A.54}$$

Consider next the corner terms that occur where the boundaries of the WDW patch intersect the cutoff surface at r_Δ. Focussing on the contribution on the right side of the future boundary of the WDW patch, the relevant null normal is

$$k_F=\alpha(dt+dr^*)\,. \tag{A.55}$$

To determine the relevant dot products appearing in the joint term we need the form of the auxillary future/outward pointing unit vector $\hat{s}$. In the present case $\hat{s}=\sqrt{|f^2(r_\Delta)|}dt$ is the appropriate choice. We can then work out the sign ε appearing in the definition of the joint term — see (2.60). We find here that $\varepsilon=+1$. We then find the following result for the joint term

$$I^{F,R}_{\text{jnt}}=-\frac{\Omega_{2N+1}}{16\pi G_N}{r_\Delta}^{2N}h(r_\Delta)\log\frac{|f^2(r_\Delta)|}{\alpha^2}\,. \tag{A.56}$$

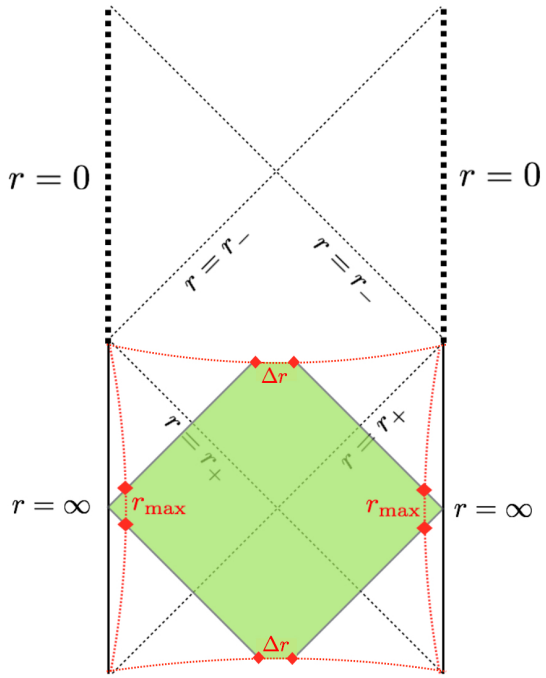

Figure A.1: The WDW patch with the alternative regularization scheme, where the future and past tips are cut off and replaced with a regularization surface at $r = \Delta r$. This introduces four new joints that are shown in the figure as red diamonds.

There are four joints of this kind, giving the total

$$I_{\text{jnt}} = -\frac{\Omega_{2N+1}}{4\pi G_N} {r_\Delta}^{2N} h(r_\Delta) \log \frac{|f^2(r_\Delta)|}{\alpha^2} \,. \tag{A.57}$$

The idea, then, is to replace the corner term appearing in section 2.4 with the combination of joint and GHY terms shown above. Note for our purposes here we will not consider the contribution of the null boundary counterterm. This is because we are interested in the limit $y = r_-/r_+ \to 0$ and the null boundary counterterm vanishes in this limit. We now examine this limit keeping r_Δ small but finite until after the limit $y \to 0$ has been performed.

The GHY term limits to precisely the GHY term in the static case,

$$\lim_{\Delta r \to 0} \lim_{y \to 0} I_{\text{GHY}} = I_{\text{GHY}}^{\text{Schw}} \,, \tag{A.58}$$

while the joint term vanishes in the limit

$$\lim_{\Delta r\to 0}\lim_{y\to 0} I_{\rm jnt} = 0\,. \tag{A.59}$$

It must be emphasized that the order of limits here is important. The $y \to 0$ limit must be taken prior to taking the $\Delta r \to 0$ limit. The entire issue associated with the order of limits problem is that this limit does not commute. Said another way, effectively what this conclusion means is that the future and past 'tips' of the WDW patch contain the following amount of action:

$$I_{\rm tip} = -\frac{N}{N+1} I^{\rm Schw}_{\rm GHY}\,,$$

in a vanishing amount of volume. Interestingly, this is exactly the limit of the corner term in the charged case. Thus, in this alternate regularization of the WDW patch the limit agrees with the Schwarzschild-AdS result. Note that for any finite y the two approaches will agree, as in that case the limits considered above will commute.

A.5 Behaviour of complexity of formation for large black holes

Here we present the details for the behaviour of the complexity of formation in the limit of large black holes. For the cases of charged black holes and also the rotating black holes considered here there are two independent limits that are of interest. The first involves holding fixed the size of the black hole, r_+/ℓ, while exploring the extremal limit $r_-/r_+ \to 1$. The second is to hold fixed r_-/r_+ while examining the behaviour of the complexity of formation for $r_+/\ell \to \infty$.

In previous work that focused on five-dimensional charged black holes [69], it was demonstrated that the entropy controls the behaviour of the complexity of formation in either limit when the black holes are large enough. In particular, those authors found that the complexity of formation diverges logarithmically as extremality is approached with a prefactor proportional to the entropy when the black holes are large. Moreover, the subleading terms in a near extremal expansion were also found to be related to the entropy. Here we wish to examine those conclusions in more detail and extend them to higher dimensions. We will then contrast them with the rotating case where it is found that different thermodynamic potentials control the different limits.

A.5.1 Charged black holes: complexity equals volume

To understand our results in the rotating case, it will be important to have an understanding of how the relevant computations play out for charged black holes. In this case, the complexity of formation is given by the following integral:

$$\Delta\mathcal{C}_{\mathcal{V}} = \frac{\Omega_{D-2}}{2G_N R}\lim_{r_{\max}\to\infty}\left[\int_{r_+}^{r_{\max}}\frac{r^{D-2}}{\sqrt{f_Q(r)}}dr - \int_0^{r_{\max}}\frac{r^{D-2}}{\sqrt{f_0(r)}}dr\right]. \tag{A.60}$$

To illustrate a particular example, we consider the five dimensional case. In five dimensions, the above integrals can be worked out to be

$$\begin{aligned}\frac{2G_N R}{\Omega_{D-2}}\Delta\mathcal{C}_{\mathcal{V}} = \ell^4\alpha^4\int_1^\infty x^3\Bigg[&\frac{x^2}{\sqrt{(x^2-1)(1+x-\epsilon)(-1+x+\epsilon)}\sqrt{k+\alpha^2(2+x^2+\epsilon(\epsilon-2))}}\\ &-\frac{1}{\sqrt{k+\alpha^2x^2}}\Bigg]dx - \frac{\ell^4}{3}\left[2k^{3/2}+(\alpha^2-2k)\sqrt{k+\alpha^2}\right]\end{aligned} \tag{A.61}$$

where we have defined

$$x \equiv \frac{r}{r_+}, \quad \alpha \equiv \frac{r_+}{\ell}, \quad \epsilon \equiv 1-\frac{r_-}{r_+}. \tag{A.62}$$

Our main objective here will be to try to understand how the resulting integral scales with α. While this is not so hard for these charged black holes, it will be considerably more involved for the rotating ones. So we will use the simpler setting of charged black holes to illustrate our ideas.

Although it is not our main focus, let us mention here the case of planar charged black holes. For these solutions, the dependence of complexity of formation on the quantity $\alpha = r_+/\ell$ completely factors out of the integral, leaving a result dependent only on $\epsilon = 1-r_-/r_+$. In five dimensions the remaining integral can be evaluated explicitly, giving the final result:

$$\Delta\mathcal{C}_{\mathcal{V}}^{k=0,D=5} = \frac{S\ell}{R}\frac{(1-\epsilon+\epsilon^2)(3-3\epsilon+\epsilon^2)}{6\sqrt{\epsilon(2-\epsilon)}}E\left[\frac{3-4\epsilon+2\epsilon^2}{\epsilon(\epsilon-2)}\right]. \tag{A.63}$$

Here S is the black hole entropy, while $E(X)$ refers to the elliptic integral of the first kind. We see clearly here that, for planar black holes, the only dependence on the black hole size is through the entropy. This property extends directly to all higher dimensions, though the resulting integrals no longer yield such a simple final result.

From a heuristic examination of the integrals above, it is not too hard to become convinced that as $\alpha\to\infty$ the behaviour of the spherical ($k=+1$) black holes will match

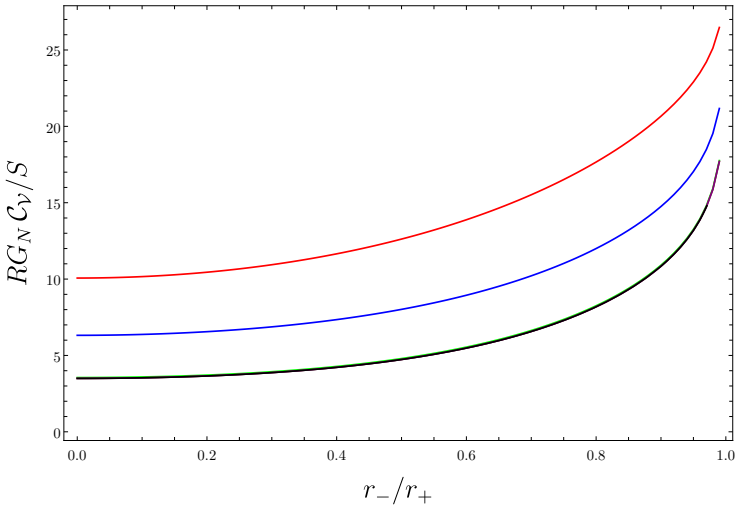

Figure A.2: A plot of the complexity of formation within the CV conjecture for five dimensional, spherical ($k = +1$) charged black holes. We have normalized the complexity of formation by the entropy and the curves shown correspond to $r_+/\ell = 1/2, 1, 10, 50, 100$ in order from top to bottom. The last three curves are visually indistinguishable. Imposed on the plot in a black curve is the complexity of formation for the planar $k = 0$ charged black hole. This curve coincides with the last three plots for the spherical charged black holes.

that of the planar black holes. We illustrate this with a numerical evaluation of the complexity of formation in figure A.2. In this figure we have normalized the complexity of formation by dividing by the entropy

$$S = \frac{\Omega_3 r_+^3}{4G_N} \tag{A.64}$$

and have shown the result as a function of r_-/r_+ for several values of r_+/ℓ. The plot illustrates that when r_+/ℓ is small the curves can be distinguished. However, as r_+/ℓ becomes large the results all converge to the planar case (shown here as the black curve). This illustrates that, for large black holes at fixed $\epsilon = r_-/r_+ - 1$, the entropy completely controls the complexity of formation.

For charged black holes it is also not too difficult to confirm this conclusion analytically. Expanding (A.61) in the large α limit for five-dimensional spherical ($k = +1$) black holes gives

$$\Delta\mathcal{C}_\mathcal{V} = \Delta\mathcal{C}_\mathcal{V}^{k=0,D=5} + \mathcal{O}(S^{2/3})\,. \tag{A.65}$$

While an analytic study is possible in the charged case, it will turn out to be much more difficult in the rotating case. For this reason we will discuss a numerical approach to determine the dependence of the complexity of formation on the horizon radius for large black holes. Suppose that

$$\Delta\mathcal{C}_\mathcal{V} \sim (r_+/\ell)^\gamma \tag{A.66}$$

for some power γ. A convenient way to determine the value of γ is the following. We consider the ratio

$$R(\beta) = \frac{RG_N\Delta\mathcal{C}_\mathcal{V}}{(r_+/\ell)^\beta} \sim (r_+/\ell)^{\gamma-\beta}\,. \tag{A.67}$$

We then take the logarithm of this ratio treated as a function of both (r_+/ℓ) and β. For each value of β, we compute $R(\beta)$ for several (large) values of r_+/ℓ and fit the resulting data to a linear model, and extract the slope of the numerical model. We explore the β parameter range until the slope determined in this way is zero. The value of β for which the slope vanishes corresponds to the case $\beta = \gamma$, allowing us to extract how the complexity of formation depends on the size of the black holes.

This scheme is illustrated in figure A.3 for five, seven, and nine dimensions. In each case it is clear from the plot that the slopes vanish for $\beta = 3, 5, 7$, respectively (but this can be confirmed to much higher precision numerically). This numerical finding is consistent with the results discussed above: In general dimensions, the complexity of formation for large charged black holes is controlled by the entropy and nothing more.

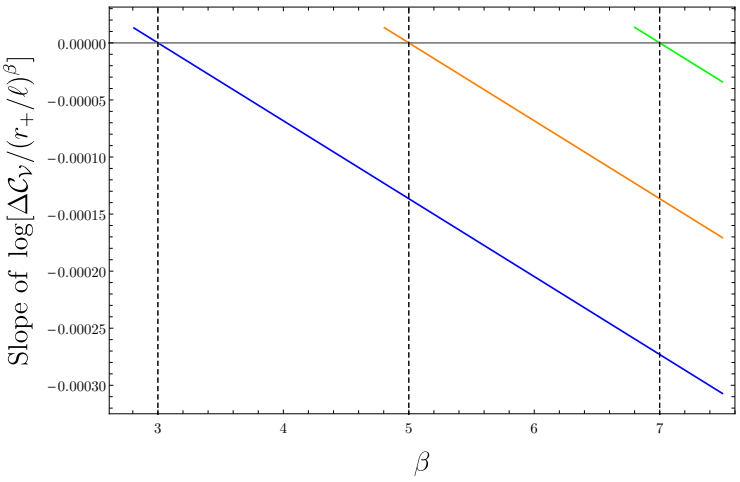

Figure A.3: The slope of the logarithm of the ratio $R(\beta)$ for several dimensions. The curves correspond to 5 dimensions (blue, left), 7 dimensions (orange, center), and 9 dimensions (green, right). For each value of β the integrals have been evaluated for 500 points laying between $r_+/\ell = 10,000$ and $r_+/\ell = 20,000$. The slope is extracted by performing a linear fit to this data.

A.5.2 Rotating black holes: complexity equals volume

Let us now consider the rotating black holes, which are the main topic of our interest here. Once again for ease of presentation we will present detailed equations only in the five dimensional case and will comment how the situation plays out in higher (odd) dimensions.

The complexity of formation for rotating black holes according to the CV conjecture is

$$\Delta\mathcal{C}_\mathcal{V} = \lim_{r_{\max}\to\infty} \frac{2\Omega_{D-2}}{G_N R}\left[\int_{r_+}^{r_{\max}} h(r) r^{D-3} g(r)\, dr - \int_0^{r_{\max}^{\text{AdS}}} \frac{r^{D-2}}{\sqrt{f_0(r)}}\, dr\right]. \tag{A.68}$$

As in the charged case, there are two limits that are interesting to consider here. We can consider holding the size of the black hole r_+/ℓ fixed and examine the extremal limit $\epsilon = (1 - r_-/r_+) \to 0$ or vice versa. Let us first consider the former.

To understand the leading behaviour in the extremal limit we split the integrand for

the black hole into two parts:

$$\int_{r_+}^{r_{\rm max}} h(r) r^{D-3} g(r)\, dr = \int_{r_+}^{r_{\rm max}} \frac{h(r_+) r_+^{D-3}\sqrt{G(r_+)}}{\sqrt{(r^2-r_+^2)(r^2-r_-^2)}}\, dr + \int_{r_+}^{r_{\rm max}} \frac{\left[h(r) r^{D-3}\sqrt{G(r)} - h(r_+) r_+^{D-3}\sqrt{G(r_+)}\right]}{\sqrt{(r^2-r_+^2)(r^2-r_-^2)}}\, dr\,. \quad \text{(A.69)}$$

In the first term we have isolated a part of the integral that will behave like $\sim 1/(r-r_+)$ in the extremal limit, and so we expect a logarithmic singularity for this term. The second term does not exhibit such behaviour in the extremal limit: the behaviour of the numerator near $r = r_+$ will cancel the blow up due to the denominator. Therefore, near $\epsilon = 0$, it is the asymptotics of the first integral that we must understand.

The first integral converges when integrated between r_+ and ∞, and so we extend the integration domain $r_{\rm max} \to \infty$. The result can then be expressed in terms of elliptic integrals:

$$\int_{r_+}^{\infty} \frac{h(r_+) r_+^{D-3}\sqrt{G(r_+)}}{\sqrt{(r^2-r_+^2)(r^2-r_-^2)}}\, dr = h(r_+) r_+^{D-4}\sqrt{G(r_+)} E(1-\epsilon) \quad \text{(A.70)}$$

where E is the elliptic integral of the first kind. The remaining integrals cannot be evaluated in a simple closed form, but luckily this will not trouble us here (yet). Expanding this expression near $\epsilon = 0$ and noting that this will be the dominant contribution to the complexity of formation in this limit, we find that in all dimensions

$$\Delta \mathcal{C}_{\mathcal{V}} \underset{\epsilon\to 0}{\approx} \frac{\Omega_{D-2} h(r_+) r_+^{D-4}\sqrt{G(r_+)}}{G_N R} \log\frac{8}{\epsilon} + \mathcal{O}(\epsilon, \epsilon\log\epsilon). \quad \text{(A.71)}$$

It is tempting to expand the prefactor appearing here to understand how it behaves for large black holes. The behaviour is given by

$$\frac{\Omega_{D-2} h(r_+) r_+^{D-4}\sqrt{G(r_+)}}{G_N R} \underset{r_+/\ell\to\infty}{\approx} \frac{4\sqrt{2}\, S}{\sqrt{(N+1)(N+2)}} \quad \text{(A.72)}$$

where S is the black hole entropy. So it is tempting to conclude that the complexity of formation (at least near extremality) is controlled by the entropy. However, the situation is more subtle. First, while the expansion just presented above holds provided $\epsilon \to 0$, it does not follow that the subleading terms in the ϵ expansion will always be subleading for sufficiently large r_+/ℓ. What is true is that, for fixed r_+/ℓ, one can find an ϵ that is small enough such that the entropy will control the behaviour near extremality. However, in the

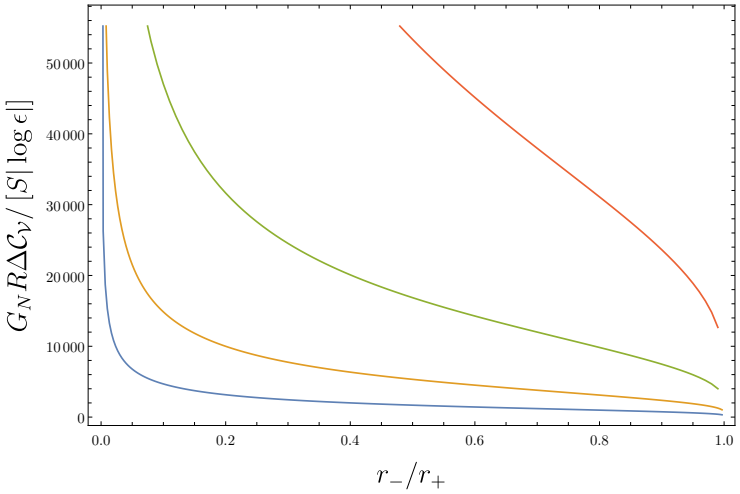

Figure A.4: A plot of $\Delta\mathcal{C}_{\mathcal{V}}$ normalized by the entropy in five dimensions. The graph displays four curves corresponding to $r_+/\ell = 10^5, 10^6, 10^7, 10^8$. The curves are plotted as a function of $\epsilon = 1 - r_-/r_+$. The value of r_+/ℓ increases from the blue curve to the red curve.

general situation the entropy does not control the complexity of formation, as we will now explain.

The process of understanding the behaviour of the complexity of formation for large black holes involves extracting the leading r_+/ℓ dependence of the integrals presented above. Despite a number of attempts, we have been unable to understand this problem from an analytical perspective, and therefore we resort to numerics. In figure A.4 we show the ratio of the complexity of formation normalized by the entropy for several large values of r_+/ℓ. It becomes clear that the entropy *does not* control the complexity of rotating formation for large black holes. This figure should be compared with figure A.2 to see the stark difference relative to the charged case.

Note that the entropy can be written as

$$S = \frac{\Omega_{2N+1}}{4} r_+^{2N+1} \sqrt{(1 + \frac{r_+^2}{\ell^2}(\epsilon - 1)^2) P(\epsilon)} \tag{A.73}$$

where $P(\epsilon)$ is a polynomial in ϵ that becomes rather complicated in higher dimensions and the general form is not important. This means that the entropy interpolates between two different scaling regimes. In the limit of slow rotation ($\epsilon \to 1$) the entropy scales as

$$S \underset{\epsilon \to 1}{\sim} \left(\frac{r_+}{\ell}\right)^{2N+1} = \left(\frac{r_+}{\ell}\right)^{D-2} \tag{A.74}$$

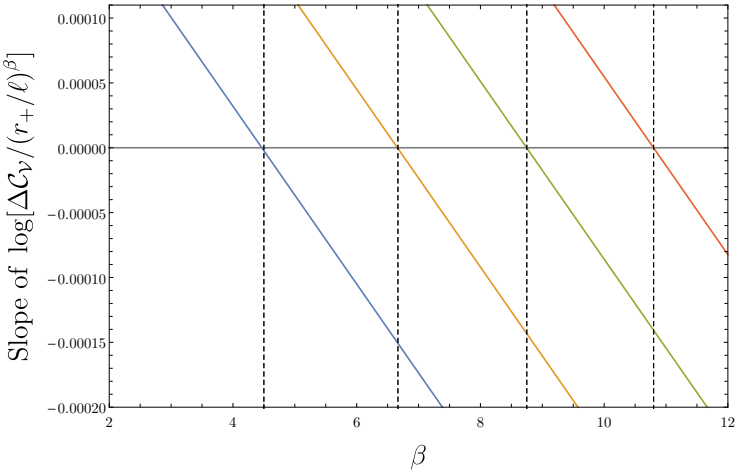

Figure A.5: The slope of the logarithm of the ratio $R(\beta)$ for rotating black holes in several dimensions. The curves correspond to 5,7, 9, 11 dimensions from left to right, respectively. For each value of β the integrals have been evaluated for 500 points laying between $r_+/\ell = 10,000$ and $r_+/\ell = 20,000$. The slope is extracted by performing a linear fit to this data. In all cases we have set $\epsilon = 10^{-10}$ to probe close to extremality. Vertical dashed lines have been added to aid in seeing where the slopes cross the horizontal axis.

for large black holes, while in the near extremal limit the entropy scales like

$$S \underset{\epsilon\to 0}{\sim} \left(\frac{r_+}{\ell}\right)^{2N+2} = \left(\frac{r_+}{\ell}\right)^{D-1} \tag{A.75}$$

for large rotating black holes. Although it is not immediately clear from figure A.4, the entropy does match the scaling decently near $r_-/r_+ \approx 0$ — which is expected since this scaling holds for the Schwarzschild-AdS black hole [64] — but fails miserably closer to extremality.

Using the same numerical scheme described in the previous section for charged black holes we can understand how the complexity of formation behaves as a function of r_+/ℓ for large black holes. The objective is to understand this scaling close to extremality where the departure from entropic scaling is most severe. To briefly recap, the process involves studying the ratio

$$R(\beta) = \frac{\Delta\mathcal{C}_\mathcal{V}}{(r_+/\ell)^\beta} \tag{A.76}$$

and numerically determining the value of β so that $R(\beta)$ exhibits no dependence on r_+/ℓ (when r_+/ℓ is large). We show a sample of this numerical scheme in figure A.5, and

Dimension	Numerical value of β	Thermodynamic volume scaling $V^{(D-2)/(D-1)}$
5	4.50000	$9/2 = 4.5$
7	6.66667	$20/3 \approx 6.66667$
9	8.75000	$35/4 = 8.75$
11	10.80000	$54/5 = 10.8$
13	12.83333	$77/6 \approx 12.83333$
15	14.85714	$104/7 \approx 14.85714$
17	16.87500	$135/8 \approx 16.87500$
19	18.88889	$170/9 \approx 18.88889$
21	20.90000	$209/10 = 20.9$
23	22.90909	$252/11 \approx 22.90909$
25	24.91667	$299/12 \approx 24.91667$
27	26.92308	$350/13 \approx 26.92308$

Table A.1: Table of numerically calculated values of β compared with the scaling of the thermodynamic volume $V^{(D-2)/(D-1)}$ for large r_+/ℓ. Here we have computed numerically the values of β according to the method outlined in the text. The data is obtained by evaluating the complexity of formation between $r_+/\ell = 10^{10}$ and $r_+/\ell = 10^{20}$ and we have fixed $\epsilon = 10^{-10}$, so we are considering the situation very close to extremality. The numerical values agree with the scaling of the thermodynamic volume to at least five decimal places in all cases. By pushing the domain of r_+/ℓ to large values, the agreement becomes even better. Note that in all cases the scaling differs from the scaling of the entropy which behaves like $(r_+/\ell)^{D-1}$ for large r_+/ℓ at fixed ϵ near extremality.

tabulate the results up to 27 dimensions in table A.1. The conclusion is that in spacetime dimension D the complexity of formation scales like

$$\Delta\mathcal{C}_{\mathcal{V}} \underset{\epsilon\to 0}{\sim} \left(\frac{r_+}{\ell}\right)^{(D+1)(D-2)/(D-1)} \tag{A.77}$$

for large black holes near extremality.

It is obvious from table A.1 that the scaling of $\Delta\mathcal{C}_{\mathcal{V}}$ is different from the scaling of the entropy. The question then becomes whether or not there is a thermodynamic parameter that *does* have this scaling. As already hinted in table A.1, the answer is that the thermodynamic volume possesses this scaling for large black holes. Isolating the dependence on r_+, the thermodynamic volume can be written schematically as

$$V = \frac{\Omega_{2N+1}}{3(N+1)}\left[r_+^{2N+2}H(\epsilon) + \frac{r_+^{2N+4}}{\ell^2}(\epsilon-1)^2K(\epsilon)\right] \tag{A.78}$$

where again $H(\epsilon)$ and $K(\epsilon)$ are messy polynomials in ϵ whose form does not matter for the information we need here. These polynomials vanish nowhere on the range $\epsilon \in [0,1]$. We therefore see that the thermodynamic volume also has two scaling regimes, behaving as $\epsilon \to 1$ like

$$V \underset{\epsilon\to 1}{\sim} \left(\frac{r_+}{\ell}\right)^{2N+2} = \left(\frac{r_+}{\ell}\right)^{D-1} \tag{A.79}$$

for large black holes, while near extremality it scales like

$$V \underset{\epsilon\to 0}{\sim} \left(\frac{r_+}{\ell}\right)^{2N+4} = \left(\frac{r_+}{\ell}\right)^{D+1} . \tag{A.80}$$

We then notice that a power of the thermodynamic volume has the appropriate scaling:

$$V^{(D-2)/(D-1)} \underset{\epsilon\to 1}{\sim} \left(\frac{r_+}{\ell}\right)^{D-2} \quad \text{and} \quad V^{(D-2)/(D-1)} \underset{\epsilon\to 0}{\sim} \left(\frac{r_+}{\ell}\right)^{(D-2)(D+1)/(D-1)} . \tag{A.81}$$

The scaling of the thermodynamic volume to this power interpolates precisely between the two scaling regimes of the complexity of formation. We show this graphically for five dimensions in figure A.6.

There are a few important things to note here:

- The power of thermodynamic volume is natural. Recall that the thermodynamic volume has dimensionality $[\text{length}]^{D-1}$, therefore to obtain a quantity that has the correct dimensions of $[\text{length}]^{D-2}$ requires precisely this power.

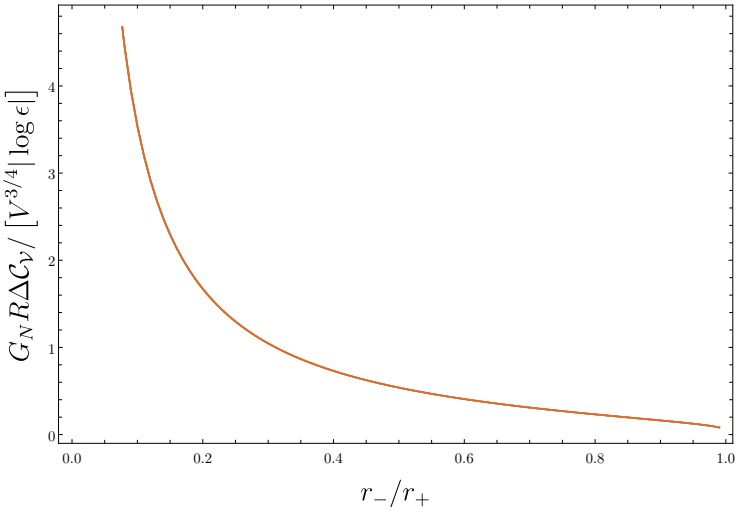

Figure A.6: A plot of $\Delta\mathcal{C}_\mathcal{V}$ normalized by the thermodynamic volume to the appropriate power in five dimensions. The graph displays four curves corresponding to $r_+/\ell = 10^5, 10^6, 10^7, 10^8$, the same as those shown in figure A.4, but these curves cannot be distinguished from one another here. The curves are plotted as a function of $\epsilon = 1 - r_-/r_+$. The value of r_+/ℓ increases from the blue curve to the red curve.

- The scaling with thermodynamic volume is consistent with the entropic scaling observed for charged black holes and the Schwarzschild black hole [64, 69]. This is because those solutions satisfy

$$S \sim V^{(D-2)/(D-1)} \,. \tag{A.82}$$

  In other words, for those solutions the thermodynamic volume and the entropy are not independent and so the results can be written in terms of either quantity. For the rotating black holes these quantities are truly independent and we observe that it is actually the expression written in terms of the thermodynamic volume that prevails.

- The convergence to "volumetric scaling" is slower for rotating black holes than it is for charged black holes. In the charged case the subleading terms die off at least as fast as ℓ/r_+, while in the rotating case they die off like $\sqrt{\ell/r_+}$.

- To the best of our knowledge there is no *a priori* reason to expect that the thermodynamic volume should be related to an extremal volume in a black hole spacetime. However, deriving such a relationship could contribute to a proof of our relationship for the complexity of formation in general situations.

- The conjectured reverse isoperimetric inequality [107] bounds the entropy in terms of the thermodynamic volume:

$$\mathcal{R}^{D-2} = \left(\frac{(D-1)V}{\Omega_{D-2}}\right)^{(D-2)/(D-1)} \left(\frac{\Omega_{D-2}}{4G_N S}\right) \geq 1\,. \tag{A.83}$$

  If our result is general, *i.e.* the complexity of formation generally scales with the thermodynamic volume for large black holes, then the reverse isoperimetric inequality can be interpreted as the statement that the entropy provides a lower bound for the complexity of formation. This bound is saturated for static black holes, but more complicated black holes have a larger complexity of formation than naively suggested by their degrees of freedom (entropy).

A.5.3 Rotating black holes: complexity equals action

It is now natural to ask whether this scaling with the thermodynamic volume is universal to both complexity proposals, or if it is a peculiar behaviour associated with the CV proposal. Recall that, as shown in section 2.4.1, the complexity of formation in the CA conjecture is given by

$$\begin{aligned}\pi\Delta\mathcal{C}_{\mathcal{A}} =& \frac{\Lambda\Omega_{2N+1}}{2(N+1)(2N+1)\pi G_N}\left[\int_{r_{m_0}}^{\infty} r^{2N+1}\left(g(r)^2h(r) - \frac{r}{1+r^2/\ell^2}\right)dr - \int_0^{r_{m_0}} \frac{r^{2(N+1)}}{1+r^2/\ell^2}dr\right] \\ &- \frac{\Omega_{2N+1}(r_{m_0})^{2N+1}}{2\pi G_N(2N+1)} - \frac{\Omega_{2N+1}}{4\pi G_N}(r_{m_0})^{2N}h(r_{m_0})\log\ell_{\rm ct}^2\Theta(r_{m_0})^2|f(r_{m_0})^2| \\ &- \frac{\Omega_{2N+1}}{2\pi G_N}\int_{r_{m_0}}^{\infty} r^{2N}\left[h(r)\frac{\Theta'}{\Theta}+1\right]dr.\end{aligned} \tag{A.84}$$

The most difficult part of the CA computation is the determination of r_{m_0}. In some instances, particularly in the limit $r_-/r_+ \to 0$, accurate determination of this parameter requires hundreds of digits of precision in the numerics. This technicality has limited our ability to probe the behaviour of the complexity of formation within the CA conjecture as broadly as the CV conjecture. However, we show in figure A.7 the result of the action computation in five dimensions. The plot makes clear that the thermodynamic volume controls the scaling of $\Delta\mathcal{C}_{\mathcal{A}}$ for large black holes, just as in the CV conjecture. While it was possible to compute the behaviour in various higher dimensions for the CV case, this is more difficult in the CA scenario. Nonetheless, we have confirmed the scaling with thermodynamic volume in seven dimensions, which suggests the same trend holds in general for CA.

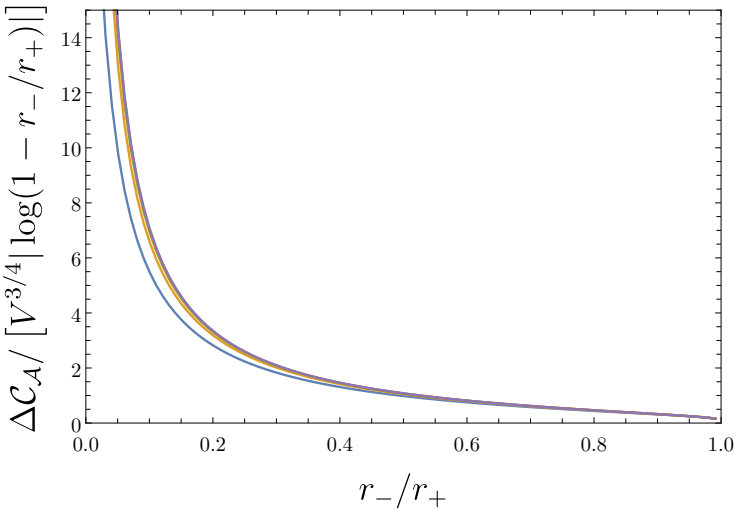

Figure A.7: A plot showing the CA complexity of formation normalized by the thermodynamic volume as a function of the ratio r_-/r_+ in five dimensions. The plot shows curves for fixed $r_+/\ell = 10, 10^2, 10^3, 10^4, 10^5, 10^6$ and 10^7, however after $r_+/\ell = 1000$ the curves are visually indistinguishable. Here we have set $\ell_{\rm ct} = \ell$.

A.6 Null hypersurfaces in Kerr-(A)dS spacetimes

As discussed in section 2.2, the study of holographic complexity in rotating spacetimes require a proper understanding of the null hypersurfaces of the spacetime. We have partly side-stepped this issue by considering equal-rotating odd-dimensional rotating black holes, which enjoy additional symmetry that makes the computations tractable. The important case of Kerr-AdS black hole remains to be fully studied and understood. In this section of the appendix, which is based on [3, 4], we initiate the study of null hypersurfaces in Kerr-AdS black holes and discuss a number of interesting implications for the formation of caustics in the spacetime.

Null hypersurfaces of the Kerr geometry were first systematically studied in [125], where a three-dimensional null slicing of the spacetime was obtained and its properties studied. These hypersurfaces were found to possess no caustics, which make them ideal for studying initial-value problems and wave propagation in Kerr geometry. This type of analysis has never been extended to other rotating black holes, and our goal here is to address this deficit by investigating null hypersurfaces for the Kerr-(A)dS black holes. We find that a similar three-dimensional null foliation of Kerr-(A)dS spacetimes can be obtained and

prove that it also develops no caustics. Furthermore, we comment on the difference in the behaviour of light cones between rotating AdS, flat, and dS geometries. Besides the desire for completeness, one application of these results motivating this study is understanding the causal structure of Kerr-(A)dS spacetimes. Other applications include numerical general relativity [298] and studying the propagation of wave-fronts [299] in rotating spacetimes with a cosmological constant.

The plan for this section of the appendix is as follows: in subsection A.6.1, we provide the most general solution for the null hypersurfaces $t \pm r^* = \text{const}$ in Kerr-(A)dS spacetimes in terms of elliptic integrals. In subsection A.6.2, and as a consistency check, the $m \to 0$ limit of the solution is taken and shown to correspond to light cones in vacuum (A)dS spacetimes. In subsection A.6.3, a three-dimensional foliation of the Kerr-(A)dS geometry is obtained and shown in subsection A.6.4 to possess no caustics for $r > 0$. As an application, subsection A.6.5 constructs the Kruskal coordinates for the Kerr-(A)dS spacetime. We summarize in subsection A.6.6.

Note that, in this section of the appendix, we use L to denote the (A)dS length.

A.6.1 Preliminaries

The Kerr-(A)dS metric of the (3+1)-dimensional rotating black hole in Boyer-Lindquist coordinates is [300]

$$ds^2 = -\frac{\Delta_r}{\Sigma^2}\left(dt - \frac{a}{\Xi}\sin^2\theta\, d\phi\right)^2 + \frac{\Sigma^2}{\Delta_r}dr^2 + \frac{\Sigma^2}{\Delta_\theta}d\theta^2 + \frac{\Delta_\theta}{\Sigma^2}\sin^2\theta\left(a\, dt - \frac{r^2+a^2}{\Xi}d\phi\right)^2 \tag{A.85}$$

where

$$\Delta_r = \left(r^2+a^2\right)\left(1+\frac{r^2}{\epsilon L^2}\right) - 2mr, \quad \Xi = 1 - \frac{a^2}{\epsilon L^2}, \quad \Delta_\theta = 1 - \frac{a^2\cos^2\theta}{\epsilon L^2}, \quad \Sigma^2 = r^2 + a^2\cos^2\theta \tag{A.86}$$

where $\epsilon = +1$ for AdS and $\epsilon = -1$ for dS spacetimes, with $\Delta_r(r_+) = 0$ defining the outer horizon r_+ of the black hole. The inner and cosmological horizons are respectively defined from $\Delta_r(r_-) = 0$ and $\Delta_r(r_c) = 0$, the latter being present only for $\epsilon = -1$. The rotation parameter is bounded by $a < L$. The relevant thermodynamic quantities are

$$\begin{aligned} &M = \frac{m}{G_N\Xi^2}, \; J = \frac{ma}{G_N\Xi^2}, \; \Omega_\pm = \frac{a\left(1+\frac{r_\pm^2}{\epsilon L^2}\right)}{r_\pm^2 + a^2}, \\ &T = \frac{r_+}{2\pi}\left(1+\frac{r_+^2}{\epsilon L^2}\right)\frac{1}{r_+^2+a^2} - \frac{1}{4\pi r_+}\left(1-\frac{r_+^2}{\epsilon L^2}\right), \; S = \frac{\pi r_+^2}{4G_N} \end{aligned} \tag{A.87}$$

and are respectively the mass, angular momentum, horizon angular velocity, temperature, and entropy [301]. The metric is regular everywhere away from the symmetry axis for AdS, while it is regular and static only for $r < L$ in dS. Below, we will assume that $r > 0$ for AdS and $r < L$ for dS, unless otherwise stated (i.e. in subsection A.6.4).

We want to find the null hypersurfaces $\Phi(x) = \text{const}$ in the spacetime (A.85). Define the ingoing/outgoing Eddington-Finkelstein coordinates by

$$v = t + r^*, \qquad u = t - r^* \tag{A.88}$$

where the (tortoise) coordinate r^* will be defined below. The condition of the surfaces defined by $v = \text{const}$ being null translates to

$$g^{\alpha\beta}\partial_\alpha v \partial_\beta v = g^{tt} + g^{rr}(\partial_r r^*)^2 + g^{\theta\theta}(\partial_\theta r^*)^2 = 0. \tag{A.89}$$

Thus, the problem of finding the null hypersurfaces reduces to solving the PDE (A.89) for $r^*(r,\theta)$[50]. For the metric (A.85),

$$g^{tt} = \frac{g_{\phi\phi}}{g_{tt}g_{\phi\phi} - g_{t\phi}^2} = \frac{\left[a^2\Delta_r \sin^2\theta - \Delta_\theta(r^2+a^2)^2\right]}{\Delta_r\Delta_\theta\Sigma^2} \tag{A.90}$$

yielding

$$\Delta_r(\partial_r r^*)^2 + \Delta_\theta(\partial_\theta r^*)^2 = \frac{(r^2+a^2)^2}{\Delta_r} - \frac{a^2\sin^2\theta}{\Delta_\theta} \tag{A.91}$$

for the PDE (A.89). In the limit $L \to \infty$ this reduces to the asymptotically flat case [125]

$$\Delta(\partial_r r^*)^2 + (\partial_\theta r^*)^2 = \frac{(r^2+a^2)^2}{\Delta} - a^2\sin^2\theta \tag{A.92}$$

where now $\Delta \equiv \lim_{L\to\infty}\Delta_r = r^2 + a^2 - 2mr$.

This separable form allows us to easily guess an ansatz for $r^*(r,\theta)$. First, define

$$\begin{aligned} Q^2(r) &= \Xi^2\left[(r^2+a^2)^2 - a^2\lambda\Delta_r\right], \\ P^2(\theta) &= \Xi^2 a^2\left[\lambda\Delta_\theta - \sin^2\theta\right] \end{aligned} \tag{A.93}$$

[50]Note that, in the case of odd-dimensional equal-spinning black hole, the angular dependence drops and we have $r^*(r)$ only, which is considerably simpler and does not require solving PDEs.

where λ is an arbitrary constant. Then, it is clear that choosing

$$\partial_r r^* = \frac{Q(r)}{\Delta_r}, \qquad \partial_\theta r^* = \frac{P(\theta)}{\Delta_\theta} \tag{A.94}$$

would satisfy (A.91). Hence a solution to (A.91) is obtained by solving the exact integral

$$dr^* = \frac{Q}{\Delta_r} dr + \frac{P}{\Delta_\theta} d\theta. \tag{A.95}$$

To find a general solution $r^*(r,\theta)$ of (A.91) that is independent of λ we follow the procedure in [125] and assume first that λ is now a function of r and θ. In this case, $r^* = \rho(r,\theta,\lambda)$ where

$$d\rho = \frac{Q}{\Delta_r} dr + \frac{P}{\Delta_\theta} d\theta + \frac{a^2}{2} F d\lambda \tag{A.96}$$

where $\partial_\lambda \rho(r,\theta,\lambda) = \frac{a^2}{2} F(r,\theta,\lambda)$, and

$$F(r,\theta,\lambda) = \int_r^\infty \frac{1}{Q(r',\lambda)} dr' + \int_0^\theta \frac{1}{P(\theta',\lambda)} d\theta' + g'(\lambda). \tag{A.97}$$

The condition (A.95) implies that

$$F(r,\theta,\lambda) = 0 \tag{A.98}$$

which fixes the dependence of λ on (r,θ) for any given choice of the function $g[\lambda(r,\theta)]$. The explicit form of the general solution of (A.96) is then

$$\rho(r,\theta,\lambda) = \int_0^r \frac{Q}{\Delta_r} dr + \int_0^\theta \frac{P}{\Delta_\theta} d\theta + \frac{a^2}{2} g(\lambda). \tag{A.99}$$

Once $g(\lambda)$ is chosen, the exact integrals in (A.99) and (A.98) are performed assuming that λ is a constant. Then, (A.98) is used to solve for $\lambda(r,\theta)$, which in turn is substituted into the result obtained upon integrating (A.99). The net result is that $r^*(r,\theta) = \rho(r,\theta,\lambda(r,\theta))$ can be explicitly obtained.

A.6.2 $m \to 0$ limit: light cones in vacuum (A)dS metric

Here, we verify the expressions for the light cones above by taking the $m \to 0$ limit and showing that they reduce to light cones in vacuum (A)dS spacetime. We begin by simplifying the metric (A.85) using the coordinate transformation [302]

$$t \to \Xi t, \qquad \phi \to \Xi^{1/2} \phi - \frac{a\Xi}{\epsilon L^2} t \tag{A.100}$$

yielding

$$ds^2 = -\frac{\Delta_\theta}{\Sigma^2}\left[\Delta_r\Delta_\theta - a^2\sin^2\theta\big(1+\frac{r^2}{L^2}\big)^2\right]dt^2 + \frac{\Sigma^2}{\Delta_r}dr^2 + \frac{\Sigma^2}{\Delta_\theta}d\theta^2 + \frac{\sin^2\theta}{\Sigma^2\Xi}\left[(r^2+a^2)^2\Delta_\theta - a^2\Delta_r\sin^2\theta\right]d\phi^2 - \frac{4mra\Delta_\theta\sin^2\theta}{\Sigma^2\Xi^{1/2}}dtd\phi. \tag{A.101}$$

Taking the $m \to 0$ limit now gives

$$ds^2 = -\Xi\Delta_\theta\left(1+\frac{r^2}{\epsilon L^2}\right)dt^2 + \frac{\Sigma^2}{(r^2+a^2)\left(1+\frac{r^2}{L^2}\right)}dr^2 + \frac{\Sigma^2}{\Delta_\theta}d\theta^2 + \big(r^2+a^2\big)\sin^2\theta d\phi^2. \tag{A.102}$$

This metric is just the vacuum (A)dS metric

$$ds^2 = -\left(1+\frac{r^2}{\epsilon L^2}\right)dt^2 + \left(1+\frac{r^2}{\epsilon L^2}\right)^{-1}dr^2 + r^2d\theta^2 + r^2\sin^2\theta d\phi^2 \tag{A.103}$$

where the coordinate transformation from (A.103) to (A.102) is given by [303]

$$t \to \Xi t, \tag{A.104}$$

$$r \to \sqrt{\frac{r^2\left(1-\frac{a^2\cos^2\theta}{\epsilon L^2}\right)+a^2\sin^2\theta}{\Xi}}, \tag{A.105}$$

$$\theta \to \cos^{-1}\left(\frac{r\sqrt{\Xi}\cos\theta}{\sqrt{r^2\left(1-\frac{a^2\cos^2\theta}{\epsilon L^2}\right)+a^2\sin^2\theta}}\right), \tag{A.106}$$

$$\phi \to \sqrt{\Xi}\phi. \tag{A.107}$$

In the limit $m \to 0$,

$$Q \to Q_0 = \Xi\sqrt{(r^2+a^2)\left[r^2+a^2-a^2\lambda\big(1+\frac{r^2}{\epsilon L^2}\big)\right]} \tag{A.108}$$

and P remains the same. To simplify the integrals, we make the substitution

$$r = \frac{a\sqrt{1-\lambda}\sin\chi}{\sqrt{\lambda\Delta_\chi - \sin^2\chi}} \tag{A.109}$$

where $\Delta_\chi \equiv \lim_{\theta\to\chi}\Delta_\theta$, from which it follows that

$$\frac{dr}{Q_0} = \frac{d\chi}{a\Xi\sqrt{\lambda - \sin^2\chi - \frac{a^2\lambda\cos^2\chi}{\epsilon L^2}}} \tag{A.110}$$

The function F in (A.97) becomes

$$\begin{aligned} F(r,\theta,\lambda) &= \int_{\chi(r,\lambda)}^{\theta^*} \frac{d\chi'}{a\Xi\sqrt{\lambda - \sin^2\chi' - \frac{a^2\lambda\cos^2\chi'}{\epsilon L^2}}} + \int_0^{\theta} \frac{d\theta'}{a\Xi\sqrt{\lambda - \sin^2\theta' - \frac{a^2\lambda\cos^2\theta'}{\epsilon L^2}}} + g'(\lambda) \\ &= \int_{\chi(r,\lambda)}^{\theta} \frac{d\chi'}{a\Xi\sqrt{\lambda - \sin^2\chi' - \frac{a^2\lambda\cos^2\chi'}{\epsilon L^2}}} + \int_0^{\theta^*} \frac{d\chi'}{a\Xi\sqrt{\lambda - \sin^2\chi' - \frac{a^2\lambda\cos^2\chi'}{\epsilon L^2}}} + g'(\lambda) \end{aligned} \tag{A.111}$$

where

$$\sin^2\theta^* = \frac{\Xi\lambda}{1 - \frac{a^2\lambda}{\epsilon L^2}} \tag{A.112}$$

and the second term in (A.111) can be absorbed into $g'(\lambda)$ since it is independent of r and θ. Choosing $g(\lambda)$ such that the overall constant term in (A.111) is 0, the constraint $F = 0$ now gives

$$\chi(r,\lambda) = \theta. \tag{A.113}$$

From (A.109), this fixes the function $\lambda(r,\theta)$ to be

$$\lambda(r,\theta) = \frac{(r^2+a^2)\sin^2\theta}{r^2\Delta_\theta + a^2\sin^2\theta}. \tag{A.114}$$

Integrating (A.95) gives

$$\begin{aligned} r^* &= \int_0^r \frac{Q_0}{\Delta_\chi}dr' + \int_0^\theta \frac{P}{\Delta_\theta}d\theta' = \int_0^{\chi(r,\lambda)} \frac{Q_0^2}{\Delta_r}\frac{d\chi'}{a\Xi\sqrt{\lambda - \sin^2\chi - \frac{a^2\lambda\cos^2\chi}{\epsilon L^2}}} + \int_0^\theta \frac{P}{\Delta_\theta}d\theta' \\ &= \int_0^{\chi(r,\lambda)} \frac{a\Xi\lambda(1-\lambda)}{(\lambda - \sin^2\chi')\sqrt{\lambda - \sin^2\chi' - \frac{a^2\lambda\cos^2\chi'}{\epsilon L^2}}}d\chi' + \int_0^{\chi(r,\lambda)} \frac{a\Xi\sqrt{\lambda - \sin^2\chi - \frac{a^2\lambda\cos^2\chi}{\epsilon L^2}}}{1 - \frac{a^2\lambda\cos^2\chi'}{\epsilon L^2}}d\chi' \end{aligned} \tag{A.115}$$

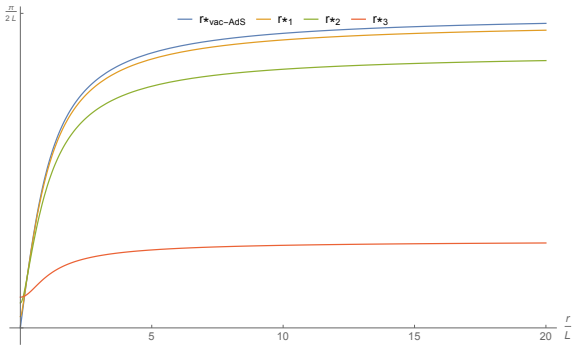

(a) AdS vacuum

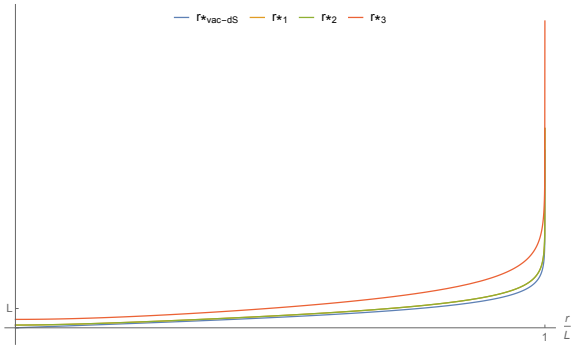

(b) dS vacuum

Figure A.8: The tortoise coordinate of (a) vacuum AdS, $r^* = L\tan^{-1}\left(\frac{r}{L}\right)$, and (b) vacuum dS, $r^* = L\tanh^{-1} = \left(\frac{r}{L}\right)$, compared with the numerical solution of (A.115) with $r_1 : a/L = 0.15$ (orange), $r_2 : a/L = 0.35$ (green), $r_3 : a/L = 0.85$ (red) for $\theta = \frac{\pi}{8}$. Convergence of (A.115) in the limit $a \to 0$ is implied, as expected from the transformation (A.104)-(A.107).

and upon substituting $\lambda(r,\theta)$ from (A.114) into the result gives $r^* = r^*(r,\theta)$ for (A)dS spacetime. The result of this integration in (A.115) can be written in terms of elliptic integrals which, in the limit $L \to \infty$ reduce to the flat space case [125]

$$r^* = \sqrt{r^2 + a^2\sin^2\theta} \tag{A.116}$$

as we show in the appendix of [3], where $\lambda = \sin\theta_*$ from (A.112). In the limit $a \to 0$ the expression for r^* reduces to the tortoise coordinate in vacuum (A)dS

$$r^*_{\text{vac-AdS}}(r) = L\tan^{-1}\left(\frac{r}{L}\right), \quad r^*_{\text{vac-dS}}(r) = L\tanh^{-1}\left(\frac{r}{L}\right) \tag{A.117}$$

which we illustrate numerically in figure A.8.

Thus, the surfaces $t \pm r^* = \text{const}$, with $r^*(r,\theta)$ given by (A.115), are the null hypersurfaces of vacuum (A)dS.

A.6.3 Properties of axisymmetric null hypersurfaces

The condition $F = 0$ implies that $dF = 0$, yielding

$$\mu d\lambda = -\frac{dr}{Q} + \frac{d\theta}{P}, \qquad \mu \equiv -\partial_\lambda F \tag{A.118}$$

from (A.97). In conjunction with (A.95), this shows that lines of constant r^* and λ are orthogonal, $\nabla r^*.\nabla\lambda = 0$, with respect to the intrinsic 2-metric

$$d\sigma^2 = \Sigma^2 \left[\frac{dr^2}{\Delta_r} + \frac{d\theta^2}{\Delta_\theta}\right] \tag{A.119}$$

of the (t,ϕ) sections of the Kerr-(A)dS spacetime. This proves that r_* and λ are orthogonal to one another on surfaces of constant (t,ϕ). Since λ is independent of t and ϕ, this in turn implies that λ is constant along the null generators in (A.88)

$$\ell^\alpha \partial_\alpha \lambda = 0 \qquad n^\alpha \partial_\alpha \lambda = 0 \tag{A.120}$$

where $\ell_\alpha = -\partial_\alpha v$ and $n_\alpha = -\partial_\alpha u$, with (u,v) given in (A.88). This follows from the fact that λ is independent of the coordinates t and ϕ. Along with the integrability of (A.118), this ensures that λ is constant along these null generators, and is a good coordinate, where asymptotically λ is obtained from $P \to 0$.

The 2-metric (A.119) can be written in (r^*,λ) coordinates instead of (r,θ) coordinates. It can easily be checked that

$$d\sigma^2 = \frac{1}{\Xi^2 R^2}\left[\Delta_r \Delta_\theta dr^{*2} + P^2 Q^2 \mu^2 d\lambda^2\right] \tag{A.121}$$

where

$$\begin{aligned} R^2 &\equiv \frac{g_{\phi\phi}}{\sin^2\theta} \\ &= \frac{\Delta_\theta (r^2+a^2)^2 - \Delta_r a^2 \sin^2\theta}{\Sigma^2 \Xi^2}. \end{aligned} \tag{A.122}$$

We can rearrange (A.90) so that

$$\begin{aligned} g_{tt} - \frac{g_{t\phi}^2}{g_{\phi\phi}} &= \frac{1}{g^{tt}}, \\ g_{tt} - \omega_B^2 g_{\phi\phi} &= \frac{1}{g^{tt}}, \\ \frac{\Delta_r - a^2\Delta_\theta \sin^2\theta}{\Sigma^2} + \omega_B^2 R^2 \sin^2\theta &= \frac{\Delta_r \Delta_\theta}{\Xi^2 R^2}, \end{aligned} \tag{A.123}$$

where

$$\omega_B \equiv -\frac{g_{t\phi}}{g_{\phi\phi}} = a\frac{\Delta_\theta(r^2+a^2) - \Delta_r}{\Xi\Sigma^2 R^2} \tag{A.124}$$

is the angular velocity [304] of inertial frame dragging, due to the rotation of the black hole. This allows us to rewrite the Kerr-(A)dS metric (A.85) in (t, r^*, λ, ϕ) coordinates as

$$ds^2 = \frac{\Delta_r\Delta_\theta}{\Xi^2 R^2}\left(dr^{*2} - dt^2\right) + R^2\sin^2\theta(d\phi - \omega_B dt)^2 + \frac{P^2Q^2}{\Xi^2 R^2}\mu^2 d\lambda^2. \tag{A.125}$$

This form of the metric has distinct advantages over (A.85): since the ingoing and outgoing null generators, defined in (A.88), are constant ($dv = du = 0$), then $dr_*^2 = dt^2$. In these coordinates, we can explicitly write the components of the null vectors ℓ_α and n_α defined in (A.120) as

$$\ell_\alpha = \left[-\frac{\Delta_r\Delta_\theta}{2\Xi^2 R^2 A}, -\frac{\Delta_r\Delta_\theta}{2\Xi^2 R^2 A}, 0, 0\right] \tag{A.126}$$

and

$$n_\alpha = [-A, A, 0, 0] \tag{A.127}$$

where A is an arbitrary constant, and we have imposed the normalization condition $\ell.n = -1$. Using this, the induced metric on the associated null hypersurface is

$$h_{\mu\nu} = \ell_\mu n_\nu + n_\mu \ell_\nu + g_{\mu\nu} \tag{A.128}$$

or alternatively

$$dh^2 = R^2\sin^2\theta\,(d\phi - \omega dt)^2 + \frac{P^2Q^2\mu^2}{\Xi^2 R^2}d\lambda^2 \tag{A.129}$$

which has one null and 2 spatial directions, and so has vanishing determinant. Even more simply we have

$$h^{\mu\nu} = \mathrm{diag}[0, 0, s^{ab}] \tag{A.130}$$

where

$$s^{ab} = \text{diag}\left[\frac{\Xi^2 R^2}{P^2 Q^2 \mu^2}, \frac{1}{R^2 \sin^2\theta}\right] \tag{A.131}$$

is the inverse of the induced metric on a 2-dimensional constant u slice of the null hypersurface. The form of the hypersurface metric shows that the null generators are themselves rotating with the ZAMO angular velocity ω, relative to observers at infinity. This can also be seen directly from the fact that $\ell_\phi = -\partial_\phi v = 0$ and $n_\phi = -\partial_\phi u = 0$. Also note that inversion of the differentials (A.95) and (A.118) gives

$$\begin{aligned} \Xi^2\Sigma^2 R^2 dr &= \Delta_r Q\left[\Delta_\theta dr^* - P^2\mu d\lambda\right], \\ \Xi^2\Sigma^2 R^2 d\theta &= \Delta_\theta P\left[\Delta_r dr^* + Q^2\mu d\lambda\right]. \end{aligned} \tag{A.132}$$

We pause to comment on the construction of quasi-spherical light cones. These surfaces are those that reduce to the light cones of (A)dS spacetime as $r \to \infty$. We first note that insertion of (A.114) into (A.112) yields

$$\sin^2\theta^* = \frac{(r^2 + a^2)\sin^2\theta}{r^2 + a^2\sin^2\theta} \tag{A.133}$$

which is the same relation as in the asymptotically flat case [125], and we have $\theta^*(r \to \infty, \theta) = \theta$. Requiring this asymptotic condition and the relation (A.112) to hold in the Kerr-(A)dS spacetime fixes the function $g'(\lambda)$ in (A.97) to yield the relation

$$F(r,\theta,\lambda) = \int_r^\infty \frac{1}{Q(r',\lambda)} dr' - \int_\theta^{\theta^*} \frac{1}{P(\theta',\lambda)} d\theta'. \tag{A.134}$$

The equations of the quasi-spherical hypersurfaces are respectively given by $v = t + r^*(r,\theta) = v_0$ and $u = t - r^*(r,\theta) = u_0$ where (u_0, v_0) are both constants, and $r^* = \rho(r,\theta,\lambda(r,\theta))$, with the function $\lambda(r,\theta)$ determined by setting $F = 0$.

A.6.4 The absence of caustics

The condition for caustic formation is where the determinant of the inverse induced metric s^{ab} in (A.131) becomes singular

$$PQ\mu\sin\theta \to 0 \tag{A.135}$$

where μ is defined in (A.118). Interpreting the metric s_{ab} as describing the two-dimensional surface along which a null ray moves, this metric will not be degenerate, i.e. will have a

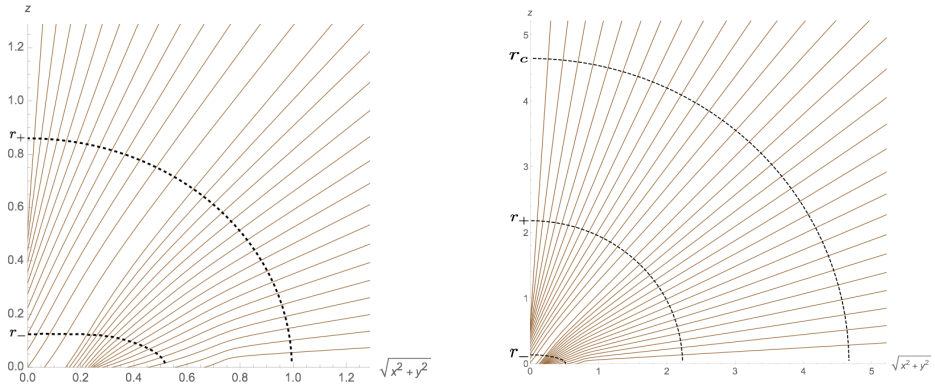

(a) Kerr-AdS (b) Kerr-dS

Figure A.9: Projection of the path of null generators onto the Cartesian plane ($\sqrt{x^2+y^2} = \sqrt{r^2+a^2}\sin\theta, z = r\cos\theta$) for (a) Kerr-AdS spacetime with $m = L = 2a = 1$, and (b) Kerr-dS spacetime with $m = 2a = 1$ and $L \approx 6.12372$. In both cases, the light sheets do not converge to form a caustic near the black hole. Also shown are the various horizons of the spacetime r_i, $i = -, +, c$.

nonzero volume, unless a caustic forms. This is precisely condition (A.135). In the limit $m \to 0$, the light cones in vacuum (A)dS spacetime have no caustics. Light cones in the Kerr metric were shown to be free of caustics in [125]. Here, we show that the proof of [125] also extends to Kerr-(A)dS spacetimes.

The proof proceeds by showing that each factor in (A.135) for $m > 0$ increases along an ingoing null generator of fixed λ and decreasing r, which proves that (A.135) will not be satisfied in Kerr-(A)dS since it is not satisfied in its $m \to 0$ limit. Initially, when $r \to \infty$, it is clear from (A.109) that $\lambda > 0$. From (A.118) and (A.93), $P > 0$ increases as r decreases along the generator of fixed λ. Also, from (A.93), it is clear that $Q > Q_0 > 0$.

The remaining task is to show that μ and θ both increase with increasing m, while r and λ are kept fixed, that is

$$\left(\frac{\partial\theta}{\partial m}\right)_{r,\lambda} > 0 \qquad \left(\frac{\partial\mu}{\partial m}\right)_{r,\lambda} > 0 \tag{A.136}$$

provided $r > 0$ and $\theta_* < \pi/2$. From (A.97) and the condition $F = 0$, it is straightforward to show that

$$\left(\frac{\partial\theta}{\partial m}\right)_{r,\lambda} = a^2\lambda P \int_r^\infty \frac{r'dr'}{Q^3(r',\lambda,m)}. \tag{A.137}$$

Similarly, from (A.118) and (A.97),

$$\begin{aligned}\left(\frac{\partial\mu}{\partial m}\right)_{r,\lambda} &= \frac{\partial\mu}{\partial m} + \frac{\partial\mu}{\partial\theta}\left(\frac{\partial\theta}{\partial m}\right)_{r,\lambda} \\ &= a^2\left(1+\frac{a^2\lambda\Delta_\theta}{2P^2}\right)\int_r^\infty \frac{r'dr'}{Q^3(r',\lambda,m)} \\ &\quad + \frac{3}{2}a^4\lambda\int_r^\infty \frac{r'\Delta_r(r',m)dr'}{Q^5(r',\lambda,m)}\end{aligned} \tag{A.138}$$

Both expressions (A.137) and (A.138) are clearly positive regardless of the sign of the cosmological constant. Therefore, the condition (A.135) is never satisfied in Kerr-(A)dS and the null hypersurfaces (A.131) do not develop caustics when propagated toward $r \to 0$.

In figure A.9, the λ = const. curves were obtained for Kerr-AdS (figure A.9a) and Kerr-dS (figure A.9b) spacetimes by numerically solving the evolution equations of the null generators along ingoing null hypersurfaces

$$l^\alpha = \frac{dx^\alpha}{d\tau} = -g^{\alpha\beta}\partial_\beta v \tag{A.139}$$

where τ is the affine parameter along the null path. In particular, (A.139) yield

$$\dot{r} = -\frac{Q}{\Sigma^2}, \qquad \dot{\theta} = -\frac{P}{\Sigma^2} \tag{A.140}$$

which we numerically integrate to plot the null paths in figure A.9. Also shown are the spacetime horizons: r_-, r_+, and r_c for Kerr-dS. Figure A.9 shows that no caustics are formed in both spacetimes near the black hole singularity.

As in the asymptotically flat case, we find that if we extend the spacetime to $r < 0$, then null rays moving inward toward the origin in the $r > 0$ sheet are deflected outward by the ring singularity and defocused. Upon passing through the $r = 0$ disc they are refocused and form a caustic in the $r < 0$ region.

A.6.5 Kruskal coordinates

Using the transformations

$$-\frac{dU}{\kappa U} = d(t-r^*) = du, \qquad \frac{dV}{\kappa V} = d(t+r^*) = dv \tag{A.141}$$

we can rewrite the metric (A.125) as

$$ds^2 = \frac{\Delta_r \Delta_\theta}{\Xi^2 R^2} \frac{dU dV}{\kappa^2 UV} + R^2 \sin^2\theta \left(d\phi - \frac{\omega_B}{2\kappa} \left(\frac{dV}{V} - \frac{dU}{U} \right) \right)^2 + \frac{P^2 Q^2}{\Xi^2 R^2} \mu^2 d\lambda^2 \tag{A.142}$$

where $\kappa = \kappa_i$ is the surface gravity

$$\kappa_i = \frac{d\Delta_r}{dr} |_{r=r_i} \qquad i = +, -, c \tag{A.143}$$

for the respective outer, inner, and (for $\epsilon = -1$) cosmological horizon as relevant. Since

$$UV = -e^{2\kappa r^*} \qquad \frac{V}{U} = -e^{2\kappa t} \tag{A.144}$$

it is clear that the first term in the metric is regular at the horizon surfaces $U = 0$ and $V = 0$. However the second term in (A.142) is not regular on these surfaces. This defect can be overcome by defining

$$\varphi_+ = \phi + \alpha(r, \lambda) \qquad \varphi_- = \phi - \alpha(r, \lambda) \tag{A.145}$$

where

$$\alpha(r, \lambda) = a\Xi^3 \left[\int_0^r \frac{r'^2 + a^2}{\Delta_r(r') Q(r', \lambda)} dr' - \int_0^\theta \frac{1}{\Delta_\theta(\theta') P(\theta', \lambda)} d\theta' \right]. \tag{A.146}$$

Then, from (A.132), (A.124), and (A.93),

$$d\alpha = \omega_B dr^* - N d\lambda \tag{A.147}$$

where

$$N \equiv a\mu\Xi \frac{(r^2 + a^2)P^2 + Q^2}{\Sigma^2 R^2} - \frac{a^3 \Xi^3}{2} \left[\int_0^r \frac{r'^2 + a^2}{Q^3(r', \lambda)} dr' + \int_0^\theta \frac{1}{P^3(\theta', \lambda)} d\theta' \right]. \tag{A.148}$$

Hence, the metric (A.125) becomes

$$ds^2 = \frac{\Delta_r \Delta_\theta}{\Xi^2 R^2} \frac{dU dV}{\kappa^2 UV} + R^2 \sin^2\theta (d\varphi_+ - \omega_B dv + N d\lambda)^2 + \frac{P^2 Q^2}{\Xi^2 R^2} \mu^2 d\lambda^2 \tag{A.149}$$

or alternatively

$$ds^2 = \frac{\Delta_r \Delta_\theta}{\Xi^2 R^2} \frac{dU dV}{\kappa^2 UV} + R^2 \sin^2\theta (d\varphi_- - \omega_B du - N d\lambda)^2 + \frac{P^2 Q^2}{\Xi^2 R^2} \mu^2 d\lambda^2 \tag{A.150}$$

depending on which sheet is of interest. For example, (A.149) is regular for the future horizons for both outer and inner horizons of the black hole (or the future cosmological horizon in Kerr-dS), where φ_+ is constant along each ingoing generator and v is constant along ingoing light sheets. Alternatively, (A.150) is regular for the past horizons for both outer and inner horizons of the black hole (or the past cosmological horizon in Kerr-dS), where φ_- is constant along each outgoing generator and u is constant along outgoing light sheets. In both cases the function N is regular.

A.6.6 Summary

We have described a three-dimensional foliation of Kerr-(A)dS spacetimes in terms of quasi-spherical light cones, extending the construction in the asymptotically flat case [125]. We find that both spacetimes are free of caustics for $r > 0$. The limit of zero mass of this foliation was taken and we proved that it reduces to light cones in vacuum (A)dS spacetime, which is an important consistency check. As an application, we derived a generalization of Kruskal coordinates for Kerr-(A)dS based on these quasi-spherical light cones.

These results should prove useful in understanding the causal structure of Kerr-(A)dS spacetimes, in numerical general relativity [298], and understanding wave propagation [299] in rotating spacetimes with a cosmological constant. It is likewise natural to consider a similar type of analysis to study the properties of light cones in more exotic rotating spacetimes or in higher dimensions. Furthermore, this analysis of light cones may prove useful in a numerical study of holographic complexity for Kerr-AdS black holes.

Appendix B

Appendices to chapter 3

B.1 An alternative construction of the three-boundary black hole

We constructed a three-boundary black hole in section 3.2.1 by choosing some AdS_3 isometries and taking a quotient by the group Γ that they generate. Although the representation of the generators used there is convenient for calculation, it makes the third asymptotic region (whose horizon is generated by $\gamma_1^{-1}\gamma_2$ and $\gamma_1\gamma_2^{-1}$) appear to be on a different footing than the other two. In particular, as described in the standard AdS_3 conformal frame the coordinate size of this third region vanishes in the hot limit. To show that this is an artifact of our choice of generators, we give an alternative representation below where the coordinate size of the third boundary is non-vanishing in the hot limit. For simplicity, we focus on the non-rotating case which is generated by a diagonal subgroup of isometries where $\gamma_L = \gamma_R \equiv \gamma$. Dropping this diagonal restriction will give a generalized to the rotating case.

We begin with the most general form of a $SL(2,\mathbb{R})$ generator:

$$\xi = x_1 J_1 + x_2 J_2 + x_3 J_3. \tag{B.1}$$

This generator is hyperbolic when $x_1^2 + x_2^2 - x_3^2 > 0$, which is equivalent to the requirement $\operatorname{Tr} e^{\xi} > 2$. The length of horizon generated by $\gamma = e^{\xi}$ is

$$\ell = 2\cosh^{-1}\frac{\operatorname{Tr}\gamma}{2} = \sqrt{x_1^2 + x_2^2 - x_3^2}. \tag{B.2}$$

It is thus natural to parametrize our generator as

$$\xi = \ell(\cosh\alpha \sin\beta J_1 + \cosh\alpha\cos\beta J_2 - \sinh\alpha J_3) \equiv \ell(\vec{a}\cdot\vec{J}) \tag{B.3}$$

where the generator is written as an inner product taken with signature $(++-)$, where $\vec{a} = (\cosh\alpha\sin\beta, \cosh\alpha\cos\beta, \sinh\alpha)$, and $\vec{J} = (J_1, J_2, J_3)$.

To make a three-boundary wormhole, we choose two such generators

$$\xi_1 = \ell_1(\cosh\alpha_1 \sin\beta_1 J_1 + \cosh\alpha_1\cos\beta_1 J_2 - \sinh\alpha_1 J_3) = \ell_1(\vec{a}_1\cdot\vec{J}) \tag{B.4}$$

$$\xi_2 = \ell_2(\cosh\alpha_2 \sin\beta_2 J_1 + \cosh\alpha_2\cos\beta_2 J_2 - \sinh\alpha_2 J_3) = \ell_2(\vec{a}_2\cdot\vec{J}), \tag{B.5}$$

so that the corresponding group elements are $\gamma_1 = e^{\xi_1}$ and $\gamma_2 = e^{\xi_2}$. Then the group element related to the third asymptotic region is $\gamma_3 = -\gamma_1^{-1}\gamma_2$. As a result, the horizon length of the third region are related to our parameters by

$$\cosh\frac{\ell_3}{2} = -\cosh\frac{\ell_1}{2}\cosh\frac{\ell_2}{2} + \sinh\frac{\ell_1}{2}\sinh\frac{\ell_2}{2}(\vec{a}_1\cdot\vec{a}_2). \tag{B.6}$$

Note that our geometry depends only on the three parameters $\{\ell_1, \ell_2, \vec{a}_1\cdot\vec{a}_2\}$, or equivalently $\{\ell_1, \ell_2, \ell_3\}$. This gives the expected three-dimensional moduli space for a non-rotating 3-boundary wormhole.

Our previous representation corresponds to the choice $\vec{a}_1 = (0, -1, 0)$ and $\vec{a}_2 = (0, -\cosh\alpha, -\sinh\alpha)$. These choices reproduce our previous results. In particular, our previous representation does not involve J_1.

However, this choice is far from unique. The only real restriction on the form of the generators is that the geometry not become the one-boundary torus wormhole described in [166]. To make a $(3,0)$ wormhole, the bulk geodesic connecting the fixed points of γ_1 must not cross that connecting the fixed points of γ_2, while they cross each other in the $(1,1)$ wormhole construction.

To be definite, let us choose generators with

$$\alpha_1 = -\alpha_2 = \alpha, \quad \beta_1 = -\beta_2 = \beta = \frac{\pi}{4}. \tag{B.7}$$

This ansatz still allows the freedom to vary the horizon lengths by tuning ℓ_1, ℓ_2, α. Then, as we did in section 3.2.2, we could calculate the eigenvectors of the γ_i's and analyze the fixed points on the boundary in the hot limit, and those fixed points are also endpoints of the horizons. For the non-rotating case, all the fixed points are on the $t = 0$ slice, and here

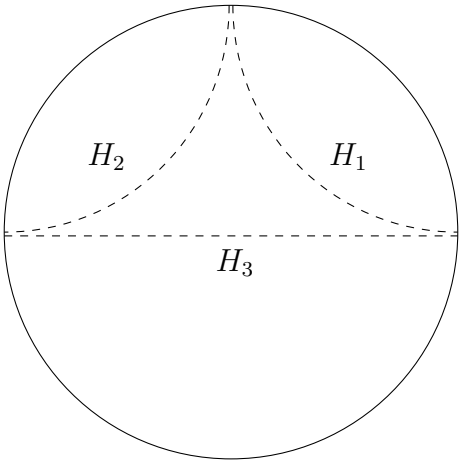

Figure B.1: The three-boundary wormhole in the hot limit under our alternative construction with $\alpha_1 = -\alpha_2 = \alpha, \beta_1 = -\beta_2 = \beta = \frac{\pi}{4}$, where H_1, H_2 and H_3 are the three horizons. The fixed points of distinct generators become close to each other in this limit, but each asymptotic region remains a finite size.

we take $\phi \in [0, 2\pi)$. As shown in figure B.1, in the hot limit the endpoints of H_1 approach $\phi = 3\pi/2$ and $\phi = \pi$, while the endpoints of H_2 approach $\phi = 3\pi/2$ and $\phi = 0$, and ethe ndpoints of H_3 approach $\phi = 0$ and $\phi = \pi$. Recalling that H_3 is generally described by a pair of geodesics in the AdS_3 covering space, we see that one of these geodesics still shrinks to zero coordinate size along the boundary in this limit, though the other part of H_3 remains of finite size.

B.2 Minimal distance between horizons in the hot limit

We now generalize (3.58) to the case of the rotating $(3, 0)$ geometry. We focus on the distance d_{12} between H_1 and H_2 since it is the simplest in our representation of the geometry. Due to the symmetry of the construction, the point on H_1 that is closest to H_2 sits at the origin of global coordinates. Furthermore, if the point on H_2 that is closest to H_1 has coordinates (t_m, r_m, ϕ_m), then $t_m = 0$ by left-right symmetry (see figure 3.6b) and we can set the angular coordinate such that $\phi_m = 0$. Recall that any geodesic in AdS_3 can be viewed as the intersection of a plane in the embedding space (3.2) that passes through the origin with the hyperboloid of AdS_3. The idea here is to find the two vectors that span the

plane defining H_2, then use them to find r_m. Using the geodesic distance equation (3.10), we can then find d_{12}.

Suppose that the left and right corners of the diamond of H_2 have coordinates $(-t_0, -\phi_0)$ and (t_0, ϕ_0), respectively, at the boundary. Using (3.36) and (3.35), it is straightforward to show that

$$t_0 = \tan^{-1} e^{-\alpha} - \tan^{-1} e^{-\tilde{\alpha}} \tag{B.8}$$

$$\phi_0 = \tan^{-1} e^{-\alpha} + \tan^{-1} e^{-\tilde{\alpha}}. \tag{B.9}$$

Then, in embedding space, the vectors $\vec{v}_i = (X_i, Y_i, U_i, V_i)$ that point from the origin to the points $(-t_0, -\phi_0)$ and (t_0, ϕ_0) at the boundary can be found using (3.3) to be

$$\vec{v}_L = (\cos\phi_0, -\sin\phi_0, \cos t_0, -\sin t_0) \quad \text{and} \quad \vec{v}_R = (\cos\phi_0, \sin\phi_0, \cos t_0, \sin t_0)\,. \tag{B.10}$$

The vector connecting the origin with $(0, r_m, 0)$ is parallel to $\vec{v}_L + \vec{v}_R$. From this, it is easy to show that

$$\frac{r_m}{\sqrt{1+r_m^2}} = \frac{\cos\phi_0}{\cos t_0} \tag{B.11}$$

The matrix representation of $(0, r_m, 0)$ is

$$p_m = \begin{pmatrix} \sqrt{1+r_m^2} + r_m & 0 \\ 0 & \sqrt{1+r_m^2} - r_m, \end{pmatrix} \tag{B.12}$$

So, using (3.10), the minimal distance between H_1 and H_2 is the geodesic distance between p_m and the origin and is given by

$$d_{12} = \cosh^{-1}\left(\frac{\mathrm{Tr}\, p_m}{2}\right) = \cosh^{-1}\left(\sqrt{1+r_m^2}\right). \tag{B.13}$$

Combining this with (B.11) gives

$$d_{12} = \tanh^{-1}\left(\frac{\cos\phi_0}{\cos t_0}\right). \tag{B.14}$$

After some algebra, this can be simplified to

$$d_{12} = \frac{\alpha + \tilde{\alpha}}{2}. \tag{B.15}$$

which implies that $\alpha, \tilde{\alpha} \geq 0$. As a consistency check, note that in the non-rotating case where $\ell_i = \tilde{\ell}_i$, we have

$$\alpha = \tilde{\alpha} \Rightarrow d_{12} = \alpha, \tag{B.16}$$

which is precisely (3.59) as quoted in section 3.2.4. Other minimal geodesic distances (i.e. d_{23} and d_{13}) can be obtained from (B.15) by simple permutations. This completes our generalization of the minimal geodesic distance equation to the rotating case. That the angular domain D_ϕ over which d_{12} is exponentially small is also large compared with the AdS length scale in the rotating case follows from the same analysis as in [161] through an appropriate choice of the Cauchy slice on which the distance is calculated.

B.2.1 The large horizon limit near extremality

This is the limit where

$$\ell_i \to \infty \quad \text{and} \quad \tilde{\ell}_i \to 0 \quad \Leftrightarrow \quad h_i \to \infty \quad \text{and} \quad T_{H,i} \to 0. \tag{B.17}$$

From (B.15), it is easy to see that the above requires

$$\alpha \to 0 \quad \text{and} \quad \tilde{\alpha} \to \infty \quad \Rightarrow \quad d_{ij} \to \infty. \tag{B.18}$$

This shows that the minimal geodesic distance between the horizons in the extremal limit will diverge. In particular, one can show that the divergence is logarithmic $d_{ij} \sim \log\left(2/\pi T_H\right) + \mathcal{O}\left(T_H^2\right)$. Note however that the hot limit studied in chapter 3 instead yields

$$\ell_i \to \infty \quad \text{and} \quad \tilde{\ell}_i \to \infty \quad \Leftrightarrow \quad h_i \to \infty \quad \text{and} \quad T_{H,i} \to \infty, \tag{B.19}$$

implying that

$$\alpha \to 0 \quad \text{and} \quad \tilde{\alpha} \to 0 \quad \Rightarrow \quad d_{ij} \to 0. \tag{B.20}$$

Thus our hot limit implies large horizons, but near extremality large horizons do not imply a hot limit. It also shows that the exponentially small local causal shadow region exists *only* in the hot limit where α and $\tilde{\alpha}$ are both small.